Universidade do Estado do Rio de Janeiro

Centro de Tecnologia e Ciências

Instituto de Física Armando Dias Tavares

Kevin Mota Amarilo

Study of associated production of Υ and $D^{*\pm}$ in pp collisions at $\sqrt{s} = 13$ TeV with the CMS detector at LHC and contributions for the maintenance, performance and upgrade of the RPC system

Rio de Janeiro

2023

Kevin Mota Amarilo

Study of associated production of Υ and D$^{*\pm}$ in pp collisions at $\sqrt{s} = 13$ TeV with the CMS detector at LHC and contributions for the maintenance, performance and upgrade of the RPC system

Tese apresentada, como requisito parcial para obtenção do título de Doutor, ao Programa de Pós-Graduação em Física, da Universidade do Estado do Rio de Janeiro.

Orientador: Prof. Dr. Wagner de Paula Carvalho
Coorientador: Prof. Dr. Alberto Franco de Sá Santoro

Rio de Janeiro
2023

CATALOGAÇÃO NA FONTE
UERJ/ REDE SIRIUS / BIBLIOTECA CTC/D

A485s Amarilo, Kevin Mota.
Study of associated production of Y and $D^{*\pm}$ in pp collisions at $\sqrt{s} = 13$ TeV with the CMS detector at LHC and contributions for the maintenance, performance and upgrade of the RPC system / Kevin Mota Amarilo. – 2023.
167 f. : il.

Orientador: Wagner de Paula Carvalho.
Coorientador: Alberto Franco de Sá Santoro.
Tese (doutorado) - Universidade do Estado do Rio de Janeiro, Instituto de Física Armando Dias Tavares.

1. Colisões (Física nuclear) – Teses. 2. Solenóide de múon compacto – Teses. 3. Grande colisor de hádrons (França e Suíça) – Teses. 4. Cromodinâmica quântica – Teses. I. Carvalho, Wagner de Paula (Orient.). II. Santoro, Alberto Franco de Sá (Coorient.). III. Universidade do Estado do Rio de Janeiro. Instituto de Física Armando Dias Tavares. IV. Título.

CDU 539.12-17

Bibliotecária: Teresa da Silva CRB7/5209

Assinatura Data

Kevin Mota Amarilo

Study of associated production of Υ and $D^{*\pm}$ in pp collisions at $\sqrt{s} = 13$ TeV with the CMS detector at LHC and contributions for the maintenance, performance and upgrade of the RPC system

Tese apresentada, como requisito parcial para obtenção do título de Doutor, ao Programa de Pós-Graduação em Física, da Universidade do Estado do Rio de Janeiro.

Aprovada em 08 de maio de 2023.
Banca Examinadora:

Prof. Dr. Wagner de Paula Carvalho (Orientador)
Instituto de Física Armando Dias Tavares - UERJ

Prof. Dr. Alberto Franco de Sá Santoro (Coorientador)
Instituto de Física Armando Dias Tavares - UERJ

Prof. Dr. Jussara Marques de Miranda
Centro Brasileiro de Pesquisas Físicas

Prof. Dr. Luciano Melo Abreu
Universidade Federal da Bahia

Dr. Felipe Torres da Silva de Araújo
Universidade Técnica de AACHEN

Luiz Martins Mundim Filho
Instituto de Física Armando Dias Tavares - UERJ

Sandro Fonseca de Souza
Instituto de Física Armando Dias Tavares - UERJ

Marcia Begalli
Instituto de Física Armando Dias Tavares - UERJ

Rio de Janeiro
2023

DEDICATION

To my family.

ACKNOWLEDGEMENTS

I would like to thank all the people who were present in my life during the course of my PhD. Every exchange was important to some extent to shape us into what we are. In special, I would like to acknowledge:

- the Rio de Janeiro State University and the Armando Dias Tavares Physics Institute for the support in the course of my degree;
- the High Energy Physics GRID (HEPGRID) for the computing resources;
- the Caltech for providing access to their T2 storage. In special, I would like to express my gratitude to Harvey Newman;
- the Carlos Chagas Filho Foundation for Research Support in the State of Rio de Janeiro (FAPERJ) for the scholarship that supported me in the course of my Ph.D. degree;
- the Ministry of Education (MEC) and the Coordination of Superior Level Staff Improvement (CAPES) for the support during my doctoral stay at CERN.
- the European Organization for Nuclear Research (CERN) for the construction and operation Large Hadron Collider (LHC);
- the Compact Muon Solenoid (CMS) collaboration for providing the all the instrumentation and experimental data for this study;
- my colleagues from (DFNAE), for all the collaboration, discussions and help;
- my colleagues from CMS-RPC, in special Felipe, Gabriella, Jan, Mariana, Mapse, Mehar, Nicolas and Salvatore. Which were very important not only for the development of my research, but for the sharing a multitude of moments that made the RPC a second home for me;
- my advisor Prof. Wagner Carvalho for all the lessons and guidance during for the development of this thesis and for my career;
- my co-advisor Prof. Alberto Santoro, which was the person who brought me to the High Energy Physics field and is a source of inspiration for me;
- my family - my father, Luis, my mother Vera and my brothers Killian and Kierlin - which are the most important people in my life. This thesis is dedicated to you.

This work was carried out with the support of the Coordination for the Improvement of Higher Education Personnel - Brazil (CAPES) - Financing Code 001.

nunca cometo o mesmo erro
duas vezes
já cometo duas três
quatro cinco seis
até esse erro aprender
que só o erro tem vez

Paulo Leminski

ABSTRACT

AMARILO, K. M. *Study of associated production of* Υ *and* $D^{*\pm}$ *in pp collisions at* $\sqrt{s} = 13$ *TeV with the CMS detector at LHC and contributions for the maintenance, performance and upgrade of the RPC system.* 2023. 167 f. Tese (Doutorado em Física) – Instituto de Física Armando Dias Tavares, Universidade do Estado do Rio de Janeiro, Rio de Janeiro, 2023.

This work presents the analysis of the associated production of Υ and $\mathrm{D}^{*\pm}$ using pp collision data collected by CMS, at $\sqrt{s} = 13$ TeV, with integrated luminosity of 123 fb^{-1}. The associated production of Υ and open charm hadrons is considered a golden channel to study the double-parton scattering (DPS), as the single-parton scattering contribution (SPS) is expected to be negligible. The reconstruction of the two mesons is done through $\Upsilon(nS) \to \mu^+\mu^-$ and $D^{*+} \to D^0\pi^+ \to K^-\pi^+\pi^+$ decay channels. A fiducial cross section for the Υ + D^* production is measured and, by assuming that the production occurs exclusively via DPS, a lower limit of the effective cross section of 7.5 ± 1.1 mb is obtained. Apart from the analysis, this document also discuss the work done for the CMS RPC project on the maintenance and commissioning, in preparation for the new data taking period (Run 3), and the R&D of the new iRPC detectors expected to be installed in CMS during the Phase 2 upgrade.

Keywords: Multiple parton scattering. Quantum chromodynamics. Compact muon solenoid. Resistive plate chambers.

RESUMO

AMARILO, K. M. *Estudo da produção associada de* Υ *and* $D^{*\pm}$ *em colisões pp em* $\sqrt{s} = 13$ *TeV com o detector CMS no LHC e contribuições para a manutenção, performance e upgrade do sistema de RPC.* 2023. 167 f. Tese (Doutorado em Física) – Instituto de Física Armando Dias Tavares, Universidade do Estado do Rio de Janeiro, Rio de Janeiro, 2023.

Esse trabalho apresenta a análise da produção associada de Υ e $\mathrm{D}^{*\pm}$ usando dados de colisões pp coletadas pelo CMS, em $\sqrt{s} = 13$ TeV, com luminosidade integrada de 123 fb^{-1}. A produção associada de Υ e hádrons *open charm* é considerada muito interessante para estudar o espalhamento duplo de pártons (da sigla em inglês, DPS), uma vez que é esperado que a contribuição do espalhamento simples de pártons (da sigla em inglês, SPS) seja negligível. A reconstrução dos dois mésons é feita pelos canais de decaimento $\Upsilon(nS) \to \mu^+\mu^-$ e $D^{*+} \to D^0\pi^+ \to K^-\pi^+\pi^+$. A seção de choque fiducial para a produção de Υ + D^* é medida e, assumindo que a produção é feita exclusivamente via DPS, usada para obter um limite inferior de 7.5 ± 1.1 mb para a seção de choque efetiva. Além da análise, esse documento também discute os trabalhos desenvolvidos na manutenção e comissionamento dos detectores do projeto CMS RPC, em preparação para o novo período de tomada de dados (Run 3), e da P&D dos novos detectores iRPC que devem ser instalados no CMS durante o upgrade fase 2.

Palavras-chave: Múltiplo espalhamento partônico. Cromodinâmica quântica. Solenoide compacto de muons. Câmara de placas resistivas.

LIST OF FIGURES

LIST OF TABLES

LIST OF ABBREVIATIONS

ADC	Analog-to-Digital Converter
AFS	Axial Field Spectrometer
ALEPH	Apparatus for LEP PHysics
ALICE	A Large Ion Collider Experiment
ATLAS	A Toroidal LHC Apparatus
BSM	Beyond Standard Model
BX	Bunch Crossing
CDF	Collider Detector at Fermilab
CERN	Organisation Européenne pour la Recherche Nucléaire/European Organization for Nuclear Research
CMS	Compact Muon Solenoid
CSC	Cathode Strip Chambers
D0	D0 experiment
DCS	Detector Control System
DIP	Data Interchange Protocol
DSS	Detector Safety System
DPS	Double-Parton Scattering
DT	Drift Tubes
EB	ECAL Barrel
ECAL	Electromagnetic Calorimeter
EE	ECAL Endcap
FEB	Front-End Board
FSR	Final State Radiation
GIF	Gamma Irradiation Facility
GUI	Graphical User Interface
GWP	Global Warming Potential
FPGA	Field Programmable Gate Arrays
FSM	Finite State Machine
GEM	Gas-Electron Multiplier
HB	HCAL Barrel
HCAL	Hadronic Calorimeter
HE	HCAL Endcaps
HF	Forward Calorimeter
HLT	High Level Trigger
HL-LHC	High Luminosity LHC
HO	HCAL Outer Calorimeter

HPL	High Pressure Laminate
HV	High Voltage
IP	Interaction Point
ISR	Initial State Radiation
JCOP	Joint Control Project
iRPC	improved RPC
LEP	Large Electron-Positron Collider
LHC	Large Hadron Collider
LHCb	Large Hadron Collider beauty
LO	Leading Order
LS2	Long Shutdown 2
LV	Low Voltage
MC	Monte Carlo
MPS	Multiple Parton Scattering
MWPC	Multiwire Proportional Chamber
NLO	Next-to-Leading Order
NNLO	Next-to-Next-to-Leading Order
N^3LO	Next-to-NNLO
NRQCD	Non-Relativistic Quantum Chromodynamics
OPC	Open Platform Communications
PDF	Parton Distribution Function
PET	Polyethylene Terephthalate
PF	Particle Flow
pQCD	Perturbative Quantum Chromodynamics
PSB	Proton Synchrotron Booster
PS	Proton Synchrotron
PSX	PVSS SOAP Exchange
PV	Primary Vertex
QCD	Quantum Chromodynamics
QED	Quantum Electrodynamics
QFT	Quantum Field Theory
RF	Radiofrequency
RPC	Resistive Plate Chamber
R&D	Research and Development
SCADA	Supervisory Control And Data Acquisition
SHiP	Search for Hidden Particles
SM	Standard Model
SOAP	Simple Object Access Protocol
SPS	Single-Parton Scattering

SV	Secondary Vertex
TDC	Time-to-Digital Converter
TEC	Tracker Endcap
TIB	Tracker Inner Barrel
TID	Tracker Inner Disks
TOB	Tracker Outer Barrel
UV	Ultraviolet
VME	Versa Module Europa
WP	Working Point

LIST OF SYMBOLS

BR	Branching Fraction
$\sqrt{s}$	Center-of-mass energy
α_s	Coupling constant of QCD
σ	Cross section
σ_{eff}	Effective cross section
$\mathcal{L}$	Instantaneous luminosity
L	Integrated luminosity
μ_F	Factorization scale
p_T	Transverse momentum
ϕ	Azimuthal Angle
θ	Polar Angle
η	Pseudorapidity
y	Rapidity
h	Planck constant
$\hbar$	Reduced Planck constant
c	Speed of Light
ϵ_0	Vaccum electric permittivity
eff	Efficiency
HV	High Voltage
R	Resistance
I	Electric Current
dl	decay length
dl_{err}	decay length error
dl_{sig}	decay length significance
$\vec{p}$	Trimomentum
$\cos\alpha$	Cosine of the pointing angle
m	Invariant mass
CB	Cristall Ball distribution
T_n	Chebychev polynomial of order n
Acc	Acceptance

CONTENTS

INTRODUCTION

The Standard Model (SM) of particles (1–3) is currently the best theoretical framework for describing the behavior of the subatomic particles and three of the four fundamental interactions. It was able to not only predict the existence of many particles, such as the W and Z bosons, the gluon and the top and bottom quarks, but also their properties. The last big discovery from the SM was the Higgs boson, in 2012 by both the ATLAS and CMS experiments in proton-proton (pp) collisions at LHC (4, 5). Nowadays, with the huge amount of data recorded from LHC collisions, the SM measurements have reached high precision and there is great expectation for the discovery of physics beyond the SM leading to a broader understanding of the universe.

During pp collisions at LHC energies, more often than not, more than one pair of partons (quark or gluon) can interact in a single collision (6), this is known as Multiple Parton Scattering (MPS) and is one of the predictions of the SM. While it is within the current physics framework, the model still need more refinement. Also, the analysis of the experimental data can be difficult to interpret, as the multiple interactions lead to additional activity in the detector. The MPS can be an important background, as it can mimic signals of new physics and it is expected to have greater contribution at higher energies.

The first observation of MPS was done by the AFS Collaboration by analyzing events with four-jets (7). It was shown that the number of events could only be explained by considering that more than one parton from each proton interacted. Later, CDF and D0 made important contributions at Tevatron by exploring data with multiple jets and with more than one quarkonia (8–14). ATLAS, CMS and LHCb, are doing many measurements with much more precision than ever (15–20), being able to explore much rarer signatures, such as the triple J/ψ (21).

Profiting from the high integrated luminosity recorded by CMS during Run 2 (123 fb^{-1}) at a center-of-mass energy of 13 TeV, this thesis aims to contribute to the study of MPS by doing a measurement of the associated production of $\Upsilon(nS)$ + D$^{*\pm}$. This can be compared to a measurement done by LHCb for $\Upsilon(1S)$ + D^0 and $\Upsilon(1S)$ + D$^+$ (22). Previous measurements of MPS show that there are differences in measurements performed at central and forward rapidities.

In addition to the physics analysis, this document also describes the contributions given by the author to the CMS RPC project. Maintenance, operation and commissioning work was carried out on the current subdetector, as well as in R&D for the upgrade of the new iRPCs.

This work is structured as follows. Chapter 1 presents a theoretical overview of the Standard Model and the multiple parton scattering processes, focusing on the main channel of analysis $\Upsilon(nS)$+D$^{*\pm}$. General aspects of the collider and the experimental apparatus are discussed in Chapter 2. Chapter 3 reviews the gaseous detectors with emphasis on the resistive plate chambers in CMS and the contributions given by the author to the CMS RPC project. Chapter 4 describes the physics analysis of the associated production of $\Upsilon(nS)$+ D$^{*\pm}$ using the CMS Run 2 data. Finally, the summary and perspectives of future developments are presented.

Throughout this document, the following conventions are adopted:

- Lowercase latin indexes, e.g. i, j and k, vary on the three spatial coordinates, generally as 1, 2 e 3 or x, y e z;
- Lowercase greek indexes, e.g. μ, ν and λ, vary on the four spacetime coordinates;
- The Einstein summation convention is used.
- The speed of light (c), the reduced Planck constant ($\hbar = \frac{h}{2\pi}$) and the vacuum electric permittivity (ϵ_0) are equal to one.
- Both particle and antiparticle states are considered for the cross section calculation.

1 STANDARD MODEL OF PARTICLES AND MULTIPLE PARTON SCATTERING

This chapter aims to give a theoretical background for this work, an introduction on the Standard Model, which describes the matter building blocks and relevant interactions on the subatomic realm, with exception to the gravity, will be presented. Then the relevant aspects of the QCD (Quantum Chromodynamics) will be discussed, with emphasis to the effective theory NRQCD (Non-Relativistic QCD), which is applied in the context of the quarkonia study. Important concepts on the MPS (Multiple Parton Scattering), which plays an important role on the production of associated production of a quarkonia and a charmed meson will be examined. To finalize, some remarks of the studied channel will be discussed.

1.1 **Standard Model**

The Standard Model (SM) refers to the set of theories that comprises our current understanding of the particle physics and their interactions (23, 24). Even though many phenomena are left without explanation, it passed through many tests from its development on the 70's[1].

The formulation of the SM is done via the Quantum Field Theory (QFT), in fact, the SM is a QFT of the local gauge group $SU_c(3) \times SU_L(2) \times U_Y(1)$. The SM describes three of the four fundamental interactions, explaining all phenomena in the Universe based on a set of quantum objects with well defined properties often referred to as "fundamental particles".

The generators of the symmetry groups form a set of spin-1 bosons that mediates the interactions. The particles associated to the $SU_c(3)$ are called gluons. They carry a charge named color and are massless. The particles that couple with gluons can interact via the strong interaction. The theory that explains the strong interaction is the Quantum Chromodynamics (QCD) and will be further discussed in the Section 1.2. The groups $SU_L(2) \times U_Y(1)$ refers to the electroweak interaction, which gives rise to three bosons of the weak isospin (W_1, W_2 and W_3) and one boson (B) of the weak hypercharge Y. The spontaneous symmetry breaking in the Higgs mechanism gives rise to the three massive mediators (Z, W^+ and W^-) of the weak interaction and one massless (photon) of the electromagnetic interaction.

---

[1] For example, the prediction of particles (e.g. the top quark and the Higgs boson) and their properties with great accuracy.

Besides the spin-1 mediators, there are spin-1/2 fundamental particles, which are grouped into doublets, also referred to as generations. These spin-1/2 particles are further divided into quarks, which experience the strong interaction, and leptons, which are not affected by this interaction.

According to our current knowledge, there are three generations of each, leptons and quarks.

There are six of leptons: electron (e), muon (μ), tau (τ), electron neutrino (ν_e), muon neutrino (ν_μ) and tau neutrino (ν_τ)

The hadrons (e.g. the proton, neutron, etc.) are the particles that take side in the strong interactions. They were all found to be bound states of six particles called quarks. Those are: up (u), down (d), strange (s), charm (c), bottom (b) and top (t).

To finalize, there is also a spin-0 field that was introduced in the SM to solve the problem of the particles masses[2]. This field is responsible to "give" mass to the SM particles[3]. The masses of the Z and $W^{\pm}$ bosons are given by the Higgs mechanism, which results in an additional boson with spin 0 called the Higgs boson (28–30). The fermion masses are obtained through a Yukawa interaction between the Higgs and fermion fields.

The Figure 1 summarizes all the fundamental particles of the SM.

1.2 Quantum Chromodynamics

The QCD is the theory of the strong interactions. It is a development from 50 years ago to explain the phenomena of the hadronic matter. The first developments of a theory for the strong interaction began with Murray Gell-Mann and George Zweig to describe the new Δ particles, the hyperons and the K mesons. Independently, they proposed that the observed hadrons were bound states of particles forming a SU(3) triplet. It was possible to predict new particles as well as to explain the difference in the masses of the hadrons, with the quark model called "eightfold way" (32).

Later, the color charge was added to the model to explain bound states with three of the same-flavor of quark, which could not exist because the wave function of such state should be anti-symmetric to obey the Pauli principle. The three color charges (red, green and blue) were introduced so that the wave function of the hadrons are anti-symmetric on the color indices.

The number of colors can be confirmed by examination of the cross section of

---

[2] The invariance of the theory under $SU_c(3) \times SU_L(2) \times U_Y(1)$ transformations implies that the masses of the particles should be zero.

[3] The neutrino mass is still a puzzle. The neutrino oscillation implies that neutrino have mass (25–27). The interaction with Higgs boson requires a right-handed neutrino.

Figure 1 - Elementary particles of the Standard Model.

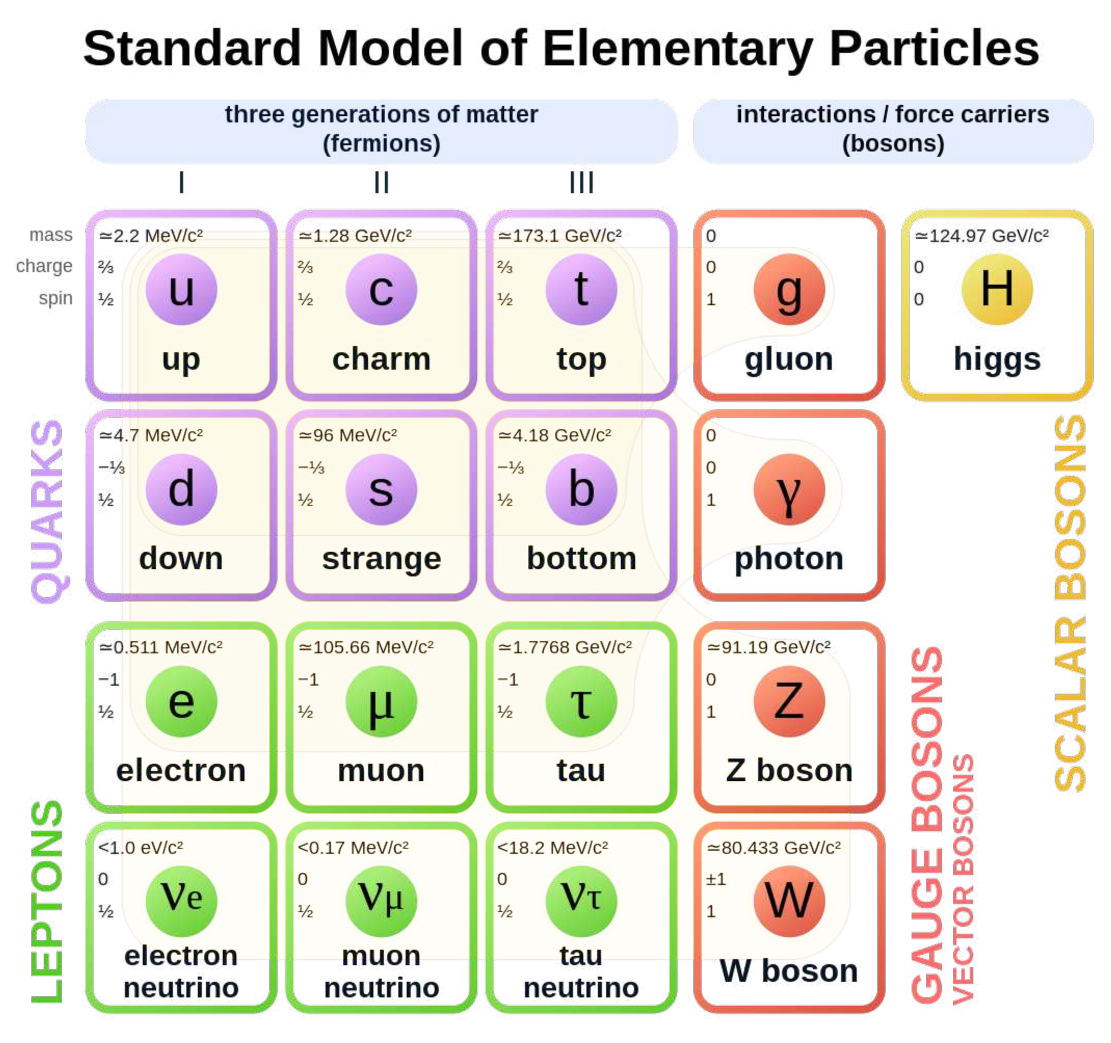

Legend: The elementary particles that are part of the Standard Model. Their mass, charge and spin are specified in their box. They are separated in the quarks, leptons, gauge bosons and scalar bosons.

Source: STANDARD Model of Elementary Particles, 2023.

electron-positron annihilation into hadrons, which depends on the square of the charges of the quarks and the number of colors. When comparing to the $e^+e^- \rightarrow \mu^+\mu^-$ annihilation[4]

$$R = \frac{\sigma(e^+e^- \rightarrow \text{hadrons})}{\sigma(e^+e^- \rightarrow \mu^+\mu^-)} = n_c \times \sum_q Q_q^2 \tag{1}$$

where n_c is the number of colors, Q is the electric charge and the subscript q is the quark flavour. Figure 2 shows the measurement of R in electron-positron collisions.

Figure 2 - Cross section and R in electron-positron collisions.

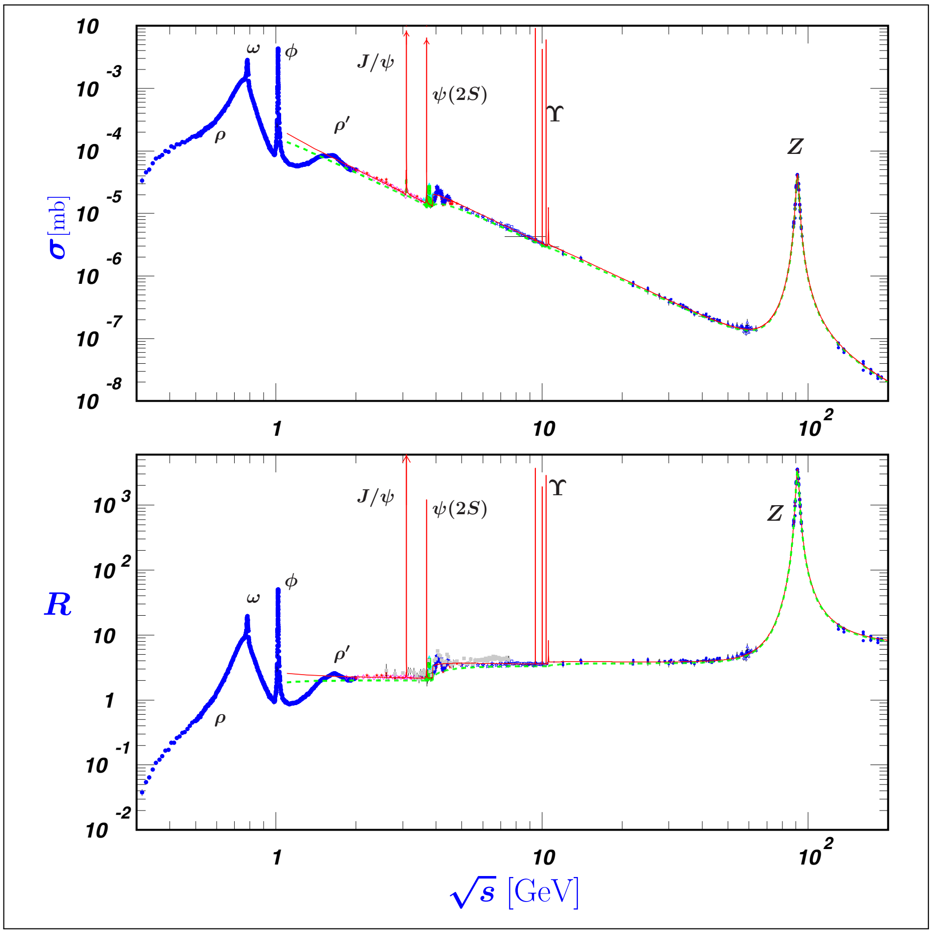

Legend: Data (blue) on the total cross section of $\sigma(e^+e^- \rightarrow \text{hadrons})$ and the ratio $R = \sigma(e^+e^- \rightarrow \text{hadrons})/\sigma(e^+e^- \rightarrow \mu^+\mu^-)$. The broken curve (green) is a naive quark-parton model prediction, and the solid one (red) is 3-loop perturbative QCD prediction.

Source: WORKMAN, 2022, p. 773.

The QCD was introduced to explain the quark model and its properties as a non-

---

[4] This is a naive approximation, and can be corrected by higher order perturbative QCD calculations.

abelian SU(3) gauge theory (34). The Lagrangian of QCD is

$$\mathcal{L}_{QCD} = \sum_f \overline{\psi}_{f,a}(i\delta_{ab}\not{D} - m_f\delta_{ab})\psi_{f,b} - \frac{1}{4}G^a_{\mu\nu}G^{a\mu\nu}, \tag{2}$$

where $\psi_{f,a}$ are quark field spinors for a quark of flavor q, mass m_f and a color-index a that runs from a = 1 to 3 (for red, green and blue). The $\not{D}$ is the covariant derivative, defined as

$$\not{D} = \gamma^\mu(\partial_\mu - ig_s A^a_\mu), \tag{3}$$

where A_μ represents the gluon fields, which are generators of the SU(3) gauge group. The g_s is the gauge coupling constant. The second term of the Lagrangian represents the kinetic term of the gluonic fields. They are expressed in terms of the field strength tensor $G^a_{\mu\nu}$ which is written in terms of the gluon fields as

$$G^a_{\mu\nu} = \partial_\mu A^a_\nu - \partial_\nu A^a_\mu + g_s f^{abc} A^b_\mu A^c_\nu, \tag{4}$$

where f^{abc} are the structure constants of the SU(3) group. If the $f_{abc} = 0$ we have an abelian theory.

The coupling of the gluon fields with themselves occurs the gluons carry color. Therefore, the QCD Feynman rules admit vertexes with three and four gluons as shown in Fig. 3. In comparison, there is only one vertex in the QED Feynman rules, with two fermions and one photon, since the photon caries no electric charge.

Figure 3 - QCD Feynman diagram vertex.

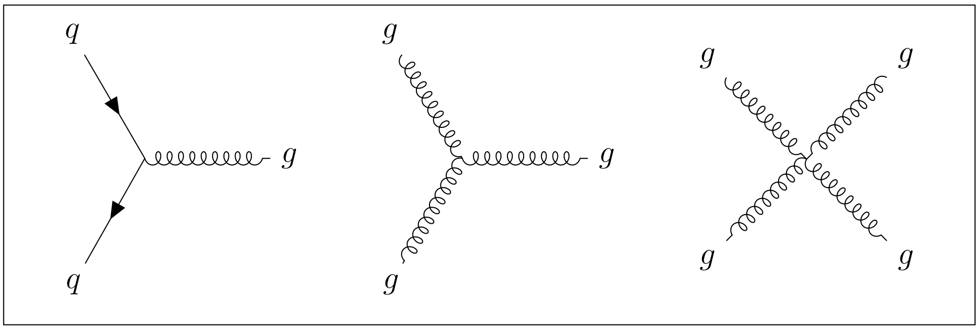

Legend: The allowed vertex in QCD. Besides the quark-gluon coupling represented by the first diagram from left to right, resembling the QED vertex, there are two more diagrams representing gluon-gluon interaction.

Source: The author, 2023.

Only color-singlet (i.e. color neutral) particles are observed, therefore quarks and gluons are not directly detected free in the Nature. There are two types of hadrons which are commonly probed in experiments - the mesons, formed by the combination of a quark and an antiquark

$$(q\overline{q}) \rightarrow (q_r\overline{q}_r + q_g\overline{q}_g + q_b\overline{q}_b) \tag{5}$$

and the baryons formed by a combination of three quarks or three antiquarks

$$(qqq) \rightarrow (q_rq_gq_b - q_gq_rq_b + q_bq_rq_g - q_rq_bq_g + q_gq_bq_r - q_bq_gq_r). \tag{6}$$

Other kinds of states, such as tetraquarks or pentaquarks (4 and 5 quark and antiquark bound states, respectively, commonly called exotic) are possible (35, 36), a list of such states observed in LHC can be found in (37). Also, gluon-gluon bound states are possible, known as glueball or gluonium, but were never observed (38).

QCD has two very unique properties, asymptotic freedom and color confinement. Asymptotic freedom states that in the limit of high energies, the coupling constant of the QCD ($\alpha_s = \frac{g_s}{4\pi}$) becomes small (39,40) and it can be treated perturbatively. Measurements of α_s are shown in Figure 4, which illustrates this behavior. Color confinement express the fact that free quarks are not observed. It is understood as a consequence of gluon self-interaction and the consequent increase of potential energy due to the color field as two quarks in a hadron are separated.

1.3 **Quarkonia**

The quarkonia are mesons made of a heavy quark and antiquark of the same flavour. The possible quarkonium states are the $c\overline{c}$, the charmonium, and $b\overline{b}$, the bottomonium. Light mesons (u, d and s) form physical quark-antiquark states[5] but, because of their small mass, they are actually quantum mechanical mixtures of such states. Finally, the top quark quarkonium is not expected to be found, because, due to its very high mass, the top quark decays through electroweak interaction before a bound state can be formed, but there are some signatures that could be explored in the search for the toponium (41).

The special property of the quarkonia is that they form a bound-state with radius much lower than confinement scale, thus the QCD coupling constant has lower values, so that these particles can be treated perturbatively, which leads to states that are very similar to the electromagnetic particle-antiparticle systems (23), the positronium and the muonium, from which the quarkonium name derives. Furthermore, because they are made of heavy quarks they form non-relativistic states, which are very well treated by an effective theory called NRQCD.

---

[5] The η, η', and π^0 mesons.

Figure 4 - QCD coupling constant.

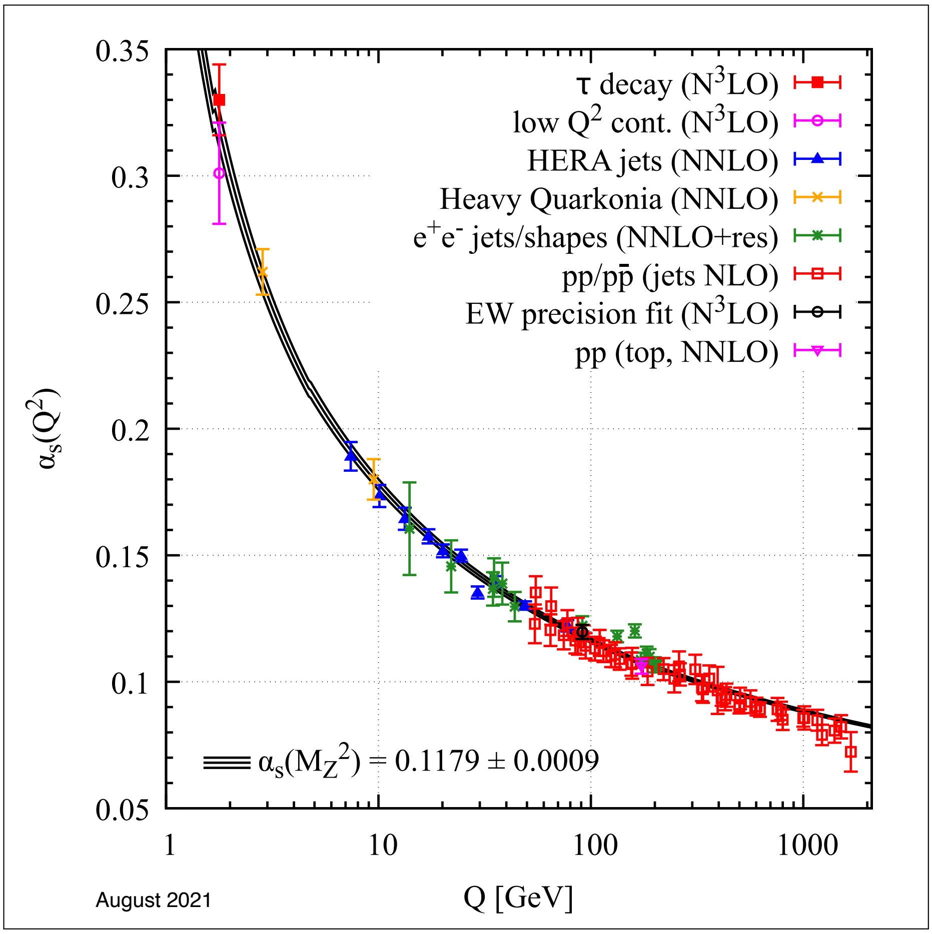

Legend: Summary of measurements of α_s as a function of the energy scale Q. The respective degree of QCD perturbation theory used in the extraction of α_s is indicated in brackets (NLO: next-to-leading order; NNLO: next-to-next-to-leading order; NNLO+res.: NNLO matched to a resummed calculation; N^{3}LO: next-to-NNLO)

Source: WORKMAN, 2022, p. 164.

The $c\bar{c}$ and $b\bar{b}$ bound states may be classified with respect to their principal quantum number, n, angular momentum quantum numbers, l and m, and spin quantum numbers, s and s_z, using the same spectroscopic notation used in atoms. Figure 5 shows the quarkonium spectrum.

Figure 5 - Quarkonium spectrum.

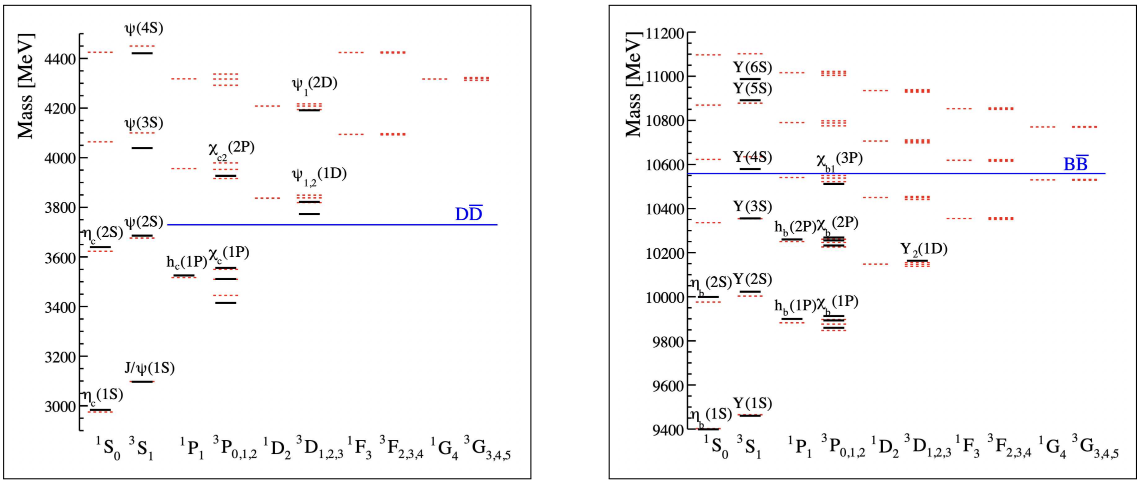

(a) (b)

Legend: Current status of the charmonium (a) and bottomonium (b) spectra. The dashed lines indicate the expected states and their masses. The solid lines indicates the experimentally established quarkonia states. The open-flavor threshold is indicated in the blue line. Experimental results show a much richer spectrum, with many exotic quarkonium-like states (42).

Source: OLSEN et al., 2018, p. 5–6.

The discovery of the J/ψ, in 1974 (44,45), allowed to identify the charm quark, confirming the quarks as real particles and not mathematical entities to explain the hadrons. This triggered many changes in the understanding of particle physics which is today known as November Revolution. Later, the Υ meson was discovered in 1977 (46), the first particle containing b quarks.

Still today, the quarkonia are of very interest in particle physics, because they are easy to be treated experimentally and have high yields in the LHC energy scale. They appear as products of decays of exotic states (47–49), B mesons and Higgs boson (50) and can hint properties of the Quark-Gluon Plasma (51, 52).

1.4 Multiple Parton Scattering

Protons are not elementary particles, they are formed by a bound state of uud quarks, called valence quarks, the gluons that bind the valence quarks together and the sea quarks and antiquarks, which are formed by the interaction of the gluons in the protons. All of them are collectively referred to as partons.

Therefore, as opposed to the electron-positron collision, one cannot determine the initial states of a proton-proton (pp) collision and the calculation of the perturbative cross sections are determined be the factorization theorem (53). If one parton from each proton interact, cross section can be determined as

$$\sigma_A = \sum_{i,j} \int dx_i \; dx_j \; f_i(x_i, \mu_F) \; f_j(x_j, \mu_F) \cdot \hat{\sigma}^X_{i,j}(x_i, x_j, \mu_F) \tag{7}$$

where, i and j are the interacting partons, x_i (x_j) is the momentum fraction carried by the parton i (j), $f(x, \mu_F)$ is the parton distribution function (PDF), which is defined as the probability density for finding a parton with a certain longitudinal momentum fraction x at factorization scale μ_F and $\hat{\sigma}$ is the partonic cross section that can be calculated by the perturbative QCD (pQCD). The PDFs are the non-perturbative part of the Eq. 7 and are determined experimentally (54) and are shown in Fig. 6.

Figure 6 - NNLO Parton Distribution Functions.

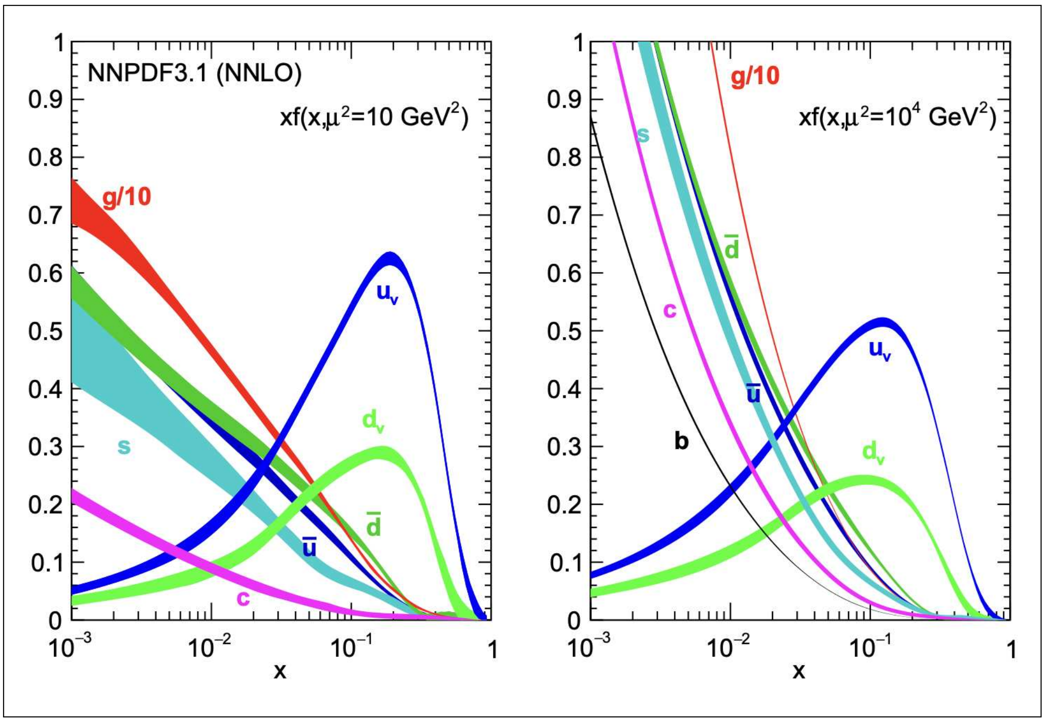

Legend: NNLO Parton distribution functions determined for $\mu_F^2 = 10$ GeV^2 (left) and 10^4 GeV^2 (right)

Source: NNPDF COLLABORATION, 2017.

It is also possible that more than one parton from each proton take part in the process, giving rise to more than one hard interaction, a process known as multiple parton scattering (MPS). In the MPS context, the pp interaction with one hard interaction is called single-parton scattering (SPS) and first extension is the double-parton scattering (DPS), where two hard interactions happen. Figure 7 shows the SPS and DPS examples.

Figure 7 - Single-parton scattering and double-parton Scattering sketches.

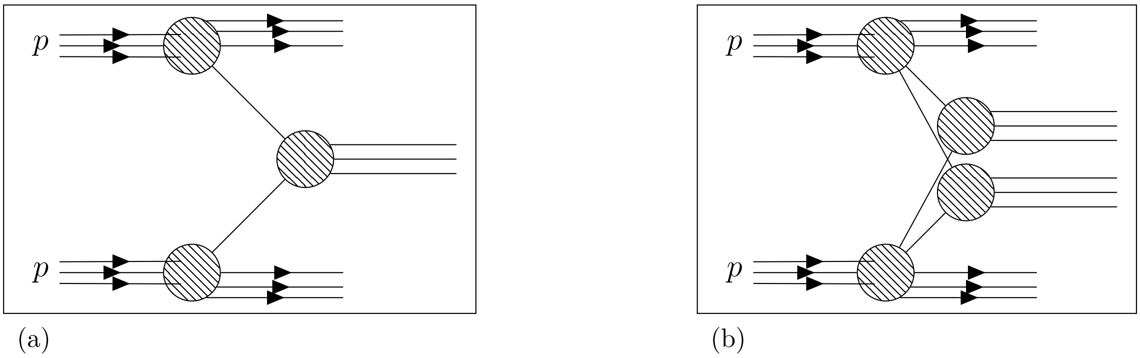

(a) (b)

Legend: A comparison of the single-parton scattering (a) and double-parton scattering (b). The difference between the two are the number of partons coming from each proton. The hadrons formed in (b) are uncorrelated, and have different kinematic distributions than (a)

Source: The author, 2023.

The factorization can also be used in the MPS. For the DPS, the cross section is calculated by the formula (55)

$$\begin{aligned}\sigma_{AB}^{DPS} = \frac{m}{2} \sum_{i,j,k,l} \int & \Gamma_{ij}(x_1, x_2, b, \mu_1, \mu_2)\ \hat{\sigma}_{ik}^{A}(x_1, x_1', \mu_1)\ \hat{\sigma}_{jl}^{B}(x_2, x_2', \mu_2) \\ & \times \Gamma_{kl}(x_1', x_2', b, \mu_1, \mu_2)\ dx_1\ dx_2\ dx_1'\ dx_2'\ d^2b,\end{aligned} \tag{8}$$

where the m is a double count factor, m equals 1 if process A = process B and 2 otherwise. The $\Gamma_{ij}(x_1, x_1, b, \mu_1, \mu_2)$ are the generalized double parton distributions. They may be interpreted as the inclusive probability distributions to find a parton i with longitudinal momentum fraction x_1 at scale μ_1 in the proton, in addition to a parton j with longitudinal momentum fraction x_2 at scale μ_2, with the two partons separated by a transverse distance b. And finally the $\hat{\sigma}$ is the parton-level cross section.

The multi-parton PDFs should depend on all the possible correlations between partons, such as color and flavour interactions as well as spatial and kinematics correlations. Currently there is no theoretical model capable to describe its phenomenology. So, as a simplification to the model, it is assumed that the Γ_{ij} can be separated in two components, representing the longitudinal and transverse components

$$\Gamma_{ij}(x_1, x_2, b, \mu_1, \mu_2) = D_{ij}(x_1, x_2, \mu_1, \mu_2) \cdot F(b). \tag{9}$$

The correlations in the transverse plane are very significant - as they must bind the two partons together within the same hadron. On the other hand, the correlations in the longitudinal plane are typically ignored with the assumption that, at least for small x_i values the longitudinal momenta correlations are small[6] (55). Therefore, Γ_{ij} is taken as the product of the single parton distribution functions f_i and f_j

$$\Gamma_{ij}(x_1, x_2, b, \mu_1, \mu_2) = f_j(x_1, \mu_1) \cdot f_i(x_2, \mu_2) \cdot F(b). \tag{10}$$

Under those simplifications, the DPS cross section can be expressed in terms of the SPS cross sections by plugging Eq. 10 in 8

$$\sigma_{AB}^{DPS} = \frac{m}{2}\frac{\sigma_A^{SPS} \cdot \sigma_B^{SPS}}{\sigma_{eff}}, \tag{11}$$

where m is one if $A = B$ and two if $A \neq B$, σ_A^{SPS} is the inclusive cross section of the process A and has the same formula from Eq. 7. The σ_{eff} is written as

$$\sigma_{eff} = \left[\int d^2b(F(b))^2\right]^{-1} \tag{12}$$

and it is a parameter characterizes the effective spatial area of the parton-parton interactions. Figure 8 shows a summary of measurements of σ_{eff} done by many experiments (7–20, 22, 56–59). The results shows some deviations on the measured effective cross section, which should be independent of final state.

The MPS is of great interest in the experiments as it can be an important contribution to background in multiparticle final-state processes. In high energy experiments, the MPS contribution is large, and can even overtake the SPS one (61). Figure 9 show the contribution of SPS and DPS to $c\bar{c}$ production, it is possible to see that at high enough center-of-mass energy, the DPS contribution is larger than SPS.

1.5 Associated production of Υ and Open Charm

The associated production of Υ and open charm is an interesting channel to investigate DPS (62) as it is expected that the SPS contribution is small. There is an experimental measurement from LHCb collaboration in 2015 (22) in which they concluded that the DPS cross section is at least 10 times higher than the SPS one, as expected from the theoretical study (63).

Under the hypothesis of the dominance of the DPS, LHCb extracted the values for

---

[6] At LHC energy scale, the fraction of partons with small x is large.

Figure 8 - Measurements and limits on the σ_{eff}.

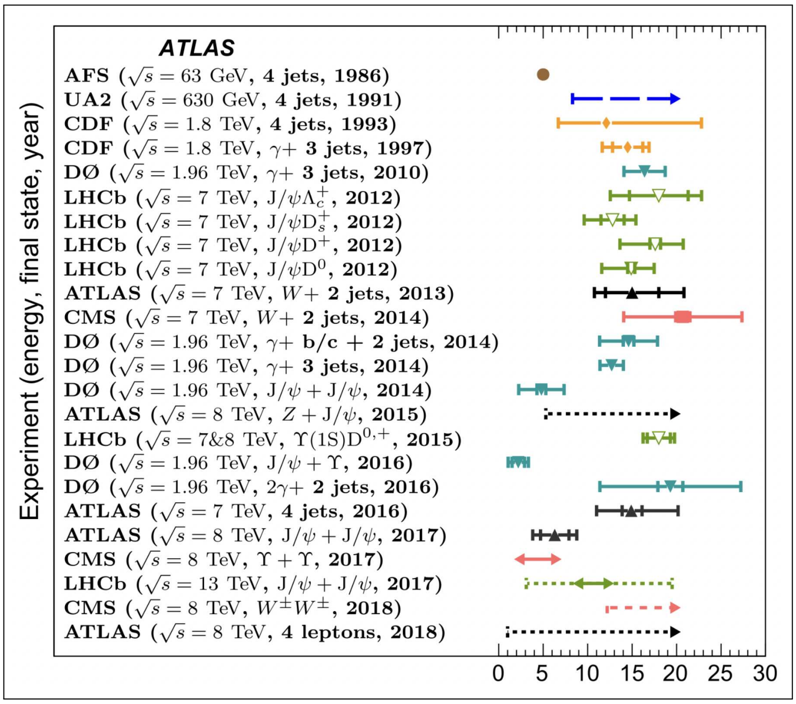

Legend: Summary of measurements and limits on the σ_{eff} determined by many experiments (7–20, 22, 56–59).

Source: ATLAS COLLABORATION, 2019.

Figure 9 - Total LO $c\bar{c}$ cross section for SPS and DPS as a function of $\sqrt{s}$.

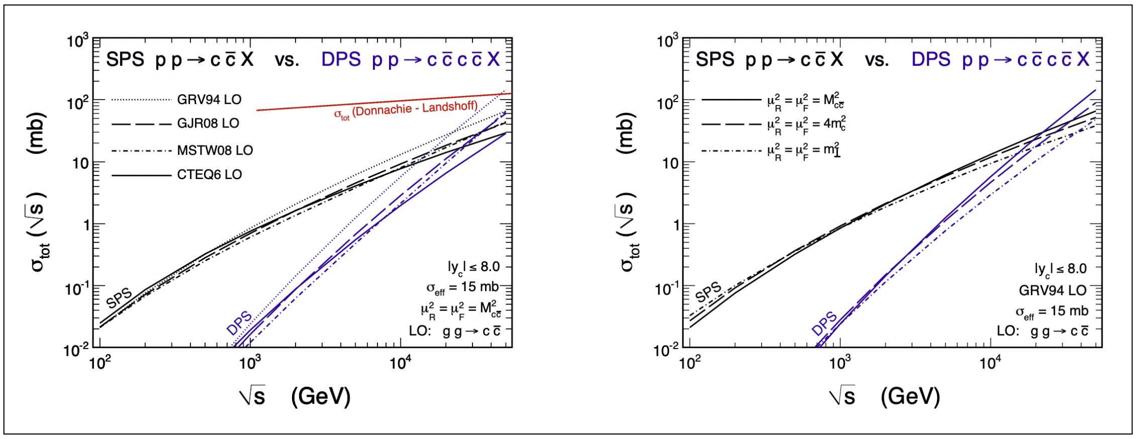

Legend: Total LO cross section for SPS and DPS as a function of center-of-mass energy (left) and uncertainties due to the choice of (factorization, renormalisation) scales (right).

Source: LUSZCZAK et al., 2012, p. 4.

the fiducial and effective cross section

$$
\begin{aligned}
BR_{Y\to\mu^+\mu^-} \times \sigma^{Y(1S)D^0}_{\sqrt{s}=7\,\mathrm{TeV}} &= 155 \pm 21(\mathrm{stat}) \pm 7(\mathrm{syst})\,\mathrm{pb},\\
BR_{Y\to\mu^+\mu^-} \times \sigma^{Y(1S)D^+}_{\sqrt{s}=7\,\mathrm{TeV}} &= 82 \pm 19(\mathrm{stat}) \pm 5(\mathrm{syst})\,\mathrm{pb},\\
BR_{Y\to\mu^+\mu^-} \times \sigma^{Y(1S)D^0}_{\sqrt{s}=8\,\mathrm{TeV}} &= 250 \pm 28(\mathrm{stat}) \pm 11(\mathrm{syst})\,\mathrm{pb},\\
BR_{Y\to\mu^+\mu^-} \times \sigma^{Y(1S)D^+}_{\sqrt{s}=8\,\mathrm{TeV}} &= 80 \pm 16(\mathrm{stat}) \pm 5(\mathrm{syst})\,\mathrm{pb},\\
\sigma_{eff}|_{\Upsilon(1S)D^0} &= 19.4 \pm 2.7(\mathrm{stat}) \pm 1.3(\mathrm{syst})\,\mathrm{mb},\\
\sigma_{eff}|_{\Upsilon(1S)D^+} &= 15.2 \pm 3.6(\mathrm{stat}) \pm 1.5(\mathrm{syst})\,\mathrm{mb}.
\end{aligned}
\tag{13}
$$

As the CMS phase space is very different from the LHCb, which covers only the frontal region ($2.0 < \eta < 5.0$), a measurement by the CMS collaboration can help to understand this channel in the central region, complementing the LHCb result, with the advantage of the higher luminosity recorded by CMS.

In order to perform a similar measurement in this thesis, the $\mathrm{D}^{*\pm}$ will be used as charmed meson because of its good signal to background ratio and broad phase-space coverage. It has three different strong or electromagnetic decays (33) with branching ratio (BR):

- $\mathrm{D}^{*+} \to \mathrm{D}^0\pi^+$: BR $= 67.7 \pm 0.5$ %,
- $\mathrm{D}^{*+} \to \mathrm{D}^+\pi^0$: BR $= 30.7 \pm 0.5$ %,
- $\mathrm{D}^{*+} \to \mathrm{D}^+\gamma$: BR $= 1.6 \pm 0.4$ %,

For this thesis, the decay chosen is $\mathrm{D}^0\pi^+$. In addition to that, D^0 also decays through the weak interaction

$\mathrm{D}^0 \to K^-\pi^+$: BR $= 3.947 \pm 0.030$ %,

adding to a total BR of 2.67 ± 0.03 %. The mass difference of D^{*+} and D^0 is small, so the momentum of the pion from the D^{*+} is also small. For this reason, this pion is often referred to as "slow" pion (π_s).

From the quarkonium side, the first three states of $\Upsilon(nS)$ will be investigated. They decay electromagnetically to two leptons with opposite charge. The two muons channel (from here on, called dimuon) was chosen, with branching ratios of:

- $\Upsilon(1S) \to \mu^+\mu^-$: BR $= 2.48 \pm 0.05$ %,
- $\Upsilon(2S) \to \mu^+\mu^-$: BR $= 1.93 \pm 0.17$ %,
- $\Upsilon(3S) \to \mu^+\mu^-$: BR $= 2.18 \pm 0.21$ %.

The Tab. 1 summarizes the properties of the particles relevant to this work. The production of the pair of particles at LHC is mainly via gluon-gluon fusion, in DPS the b and c-quarks are produced in different parton interactions while in SPS the production needs higher order Feynman diagrams shown in Fig. 10. The diagrams for the decays are shown in Figs. 11 and 12 for $b\bar{b}$ and D^{*+}.

Table 1 - Properties of the particles considered in this work

Particle	Quark content	Mass (MeV)	Lifetime (s)	$I^G(J^{PC})$
$\Upsilon(1S)$	$b\bar{b}$	9460.30 ± 0.26	-	$0^-(1^{--})$
$\Upsilon(2S)$	$b\bar{b}$	10023.26 ± 0.31	-	$0^-(1^{--})$
$\Upsilon(3S)$	$b\bar{b}$	10355.2 ± 0.5	-	$0^-(1^{--})$
μ^-	-	105.66	2.197×10^{-6}	$J = 1/2$
D^{*+}	$c\bar{d}$	2010.26 ± 0.05	-	$1/2(1^-)$
D^0	$c\bar{u}$	1864.84 ± 0.05	$(410.3 \pm 1.0) \times 10^{-15}$	$1/2(0^-)$
K$^-$	$s\bar{u}$	493.677 ± 0.016	$(1.2379 \pm 0.0020) \times 10^{-8}$	$1/2(0^-)$
π^+	$u\bar{d}$	139.57039 ± 0.00018	$2.6033 \pm 0.0005 \times 10^{-8}$	$1^-(0^-)$

Legend: Summary of the properties of the particles relevant to this work. The last column shows their the quantum numbers - I = isospin, G = G-symmetry, J = spin, P = Parity and C = charge conjugate. For the muon only the J quantum number is relevant, for the Ds and K, G and C are not present and for the π only C is not present. The uncertainties on μ mass and lifetime were ommited.

Source: WORKMAN, 2022, p. 1240, 1349, 1474, 1475, 1543, 1578, 1942, 1954, 1966. Adapted by the author.

Figure 10 - Feynman Diagram for SPS b-quarks and c-quarks.

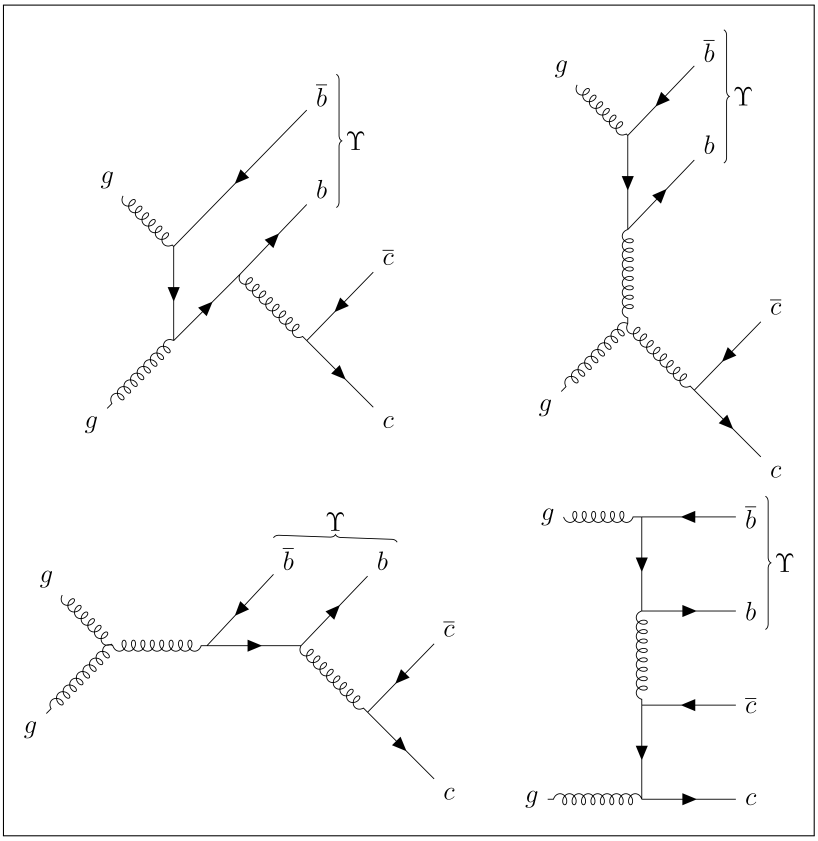

Legend: Examples of Feynman Diagrams for SPS $b\bar{b}$ and $c\bar{c}$ production.
Source: The author, 2023.

Figure 11 - Feynman Diagram for $b\bar{b} \to \mu^+\mu^-$.

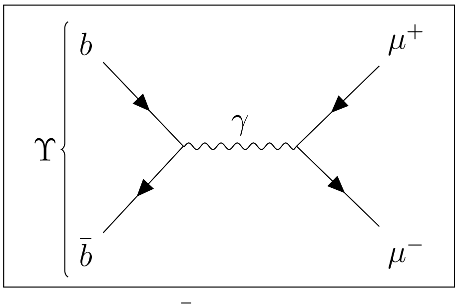

Legend: Example of Feynman diagram for $b\bar{b}$ (Υ) annihilation to dimuon.
Source: The author, 2023.

Figure 12 - Feynman Diagram for D$^{*+} \to K^-\pi^+\pi_s^+$.

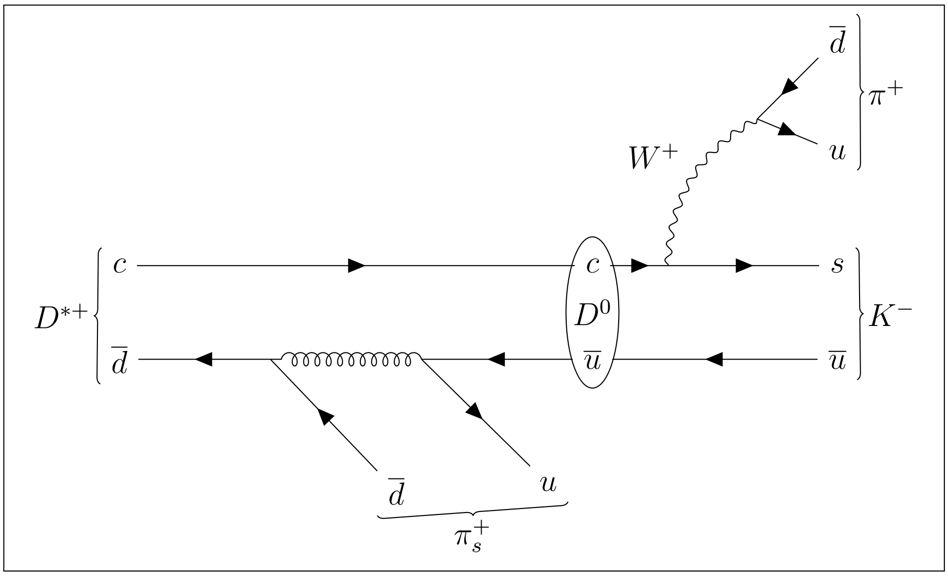

Legend: Example of Feynman diagram for D$^{*+} \to K^-\pi^+\pi^+$. The decay happens in two steps, first, the D^{*+} decays into a D^0 and a π_s^+ and then, the D^0 further decays into a K^- and a π^+.

Source: The author, 2023.

2 EXPERIMENTAL SETUP

The goal of this chapter is to introduce the experimental setup used to acquire the data. The apparatus can be divided in two parts: the accelerator, the Large Hadron Collider (LHC), which will be discussed in the section 2.1 and the particle detector, the Compact Muon Solenoid (CMS), which will be discussed in the section 2.2.

2.1 The Large Hadron Collider

The LHC is the world most powerful particle accelerator and collider. It is situated at CERN in the border of Switzerland and France inside the tunnel of 26.7 km of extension, in which the Large Electron-Positron collider, LEP, was built in the past. It is designed to collide two proton beams with centre-of-mass energy of 14 TeV with a peak instantaneous luminosity of $10^{34}\ cm^{-2}s^{-1}$. Up to Run 2, the maximum center–of–mass energy achieved was 13 TeV and the instantaneous luminosity was double the nominal $2 \cdot 10^{34}\ cm^{-2}s^{-1}$. It can also collide heavy ions (Pb) (64).

To achieve such numbers, the protons are first accelerated to 450 GeV before being injected to the machine. The injector chain is pictured in the Figure 13, it follows the sequence: Linac4[7] – Proton Synchrotron Booster (PSB) – Proton Synchrotron (PS) – Super Proton Synchrotron (SPS).

In the LHC, the protons injected are divided into two tubes and are accelerated from 450 GeV to 6.5 TeV[8]. The acceleration is accomplished by 16 radiofrequency (RF) cavities (8 per beam), the trajectory is maintained by 1232 dipoles placed along the tunnel, quadrupoles are also used to squeeze and focus the beam. All magnets are made of superconducting coils to reduce energy losses.

When the beams reach 6.5 TeV, they are directed to the interaction points (IP) by the insertion magnets, which also squeeze them further for the collision. There are 4 IP, each of them is placed at the center of each LHC experiments, namely:

- **ALICE (A Large Ion Collider Experiment):** Located at P2, it is a general purpose detector specialized in heavy ion collisions. It focuses on QCD, the strong-interaction sector of the Standard Model (66).
- **ATLAS (A Toroidal LHC Apparatus):** Located at P1 it is a general purpose detector designed to cope with the high collision rates of LHC and focus in various

---

[7] Linac2 was used up to Run 2 in the injector chain, in 2020 it was replaced by Linac4

[8] In Run 2, this amounts to $\sqrt{s} = 13\ TeV$. For Run 3 it is expected 6.8 TeV per beam or $\sqrt{s} = 13.6\ TeV$

Figure 13 - The CERN Accelerator Complex

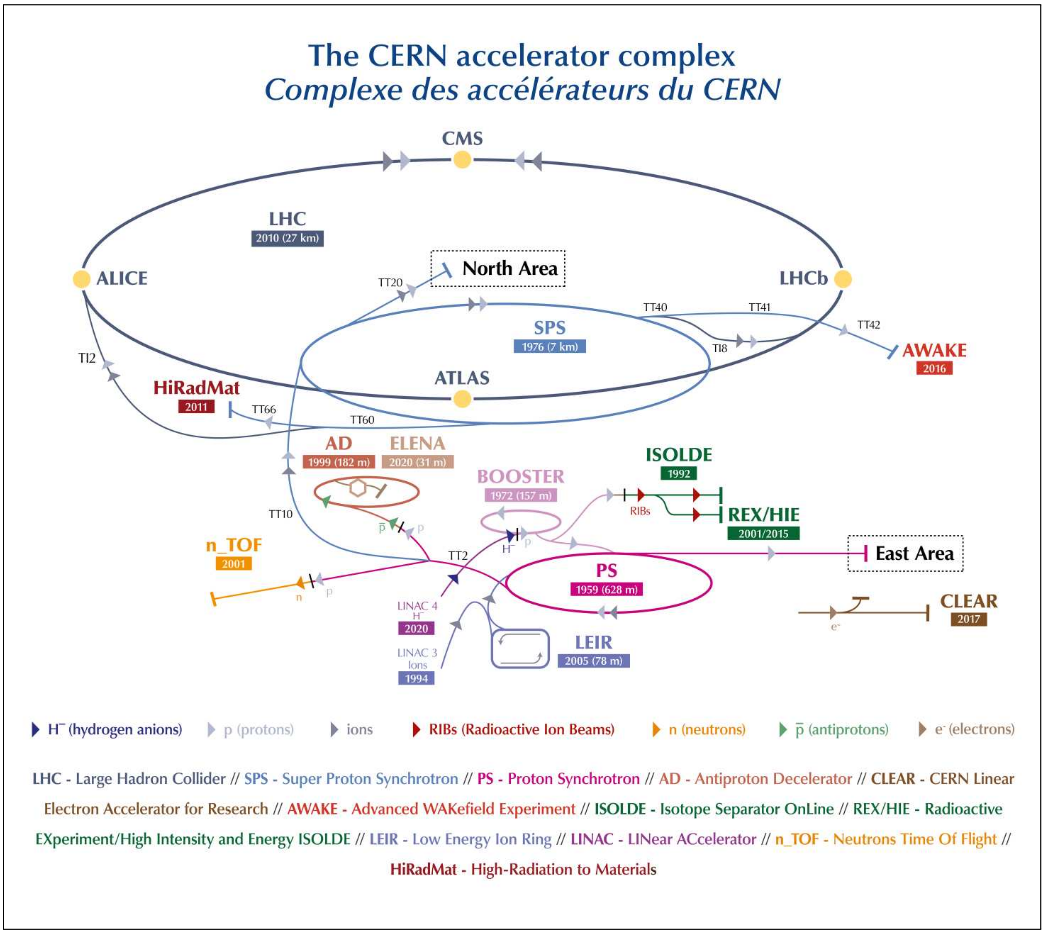

Legend: All the machines that compose the CERN accelerator complex. The LHC is the last ring colored in dark blue.

Source: MOBS et al., 2019.

aspects of the SM and BSM (Beyond Standard Model) physics in the LHC energy scale (67).

- **CMS (Compact Muon Solenoid):** Located at P5, it is a general purpose detector such as ATLAS, it is going to be further explored in the section 2.2 (68).
- **LHCb (Large Hadron Collider beauty):** Located at P8, it is an experiment focused in heavy flavour physics. Its goal is to look for indirect evidence of new physics in CP violation and rare decays of beauty and charm hadrons (69).

2.1.1 Luminosity and the HL-LHC

One of the most important parameters of an accelerator is the instantaneous luminosity it can deliver. It is defined as

$$\mathcal{L} = \frac{1}{\sigma_i}\frac{dN_i}{dt}, \tag{14}$$

where $\mathcal{L}$ is the instantaneous luminosity, N_i is the number of events of the i-labeled process and σ_i is the cross section of the process i. The integrated luminosity (L) is the integration in time of the instantaneous luminosity. Therefore, the number of events delivered by the accelerator is

$$N_i = \sigma_i L. \tag{15}$$

The integrated luminosity delivered by the LHC to the CMS detector in the course of the Run 1 and Run 2 (2010 to 2018) is presented in Figure 14.

The luminosity is very important to the statistics collected, therefore the HL-LHC project was proposed and accepted by the EU Strategy Report for High Energy Physics and the CERN Council. Its goal is to increase the peak instantaneous luminosity by a factor of 5 to extend the possibility of new discoveries and maximize the use of LHC (71). It is expected a integrated luminosity of 3000 fb^{-1} in 10-12 years. The current plan for the HL-LHC is in Figure 15.

2.2 **Compact Muon Solenoid Experiment**

The CMS is a multipurpose detector that investigates both proton-proton and lead-lead collisions at LHC. It has a cylindrical shape with 15 meters diameter and 22 m long, weighting 14 000 tonnes, being the heaviest of the LHC experiments (68). It is divided into two distinct regions, the barrel, which refers to the central part and the

Figure 14 - Integrated Luminosity delivered to CMS

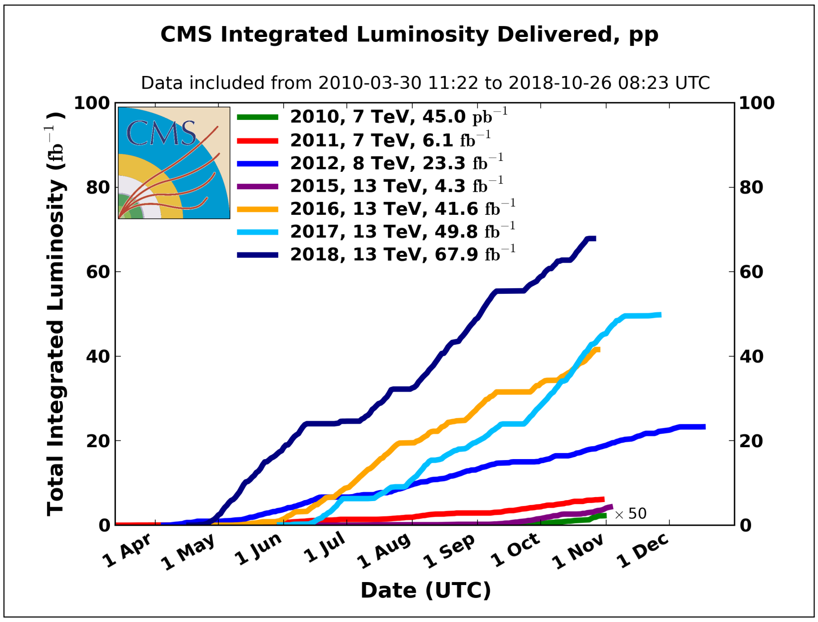

Legend: The integrated luminosity delivered to CMS by the LHC from 2010 to 2018.
Source: CMS Luminosity, 2023.

Figure 15 - LHC/HL-LHC Plan

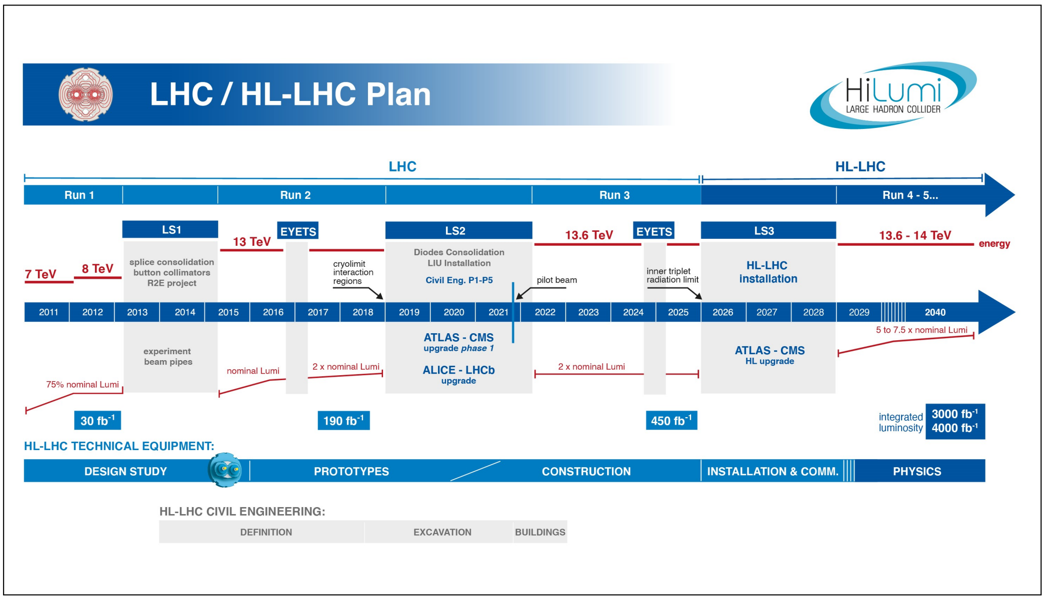

Legend: The plan for the LHC and HL-LHC from its start in 2011 to the expected end of the program in 2040.
Source: THE HL-LHC project, 2023.

endcap, for detection in the frontal region. Figure 16 shows a schematic view of the CMS detector and its components.

Figure 16 - CMS Detector Cutaway Diagram

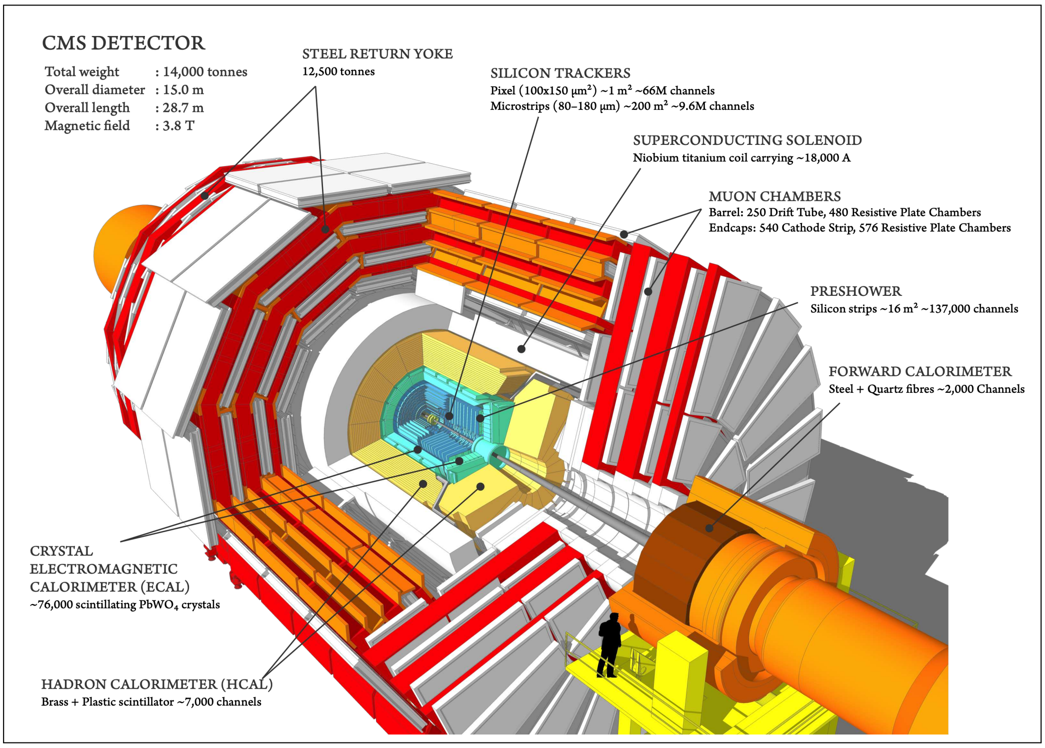

Legend: Schematic of the CMS detector showing its components.
Source: SAKUMA, 2019.

As the name implies, it is designed to make accurate identification and measurement of the transverse momentum of muons, which are very important particles as they appear in many SM and BSM processes.

An important component of the detector is the powerful 6 meters diameter superconducting solenoid, that can provide a magnetic field of 3.8 T. Such a powerful field is important in the accurate transverse momentum measurement with the bending of the trajectories of the particles.

From the innermost part, the subdetector systems that compose the CMS detector are: the tracker composed by the silicon pixel and strip tracker, the electromagnetic calorimeter (ECAL), the hadronic calorimeter (HCAL) and the Muon system.

2.2.1 CMS Coordinate system

The CMS coordinate system is pictured in the Figure 17, it is a right-handed coordinate system centered in the nominal interaction point. The x-axis points out to the center of the LHC ring, the y-axis points upwards and the z-axis follows the anticlockwise beam pointing to the Jura Mountains, in France. The azimuthal angle is measured from the positive x-axis to the position vector and the θ angle is measured from the positive z-axis to the projection of the position vector into the yz-plane.

Figure 17 - CMS Coordinate System

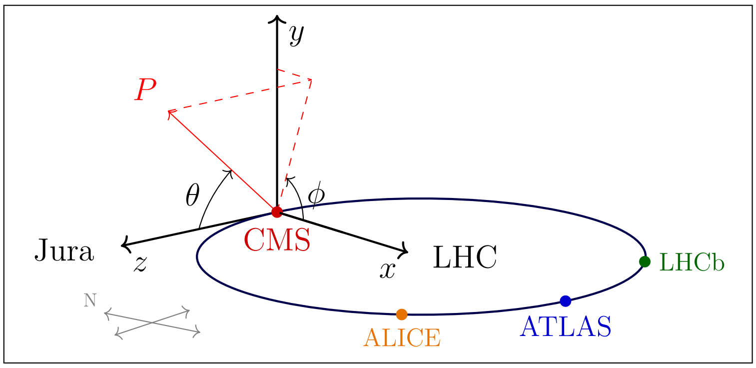

Legend: Diagram of the CMS coordinate system centred in the IP.
Source: HOW to draw diagrams in LaTeX with TikZ, 2023.

For the physics analysis, the momentum is one of the key variables of the particle as normally the theory is described in momentum space (p_x, p_y, p_z). The detector measures the momentum in terms of the transverse momentum (p_T), pseudorapidity (η), and the azimuthal angle (ϕ). The p_T is defined as:

$$p_T = \sqrt{p_x^2 + p_y^2}, \tag{16}$$

the η is an approximation to another variable, the rapidity (y), which is invariant by Lorentz boosts in the z-axis. With respect to the beam axis, the rapidity can be written as:

$$y = \frac{1}{2} \ln \left(\frac{E + p_z}{E - p_z} \right). \tag{17}$$

But from the detector point of view it is a variable hard to be measured, as it depends on the energy of the particle. The pseudorapidity is a much more straightforward measurement as it is defined as

$$\eta = -\ln \left[\tan \left(\frac{\theta}{2} \right) \right], \tag{18}$$

depending only on the θ angle. Furthermore, $\eta \approx y$ providing that the energy of the particle is much greater than its mass.

2.2.2 Tracker

The tracker is the detector closest to the IP, it is responsible to measure accurately the momentum of the charged particles and vertices positions. It is divided into two types of detectors, the Pixel tracker and the Silicon Strip tracker. Together, they provide a coverage of $|\eta| < 2.5$. A layout of the tracker detector is shown in Fig. 18

Figure 18 - CMS Tracker Detector Schematic

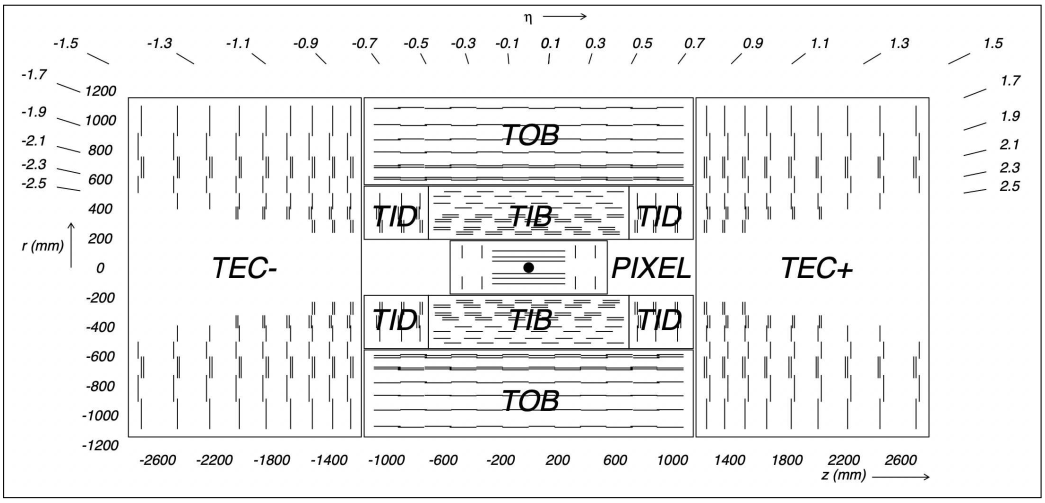

Legend: Schematic of a cross section of the tracker detector.
Source: CMS COLLABORATION, 2008, p. 30.

The pixel detector consisted of three layers in the barrel and two layers in each endcap. After Phase-1[9] upgrade, an additional layer was added to the barrel and to each endcap as well as new readout system to minimize data losses and radiation degradation (75). The layout of the tracker before and after the Phase-1 upgrade is in Figure 19.

The Silicon Strip detector is in the outer tracker region and consists of silicon micro-strips distributed in 198 m^2. It has ten layers in the barrel region and 3 layers in each endcap. It is divided in Tracker Inner Barrel (TIB), covering the central part of the detector, the Tracker Inner Disks (TID) at the inner endcap, both are surrounded by the Tracker Outer Barrel (TOB) on the barrel, and the Tracker Endcap (TEC).

2.2.3 Electromagnetic Calorimeter

The Electromagnetic Calorimeter (ECAL) is the responsible to measure the energy of photons and electrons, so it is designed to absorb these particles. It is done by interac-

---

[9] Phase-1 upgrade happened in the Technical Stop between 2016 and 2017

Figure 19 - CMS Pixel Tracker Detector Layout

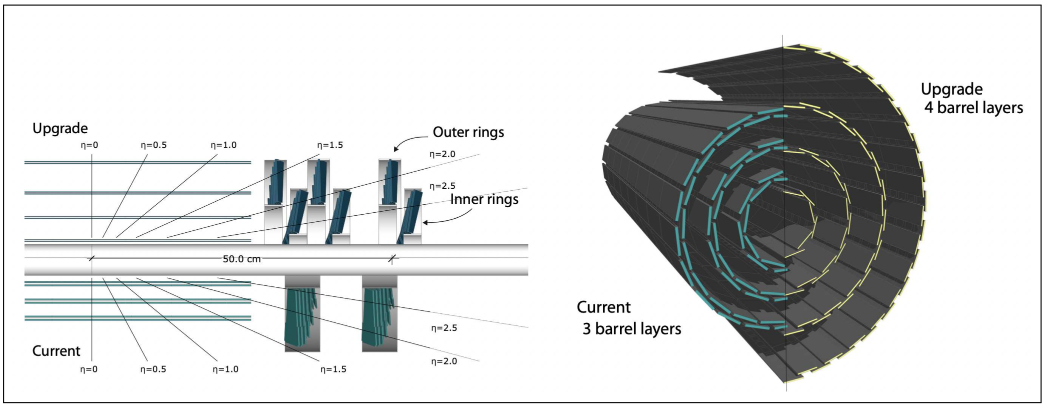

Legend: The layout of the CMS Pixel tracker detector before (labeled as current) and after the upgrade.

Source: DOMINGUEZ et al, 2012, p. 16.

tions that occur in the lead tungstate ($PbWO_4$) crystals. A number of 61 200 crystals are placed in the barrel (ECAL Barrel, EB) and 7 324 in each endcap (ECAL Endcap, EE), amounting in a total of 75 848 crystals, which are coupled with to photodetectors, with output proportional to the energy left by the particle into the crystal.

Also, in front of the endcap detector there is a Preshower detector that is composed of two layers of silicon detectors interleaved by a lead radiator. They were designed to identify the neutral pions decay into two photons and separate them from the primary photons.

Its coverage is $|\eta| < 1.48$ in the barrel region (EB) and $1.48 < |\eta| < 3.0$ in the endcap region (EE). Figure 20 shows a layout of the ECAL.

2.2.4 Hadronic Calorimeter

The Hadronic Calorimeter (HCAL) is responsible to measure the energy of the charged and neutral hadrons, being very important for jet and missing energy measurement. It covers an extended pseudorapidity region ($|\eta| < 5.2$) to enhance the missing transverse energy estimation.

It is made of layers of steel and brass alternated with very thin plastic scintillator tiles, in order to maximize the amount of absorptive material, allowing for hadronic cascades.

The HCAL is divided into four regions, the HCAL Barrel (HB) surrounded by the superconducting solenoid covering $|\eta| < 1.4$, the Outer Calorimeter (HO) outside of the solenoid, it is placed there to identify late starting showers, it covers $|\eta| < 1.26$, the HCAL Endcaps (HE), covering $1.2 < |\eta| < 3.0$ and Forward Calorimeters (HF) $3.0 < |\eta| < 5.2$

Figure 20 - CMS Electromagnetic Calorimeter layout

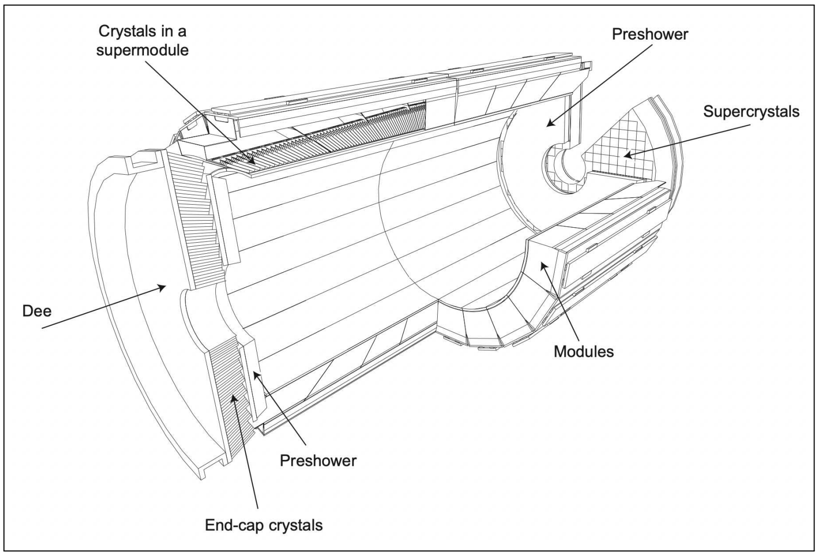

Legend: Layout of CMS electromagnetic calorimeter, showing its components.
Source: CMS COLLABORATION, 2008, p. 95.

and located at 11.2 m of the interaction point. The HF uses quartz fibers instead of brass, which provide Cherenkov light detection. Figure 21 shows a layout of the HCAL.

2.2.5 Muon Detector

The CMS detector features a very powerful muon detection system located in the most outward region of the detector. The muons played a significant contribution to many of the physics results of CMS including the Higgs discovery[10]. The goals of the Muon System are to identify, measure momentum and provide triggering for the muons. Figure 22 shows a quadrant view of the Muon System highlighting also chambers that will be installed during the Phase-2 upgrade.

The Muon System is composed of 4 different gaseous detector technologies:

- **Drift Tubes (DT):** Have a gas mixture composed of 85% Ar and 15% CO_2. The DT are located in the barrel ($|\eta| < 1.2$) providing spatial measurements for offline tracking, because of the fine spatial resolution of 100 μm, and trigger information. It is composed of 205 chambers divided in 12 sectors in ϕ and 5 wheels (longitudinal sections).

- **Cathode Strip Chambers (CSC):** Located in the endcap ($0.9 < |\eta| < 2.4$), the

---

[10] One of the first measured Higgs decay channel features four final state leptons $H \to ZZ \to 4l$.

Figure 21 - Longitudinal View of CMS Hadronic Calorimeter

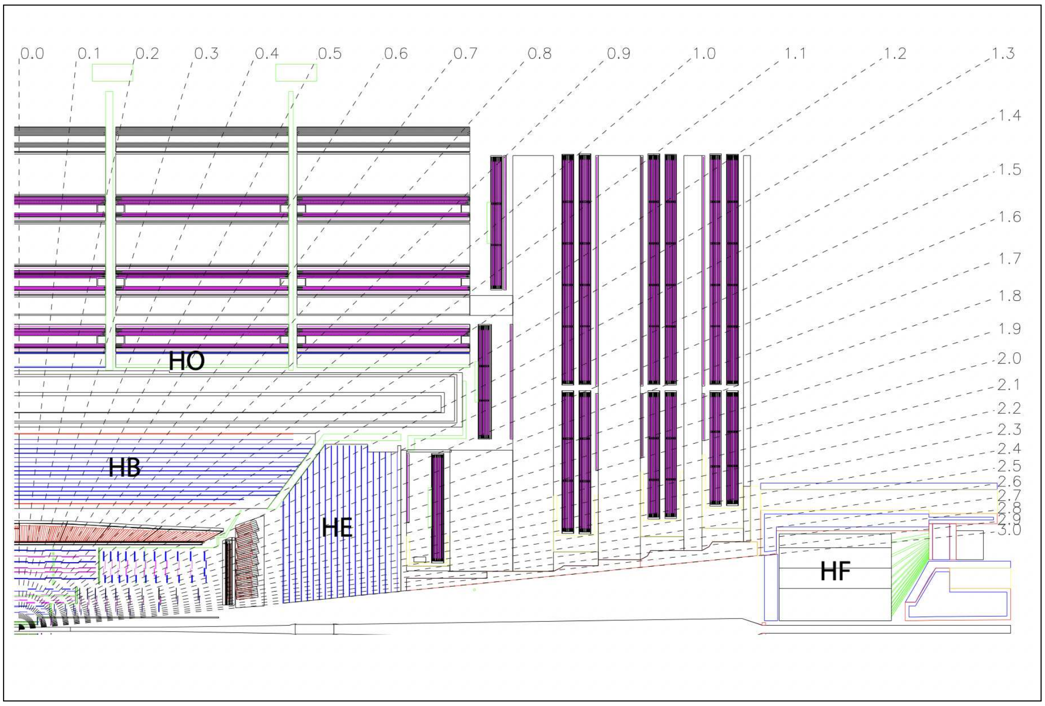

Legend: Longitudinal view of CMS hadronic calorimeter, showing its regions: HCAL Barrel (HB), Outer Calorimeter (HO), HCAL Endcaps (HE) and Forward Calorimeters (HF).
Source: CMS COLLABORATION, 2008, p. 123.

CSC subsystem is composed of 540 chambers which provide triggering and position measurements, with a spatial resolution ranging from 50 to 140 μm. The gas mixture is composed of 50% CO_2, 40% Ar, and 10% CF_4.

- **Resistive plate Chambers (RPC):** Located in both regions, barrel and endcap, covering $|\eta| < 1.9$. It is used mainly for triggering, due to its timing capabilities. The CMS RPC system will be better discussed in the chapter 3.

- **Gas-Electron Multiplier (GEM):** The GEMs were installed after Run 2, during the LHC Long-Shutdown period (LS2). They have both, good spatial and time resolution, complementing the CSCs high particle rate forward region ($1.6 < |\eta| < 2.2$).

2.2.6 Trigger and Data Acquisition

The proton-proton collision rate in LHC is extremely high, the bunch crossing (BX) frequency is 40 MHz and in each one of them many collisions can happen. It would be impossible to store and process this amount of events. To cope with these numbers, CMS uses a two tiered trigger to reduce the event rate to about 1 kHz.

Figure 22 - Quadrant View of the CMS Muon System

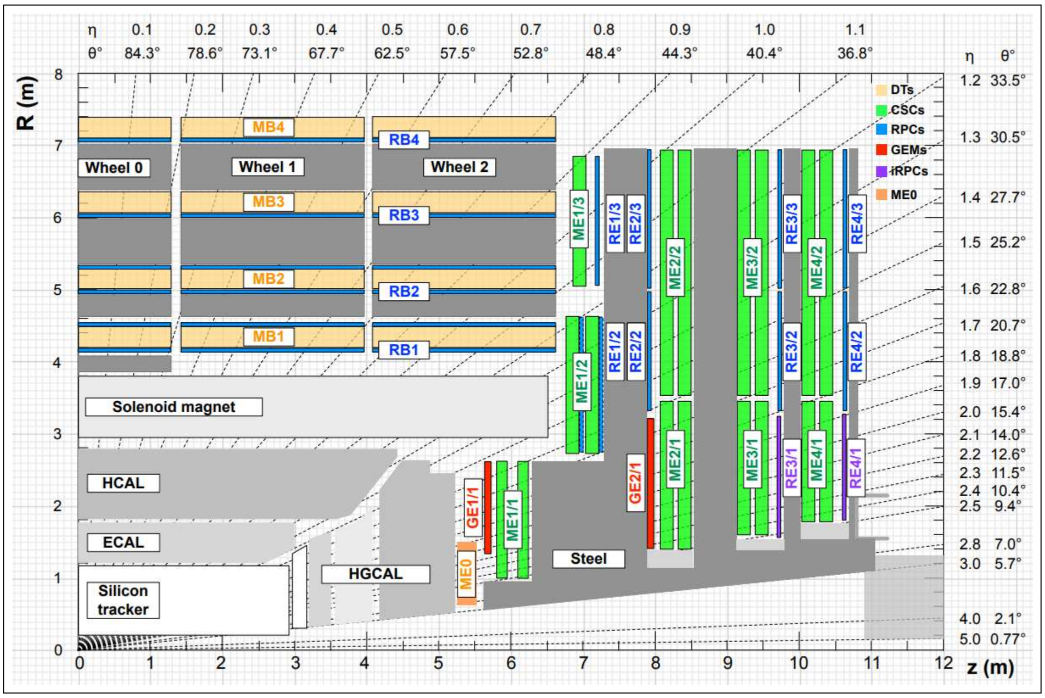

Legend: A quadrant view of the CMS detector highlighting its muon system after the phase-2 upgrade (RE3/1, RE4/1, GE1/1, GE2/1, ME0). DTs are coloured in yellow, CSCs in Green, RPCs in blue and GEMs in red and in orange. During LS2 the chambers GE1/1 were installed and are participating in Run 3

Source: CMS COLLABORATION, 2017b, p. 16.

First the event passes through a first level trigger called L1, which uses custom hardware processors information directly from the calorimeters and the muon detectors, to reduce the event rate to around 100 kHz. The L1 trigger relies on the transferring the data in optical links and processing it using FPGAs (Field Programmable Gate Arrays) to deliver the maximum readout speed and minimum latency (77).

The High Level Trigger (HLT) further processes the events accepted by the L1, doing more refined analysis on the events, which includes particle tracking. This trigger tier is centred in the concept of HLT path, which is a structured set of algorithms that selects the events. Those are simplified versions of the offline reconstruction algorithms, which run in a computing farm. Finally, the HLT chooses the data to be stored, by putting together the selected events accepted by a collection of HLT paths, forming a trigger menu.

2.2.7 The Particle Flow Algorithm

All the events accepted by the HLT are recorded and processed in the offline analysis in order to build the physics objects[11], which are reconstructed from the input from all the different subdetectors using an algorithm called Particle Flow (PF) (78).

The particles originating from the collisions leave signals in the detectors starting by the tracker, in which charged particles leave signals (hits) that serve as input to find their trajectories (tracks) and their point of origin (vertices). The magnetic field bends the charged particles tracks, making it possible to determine their momentum. Electrons and photons are absorbed by the electromagnetic calorimeter (ECAL), creating electromagnetic showers, and making it possible to measure their direction and energy. Charged and neutral hadrons initiate a hadronic shower, which is fully absorbed by the hadron calorimeter (HCAL), so that their direction and energy can be estimated. Muons and neutrinos travel through the calorimeters with almost no interaction. Muons produce additional hits in the muon system. Neutrinos pass undetected, so a missing energy can be attributed to its presence in the event. Figure 23 shows the signals left in the detector by different particles.

The Particle Flow was first used by the ALEPH detector, at LEP (79). A very important requirement is a fine spatial granularity of the detector layers, since a course granularity can make signal from different objects to be merged, reducing the reconstruction and identification capabilities.

The PF is well suited for CMS because: the high magnetic field separates the jet's

---

[11] Such as muons, electrons, photons, jets, missing transverse energy, etc.

Figure 23 - Particle interactions in the parts of the CMS detector

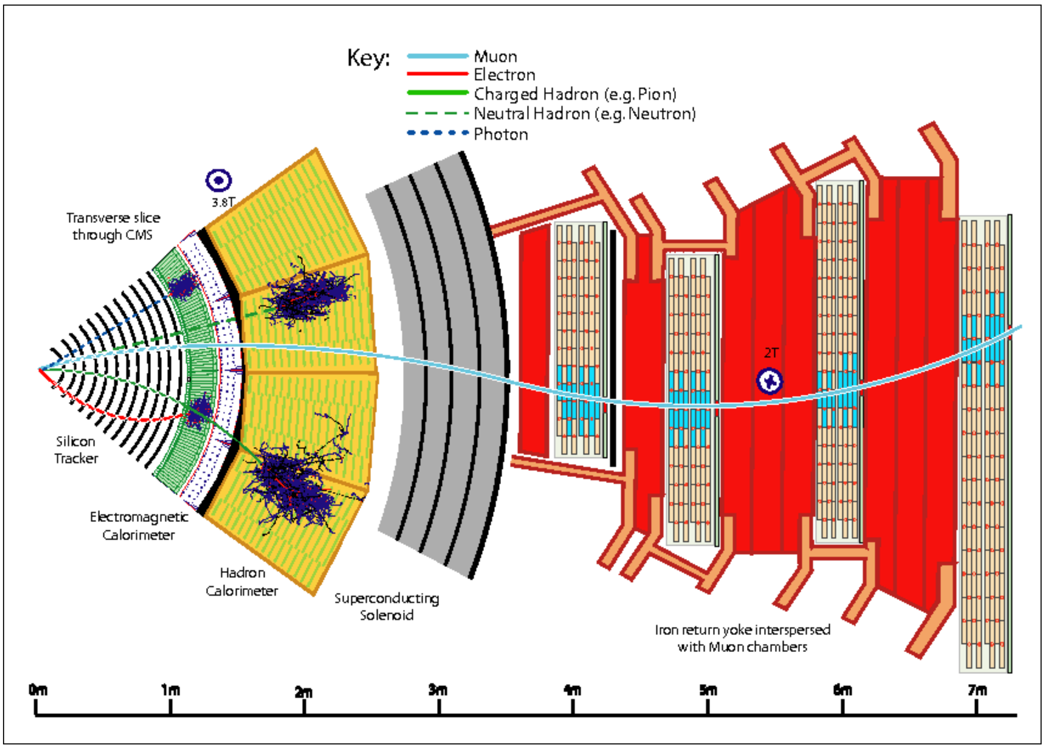

Legend: A drawing of the different particle interactions occurring in the CMS detector.
Source: CMS COLLABORATION, 2017c, p. 2.

charged and neutral hadrons energy deposits in the calorimeters, the fine grained tracker can provide a pure and efficient charged particle trajectory reconstruction in jets with transverse momentum up to around 1 TeV, a highly segmented ECAL allows a very good separation of energy clusters from different particles, a course segmented HCAL, which can still separate the charged and neutral hadrons clusters, and very good muon system which provide muon identification.

3 THE CMS RESISTIVE PLATE CHAMBERS

This chapter will discuss the CMS RPC system, where the author worked actively. A brief history of gaseous detectors will be presented, with focus on the RPC detector. The CMS RPC project will be introduced and the author's contributions will be presented.

3.1 Brief history of gaseous detectors

The first gaseous detector was introduced by E. Rutherford and H. Geiger in 1908 (80). The device consisted in a thin wire, the anode, coaxial to a cylindrical cathode filled with gas. Its working principle is the following. When an ionizing particle passes through the gas, it knocks out electrons from the gas molecules. By applying a difference of potential to the device, the released electrons accelerate to the anode and inelastic collisions with other gas molecules occurs, multiplying the effect of the primary ionization, in the so-called avalanche process, which was studied by John Sealy Townsend, between 1897 to 1901 (81). An illustration of the avalanche formation in gaseous detectors is shown in Fig. 24. This kind of detector is still used up to today, mainly on radiation detection and monitoring.

Figure 24 - Avalanche formation in gaseous detectors

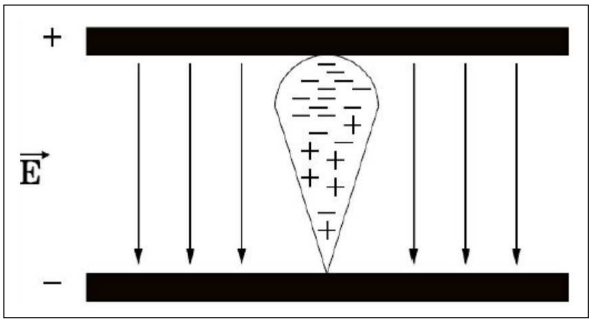

Legend: The formation of an avalanche in gaseous detectors. The ionised electrons drift towards the anode because of the external electric field. As they accelerate, new electrons-ion pairs are formed multiplying the initial ionisation. The drop-like shape of the avalanche is caused by the difference in the drift velocity of electrons and ions.

Source: SHOPOVA, 2018, p. 39.

This detector operation depends on the applied voltage as shown Fig. 25. At lower electric field strength, the electron and ions drift with no avalanche multiplication and the number of electron-ion pairs is independent of the voltage, and this is called ionization chamber mode. At the proportional mode the avalanche process occurs for each ionization, so that the number of electron-ion pairs is proportional to the energy deposited by the ionizing particle in the detector. Finally, at even higher voltage, in the Geiger-Müller counter region, there is emission of UV photons creating multiple avalanches along the anode wire (83). Also, at higher voltage levels the avalanches can increase into streamers, and even to sparks.

Figure 25 - Gaseous Counter Characteristic Curve

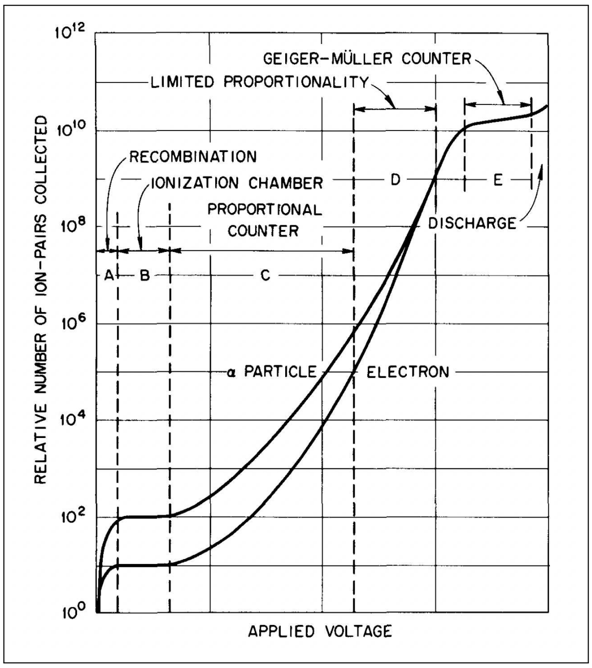

Legend: Curve of the relative number of ion pairs collected in a gaseous counter as a function of the applied voltage.

Source: O'KELLEY, 1961, p. 77.

But these devices are not suitable for the use in high-energy particle physics tracking. From the 1930s to the 1960s, the research on experimental particle physics was mainly done using cloud chambers and bubble chambers, which have excellent imaging capabilities, with the major drawback of being active only during a selected time interval, being unsuitable to analysis of rare events (84).

The first gaseous detector to be able to have a very good tracking capability was the spark chamber (85). On this one, rather than a constant voltage applied to its terminals, they had a pulsed high voltage applied to a parallel-plate gap shortly after the detection of a coincidence signal from scintillation detectors. A visible track would grow from the ionization trail left in the gas. Combined to a photography readout, they became great assets to particle detection, with a major drawback, the slow rates they could operate on, around dozens of Hertz (84).

In 1968, Georges Charpak created the multiwire proportional chamber (MWPC) (86). A schematic of a MWPC is shown in Fig. 26. It had a fast electronic readout, capable of withstanding high rates, excellent space resolution and was a continuously operating device. It was a major development in the particle detector field, the MWPCs and other detectors based on it[12] replaced other detectors with photographic readout. Still, a major drawback of such detectors was the time resolution, in the order of μs, because the drift time variates a lot depending on the position where the primary electron is created.

Figure 26 - Multiwire Proportional Chamber Schematic

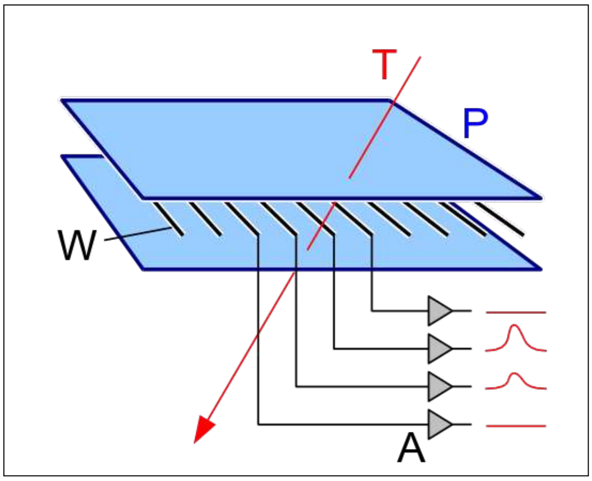

Legend: A schematic of a multiwire proportinal chamber. The blue plates are the cathodes and the wires are the anodes. When the a particle ionises the gas, the electrons drift towards the wires and, because of the avalanche multiplication, many electron are collected and a measurable signal is obtained at the anodes.

Source: WIRE chamber schematic, 2005.

Parallel-plate geometry detectors tend to perform better on the time resolution, because the electric field is uniform, so that all the gas volume is available for amplification, providing excellent timing capabilities (88). A successful implementation of the parallel-plate geometry are the resistive plate chambers.

3.2 Resistive Plate Chambers

The RPC was created in 1981 by Santonico and Cardarelli (89). This detector is very similar to a spark chamber, but with a major difference, its electrodes are made of materials with high electrical resistivity, in the order of $10^{10} - 10^{12}$ Ωcm, normally made of high pressure laminate (HPL), also known as Bakelite, or glass. The electrodes plates are coated with a conductive layer to provide good connection to the applied high voltage (HV).

---

[12] Such as drift chambers, time projection chambers, etc.

The two plates form a region where a mixture of gases is flushed, denominated gas gap. The thickness normally goes from 1-2 mm[13] and it is maintained constant by a network of spacers distributed throughout the plane. The signal readout is independent of the HV, it can be performed by copper strips or pads where the avalanche induces signals. A typical design of a RPC chamber is shown in Fig. 27.

Figure 27 - Resistive Plate Chamber Schematic

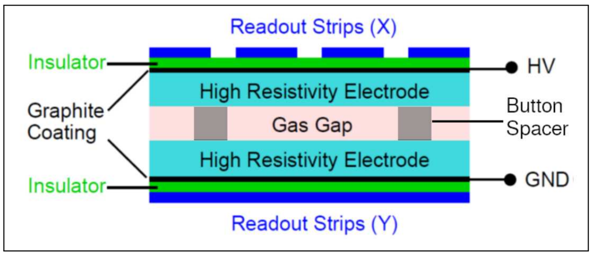

Legend: A Schematic of a typical RPC with one gap and readout by strips in two directions
Source: MONDAL, 2019, p. 1

The gas mixture is very important for efficient operation of the RPC. Normally, a mixture of tetrafluoroethane ($C_2H_2F_4$), commercially known as R134a or Freon to enhance ionization of the incident particles, that can compose more than 90% of the mixture, isobutane (iC_4H_{10}) as a quencher gas and sulfur hexafluoride (SF_6) to improve the electronegativity of the mixture and reduce the secondary ionization. Nowadays, the search of eco-friendly gas mixtures is a very active research field for the RPCs. The replacement is very important for the R134a and SF_6 as they contribute the most to the high global warming potential (GWP) of the mixture. The commercial replacement to the R134a are the HydroFluoroOlefyns (HFOs), for example the HFO1234ze ($C_3H_2F_4$) which brings the HV working point (WP) of the RPCs to higher values. Normally, it is added CO_2 or Helium to the HFO to bring the WP to a lower level. For the SF_6 some gases are being considered, for example, 3M Novec 5110, 3M Novec 4710, AMOLEA HFO-1224yd, etc. More details on the eco gas research can be found in (92). Some alternatives to reduce the flushing of fresh gas into the system, such as gas re-circulation systems, are also being developed (93).

The detector operates on a very high electrical field strength, in the order of 4-5 kV/mm. The authors of (94) pointed out that, when a particle passes through the gas volume, the primary electron-ion pairs give rise to a small discharge that is quenched without affecting the whole gas volume by the following mechanisms:

- Reduction of the electric field in the electrode at the region close to the discharge development, due to the high resistivity electrodes;

---

[13] Some designs have lower thickness, for instance, check (90)

- Absorption of the UV photons created in the discharge by the isobutane, preventing secondary discharges;
- Capture of the electrons in the outer region of the discharge because of the high electronegativity of the Freon.

Because of these mechanisms, the discharges in the RPC do not destroy the chamber or the front-end electronics. Furthermore, the size of the region affected by the discharge is small, leaving the rest of the chamber active, so that it can sustain higher rates. Coupling these characteristics to the excellent time resolution (some designs in the order of 50 ps), good spatial resolution (down to 50 μm in state-of-art designs (95)) and the relatively easy and cheap construction, the RPCs are very well suitable for high energy physics experiments, even for tracking. Normally, they are employed in muon systems, where it can cheaply cover an area of thousands of square meters as in the case of the CMS Experiment.

3.3 **CMS RPC System**

The CMS RPC system consists in 1056 double-gap chambers operating in avalanche mode. Each gap is constructed with two HPL sheets of bulk resistivity 1-6 $\times 10^{10}$ Ω cm. The HPL sheets are spaced 2 mm apart by a grid of plastic spacers. The internal surfaces of the gaps are coated with a 35 to 45 μm linseed oil. This treatment improves greatly the performance of the chambers, because it smooths the internal surfaces and quench UV photons (96, 97). The outside surfaces are coated with a conductive graphite paint, forming the electrodes, and isolated by a PET film. One gap is placed on top of the other with a readout of copper strips placed in between. The layout of a double-gap RPC is shown in Figure 28. Everything is placed inside an aluminum case.

Figure 28 - Double-gap CMS RPC layout

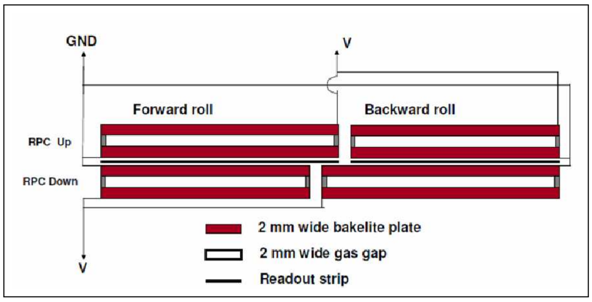

Legend: A schematic of a CMS RPC placed in the barrel region.
Source: COSTANTINI, 2013, p. 2.

The gas mixture employed, named CMS RPC standard gas mixture, is composed of 95.2 % of R134a, 4.5 % of isobutane and 0.3 % of SF_6 kept at 21 °C with relative humidity of 40-50 % to maintain the bakelite resistivity stable.

The RPC system is able to withstand high rate, of the order of 300 Hz/cm^2, have efficiency greater than 95 %, cluster size[14] less than 2 for a better spatial resolution between 0.8-1.3 cm, the time resolution is 1.5 ns making them interesting for muon triggering and BX assignment. There are RPCs both in the barrel and the endcap regions of CMS covering an area of 3500 m^2.

3.4 **CMS RPC Barrel**

In the barrel, there are 480 chambers distributed in 5 wheels (Wheel ± 2, ± 1 and 0) along the beam pipe. Each wheel consists in 4 stations (RB1-RB4) along the radius. The two inner stations consist of two RPC chambers with a DT in the middle and the two outer stations have only one RPC and one DT. Also, the wheel is divided in 12 sectors (S01-S12) along the direction of the azimuthal angle ϕ. There are two chambers in each of the stations RB1 and RB2 named "in" and "out". Due to mechanical reasons, RB3 and RB4 are further divided into two chambers (named + and −) along ϕ in all sectors but S04, S09 and S11 in RB4. Since RB4/S09 and RB4/S11 are in the feet of the barrel wheel, they have a single RPC. RB4/S04 has four chambers (named −−, −, + and ++). The layout of a RPC barrel wheel is shown in Figure 29.

Each RPC chamber is divided into partitions with respect to the pseudorapidity called rolls. Most of the chambers are divided into 2 partitions. Chambers from RB2in in wheels -1, 0 and 1 and RB2out in wheels -2 and +2 have 3 rolls. Schematics of this kind of chambers are displayed in Fig. 30.

3.5 **CMS RPC Endcap**

In the endcap, there are 576 chambers divided into the 8 disks (RE±1, RE±2, RE±3, RE±4). Each disk has 72 chambers of trapezoidal shape divided in 2 concentric rings and 36 sectors. Each chamber is divided into 3 rolls, named A, B and C. The higher segmentation with respect to the barrel is driven by the higher particle multiplicity in the frontal regions. A layout of the Endcap geometry is shown in Fig. 31.

---

[14] number of adjacent strips fired in a single muon hit

Figure 29 - CMS RPC barrel layout

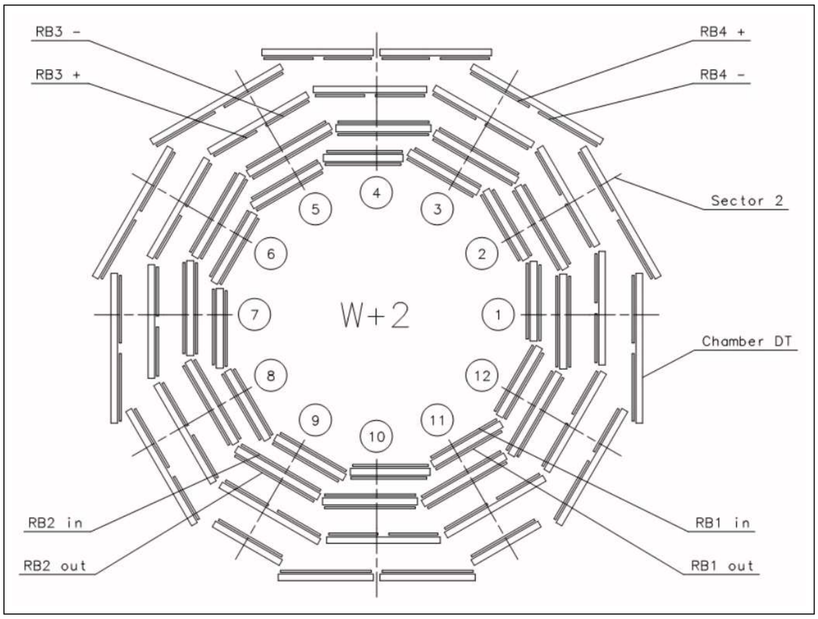

Legend: Layout of RPCs placed in the CMS barrel region. They are distributed along 4 stations and 12 sectors for each wheel.

Source: CMS COLLABORATION, 2008, p. 218.

Figure 30 - Barrel CMS RPCs division in rolls.

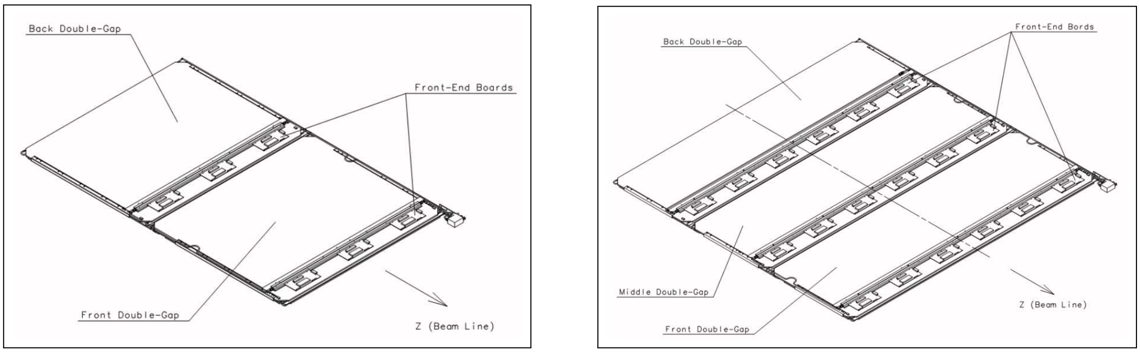

(a) (b)

Legend: Layout of chambers in CMS barrel divided into two rolls (a) and three rolls (b).

Source: CMS COLLABORATION, 2008, p. 219–220.

Figure 31 - CMS RPC endcap layout

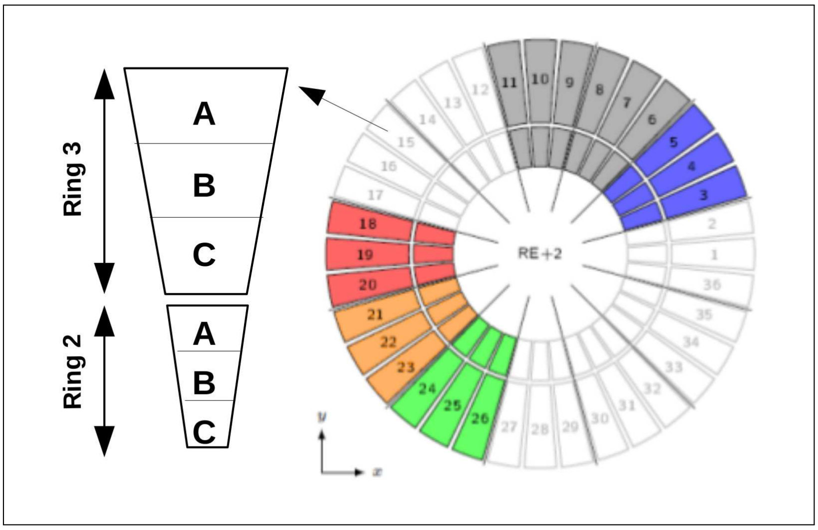

Legend: Layout of the RPCs placed in the CMS endcap region. They are distributed in 2 rings and 36 sectors for each disk.

Source: CMS COLLABORATION, 2016.

3.6 RPC Upgrade for Phase-2

The new requirements of the HL-LHC upgrade in terms of pile-up, background and detector ageing will pose a big challenge for the correct muon identification and transverse momentum determination. The full muon system is preparing upgrades for the HL-LHC. For the RPC system in particular, two important developments are foreseen.

The first upgrade is the replacement of the off-detector electronics (called link system). The current link system role is to process, synchronize and zero-suppress the signals coming from the RPC Front-End Boards (FEB) providing the RPC hits in a BX. The new link system will be able to deliver time of the hits, bringing the full timing potential of this detector. Also, it will employ techniques and materials to suppress problems and deterioration caused by the high radiation environment.

The second upgrade is the extension of the RPC coverage from $|\eta| = 1.9$ to 2.4 with the new improved RPC (iRPC) detectors. An extensive R&D program is taking place to fulfil the demanding conditions of the HL-LHC. Two new RPC layers are going to be installed in the innermost rings of the disks RE±4 and RE±3. The new chambers will have a complete new design, with double-gap chambers with 1.4 mm gap thickness, to improve the time resolution. Also, the signal readout will be done in the two sides of the strip plane, enabling the determination of the position in the 2D plane by a completely new front-end electronics. The position in the dimension transversal of the strip is determined by the position of the fired strip and the position along the strip is determined by the difference of the time of arrival at the two ends of the strip.

Regarding the current system, longevity tests are taking place at CERN GIF++ facility (100). The chambers are irradiated with a 12.6 TBq source in order to simulate the background conditions of the HL-LHC. The tested RPCs showed stable performance with rates up to 600 Hz/cm^2 and with 93 % of the expected integrated charge (101).

A complete review of the muon system upgrade can be found in (76).

3.7 Author's contribution to the CMS RPC Project

During my Ph.D., there were many opportunities to contribute to the CMS RPC project. This section highlights the author most important contributions.

3.7.1 Standard maintenance during Long Shutdown 2

From December 2018 to March 2022, the LHC machine ceased operation for maintenance and upgrades in the accelerator complex in a period called Long Shutdown 2 (LS2). This time was an important moment for CMS maintenance and upgrades in preparation for the next data taking period (Run 3). In particular, the CMS RPC system underwent an intensive maintenance program to recover as much as possible the defects of the system. Also, in preparation for the future installation of the iRPCs chambers cooling and cable services for the new detectors were installed.

An extensive HV and low voltage (LV) maintenance campaign was performed. The goal of HV maintenance was to identify the problematic parts of the HV power system and to fix it in the best possible way, recovering the performance of the chambers. A RPC chamber can have problems in one of the gaps or both, when the problem is in one of the gaps the efficiency of such chamber can decrease as much as 15 %, but it is recoverable with the increase of the applied HV, although it is not optimal as the current increases and the chamber's longevity is affected.

The problems in HV were normally in one of the HV connectors, either because of bad connection, which was solved by a proper connection, or by defective connector, as shown in Fig. 32. If this was the case, the replacement of the connector or the use of spare channels was enough to bring back the gap to a good performance. In some cases, the gaps themselves were problematic, for example, because of problems with gas leakage. A total of 65 HV channels were repaired during LS2.

The LV maintenance aim was to ensure a proper operation and configuration of the detector electronics and ensure a good functionality of the LV power boards and communication buses. A total of 12 LV problems were fixed.

Another important activity was the extraction of the chambers from the two RE4

Figure 32 - Defective HV connector

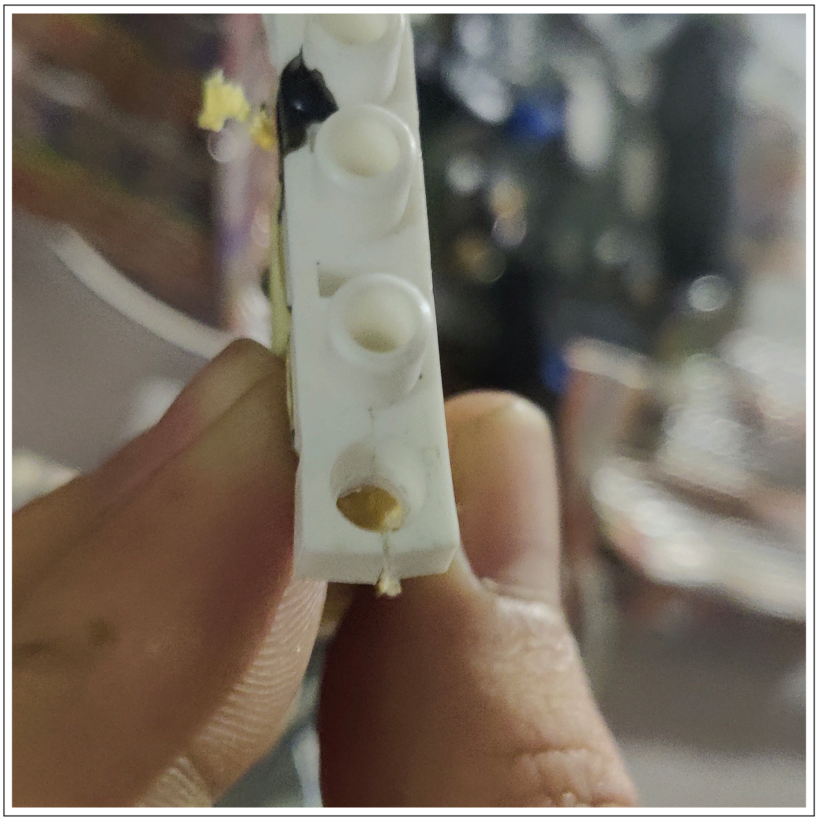

Legend: Example of defective HV connector. It is possible to see a crack in the connector on the bottom of the image. This problem compromises the proper isolation of the HV connector.

Source: The author, 2023.

stations to allow the CSC ME4/1 chambers extraction for electronics refurbishment. The chambers were brought to the surface, and accommodated in a new laboratory with controlled environmental conditions and the infrastructure needed to test them (HV, LV and gas). All needed reparation and revalidation was done in this laboratory, before all the chambers were installed back.

The most crucial activity, was gas system consolidation. The aim was to minimize the environmental impact of the RPC system. The actions taken were:

- Gas leakage identification and repair. Often, the problems with the gas leaks were because of broken gas pipes and inlets inside the chambers. An endoscope was employed to find the problematic points and reparation was done when accessible. Figure 33 shows examples of problems found with the endoscope. Out of the identified 122 leaky chambers in barrel 49 were repaired, 14 were non-recoverable.
- Recuperation of the Exhaust, which was not working during Run-2 for the installation of the first $C_2H_2F_4$ recuperation system with efficiency of 80 %, which has been developed by CERN EP-DT Gas team (93).
- Installation of automatic pressure regulation valves on the redistribution gas racks to minimize pressure variations in the chambers, which can be a possible source of new leaks.
- Shutdown of the remaining leaky chambers which were not possible to repair, to keep the amount of fresh gas added to the system at a minimum.

A summary of the activities in LS2 can be found in (102).

The performance of the repaired chambers can be seen in Figs. 34 and 35 as a comparison between cosmic-rays data-taking of 2018 and 2021. There was great improvement, 34 rolls were recovered by gas leak repairs and the HV repairs translated into a gain of 6% in the efficiency of these chambers. Overall, the results of the repairs were successful bringing higher efficiency to the repaired channels.

Figure 36 presents a comparison of the distribution of roll efficiency in pp collisions taken in 2018 and 2022 for barrel and endcap, the efficiency is equivalent, but there is a lower proportion of bad performing rolls in 2022. In barrel, chambers with gas leaks were switched off as part of a strategy to keep the gas waste to a minimum and to prevent any problems in those chambers, which may perform in good condition after reparation. This translates to a smaller number of chambers in the plot in Fig. 36a for the year 2022. It is expected that the impact to the muon system is small, since the trigger takes information from all detectors and there are many redundancies.

Other than the gains in efficiency, the maintenance had great impact to the longevity of the RPC system, keeping the system in good condition for the next years of data taking.

Figure 33 - Gas problems inside RPC chambers.

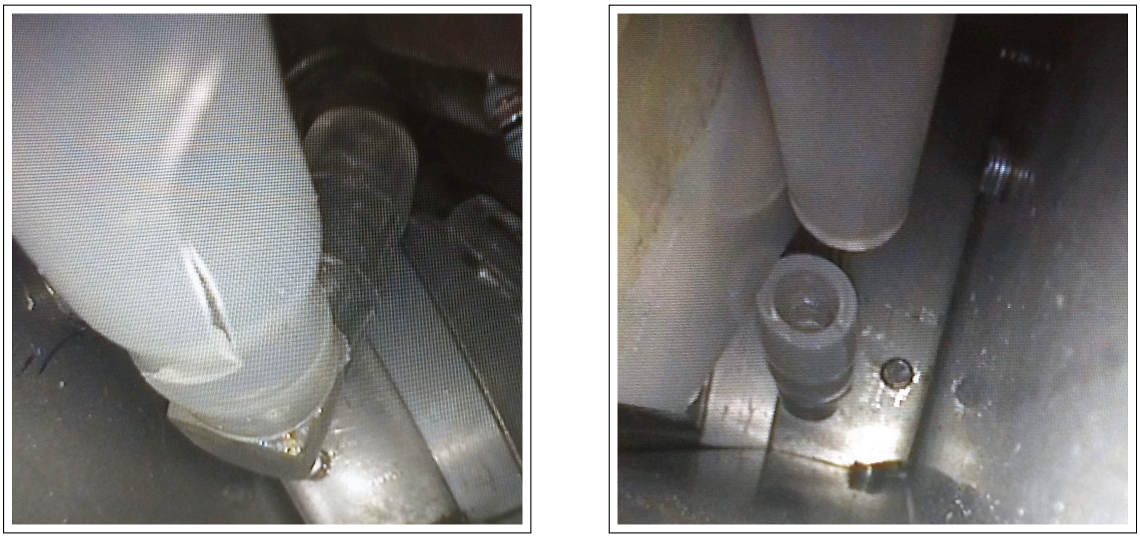

(a) (b)

Legend: Pictures taken during endoscopic inspection to find gas problems inside RPC chambers. A crack in the pipe is found in (a) and a completely cut pipe in (b)

Source: The author, 2023.

Figure 34 - Performance of repaired gas leak chambers in cosmic data taking

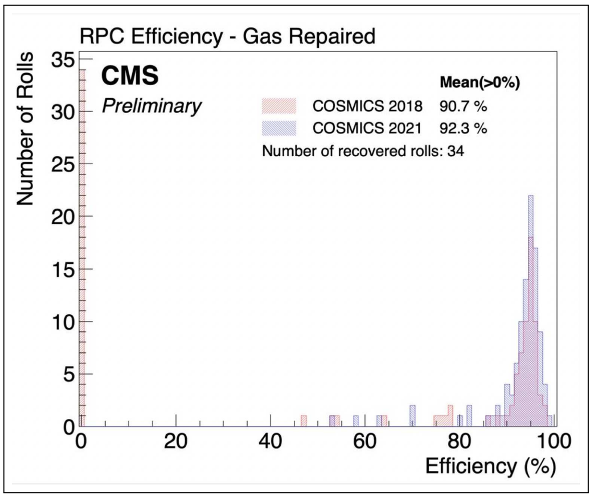

Legend: The distribution of efficiency of RPC rolls on gas repaired chambers during the Long Shutdown 2 (LS2), using cosmics data taken in 2018 (red) and 2021 (blue) for barrel region. The numbers show a significant improvement, with respect to 2018 as 34 OFF rolls from Run-2 are recovered and HV is repaired for several chambers recovering chambers from Single Gap to Double Gap operation mode.

Source: CMS COLLABORATION, 2021b.

Figure 35 - Performance of HV repaired chambers in cosmic data taking

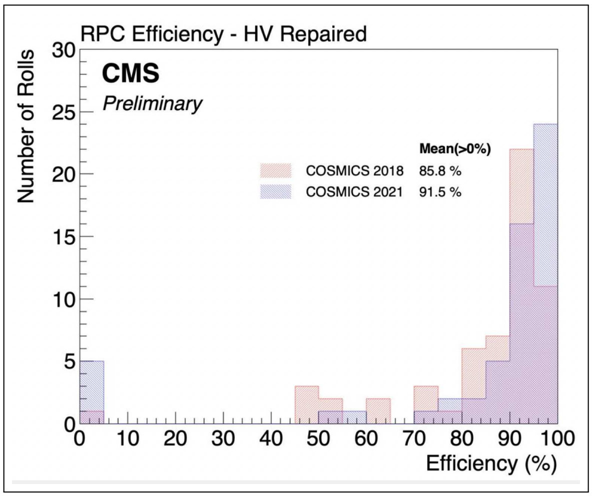

Legend: The distribution of efficiency of RPC rolls on HV repaired chambers during the Long Shutdown-2 (LS2) using cosmics data taken in 2018 (red) and 2021 (blue) for barrel region. The RPC efficiencies measured in 2021, after LS2 are comparable and in agreement with the expectations. The overall efficiency is improved by 6% due to recovery of chambers from Single Gap to Double Gap operation mode.

Source: CMS COLLABORATION, 2021b.

Figure 36 - Overall RPC efficiency in pp collisions.

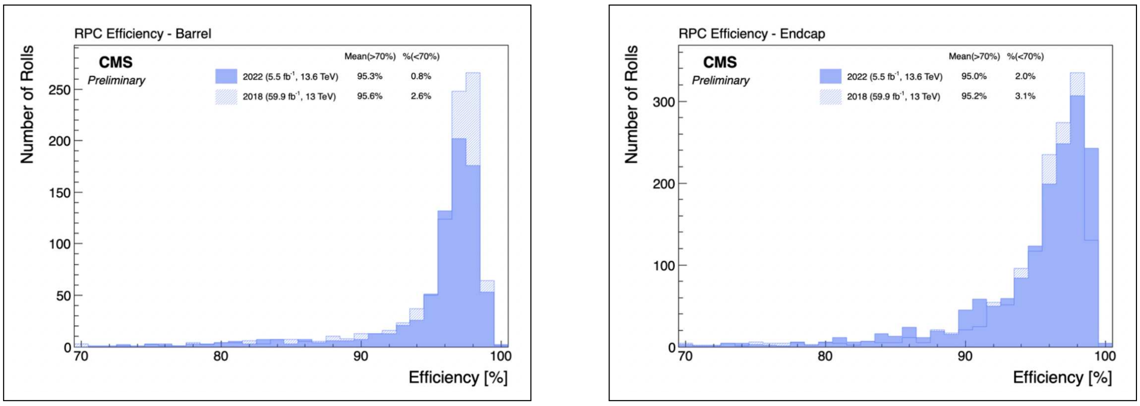

(a) (b)

Legend: Comparison of the overall RPC efficiency in 2018 and 2022 in pp collisions data taking. The barrel chambers are plotted in (a) and the endcap ones in (b). Chambers with known hardware problems (e.g. turned off due to gas leaks, noisy signal channels) were not considered.

Source: CMS COLLABORATION, 2022c.

3.7.2 RPC Detector Control System

In big experiment like CMS it is very important the use of software for all the required needs for control, monitoring and safe operation of its subsystems. The WinCC[15] SCADA (Supervisory Control And Data Acquisition) software together with the Joint Control Project (JCOP) framework form the basis of the Detector Control System (DCS) for the big experiments at LHC (105).

In CMS, each subsystem is tasked to develop a DCS for itself to be able to react to the commands passed from the CMS Central DCS. The RPC DCS is divided into several subsystems that are part of the infrastructure needed for the operation of the RPCs chambers as shown in Figure 37. Each subsystem communicates with DCS, passing information that is archived in a ORACLE database and receiving commands.

Figure 37 - CMS RPC DCS layout

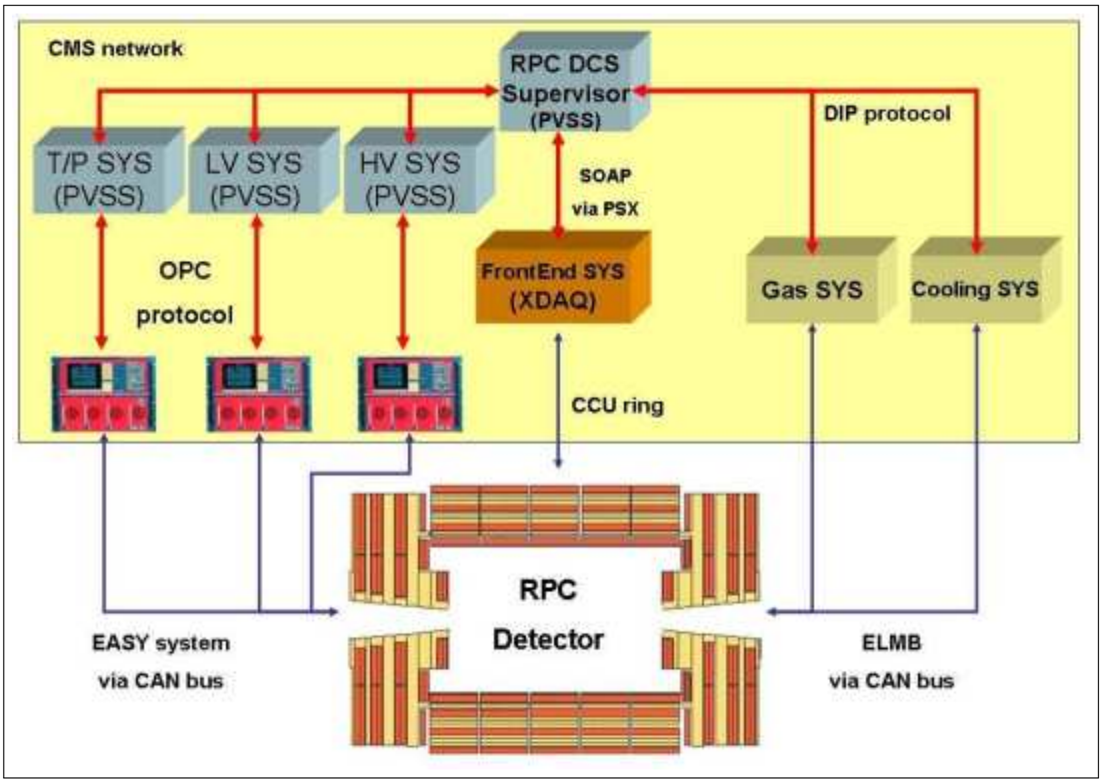

Legend: The CMS RPC DCS layout, displaying all its subsystems.
Source: POLESE, 2010, p. 2.

The Power system for HV and LV is based on the CAEN EASY project (107). It is designed to operate in hostile areas (high radiation and magnetic field strength) and connected to the DCS through the OPC protocol (108). Temperature and relative

---

[15] formerly known as PVSS

humidity (RH) sensors are read by ADCs connected to the CAEN EASY system and sent to DCS. The gas infrastructure data is acquired from Programmable Logic Controllers and distributed via DIP (109). In the same way, all the information concerning the CMS infrastructure, (e.g. Cooling, Detector Safety System (DSS), LHC and Magnet status), is available through DIP. Finally, FEB information is available through XDAQ, the online CMS framework, using SOAP (Simple Object Access Protocol) messages to PSX (110).

All these control subsystems are able to run by themselves as components of the RPC system. However, all the information is gathered around a hierarchical double-tree control structure, shown in Fig. 38, implemented through a Finite State Machine (FSM). This automation schema reduces the amount of human intervention in the system for all the repetitive tasks, and optimize recovery procedures in case of undesired states. The FSM is defined by its states and the commands. The states are:

- ON - RPC is ready for data taking.
- STANDBY - High voltages are on standby voltage (6500 V for the CMS RPCs and 5000 V for the iRPCs), low voltages are on. It is used as a safe state.
- OFF - Both high voltages and low voltages are switched-off.
- RAMPING - A transitional state, while the High voltage is moving to the desired set point.
- ERROR - A manual intervention is required and no data taking is possible.

The commands are ON, OFF and STANDBY, which effectuates the transitions to the states with same name.

The WinCC software can also be used to program a Graphical User Interface (GUI). It is developed to be an easy way for the user interact with the system, being able to control and monitor the desired parameters of the system, as well as display the important alerts. It is structured in approximately 40 panels to provide easy visualization and navigation through the system structure. The GUI can be accessed remotely, which is very important for a collaboration with people from different countries in the world, like CMS, and provides an authentication system, to prevent use from non-experts. Figure 39 displays an overview of the RPC DCS GUI.

More details on the design of the RPC DCS can be found in (106, 111)

The work done at the CMS RPC DCS was the update of the system due to the upgrade of WinCC version 3.15 to 3.16, which introduced some breaking changes, so the current software needed to be adapted to this new version, with correction of bugs and addition of new functionalities. Another task, was the creation of a new panel, shown in Fig. 40, for four iRPCs installed as a Demonstrator.

Figure 38 - CMS RPC hierarchy tree

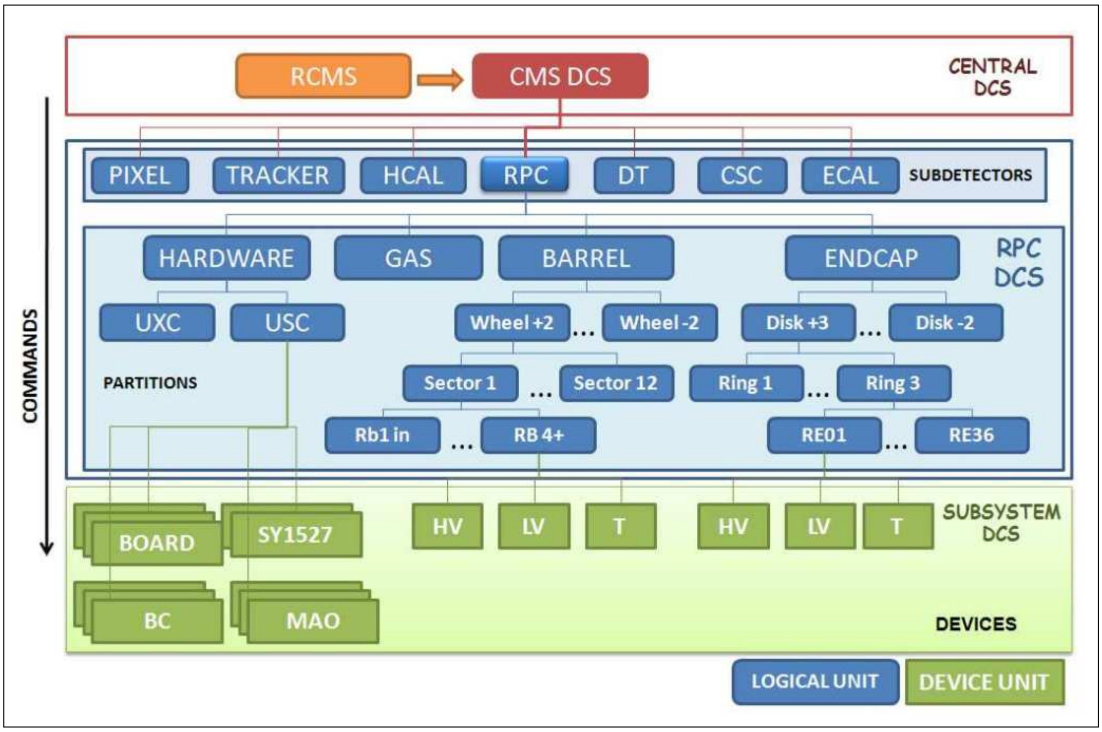

Legend: Structure of the hierarchy tree of the RPC DCS. Different branches describe the RPC system from the geographical and hardware points of view. All commands go down the hierarchy, while information and error messages are reported upwards.

Source: POLESE, 2010, p. 7.

Figure 39 - CMS RPC DCS GUI overview

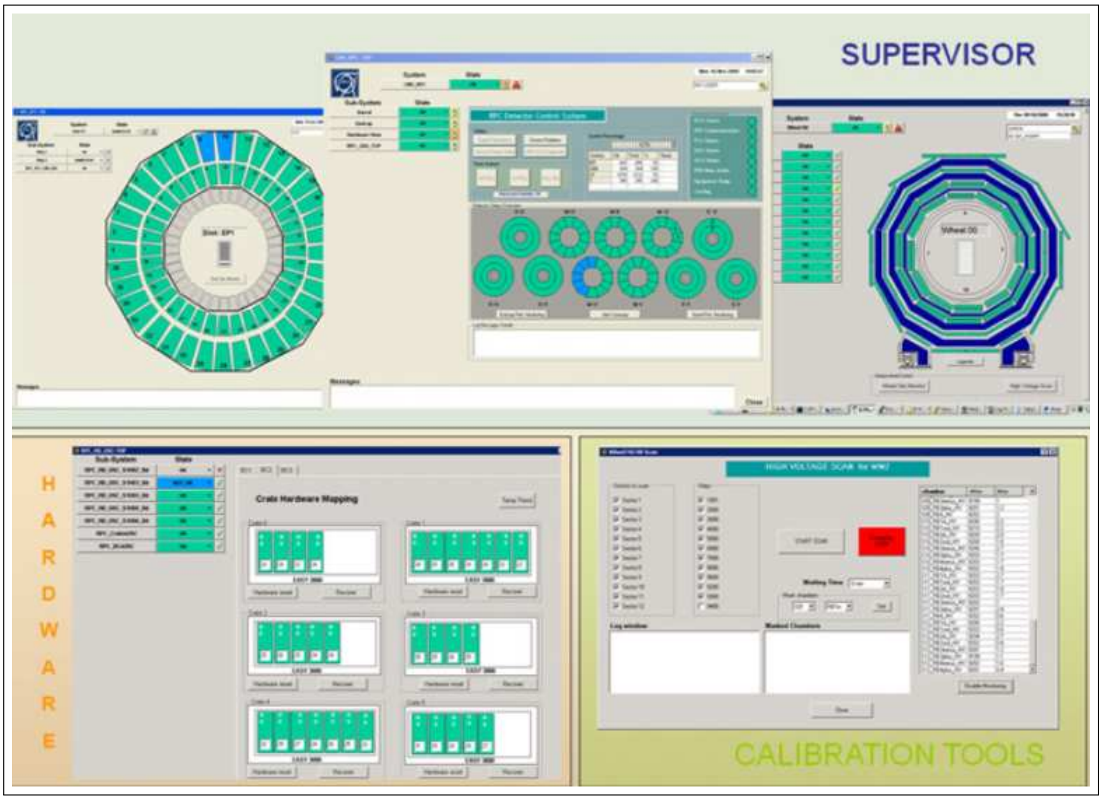

Legend: Overview of the CMS RPC DCS GUI. The panels are formed with a combination of widgets and texts to better display the system structure.

Source: POLESE, 2012, p. S26.

Figure 40 - CMS RPC DCS Demonstrator panel

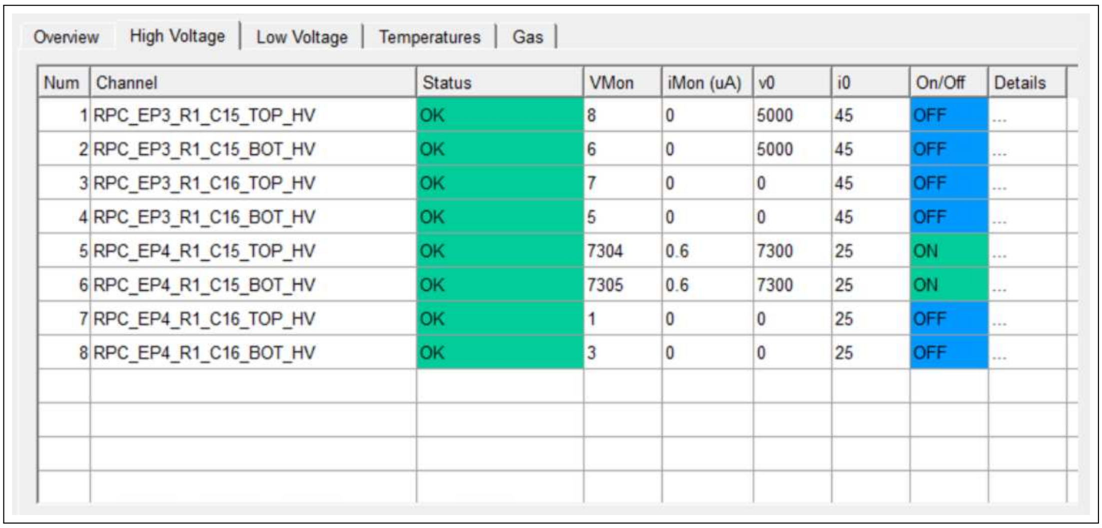

Num	Channel	Status	VMon	iMon (uA)	v0	i0	On/Off	Details
1	RPC_EP3_R1_C15_TOP_HV	OK	8	0	5000	45	OFF	...
2	RPC_EP3_R1_C15_BOT_HV	OK	6	0	5000	45	OFF	...
3	RPC_EP3_R1_C16_TOP_HV	OK	7	0	0	45	OFF	...
4	RPC_EP3_R1_C16_BOT_HV	OK	5	0	0	45	OFF	...
5	RPC_EP4_R1_C15_TOP_HV	OK	7304	0.6	7300	25	ON	...
6	RPC_EP4_R1_C15_BOT_HV	OK	7305	0.6	7300	25	ON	...
7	RPC_EP4_R1_C16_TOP_HV	OK	1	0	0	25	OFF	...
8	RPC_EP4_R1_C16_BOT_HV	OK	3	0	0	25	OFF	...

Legend: New Panel at CMS RPC DCS for the iRPC demonstrator chambers control and monitoring.

Source: The author, 2023.

The most important work was the creation of a new database schema for the gas system. Because of the big changes in the gas system, due to the gas leaks, many channels had to be swapped and some of them switched off. This created the need to change the previous schema, which was chamber-based, to a new one, with abstractions for the gas racks, gas channels and the chambers. Furthermore, the gas flow cells used were found to not be precise enough in the measurements, that are very important to the determination of whether or not the chambers are leaking. This demanded the creation of three new tables in the database schema and update of the WinCC with the new abstraction. The tables were created to facilitate the relationship between chambers, the geographical position and infrastructure they use (e.g. HV/LV/gas channels) and current "health" situation (if any of the gaps are disconnected).

The gas flow for each one of the gas channels was calibrated by a linear function, which parameters were determined by using a very precise mass flowmeter. The DCS is also tasked to use these parameters to calculate the corrected flow.

3.7.3 RPC-based tracking system at GIF++

Another task developed for the RPC Project was to help in the test beams at CERN Gamma Irradiation Facility (GIF++), to measure the performance and longevity of the RPC and iRPC chambers in the HL-LHC conditions.

GIF++ is a very singular facility, where a high energy particle beam (normally muons) and photons from a gamma source (13 TBq, ^{137}Cs), with adjustable flux, are combined (100). Tests for the muon detectors of several experiments (e.g. ATLAS, ALICE, CMS and SHiP) are taking place there.

The data acquisition is performed using a CAEN Time-to-Digital Converter (TDC) module of type V1190A where the front-end electronics of the chambers are connected. A V1718 VME controller module is responsible for the communication between the TDC and the computer where the data are stored. To host the VME controller and the TDC a 6U VME 6021 crate is used.

To determine the data taking with respect to the HV, several runs are taken for different HV points. The hits are recorded by the TDC with respect to a trigger based on the coincidence of scintillation detectors, as shown in Figure 41. All hits are recorded in a time window of 5 μs. The triggered muons show a narrow peak in Fig. 41a, so a time window is defined for the hits that are going to be taken into account for the efficiency calculation, in order to suppress the the majority of background from gammas. The time window is defined by doing a Gaussian fit to the time profile in the region of the peak and a window of 6 times sigma, centred in the mean of the fitted Gaussian is taken as the muon window, as given by Fig. 41b.

Figure 41 - RPC hits recorded by a TDC at GIF++.

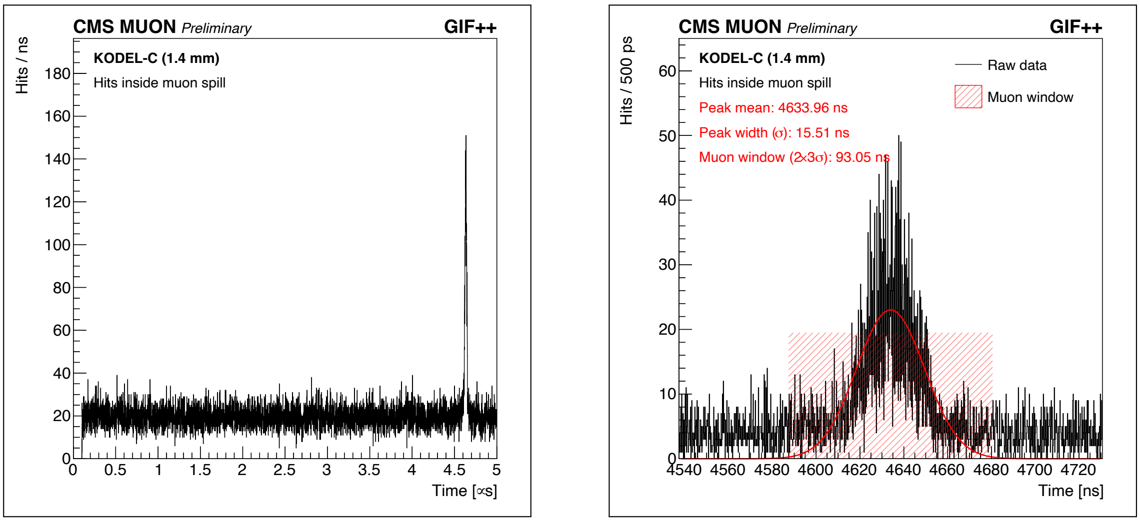

(a) (b)

Legend: Hits recorded from a 1.4 mm double-gap chamber at GIF++. In (a) it is possible to see a narrow peak that comes from the triggered muon beam and a background that comes from gammas. In (b) the time profile is zoomed in the muon beam region and a Gaussian fit is done to determine the muon time window.

Source: The author, 2023.

The efficiency is calculated by

$$\epsilon_{tot} = N_{tot}/N_{evt}, \tag{19}$$

where the N$_{tot}$ are the number of events with at least 1 hit inside the muon time window and N$_{evt}$ is the number of recorded events. However, there still is contamination of gammas which were detected inside the muon time window. One strategy to remove the gamma contribution to the efficiency is to use the Bayes probability formula for dependent measurements

$$\begin{aligned} \epsilon_{tot} &= \epsilon_{\mu} + \epsilon_{\gamma} - \epsilon_{\mu} \times \epsilon_{\gamma}, \\ \epsilon_{\mu} &= \frac{\epsilon_{tot} - \epsilon_{\gamma}}{1 - \epsilon_{\gamma}}, \end{aligned} \tag{20}$$

where ϵ_{γ} is the fake efficiency from gammas, that can be extracted by calculating the efficiency in a region outside of the muon window, and ϵ_{μ} is the real muon efficiency. This approach was used to measure the muon efficiency for CMS RPC chambers during tests beams in 1997 at the old Gamma Irradiation Facility (112). The gamma efficiency depends on the size of the time window, which is not optimal. Furthermore, for lower photon flux, the fake efficiency calculation can suffer from lower statistics.

The chambers must be validated up to the expected background rate: 600 Hz/cm^2

for the RPCs in the current CMS Muon system and up to 2 kHz/cm^2 for the new iRPCs (including the safety factor of three) (76). Such high rates can pose a challenge to the measurement, as the fake hits can bias the data-taking. So a tracking system made of RPCs was proposed to remove the background that comes from photons, taking into account the high efficiency of these chambers to muon and the fact that the photon can only be detected by the RPC after being converted to electrons, and the detection efficiency is low ($< 1\%$) (113).

Figure 42 shows the experimental setup at GIF++. There are two trolleys in the setup. The chamber under test is placed in the one closest to the gamma source (from now on referred to as KODEL-C), while two tracking RPC chambers (from now on referred to as GT1 and GT2), with their strip planes oriented perpendicular to each other to allow measurement in two directions, are installed in the trolley farther away from the gamma source. Details on the used chambers characteristics are summarized in Table 2.

Figure 42 - Experimental Setup at GIF++.

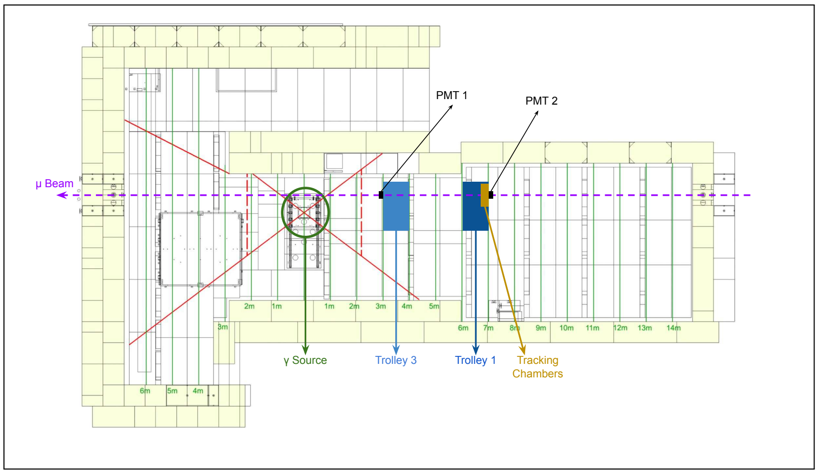

Legend: The experimental setup inside the GIF++ bunker. There are two trolleys where RPC chambers are placed for irradiation. The tracking chambers are located in the trolley farther away from the gamma source.

Source: AMARILO, 2023, p. 2.

To start the tracking analysis first the events are chosen so that there is at least one hit inside the muon time window for the two tracking chambers. This is required so that the probability of hits from background is very low. A 2D hit profile is constructed to check the alignment of the tracking chambers and the muon beam (Fig. 43). The tracking chambers positions in the trolley are adjusted so that the muon beam is centred in the run, so avoiding the muons to fall out of the detecting region by possible beam adjustments during the data taking.

The tracking algorithm relies on the assumption that the beam is perpendicular to the strip plane, therefore it is only needed to extrapolate the position of the hit from the

Table 2 - Characteristics of the chambers used in the tracking analysis

Name	Gap type	Strip Plane	Front-End Electronics
GT1 (tracking)	Double Gap HPL 2mm thickness	32 strips 1.45 cm pitch	CMS Electronics 150 fC, 100 ns port width
GT2 (tracking)	Double Gap HPL 2mm thickness	32 strips 1.45 cm pitch	CMS Electronics 150 fC, 100 ns port width
KODEL-C (test)	Double Gap HPL 1.4mm thickness	32 strips 1.94 cm pitch	Custom Electronics 75 fC, 60 ns port width

Legend: Characteristics of the chambers used for the tracking and the test chamber to evaluate the performance of the algorithm

Source: AMARILO, 2023, p. 2.

Figure 43 - 2D hit profile of tracking chambers at GIF++.

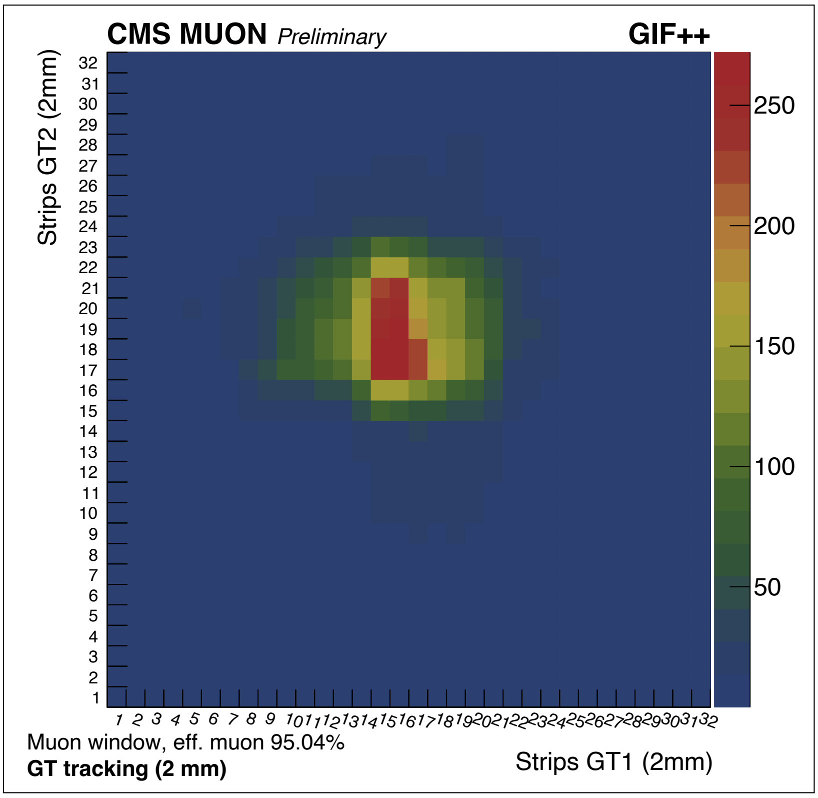

Legend: 2D hit profile from the tracking chambers at GIF++. The chambers' strip plane are oriented perpendicularly to each other so that it is possible to make a 2D hit mapping.

Source: AMARILO, 2023, p. 3.

tracking to the test chamber and check for a matching hit. For every event, the following steps are taken (114):

1. Perform the clusterization of the hits in the tracking chambers, where events with more than one cluster are rejected. The cluster barycenters are defined as the mean position in the cluster;
2. Perform the clusterization for the test chambers and calculate the clusters' barycenters;
3. Form a perpendicular track starting from the tracking cluster barycenter;
4. Check for a match in any cluster on the test chamber.

The clusterization is done by grouping hits that are adjacent and do not exceed a difference of time. The difference of time is previously determined in cosmic or with no gamma source data taking and depends on the chambers and front-end electronics and DAQ used. The cluster barycenter is defined as the geometrical mean position of the cluster. Figure 44 shows an example of an event where a matching hit was found.

Figure 44 - Example of an event recorded at GIF++ with addition to the tracking chambers.

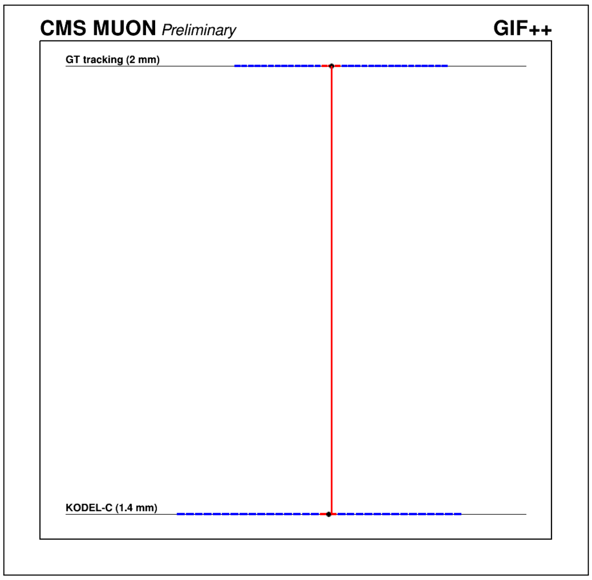

Legend: Example of one event in which the hit on tracking chamber was matched to the test chamber. The strips in red on GT and KODEL-C planes represent the hits and the point in black is the cluster barycentre.

Source: AMARILO, 2023, p. 3.

Efficiency curves of the test chambers were used to evaluate the validity of the tracking in rejecting the fake hits caused by the gammas. On Fig. 45 the efficiency curves are compared for three gamma background conditions. There are three curves in each plot. The black curve is calculated without the tracking, taking into consideration all the hits in the muon time window. For the blue one, only the hits that passed the tracking criteria were considered. Finally, for the red curve, the HV was recalculated to remove the voltage drop caused by the resistance of the electrodes using the Ohm law

$$HV_{gas} = HV_{app} - R \cdot I, \tag{21}$$

where HV$_{gas}$ is the corrected HV, HV$_{app}$ is the applied HV, R is the resistance of the electrode, determined previously by argon scans (81). This correction decouples the shift to the right of the curve on higher cluster rates, caused by the increase of the current. Therefore, HV$_{gas}$ is the effective HV applied to the gas volume.

In Fig. 45a the curves are equivalent, this behavior is expected, since at lower rates (1.8 Hz/cm^2), the currents are low, so there are no fake hits nor HV correction. In Figure 45b, the background rate becomes substantial (0.645 kHz/cm^2), so we can see a shift to the right in the curves without resistance correction, caused by the aforementioned voltage drop, which is much more noticeable in Fig. 45c (with rate of 1.804 kHz/cm^2). A decrease of the maximum efficiency with the increase of rate is expected, because of the front-end electronics dead time, but we can see an increase in the raw efficiency, which indicates a high fake hit contamination.

To finalize the discussion, the plots of the efficiency curves with tracking and with tracking and resistance correction can be seen in Fig. 46. The effect of the voltage drop on the electrodes is very noticeable in Fig. 46a and it is also possible to see the expected decrease maximum efficiency, proving that the fake hit contamination was removed using the tracking. In Fig. 46b it is still possible to see a shift to the right in the curves, this is also expected, since the high rates induce an efficiency drop in the RPCs, because of the reduction of the gas amplification caused by the space charge effect (115).

The tracking system implementation at GIF++ was successful, and was able to remove the fake hit contribution. The KODEL-C is a prototype used to evaluate the performance of the 1.4 mm gaps, the same used in the iRPC design. It showed good results in the high rate environment, even at rates higher than 2 kHz/cm^2, with increase on the working point of $\approx$650 V with efficiency loss of $\approx$ 7.5%, using a custom front-end. The iRPC front-end design has lower threshold and dead time so it is expected to perform better (116).

Figure 45 - Comparison of the tracking algorithm using efficiency curves.

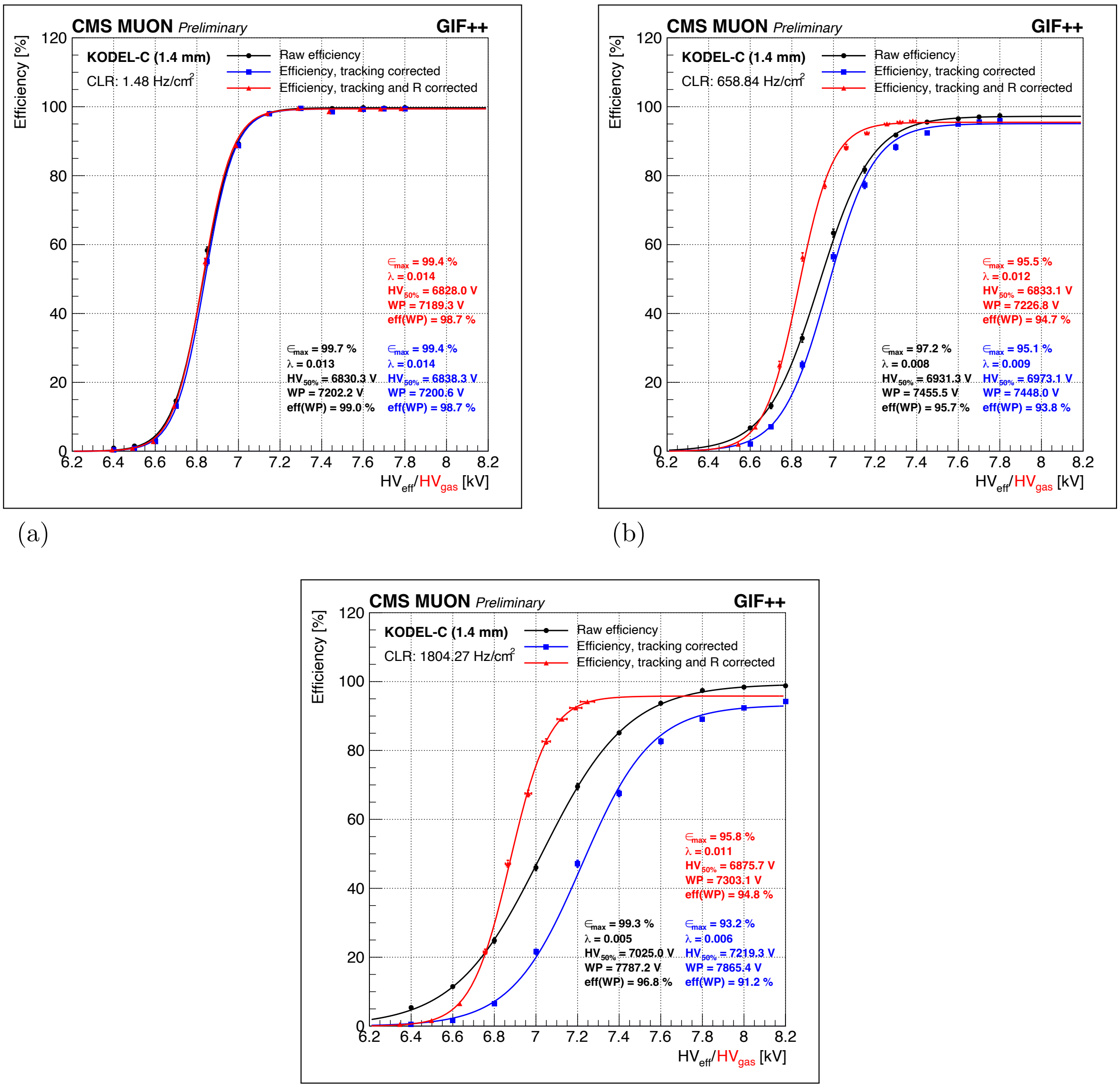

(a)

(b)

(c)

Legend: Efficiencies and their sigmoid fits measured at three photon fluxes with gamma cluster rates measured in the working point of 1.48 Hz/cm^2 (a), 0.645 kHz/cm^2 (b), and 1.804 kHz/cm^2 (c), respectively. The curve in black is the efficiency calculated with all hits inside the muon window, the blue one is with applied tracking correction and the one in red, with tracking and resistance correction.

Source: AMARILO, 2023, p. 3.

Figure 46 - Efficiency curves for various gamma background rates.

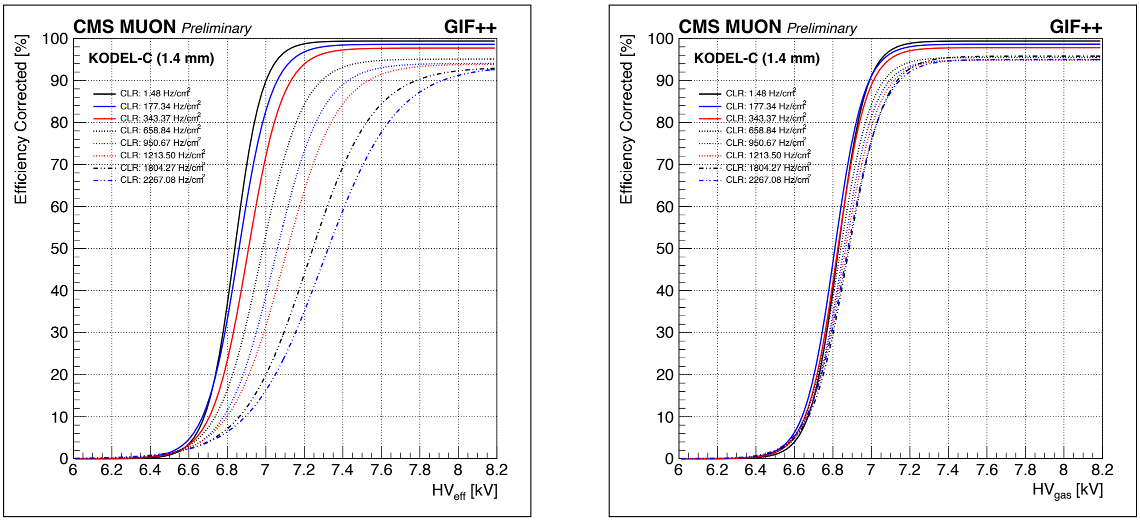

(a)

(b)

Legend: Efficiency curves for various gamma background rates. In (a) the HV applied is corrected only by pressure and temperature (HV$_{eff}$), while in (b) the HV is also corrected by the resistance of the gaps (HV$_{gas}$).

Source: AMARILO, 2023, p. 4.

4 PHYSICS ANALYSIS

This chapter will discuss about the cross section measurement of the associated production of Υ and $D^{*\pm}$ using the full CMS Run 2 data with 13 TeV center-of-mass energy. First, the data and simulation samples used will be presented. Then, the selection cuts will be discussed and the strategy to determine the signal yields and efficiency will be shown. Finally, the fiducial and effective cross sections will be evaluated and the results will be discussed.

4.1 Data sets and Simulation

4.1.1 Data Samples

The data samples were recorded by the CMS detector during the LHC Run 2 in 2016-2018 at a center-of-mass energy of 13 TeV and are composed only by events certified as good for physics analysis. The Table 3 displays all the data samples used. The total recorded luminosity of all data samples is 137.6 fb^{-1}.

From the analysis point of view, data samples are divided into four subsamples (2016APV, 2016, 2017 and 2018), to take into account the differences in the detector in the course of Run 2 (e.g. drop in the efficiency due to aging and better acceptance due to installation of new detectors).

4.1.2 Simulation Samples

The simulated samples are done via Monte Carlo (MC) simulation, where the MC method is used in programs to model the physics processes. The starting point of the simulation is the event generation, where the events following a set of physics processes of interest are created by the MC generator.

First, the parton level matrix element of the process is calculated perturbatively up to a fixed order. Next, the parton showering is done to account for the higher order effects, such as initial and final state radiation (ISR and FSR). This is followed by the hadronization, where the quarks and gluons form the hadrons and finally, the particles decay.

The interaction of the generated particles with the detector follows the event generation. In CMS, the detector response is simulated using GEANT4 (117). The result pass through the same processing chain as the real data forming the final simulated sample.

Table 3 - Data samples considered in this work

Data set
/MuOnia/Run2016B-21Feb2020_ver1_UL2016_HIPM-v1/AOD
/MuOnia/Run2016B-21Feb2020_ver2_UL2016_HIPM-v1/AOD
/MuOnia/Run2016C-21Feb2020_UL2016_HIPM-v1/AOD
/MuOnia/Run2016D-21Feb2020_UL2016_HIPM-v1/AOD
/MuOnia/Run2016E-21Feb2020_UL2016_HIPM-v1/AOD
/MuOnia/Run2016F-21Feb2020_UL2016_HIPM-v1/AOD
/MuOnia/Run2016F-21Feb2020_UL2016-v1/AOD
/MuOnia/Run2016G-21Feb2020_UL2016-v1/AOD
/MuOnia/Run2016H-21Feb2020_UL2016-v1/AOD
/MuOnia/Run2017B-09Aug2019_UL2017-v1/AOD
/MuOnia/Run2017C-09Aug2019_UL2017-v1/AOD
/MuOnia/Run2017D-09Aug2019_UL2017-v1/AOD
/MuOnia/Run2017E-09Aug2019_UL2017-v1/AOD
/MuOnia/Run2017F-09Aug2019_UL2017-v1/AOD
/MuOnia/Run2018A-12Nov2019_UL2018-v1/AOD
/MuOnia/Run2018B-12Nov2019_UL2018-v1/AOD
/MuOnia/Run2018C-12Nov2019_UL2018-v1/AOD
/MuOnia/Run2018D-12Nov2019_UL2018-v1/AOD

Legend: Data Samples used in the analysis corresponding to the full CMS Run 2 data taking.
Source: The author, 2023.

The MC samples were used in this analysis to simulate the two components of the signal, the SPS and DPS, and to extract the acceptance and efficiencies. No significant contribution from other physical processes to our experimental signature is expected, since the Υ mass is high and the selection applied to the decay length of D* is such that removes the ones that are result from B-hadrons decays. Therefore, only the combinatorial background in considered for this analysis and no MC sample is needed to model the background, which is estimated from the fits.

The DPS samples were produced using the PYTHIA8 (118) for event generation, parton showering and hadronization, which is configured using the CP5 tune (119) using the NNPDF3.1 parton distribution functions (54), the models used for $\Upsilon(nS)$ production were the color–singlet and color–octet models, which parameters were configured to match the ones of Ref. (120). To decay the heavy flavour hadrons, EVTGEN (121) was used. The SPS sample is similar to the DPS, with the addition of the HELAC-ONIA (122,123), which replaced PYTHIA8 in the event generation.

In the same way as the data, the MC samples are divided into subsamples to account for the detector differences throughout Run 2. The detector simulation is tunned to better represent the detector conditions in each subsample. Furthermore, to be able to reach a higher p_T region, the MC was divided into four dimuon p_T regions - [9, 30], [30, 60], [60, 120] and [120, inf) GeV.

Finally, some procedures were done to correct the MC to better represent the data:

- Pileup reweighting: The pileup distribution of the simulated samples is different from that of the data. A rescaling factor is applied to each event, defined as the ratio between the normalized pileup distribution for data and MC.
- Muon efficiency correction: The muon efficiency differs in data and MC. The muon efficiency is calculated to both data and MC and a scale factor defined by the ratio between data and monte carlo.

In this work, the simulated sample was used with limited statistics, specially in the lowest p_T range. A larger statistics one is being produced, but could not be finished in time to be used for the thesis conclusion.

4.2 Υ + D$^{*\pm}$ Reconstruction

The Υ + D* reconstruction is done from the reconstructed tracks in an event. As shown in Fig. 47, there are five different tracks in the final state which stem from the pair of heavy mesons - three coming from the D* and two from the Υ. The D* has a low combinatorial background when compared with other open charm mesons because of characteristic signature of a very small difference of mass between D* and D^0, restricting the phase space of the slow pion. Also, the kaon and the pion can be identified even without a particle identification detector, since the kaon should have a opposite charge to the slow pion, removing the ambiguity in the D^0 reconstruction.

Figure 47 - Drawing of an event of associated production of Υ and D^{*+}

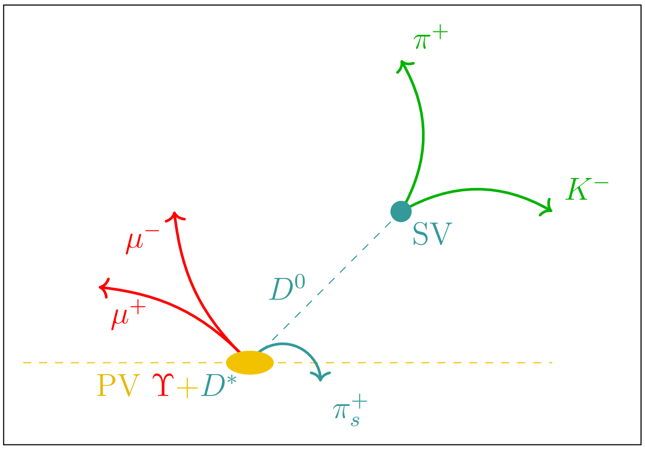

Legend: Drawing of an event of associated production of Υ and D^*. Υ decays into two opposite charge muons, while D^{*+} decays into a pion and a D^0, which later decays into a kaon and a pion.

Source: The author, 2023.

The D^* reconstruction starts by finding a suitable D^0 candidate. For this, two tracks of opposite charge are paired to check whether they form a common vertex using the Kalman Filter method (124, 125). If the fit is valid and its p-value is greater than 1%, and the invariant mass is in the range between 1.5 and 2.3 GeV, the D^0 candidate is selected. The vertex determination also allows for a better calculation of the kinematic variables of the tracks and it is called secondary vertex (SV).

A primary vertex (PV) is assigned to the D^0 candidate as the one closest in the z coordinate to the SV in order to determine the decay length, defined as

$$dl = \frac{|\vec{p}_{D^0} \cdot \Delta\vec{l}|}{|\vec{p}_{D^0}|}, \tag{22}$$

where $\vec{p}_{D^0}$ is the D^0 tri-momentum and $\Delta\vec{l}$ is the distance between the PV and SV. The decay length significance is very important because it can be used to filter a lot of background and is defined as

$$dl_{sig} = \frac{dl}{dl_{err}}, \tag{23}$$

where dl_{err} is the uncertainty of dl. Finally, another important variable is the cosine of the angle between the D^0 momentum vector and the PV-SV displacement vector (pointing angle)

$$\cos\alpha = \frac{dl}{|\Delta\vec{l}|} \ , \tag{24}$$

which express the degree of alignment between these two vectors, expected to be high for true D^0s.

After the D^0 candidate is reconstructed, a new track coming from the same PV is added to form the D^* candidate. The track momentum resolution is improved by adding the PV position to the track fit and reevaluating its four-momentum.

The $\Upsilon(nS)$ reconstruction is performed in a similar way to the D^0. Two muons with opposite charge are selected and its vertex is determined from the fit. If the vertex is valid and has a p-value greater than 1% we have a dimuon candidate. The invariant mass of the dimuon should be in the range of $8.5 < m_{\mu\mu} < 11.5$ GeV in order to be accepted as an $\Upsilon(nS)$ candidate.

Finally, in order to pair the $\Upsilon(nS)$ and the D^*, a vertex fit of the two muons and the slow pion is performed. The slow pion is used in this fit because it comes directly from the D^* decay, the other tracks are displaced because the D^0 has a considerable lifetime. If valid, the vertex p-value is determined.

In this stage of the reconstruction, very loose cuts are applied to the candidates, those are specified in the Sec. 4.3.1.

4.3 **Event Selection**

4.3.1 Preselection Cuts

Preselection cuts are applied in the reconstruction step to mitigate some of the combinatorial background and save disk space when recording the data. They are very loose and are further improved when the analysis final cuts are applied (Sec. 4.3.3). The preselection cuts both for the Υ and the D^* candidates are summarized in the Tab. 4.

Figure 48 shows the dimuon invariant mass and the Δm of the D^* after the preselection cuts. Especially for D^*, the background is still huge, so the selection cuts are very important to clean the data by improving the signal-to-background ratio.

4.3.2 Trigger

The chosen trigger strategy was to use the HLT Paths that filter dimuons. It was required that the trigger had the maximum possible rapidity coverage for discrimination

Table 4 - Preselection cuts.

Variable	Cut
D^* candidate	
Transverse momentum of K and π ($p_T^{K,\pi}$)	> 0.3 GeV
Transverse and longitudinal impact parameter of K and π track (d_{xy} and d_z)	< 0.5 cm
Transverse and longitudinal impact parameter of π_s track (d_{xy} and d_z)	< 2 cm
Longitudinal distance between D^0 vertex and PV	< 2 cm
Transverse momentum of D^0 ($p_T^{D^0}$)	> 0.9 GeV
D^0 mass cut (m_{D^0})	$1.5 < m_{D^0} < 2.3$ GeV
Mass difference between $D^{*\pm}$ and D^0 (Δm)	< 0.17 GeV
D^0 candidate vertex probability	> 0.01
Υ candidate	
Pseudorapidity separation between the two μ ($\Delta\eta_{\mu^+\mu^-}$)	< 3.0
Transverse and longitudinal impact parameter of the two μ tracks	< 0.5 cm
Longitudinal distance between the dimuon candidate vertex and the PV	< 0.5 cm
Dimuon candidate vertex probability	> 0.01
Dimuon mass range	$8.5 < m_{\mu\mu} < 11.5$ GeV

Legend: Preselection cuts used to save resources when saving the NTuples.

Source: The author, 2023.

Figure 48 - Dimuon invariant mass and Δm of D* distribution after the preselection cuts

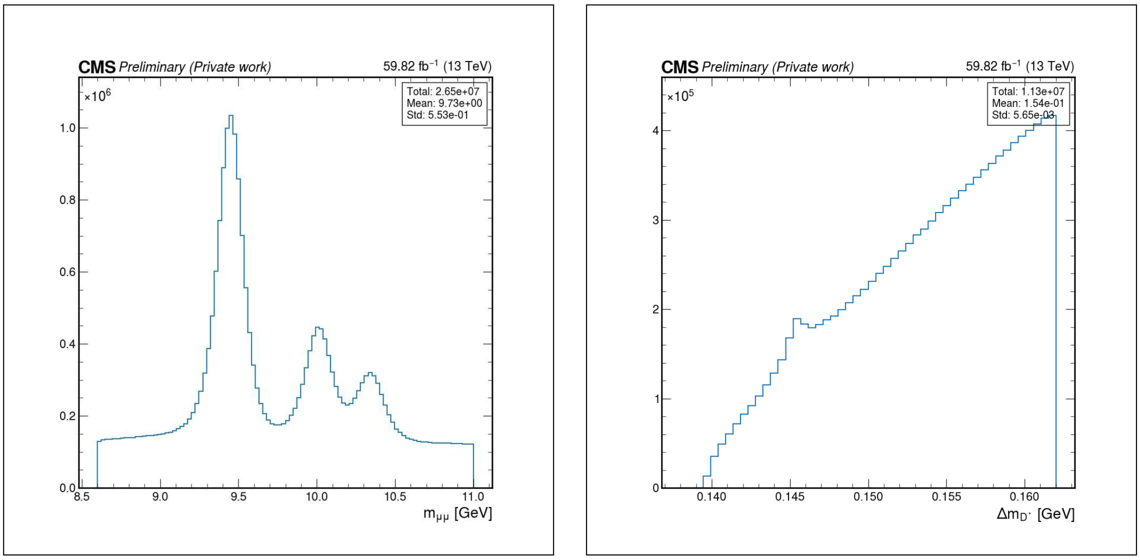

(a) (b)

Legend: Dimuon invariant mass (a) and D* Δm (b) after the preselection cuts in 2018 data. There is still a lot of background in (b), this is improved with the selection cuts.

Source: The author, 2023.

between DPS and SPS, and minimum p_T threshold. The used trigger paths are specified in Tab. 5, all of them require two muons with opposite charge, invariant mass between 8.5 and 11.5 GeV, absolute value of the reconstructed pseudorapidity < 2.5 and are unprescaled. In addition to those, there is a cut in transverse momentum, which differs for each trigger path.

In 2017, the chosen trigger was not available during the whole data-taking period, resulting in a lower recorded luminosity (27.12 out of 41.48 fb^{-1} in full 2017 data). This should not pose a problem, since the statistics is high (123.1 fb^{-1} for the three years) and the other dimuon triggers available only cover the central area of the detector, which can turn the discrimination between SPS and DPS more complicated.

4.3.3 Selection Cuts

The analysis cuts are tighter cuts applied to the data in order to define the fiducial region to be explored in the analysis and to improve the signal–to–background ratio. A summary of them is displayed in the Tabs. 6 and 7.

The cuts on Tab. 6 were based on studies using MC simulations on the expected detector acceptance to each one of the objects. The cuts on the tracks transverse momen-

Table 5 - Triggers used in this study in each year of data taking

Year	Trigger Path	p_T Cut (GeV)	Recorded L (fb^{-1})	L Uncertainty
2016APV	HLT_Dimuon13 _Upsilon	> 12.9	19.4	1.2 %
2016	HLT_Dimuon13 _Upsilon	> 12.9	16.8	1.2 %
2017	HLT_Dimuon24 _Upsilon_noCorrL1	> 13.9	27.1	2.3 %
2018	HLT_Dimuon24 _Upsilon_noCorrL1	> 13.9	59.8	2.5 %

Legend: Triggers used in this study in each year of data taking. The luminosity uncertainty for each year was taken from Refs. (126–128)

Source: The author, 2023.

Table 6 - Kinematic cuts that define the fiducial region.

Variable	Cut
μ transverse momentum (p_T^{μ})	> 3 GeV
μ pseudorapidity (η_μ)	$\lvert\eta_\mu\rvert < 2.4$
Υ transverse momentum (p_T^{Υ})	$15 < p_T^{\Upsilon} < 150$ GeV
Υ rapidity (y_Υ)	$\lvert y_\Upsilon\rvert < 2.5$
Transverse momentum of K and π ($p_T^{K,\pi}$)	> 1 GeV
Transverse momentum of π_s ($p_T^{\pi_s}$)	> 0.3 GeV
Transverse momentum of D^0 ($p_T^{D^0}$)	> 3 GeV
D* transverse momentum ($p_T^{D^*}$)	$4 < p_T^{D^*} < 80$ GeV
D* rapidity (y_{D^*})	$\lvert y_{D^*}\rvert < 2.5$

Legend: Cuts on the kinematic variables of the system that define the fiducial region of the analysis.

Source: The author, 2023.

Table 7 - Selection cuts.

Variable	Cut
D* candidate	
Track χ^2 of K and π	< 2.5
Number of valid tracker detector hits for K and π	> 4
Number of valid pixel detector hits for K and π	> 1
transverse impact parameter of K and π from PV	0.5 cm
longitudinal impact parameter of K and π from PV	$0.5/\sin\theta$ cm
Track χ^2 of π_s	< 3
Number of valid tracker detector hits for π_s	> 2
D^0 mass (m_{D^0})	$\lvert m_{D^0} - 1.864\rvert < 0.028$ GeV
D^0 cosine of the pointing angle ($\cos\alpha_{D^0}$)	> 0.99
D^0 decay length significance (dl_{sig})	> 2.7
Υ candidate	
μ soft id flag	soft id = True
Υ + D* candidate	
$\mu\mu\pi_s$ vertex probability	> 0.01
Υ + D* candidate invariant mass	> 18 GeV

Legend: Selection cuts used to improve the signal–to–background ratio.

Source: The author, 2023.

tum are very low, in special for the slow pion which is very important, as it is directly correlated to the lower limit of the D* transverse momentum, since the slow pion phase space is restricted by the low mass difference between D^0 and D^*. In CMS, the tracker detector is very important to the reconstruction at low momentum, since the tracks with low energy have a curled up trajectory all inside the tracker detector. Furthermore, the distinctive D* signature discussed in Sec. 4.2 helps in the distinction of signal and background events.

Also, the cuts on the D^0 observables listed in Tab. 7 are very important to improve the D* signal–to–background ratio so they were well tuned for this work. The cuts on the tracks are common quality cuts recommended by the CMS Tracking group.

On Tab. 7 the soft id flag refers a collection of selections on the muons well tuned my the CMS B-Physics group. They are the following :

- Muon track in tracker detector matched with at least one segment in the muon detector (in any station) in both X and Y coordinates ($< 3\sigma$).
- Number of tracker layers with hits > 5, to guarantee good p_T measurement.
- Number of pixel layers with hits > 0.
- Muon track should have high-purity flag, rejecting bad quality tracks
- Transverse and longitudinal impact parameter cuts, $d_{xy} < 0.3$ cm and $d_z < 20$ cm with respect to the primary vertex.

Figure 49 shows the dimuon invariant mass and the D* Δm after the selection cuts for the 2018 data set. As opposed to Fig. 48, the D* signal is very clean.

4.3.4 Data and MC distributions

The plots shown in this section compare shapes of the distributions in the data and the MC signal using both the SPS and DPS simulations. Figure 50 presents the p_T, y, ϕ and invariant mass distributions of the dimuon candidate. In this figure and following ones, the black dots represent the data collected by CMS, the blue histogram the DPS MC signal and the orange histogram the SPS MC signal. Also, distributions were normalized in order to compare their shapes. Figure 51 presents the p_T, y, ϕ and Δm distributions of the D* candidate. The p_T, y, ϕ, invariant mass, $\cos\alpha$ and dl_{sig} distributions of D^0 are presented in Fig. 52. Finally, Fig. 53 shows the p_T, y, ϕ and invariant mass of the associated Υ and D* system and Fig. 54 shows the difference of the p_T, y and ϕ of the associated Υ and D*.

Figure 49 - Dimuon Invariant mass and Δm of the D* distribution after the selection cuts

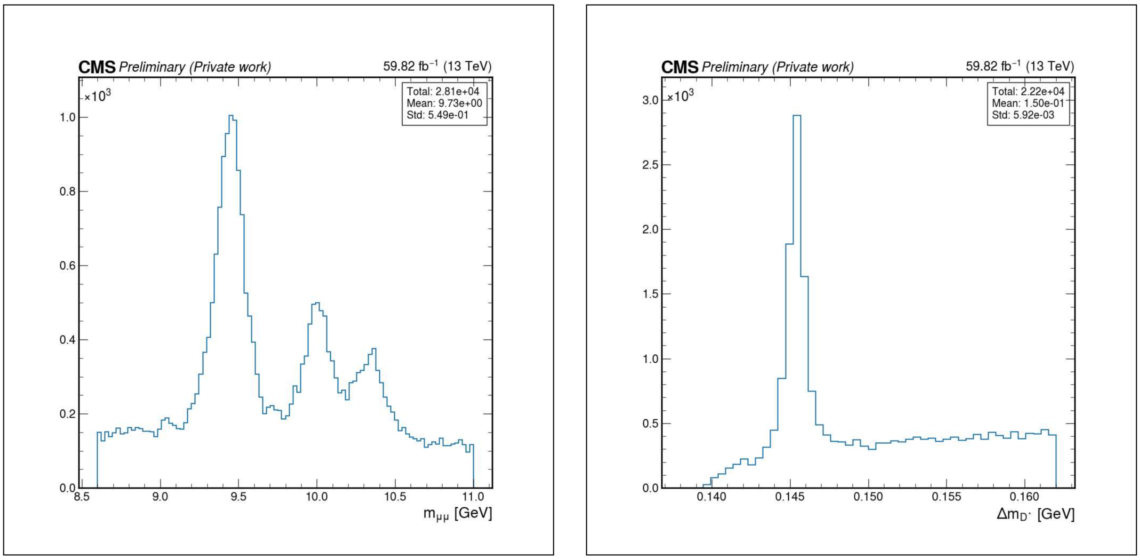

(a) (b)

Legend: Dimuon Invariant mass (a) D* Δm (b) after the selection cuts in 2018 data. Both signals from Υ and D* are well defined.

Source: The author, 2023.

The Δy has a broader distribution in the DPS than in the SPS simulation. This occurs because, in SPS, a high separation in the rapidity implies high momentum transfer and is strongly suppressed. In DPS the only suppression is due the yields in the high y region, since the two particles are uncorrelated (62). Because of this difference in the distributions, the rapidity separation was proposed to help in the determination of the DPS fraction in Ref. (129). In Fig. 54b, the data show a broader distribution, which indicates high DPS contribution in the production of associated Υ+ D*.

In Fig. 50d, one peak (corresponding to the $\Upsilon(1S)$ state) in the dimuon invariant mass distribution for the SPS MC sample, as it was difficult to put the other states in the same simulation. Also, in the Figs. 51b and 52b, which show the rapidity distribution of D* and D^0, there is a substantial difference in the frontal region. We attribute this excess to the combinatorial background in the data sample. When a more restrictive and signal enriched region is considered ($9.0 < m_{\mu\mu} < 10.6$ GeV and $0.142 < \Delta m < 0.0148$ GeV), these differences are reduced, as it is possible to see in Fig. 55.

In this section, plots using 2017 sample were used to illustrate the comparison, as the DPS MC has much more statistics than the other samples. Still, the comparison needs to be done with care, as the data has contribution from the combinatorial background and only the MC signal is available. A more careful comparison will be done in the future by using a MC to model the combinatorial (e.g. Minimum Bias, inclusive Υ and/or inclusive

D*), or by using statistical techniques to extract the signal distributions (e.g. sPlot (130)). Figures with the distributions for all the samples can be found in Appendix B.

4.4 **Signal Extraction**

The signal extraction is performed by doing a 2D fit of the dimuon invariant mass ($m_{\mu\mu}$) and D* Δm distributions shown in Fig. 56, where it is possible to infer the signal (yellow regions where the peaks are convoluted) and the background regions. To fulfill this description of the signal and background for each distribution is created and a product of both is taken as the 2D model. Each of the distribution models contains components for signal and background and a non-extended composite PDF is constructed. The fit is performed using the RooFit package.

4.4.1 Υ Model

The fit model has three signal components, one for each of the observed $\Upsilon(nS)$ states. All of them are modeled using the Crystal Ball distribution, defined as

$$CB(x;\alpha,n,\bar{x},\sigma) = N\cdot\begin{cases}\exp(-\frac{(x-\bar{x})^2}{2\sigma^2}), & \text{for } \frac{x-\bar{x}}{\sigma} > -\alpha\\ A\cdot(B-\frac{x-\bar{x}}{\sigma})^{-n}, & \text{for } \frac{x-\bar{x}}{\sigma} \leqslant -\alpha\end{cases} \tag{25}$$

where

$$\begin{aligned}A =& \left(\frac{n}{|\alpha|}\right)^n\cdot\exp\left(-\frac{|\alpha|^2}{2}\right),\\ B =& \frac{n}{|\alpha|}-|\alpha|,\\ N =& \frac{1}{\sigma(C+D)},\\ C =& \frac{n}{|\alpha|}\cdot\frac{1}{n-1}\cdot\exp\left(-\frac{|\alpha|^2}{2}\right),\\ D =& \sqrt{\frac{\pi}{2}}\left(1+\text{erf}\left(\frac{|\alpha|}{\sqrt{2}}\right)\right).\end{aligned} \tag{26}$$

N is the normalization factor and α, n, $\bar{x}$ and σ are the fit parameters and erf is the error function. The CB distribution behaves like a Gaussian for $(x-\bar{x})/\sigma$ greater than $-\alpha$ and presents a tail for values less than or equals to $-\alpha$, being able to model the effects of FSR to the dimuon invariant mass distribution.

In order to reduce the amount of free parameters of the fit, the following constraints

Figure 50 - Dimuon distributions for 2017 sample

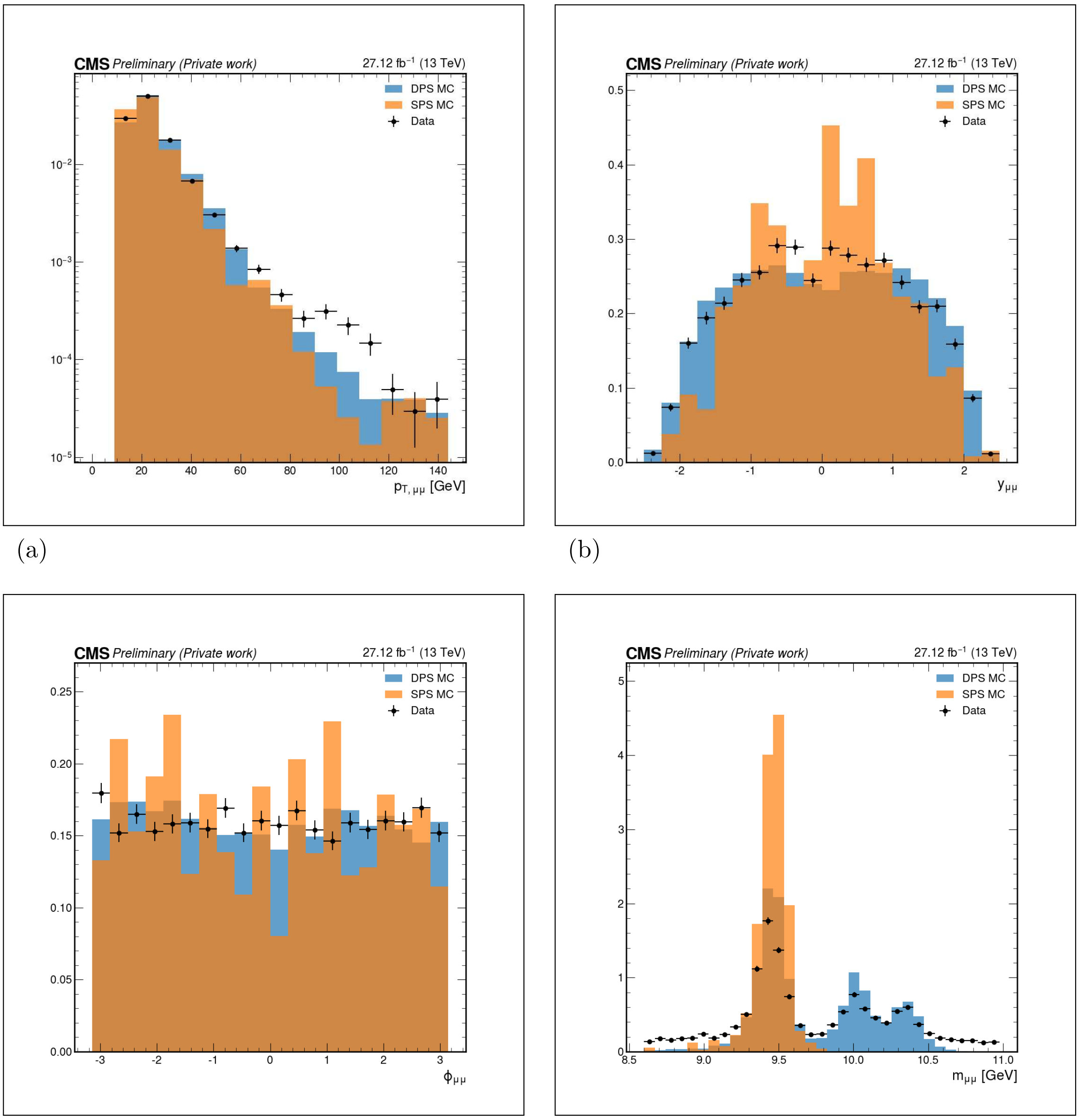

(a) (b)

(c) (d)

Legend: p_T (a), y (b) ϕ (c) and invariant mass (d) distributions for the Υ candidate using the 2017 data sample. The black dots represent the CMS Run 2 data, while the blue distribution represent the signal DPS MC simulation and the orange one the signal SPS MC simulation.

Source: The author, 2023.

Figure 51 - D* distributions for 2017 sample

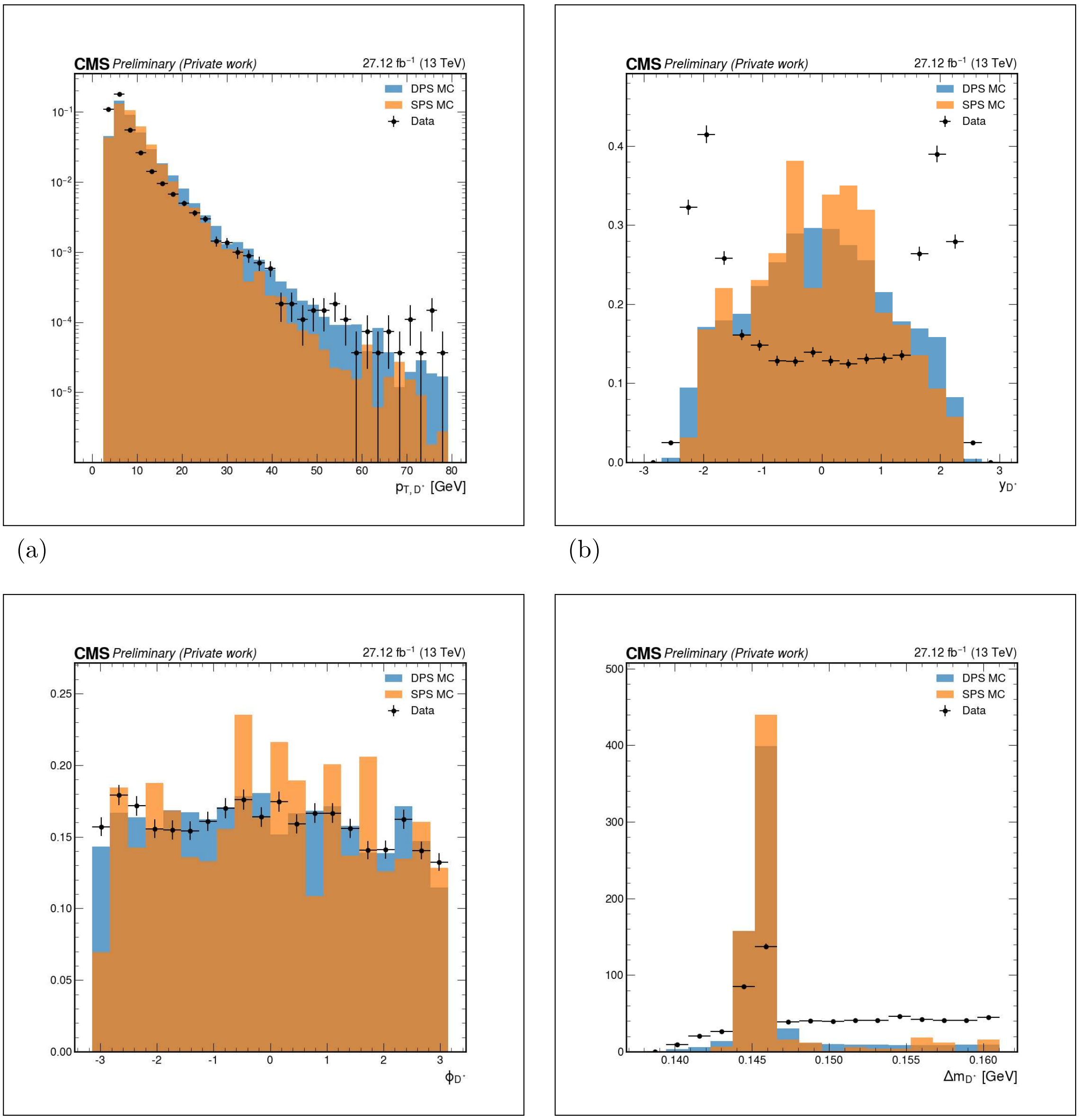

(a) (b)

(c) (d)

Legend: p_T (a), y (b), ϕ (c) and Δm (d) distributions for the D* candidate using the 2017 data sample. The black dots represent the CMS Run 2 data, while the blue distribution represents the signal DPS MC simulation and the orange one the signal SPS MC simulation.

Source: The author, 2023.

Figure 52 - D^0 distributions for 2017 sample

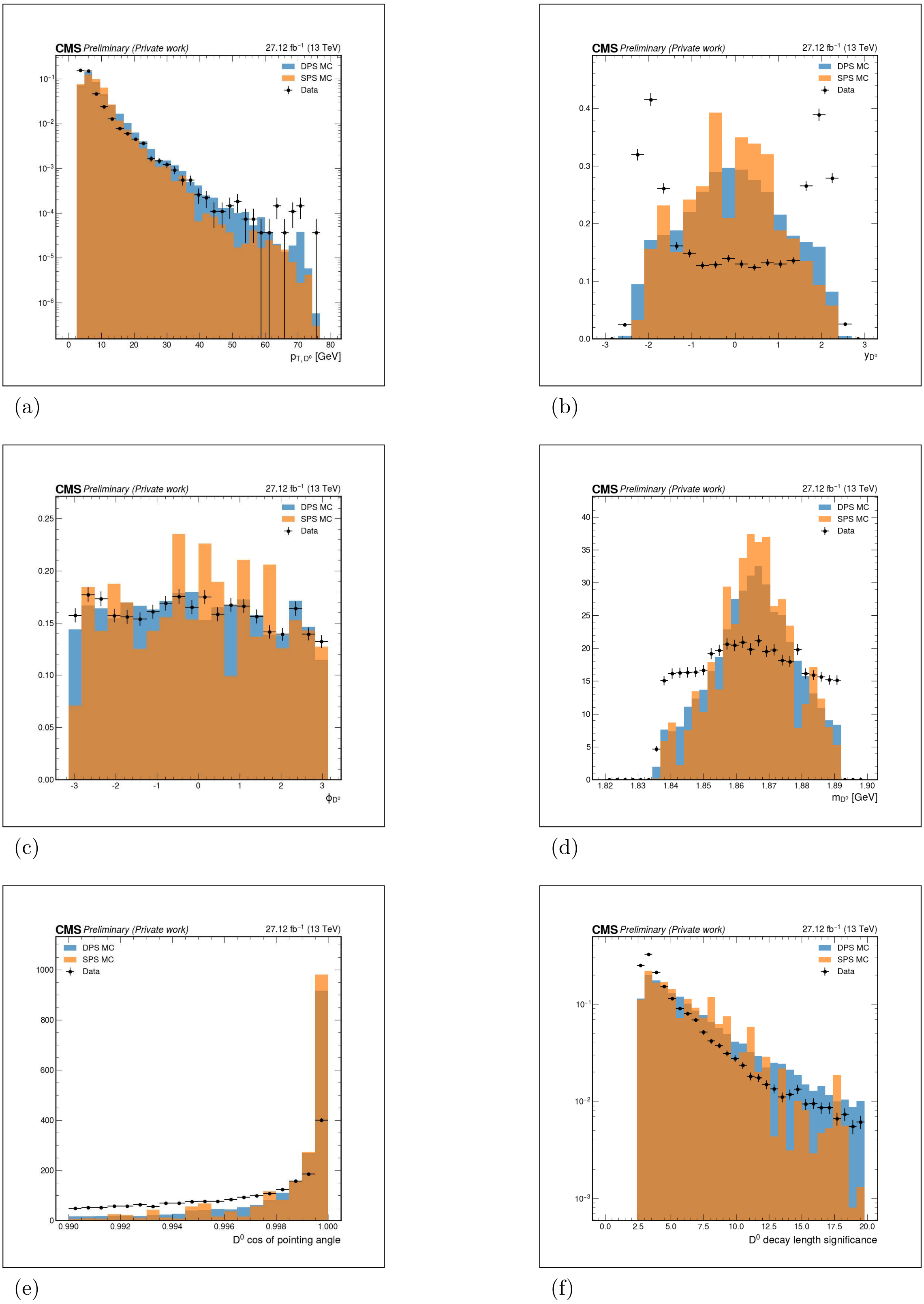

(a) (b) (c) (d) (e) (f)

Legend: p_T (a), η (b), ϕ (c), invariant mass (d), $\cos\alpha$ (e) and dl_{sig} (f) distributions for the D^0 using the 2017 data sample. The black dots represent the CMS Run 2 data, while the blue distribution represents the signal DPS MC simulation and the orange one the signal SPS MC simulation.

Source: The author, 2023.

Figure 53 - Associated Υ and D* distributions for 2017 sample

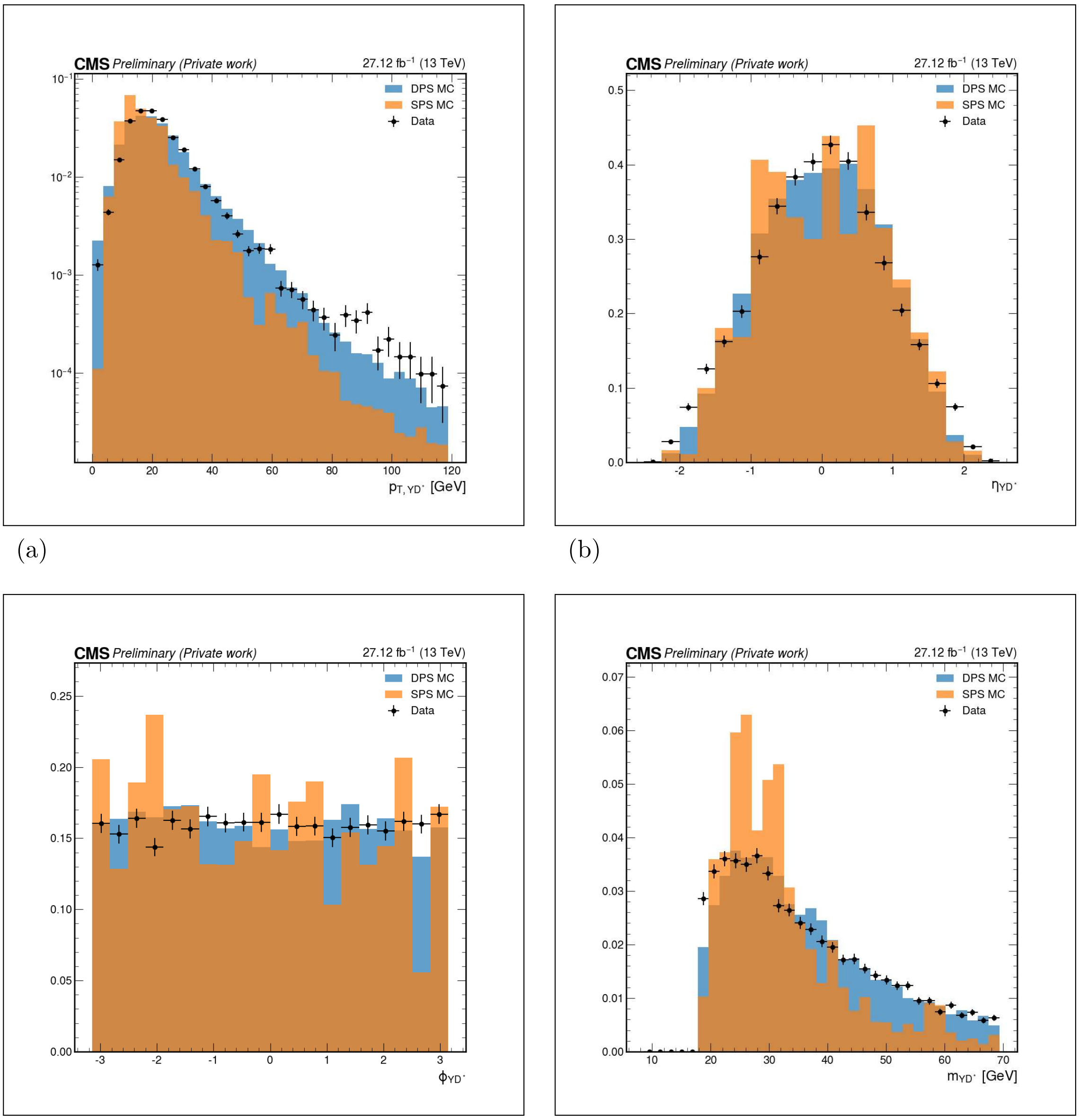

(a) (b)

(c) (d)

Legend: p$_T$ (a), y (b), ϕ (c) and invariant mass (d) distributions for the associated Υ and D* candidate using the 2017 data sample. The black dots represent the CMS Run 2 data, while the blue distribution represents the signal DPS MC simulation and the orange one the signal SPS MC simulation.

Source: The author, 2023.

Figure 54 - Associated Υ and D* Δp_T, Δy and $\Delta\phi$ distributions for 2017 sample

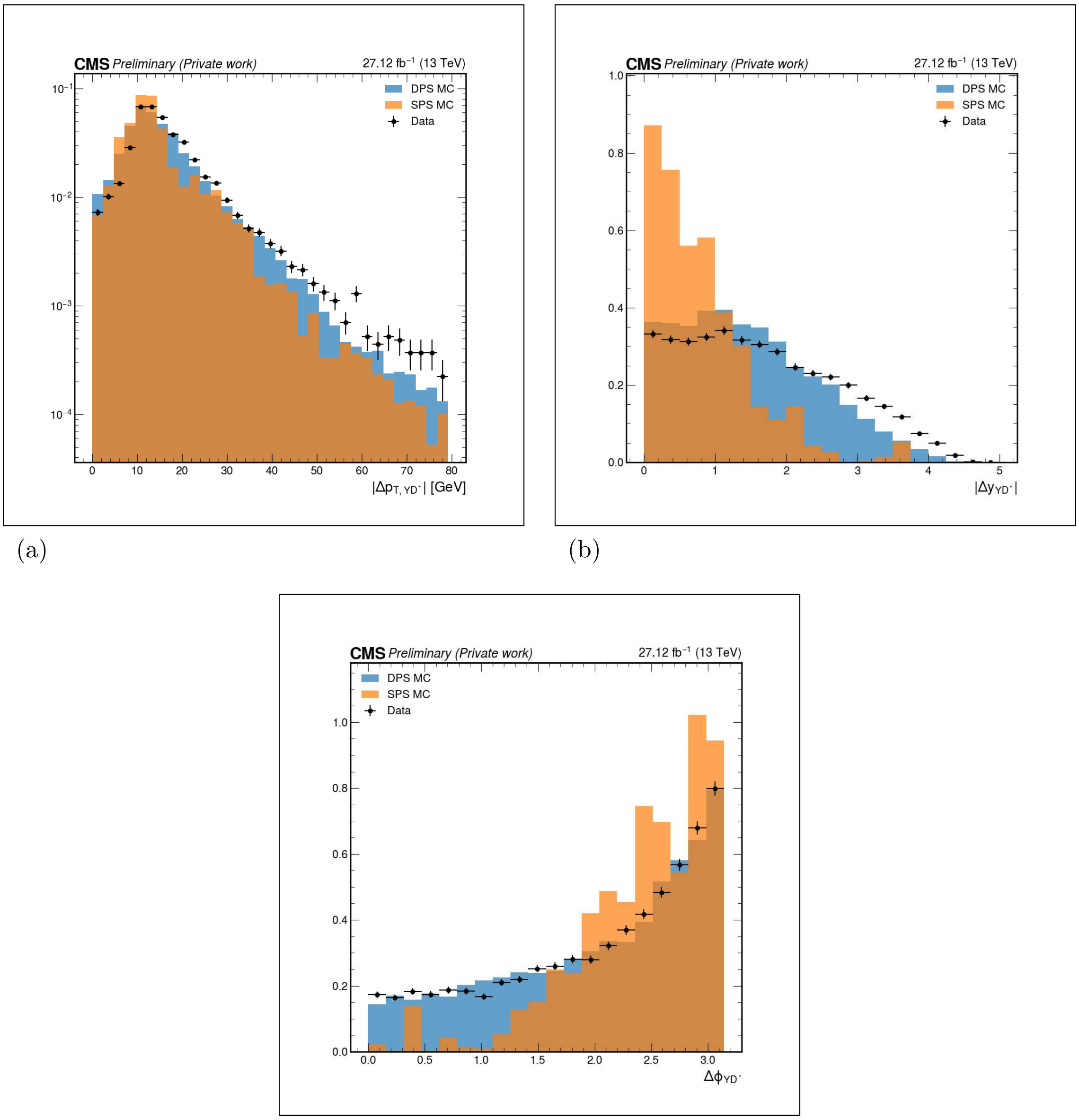

(a)

(b)

(c)

Legend: Δp_T (a), Δy (b) and $\Delta\phi$ (c) distributions for the associated Υ and D* candidate using the 2017 data sample. The black dots represent the CMS Run 2 data, while the blue distribution represents the signal DPS MC simulation and the orange one the signal SPS MC simulation.

Source: The author, 2023.

Figure 55 - D* and D^0 rapidity distributions from the 2017 samples, after restricting the data to the signal region.

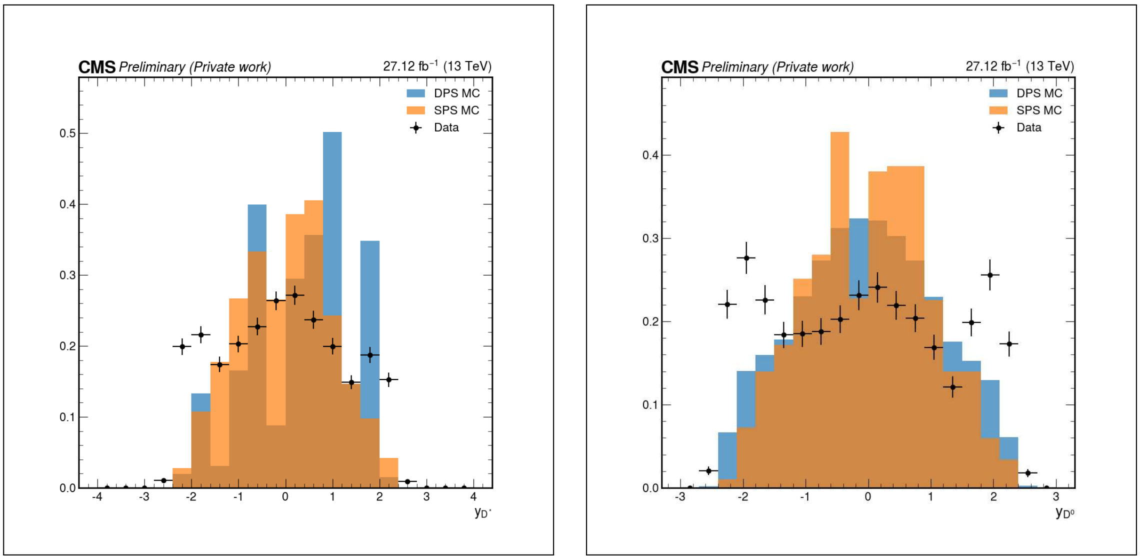

(a)

(b)

Legend: Rapidity distribution of D* (a) and of D^0 (b) using the 2017 data sample, after restricting the data to the signal region. The black dots represent the CMS Run 2 data, while the blue distribution represents the signal DPS MC simulation and the orange one the signal SPS MC simulation.

Source: The author, 2023.

Figure 56 - 2D histogram of the data after all the selection criteria and 1D projections

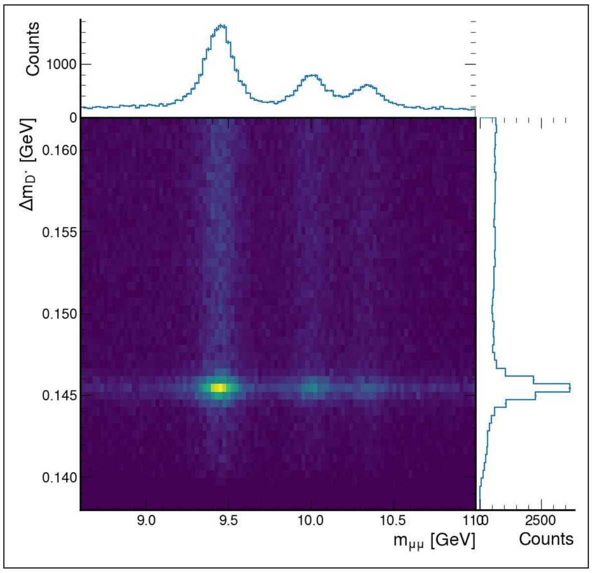

Legend: Two–dimensional histogram of the data after all the selection criteria. In the top and left is displayed the one–dimentional projection in the dimuon invariant mass and the Δm of D*.

Source: The author, 2023.

are imposed to the CB parameters:

- The mean of all the CBs are fixed to the PDG mass value of its Υ state times a mass scale (to take into account the uncertainties on muon momentum scale calibration). $\bar{x}_{\Upsilon(nS)} = m_{scale} \cdot m_{\Upsilon(nS)}$;
- The sigma of the CBs used to model 2S and 3S states are set to be proportional to their mass ratio with respect to the 1S state. Therefore, only one sigma is taken as free parameter. $\sigma_{\Upsilon(2S)} = \sigma_{1S} \times m_{\Upsilon(2S)}/m_{\Upsilon(1S)}$ and $\sigma_{\Upsilon(3S)} = \sigma_{1S} \times m_{\Upsilon(3S)}/m_{\Upsilon(1S)}$;
- The tail parameters (α and n) are set as the same for the three CBs;

Finally, the fit model for $\Upsilon(nS)$ signal is

$$S_{\Upsilon}(m_{\mu\mu}) = f_{\Upsilon(1S)} \cdot CB_{\Upsilon(1S)}(m_{\mu\mu}) + f_{\Upsilon(2S)} \cdot CB_{\Upsilon(2S)}(m_{\mu\mu}) + (1 - f_{\Upsilon(1S)} - f_{\Upsilon(2S)}) \cdot CB_{\Upsilon(3S)}(m_{\mu\mu}) \tag{27}$$

For the background, Chebychev polynomials of the first kind are used up to second order. They are defined as:

$$\begin{aligned} T_0(x) =& 1 \\ T_1(x) =& x \\ T_{n+1}(x) =& 2xT_n(x) - T_{n-1}(x). \end{aligned} \tag{28}$$

The background component is written as

$$B_\Upsilon(m_{\mu\mu}) = N[1 + b_1 T_1(m_{\mu\mu}) + b_2 T_2(m_{\mu\mu})], \tag{29}$$

where N is the normalization constant and b_1 and b_2 are free parameters of the fit.

The 1D fit of all the Run 2 data is given in Fig. 57.

Figure 57 - One dimensional fit of selected Υ data

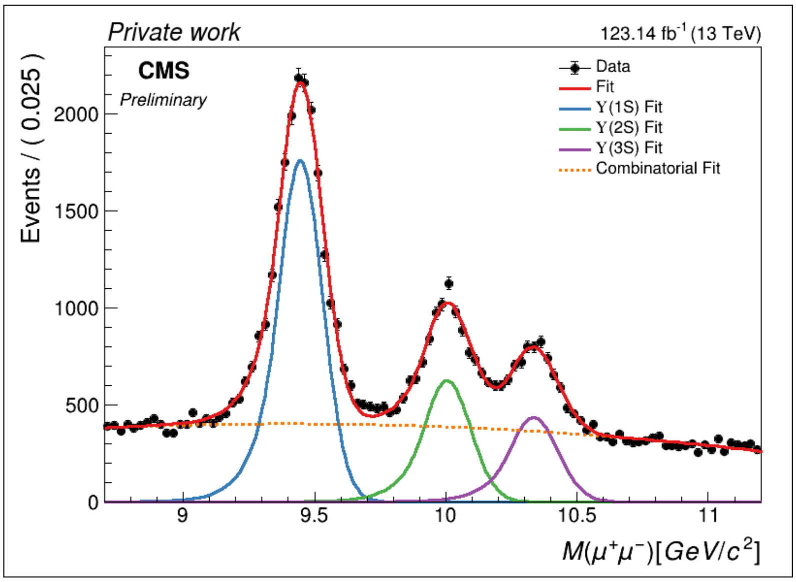

Legend: One dimensional fit of selected Υ. The fit is done to separate signal from the background for the three Υ states. The curves represent the fit of the full model (red) and each of the components (blue, green and purple for the $\Upsilon(1S)$, $\Upsilon(2S)$ and $\Upsilon(3S)$ signal and dashed orange for the combinatorial background).

Source: The author, 2023.

4.4.2 D* Model

For D* signal component, it is used a Johnson's distribution

$$S_{D^*}(\Delta m) = \frac{\delta}{\lambda\sqrt{2\pi}} \frac{1}{\sqrt{1 + \left(\frac{\Delta m - \mu}{\lambda}\right)^2}} \exp\left[-\frac{1}{2}\left(\gamma + \delta \sinh^{-1}\left(\frac{\Delta m - \mu}{\lambda}\right)\right)^2\right], \tag{30}$$

where δ, λ, γ and μ are the free parameters. This function is often used to describe the mass difference distribution in charmed meson decays where one of the decayed particles have the mass close to its mother, as it is the case of the considered D* decay.

For the D* background, a threshold function (131) given by:

$$B_{D^*}(\Delta m) = A \cdot (\Delta m - m_\pi)^B \cdot \exp[C \cdot (\Delta m - m_\pi)] \tag{31}$$

is used, where m_π is the pion mass and A, B and C are free parameters.

The 1D fit all the Run 2 data is given in Fig. 58.

Figure 58 - One dimensional fit to the selected $D^{*\pm}$ data

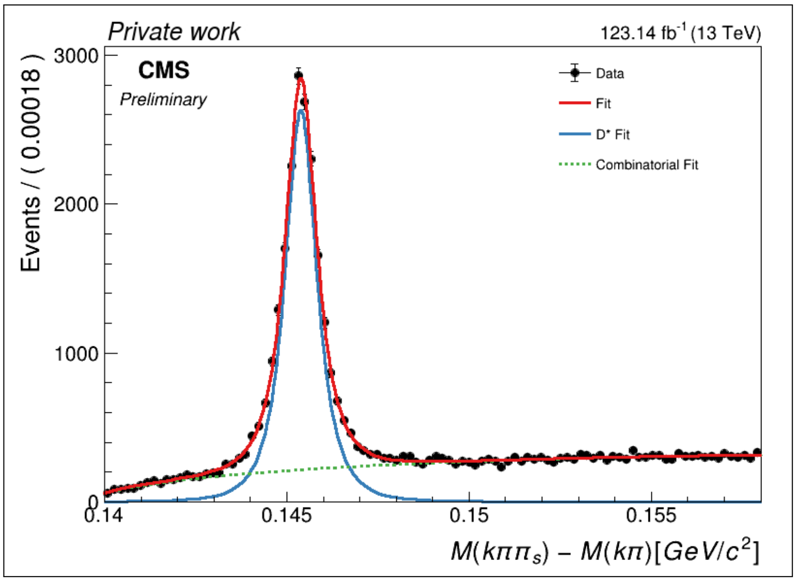

Legend: One dimensional fit to the selected $D^{*\pm}$. The curves represent the fit for the full model (red) and each of the components (blue for signal and dashed green for the combinatorial background).

Source: The author, 2023.

4.4.3 Υ + D* 2D Model

Finally, the construction of the 2D model takes into account the 4 distributions from Eqs. 27, 29, 30 and 31, creating the final four component distribution:

$$\begin{aligned} M_{\Upsilon D^*}(m_{\mu\mu}, \Delta m) = {} & f_s \cdot S_\Upsilon(m_{\mu\mu}) \cdot S_{D^*}(\Delta m) \\ & + f_{b1} \cdot S_\Upsilon(m_{\mu\mu}) \cdot B_{D^*}(\Delta m) \\ & + f_{b2} \cdot B_\Upsilon(m_{\mu\mu}) \cdot S_{D^*}(\Delta m) \\ & + (1 - f_{b1} - f_{b2}) \cdot B_\Upsilon(m_{\mu\mu}) \cdot B_{D^*}(\Delta m) \end{aligned} \tag{32}$$

The first component, composed by both signal models, is used to estimate the associated Υ and D* yield.

The projections to the dimuon invariant mass and D* Δm, extracted from the fit for all data samples, are given in Fig. 59 and the summary of the values obtained from the fit for the most relevant parameters or quantities for each of the samples is found in Tab. 8. In this table, the associated $\Upsilon(nS)$ and D* yield is represented by $N_{sig}\Upsilon(nS)$

Table 8 - Summary of fit parameters

Parameter	2016APV	2016	2017	2018
N$_{evt}$	3860	3668	6088	11775
N$_{sig}\Upsilon(1S)$	417 ± 44	457 ± 141	542 ± 60	1022 ± 64
N$_{sig}\Upsilon(2S)$	149 ± 19	207 ± 67	209 ± 26	404 ± 28
N$_{sig}\Upsilon(3S)$	116 ± 15	163 ± 53	169 ± 21	261 ± 20
m$_{scale}$	0.9983 ± 0.0003	0.9977 ± 0.0005	0.9983 ± 0.0003	0.9988 ± 0.0002
Δm (MeV)	145.37 ± 0.05	145.50 ± 0.04	145.42 ± 0.07	145.36 ± 0.03
χ^2/ndof of the Υ proj.	1.55	1.37	1.11	1.67
χ^2/ndof of the D* proj.	1.64	1.81	1.19	1.21

Legend: A summary with the most important fit parameters for each sample.

Source: The author, 2023.

Figure 59 - Projections of the two dimensional fit to the selected associated Υ+ $D^{*\pm}$ for all data samples.

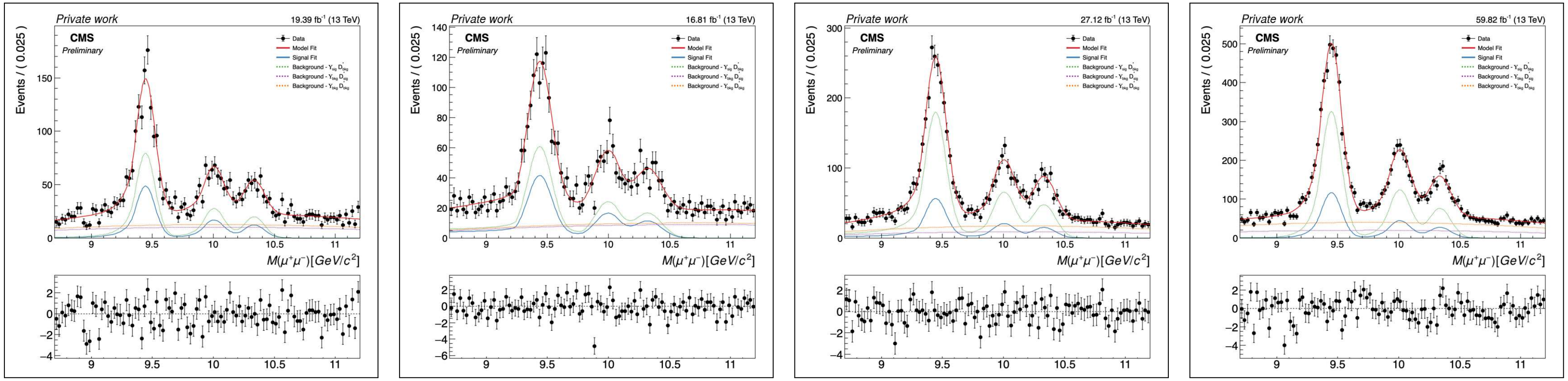

(a) 2016APV Υ projection.

(b) 2016 Υ projection.

(c) 2017 Υ projection.

(d) 2018 Υ projection.

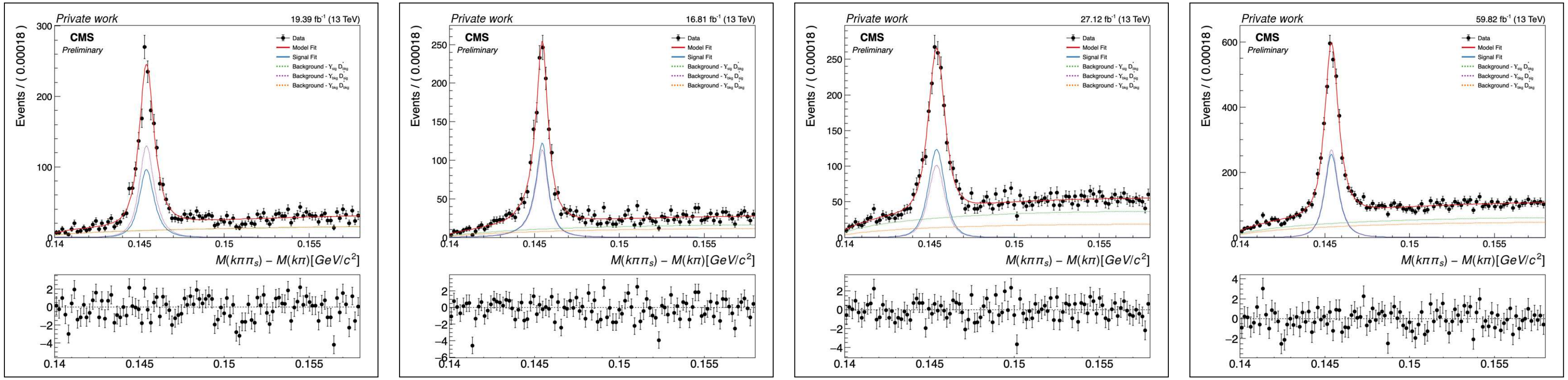

(e) 2016APV $D^{*\pm}$ projection.

(f) 2016 $D^{*\pm}$ projection.

(g) 2017 $D^{*\pm}$ projection.

(h) 2018 $D^{*\pm}$ projection.

Legend: Projections to the dimuon invariant mass (a-d) and $D^{*\pm}$ Δm (e-f) taken from the fit to the selected associated Υ+ $D^{*\pm}$ for all data samples. The curves represent the full fit (in red) and each of the components - signal (in blue and continuous line) and background components (dashed lines in green, purple and orange).

Source: The author, 2023.

Finally, the fit using all the data combined can be found in Fig. 60 and the parameter summary in Tab. 9.

Figure 60 - Projections of the two dimensional fit to the selected associated $\Upsilon+$ D$^{*\pm}$ combining all the samples.

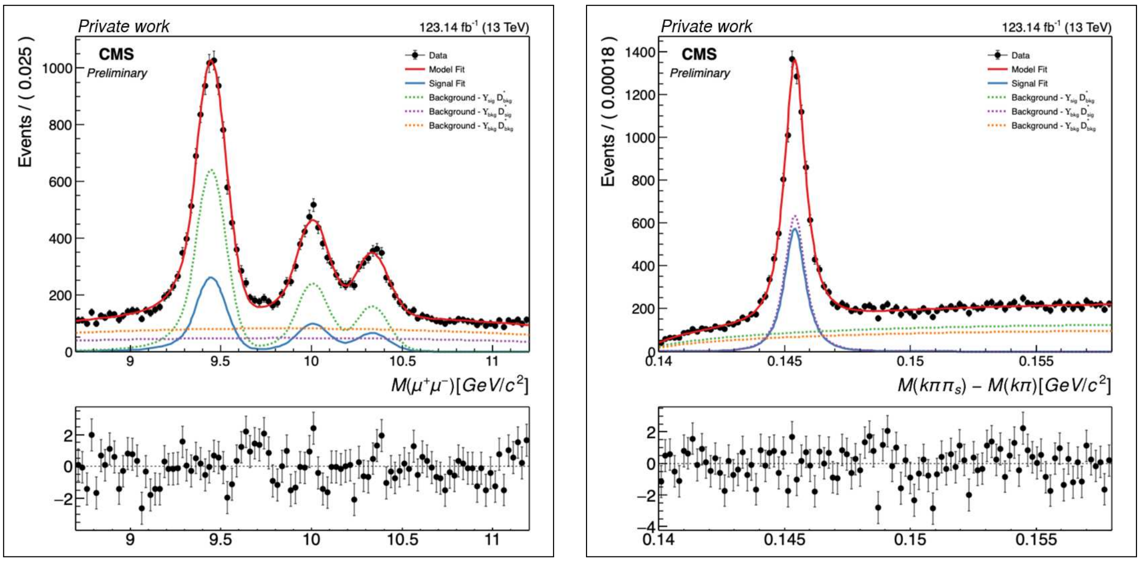

(a)

(b)

Legend: Projections to the dimuon invariant mass (a) and D$^{*\pm}$ Δm (b) taken from the fit to the selected associated $\Upsilon+$ D$^{*\pm}$ combining all data samples. The curves represent the full fit (in red) and each of the components - signal (in blue and continuous line) and background components (dashed lines in green, purple and orange).

Source: The author, 2023.

4.5 Acceptance and Efficiency

The acceptance and efficiency of the process is determined from the MC signal. The strategy for computing the acceptance and efficiency is to factorize it into the components,

$$(Acc\cdot\epsilon) = (Acc\cdot\epsilon_{precuts})^{\Upsilon}\cdot(Acc\cdot\epsilon_{precuts})^{D^*}\cdot\epsilon^{\Upsilon}_{cuts}\cdot\epsilon^{D^*}_{cuts}\cdot\epsilon_{HLT}\cdot\epsilon_{association}, \tag{33}$$

where the $Acc\cdot\epsilon_{precuts}$ is the acceptance coupled to the precuts efficiency, ϵ_{cuts} is the selection cut efficiency, ϵ_{HLT} is the trigger efficiency and the $\epsilon_{association}$ is the efficiency related to the $\Upsilon + D^*$ association criteria. Sec. 4.3 gives details of the precuts and cuts applied.

Each of the components are calculated to create two dimensional maps used to extract the efficiency of the data samples. This strategy is used to have a better deter-

Table 9 - Summary of fit parameters for the combined samples

Parameter	Value
N_{evt}	25391
$N_{sig}\Upsilon(1S)$	2365 ± 107
$N_{sig}\Upsilon(2S)$	915 ± 46
$N_{sig}\Upsilon(3S)$	651 ± 35
m_{scale}	0.9985 ± 0.0001
Δm (MeV)	145.42 ± 0.02
χ^2 Υ proj.	1.30
χ^2 $D^{*\pm}$ proj.	1.28

Legend: A summary with the most important fit parameters using data from all samples.
Source: The author, 2023.

mination of the systematic uncertainties sources, but this study could not be finished in time for the thesis conclusion.

4.5.1 Acceptance

The acceptance is calculated taking into account the precuts (Tab. 4) and the cuts that define the fiducial region of the sample on Tab. 6. The acceptance coupled to the precuts is calculated by

$$(Acc \cdot \epsilon_{precuts})^P = \frac{N^P_{reco}}{N^P_{gen}}, \tag{34}$$

where the superscript P refers either to Υ or D^*, N_{gen} is the number of generated particles within the fiducial region, and N_{reco} is the number of reconstructed particles within the same fiducial region, passing the precuts and satisfying the respective matching criteria for that kind of particle:

- For Υ: the two muons used for its reconstruction must be matched to the muons from the decay of the generated Y within a cone of $\Delta R = \sqrt{\Delta\eta^2 + \Delta\phi^2} < 0.03$.
- For D^*: The reconstructed D^* matches the generated D^* with the requirements:

$$\frac{|p_T^{reco} - p_T^{gen}|}{p_T^{gen}} < 0.2,$$
$$|\eta_{gen} - \eta_{reco}| < 0.3,$$
$$\mathrm{remainder}(|\phi_{gen} - \phi_{reco}|, 2\pi) < 0.3,$$

where the remainder(x, y) is the left over of the division x/y.

The plots of the acceptance extracted from the 2018 MC sample are given in Figs. 61 and 62 for Υ and D*, respectively. The acceptance for Υ is almost flat all in the p$_T$ and rapidity, this is expected as CMS has a very precise muon identification and reconstruction in the chosen fiducial volume. For D* the acceptance is much lower than Υ, since it is reconstructed from a 3–body decay and the slow pion is very soft, contributing for the lower values.

4.5.2 Selection Cut Efficiency

The cuts considered for this efficiency component are the ones stated in the Tab. 7 with exception to the cuts on the $\mu\mu\pi_s$ vertex probability and invariant mass of the Υ + D* candidate, which are treated separately. The denominator is the number of reconstructed events that passed the precuts criteria and the numerator is the number of events that passed the cuts and the precuts:

$$\epsilon^P_{cuts} = \frac{N^P_{reco\&cuts}}{N^P_{reco}}; \quad (P = \Upsilon, D^*). \tag{35}$$

The plots of the selection cut efficiency extracted from the 2018 MC sample are given in Figs. 63 and 64 for Υ and D*, respectively. In Fig. 63, the values of efficiency is very high as the only selection considered is the muon soft id, which is tuned for B-Physics events. On the other hand, the selection for D* in Fig. 64, has many cuts to remove the combinatorial background from D*. In Fig. 64a there is an improve in the efficiency between 4 GeV $<$ p$_T$ $<$ 30 GeV, because of the correlation between D* and slow pion transverse momentum, and the slow pion tracks are better resolved. The decline in the efficiency in the frontal region in Fig. 63b is expected in CMS as there is a lower detector coverage in the frontal region.

4.5.3 Trigger Efficiency

The triggers used depend only on the dimuons, therefore, their efficiency is only evaluated from the Υ candidates. The denominator is the number of events that passed both the precuts and cuts criteria and the numerator the number of events passing the trigger, cuts and precuts:

$$\epsilon_{HLT} = \frac{N^{\Upsilon}_{reco\&cuts\&trigger}}{N^{\Upsilon}_{reco\&cuts}} \tag{36}$$

Figure 61 - Υ acceptance of the selected associated Υ+ D* extracted from 2018 MC sample.

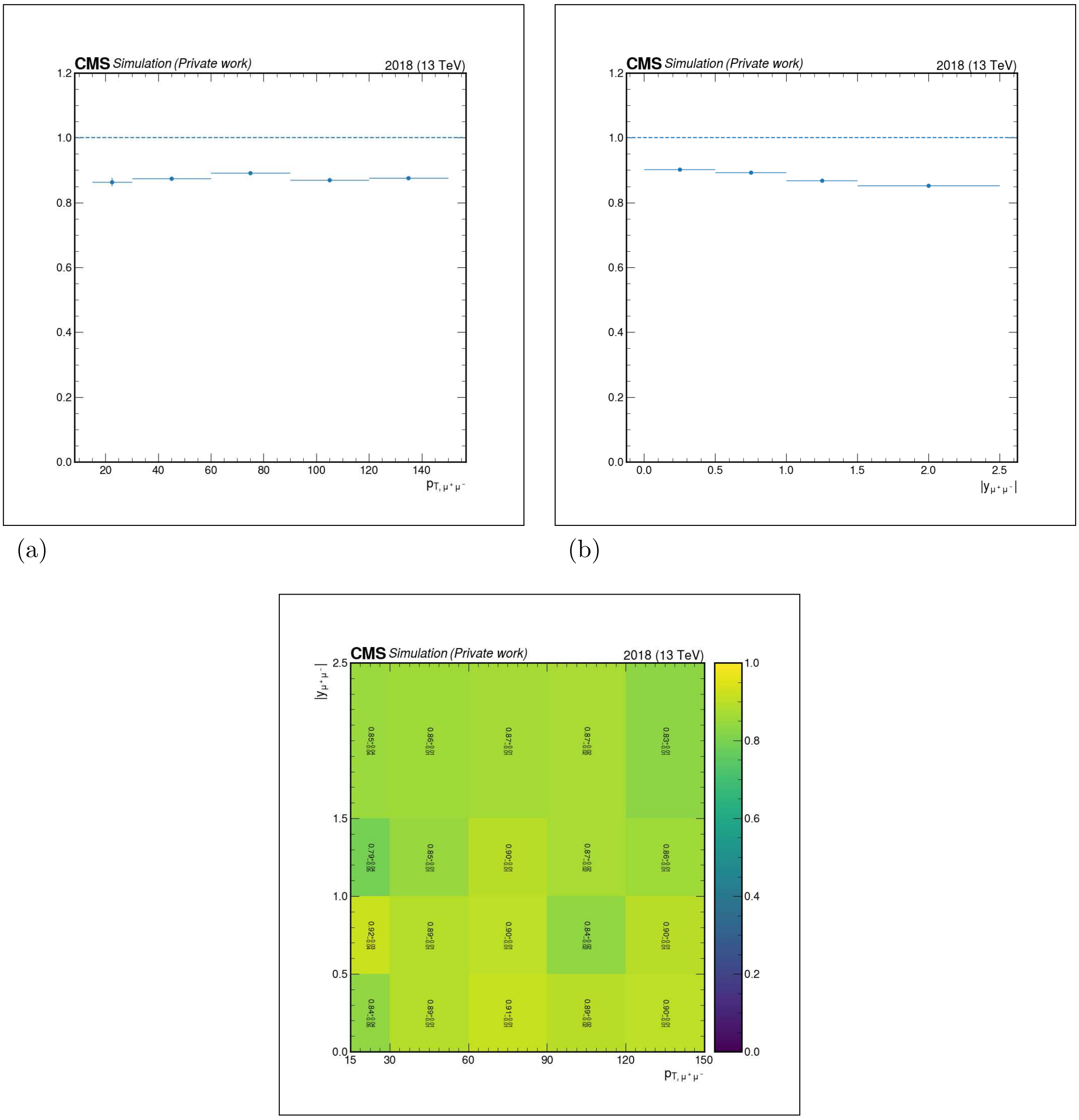

(a)

(b)

(c)

Legend: Υ acceptance extracted from the 2018 MC data sample. The acceptance is given with respect to the dimuon p_T in (a), y in (b), and in both p_T and y in (c). In (a) and (b), the horizontal dashed line is set to the upper limit of the acceptance, one.

Source: The author, 2023.

Figure 62 - D* acceptance of the selected associated Υ+ D* extracted from 2018 MC sample.

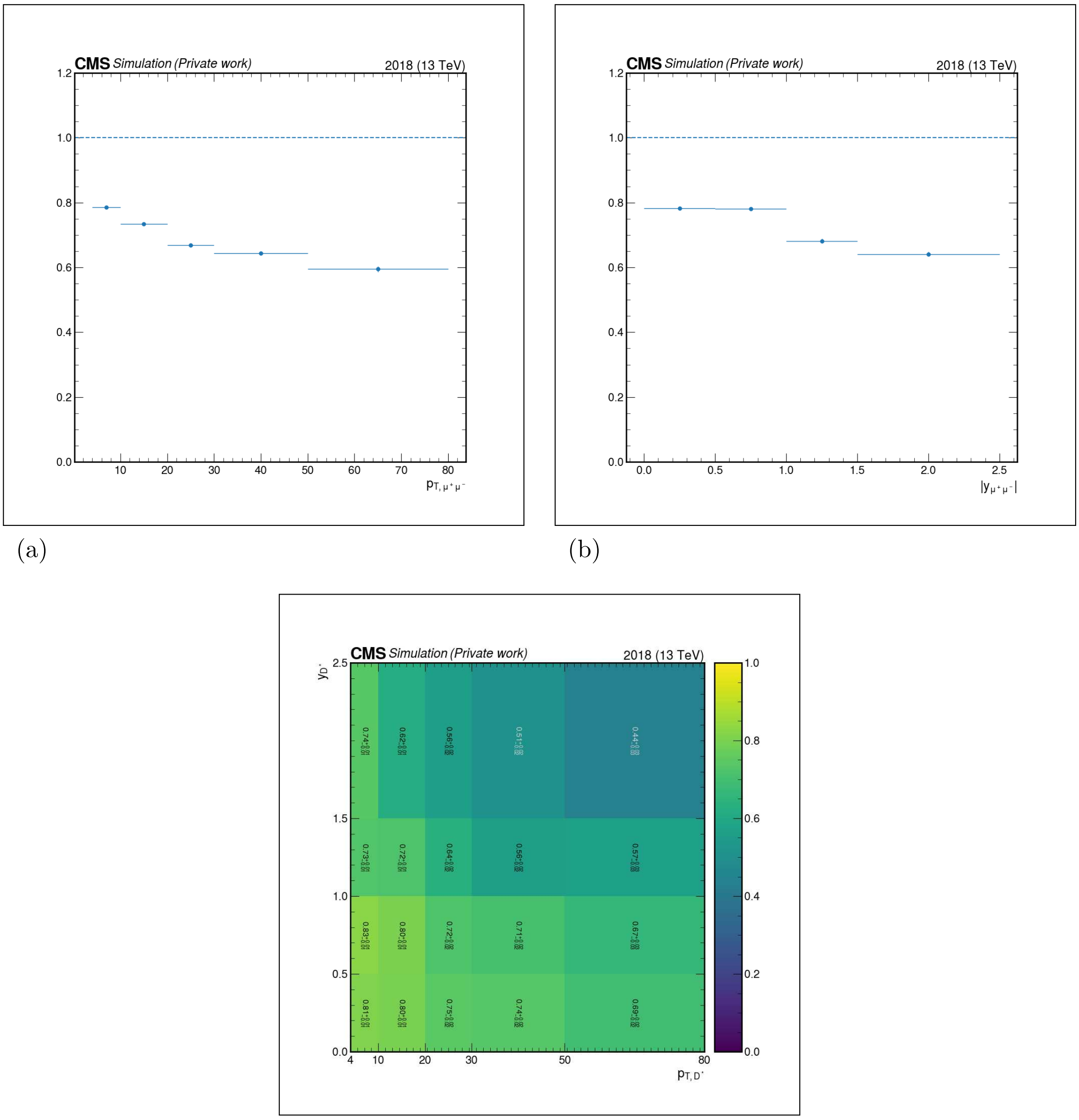

(a)

(b)

(c)

Legend: D* acceptance extracted from the 2018 MC data sample. The acceptance is given with respect to the reconstructed D* p_T in (a), y in (b), and in both p_T and y in (c). In (a) and (b), the horizontal dashed line is set to the upper limit of the acceptance, one.

Source: The author, 2023.

Figure 63 - Υ selection cut efficiency of the selected associated Υ+ D* extracted from 2018 MC sample.

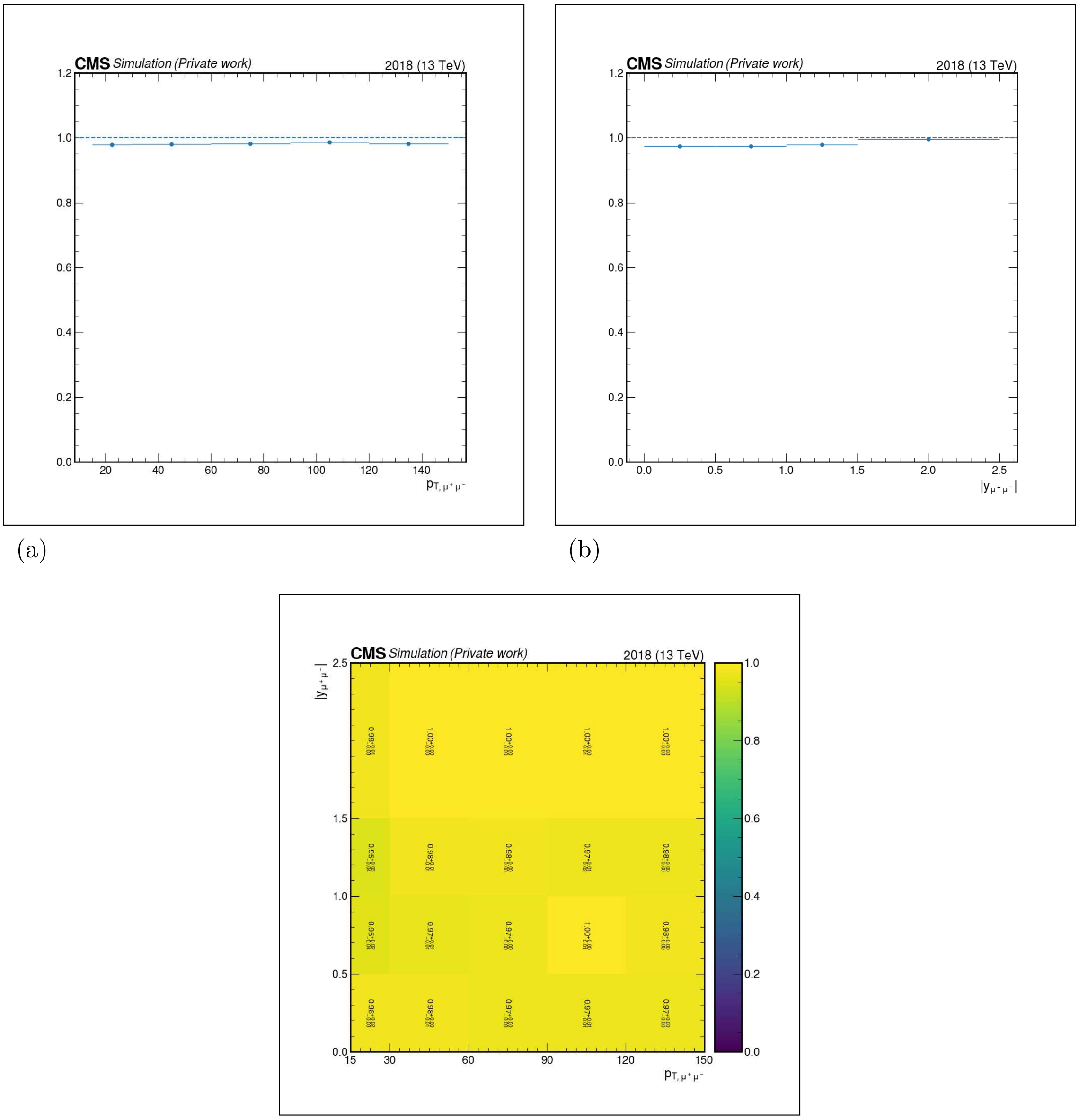

(a) (b)

(c)

Legend: Υ selection cut efficiency extracted from the 2018 MC data sample. This efficiency is given with respect to the dimuon p_T in (a), y in (b), and in both p_T and y in (c). In (a) and (b), the horizontal dashed line is set to the upper limit of the efficiency.

Source: The author, 2023.

Figure 64 - D* selection cut efficiency of the selected associated Υ+ D* extracted from 2018 MC sample.

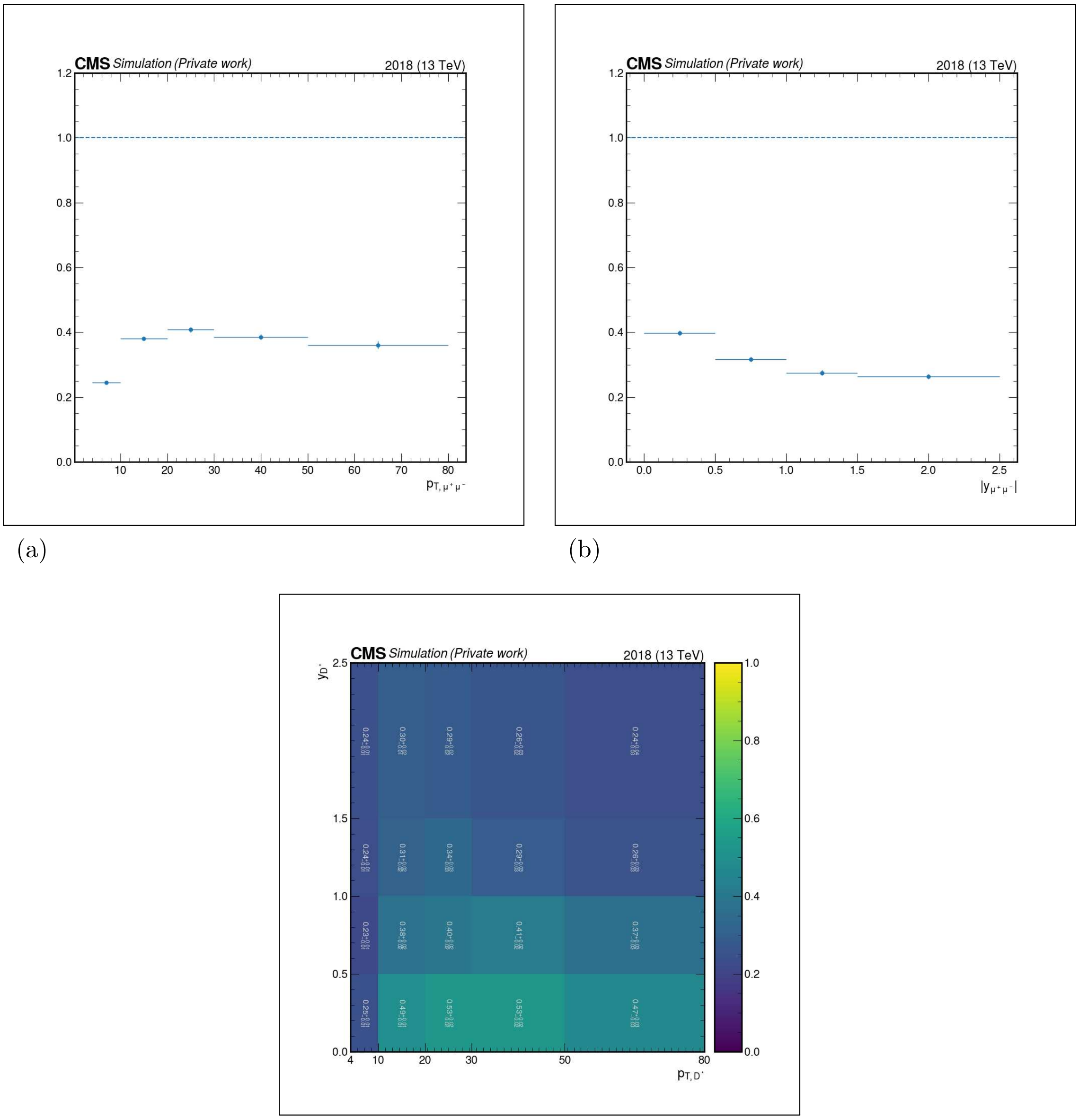

(a)

(b)

(c)

Legend: D* selection cut efficiency extracted from the 2018 MC data sample. This efficiency is given with respect to the D* p_T in (a), y in (b), and in both p_T and y in (c). In (a) and (b), the horizontal dashed line is set to the upper limit of the efficiency.

Source: The author, 2023.

The plots of the trigger efficiency extracted from the 2018 MC sample are given in Fig. 65. The trigger efficiency has expected values, since it is a dimuon trigger, it is not expected to be close to one, as the two muons have to be correctly identified and the vertex fit has to be successful.

4.5.4 Association efficiency

The last efficiency is related to the association between Υ and D^*. It is given by

$$\epsilon_{association} = \frac{N_{reco\&cuts\&trigger\&association}}{N_{reco\&cuts\&trigger}}, \tag{37}$$

where the denominator is the number of events that passed all the previous selections and the numerator is the number of events after the full selection.

The plots of the trigger efficiency extracted from the 2018 MC sample are given in Fig. 66. This efficiency determination suffers from higher statistical uncertainties because of the number of generated MC events used in this work. We expect to have a better determination once a higher statistics MC is used.

4.5.5 Total efficiency

All the efficiency maps can be found in the Appendix A. They are used to calculate the total efficiency for the cross section determination. The final efficiency for each subsample and the combination of all the data is shown in Tab. 10.

Table 10 - Total efficiency per data sample.

Sample	Total Efficiency (%)
2016APV	7.5 ± 1.5
2016	9.1 ± 2.5
2017	6.7 ± 1.6
2018	4.4 ± 1.7
Combined	6.1 ± 1.7

Legend: Total efficiency per data sample, the uncertainties shown are only statistical.
Source: The author, 2023.

It is worth noting that the uncertainties are high, in the 20 - 30 % range, because of the limited MC statistics. We expect a new MC batch with much higher statistics to become available soon, making possible to significantly improve the efficiency determina-

Figure 65 - Trigger efficiency of the selected Υ, extracted from 2018 MC sample.

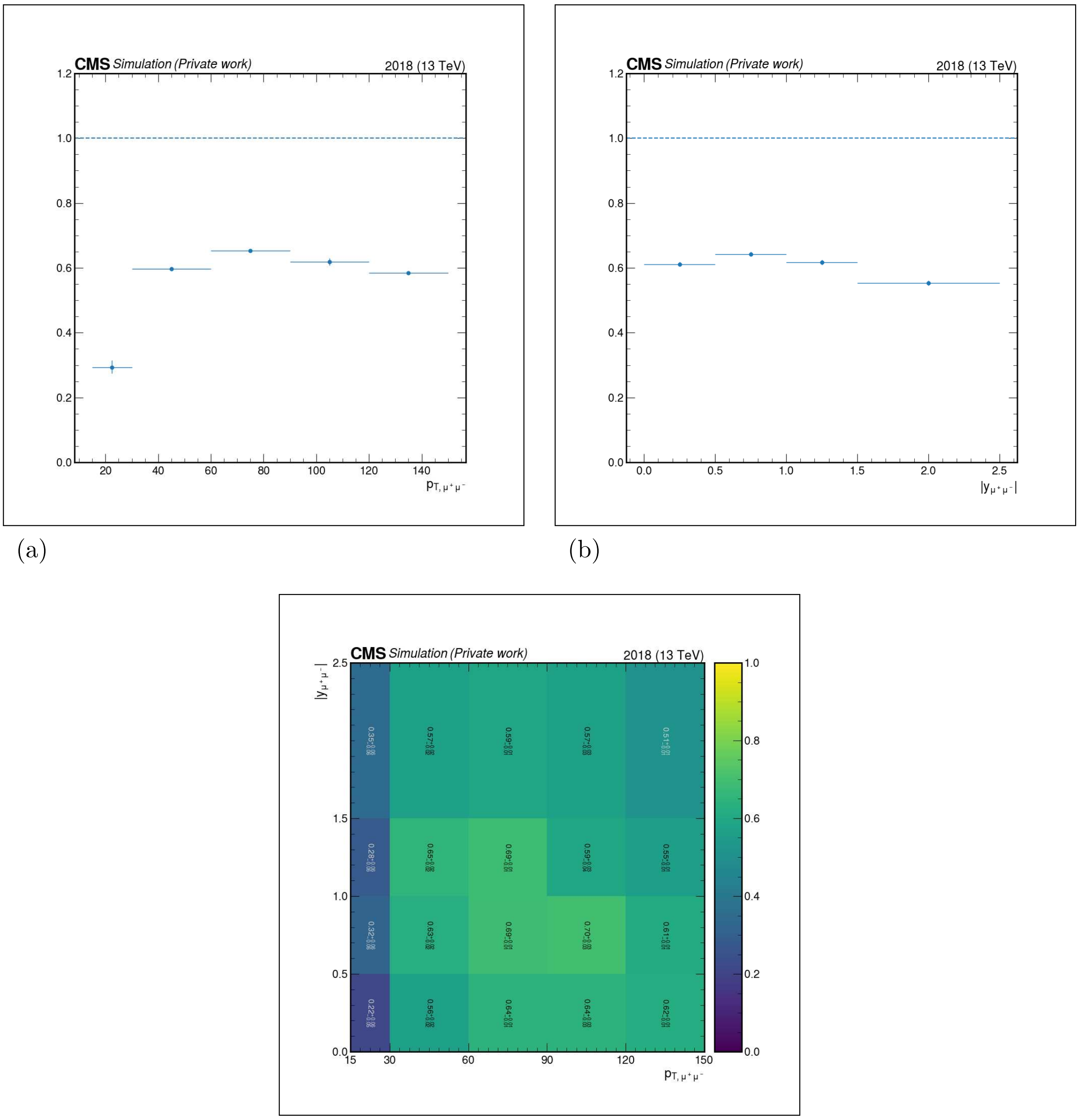

(a)

(b)

(c)

Legend: Trigger efficiency extracted from the 2018 MC data sample. This efficiency is given with respect to the dimuon p_T in (a), y in (b), and in both p_T and y in (c). In (a) and (b), the horizontal dashed line is set to the upper limit of the efficiency.

Source: The author, 2023.

Figure 66 - Association efficiency of the selected associated Υ+ D* extracted from 2018 MC sample.

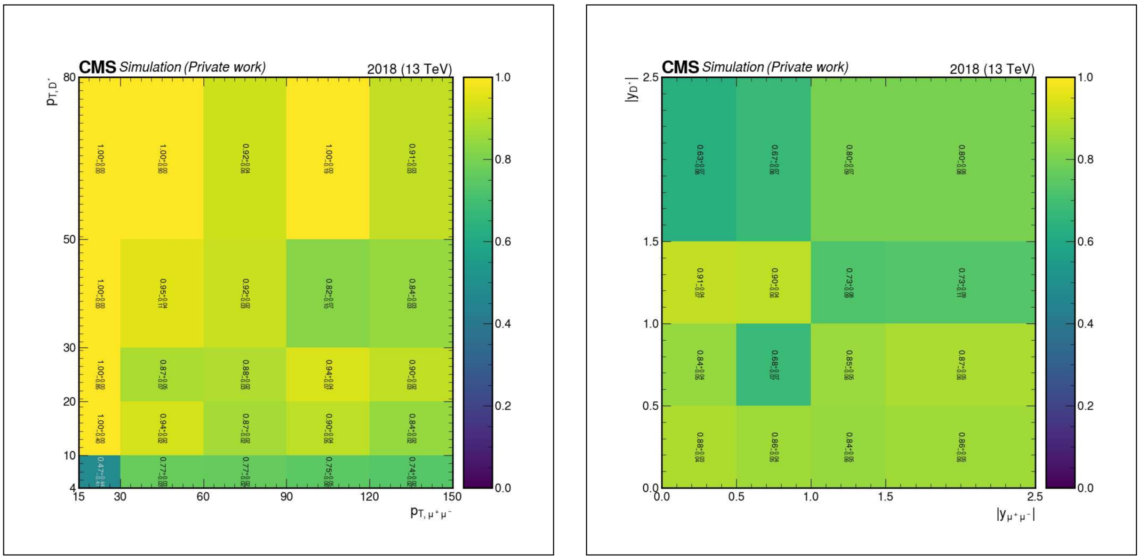

(a) (b)

Legend: Association efficiency extracted from the 2018 MC data sample. The efficiency maps are given with respect to the dimuon and D* p_T in (a) and y in (b).

Source: The author, 2023.

tion.

4.6 Associated $\Upsilon(nS)$ + D* Cross Section

4.6.1 Fiducial Cross Section

In the defined fiducial region (For Υ: $15 < p_{T,\Upsilon} < 150$ GeV and $|y_\Upsilon| < 2.5$. For D*: $4 < p_{T,D^*} < 80$ GeV and $|y_{D^*}| < 2.5$), the associated Υ + D* production cross section is calculated by the formula:

$$\sigma_{\Upsilon(nS)D^*} = \frac{N_{\Upsilon(nS)D^*}}{L \cdot eff \cdot BR(\Upsilon(nS) \to \mu^+\mu^-)BR(D^{*\pm} \to K^\mp\pi^\pm\pi^\pm)}, \tag{38}$$

where nS refers to the Υ states (1S, 2S and 3S), $N_{\Upsilon(nS)D^*}$ is the number of associated $\Upsilon(nS)$ + D* extracted from the 2D fit, L is the integrated luminosity of the sample (Sec. 4.3.2), eff is the total efficiency (Sec. 4.5.5) and $BR(\Upsilon(nS) \to \mu^+\mu^-)$ and $BR(D^{*\pm} \to K^\mp\pi^\pm\pi^\pm)$ are the branch ratios of Υ and D*, respectively. The Tab. 11 presents the fiducial cross section for each data sample and Υ state.

For each year, the cross section is stable and no major problem is found. Finally,

Table 11 - $\Upsilon(nS)$ + D* fiducial cross section per data sample.

Associated measurement	Sample	Cross section (pb)
$\Upsilon(1S)$ + D$^{*\pm}$	2016APV	482 ± 121
	2016	475 ± 203
	2017	454 ± 119
	2018	598 ± 235
$\Upsilon(2S)$ + D$^{*\pm}$	2016APV	222 ± 57
	2016	277 ± 121
	2017	225 ± 60
	2018	304 ± 119
$\Upsilon(3S)$ + D$^{*\pm}$	2016APV	152 ± 40
	2016	192 ± 85
	2017	161 ± 43
	2018	174 ± 69

Legend: $\Upsilon(nS)$ + D* cross section per data sample. The cross section is determined for each of the Υ states and its uncertainties are only statistical.

Source: The author, 2023.

to extract the cross section for all the Run 2 data, it is recommended to perform a fit to all the data, since the likelihood minimization process can provide better uncertainty estimation than other methods. For each $\Upsilon(nS)$ state, the fiducial cross section is:

$$\begin{aligned} &\sigma_{Y(1S)D^{*\pm}} = 498 \pm 151 \text{ pb}, \\ &\sigma_{Y(2S)D^{*\pm}} = 247 \pm 75 \text{ pb}, \\ &\sigma_{Y(3S)D^{*\pm}} = 156 \pm 47 \text{ pb}, \end{aligned} \qquad (39)$$

where only statistical errors are considered.

4.6.2 Effective Cross Section

The effective cross section can be determined by rearranging the Eq. 11

$$\sigma_{eff} = \frac{\sigma_{\Upsilon} \cdot \sigma_{D^*}}{\sigma_{\Upsilon D^*}^{DPS}}. \qquad (40)$$

The σ^{DPS} is different from the cross section determined in Sec. 4.6.1, as this one is composed from the SPS and DPS components. It is possible to write

$$\sigma_{\Upsilon D^*} = \sigma^{SPS}_{\Upsilon D^*} + \sigma^{DPS}_{\Upsilon D^*}. \tag{41}$$

To calculate the σ_{eff}, the fraction of the DPS contribution needs to be computed, which is normally done by inspection of the Δy and/or $\Delta\phi$ distributions (62). In this work, the fraction is assumed to be one[16], and the value presented can be assumed as a lower bound for the σ_{eff}.

Measurements of the inclusive production cross section of $\Upsilon(nS)$ and D* at the same center of mass energy performed by the CMS Collaboration can be found in Tab. 12.

Table 12 - Fiducial cross section of $\Upsilon(nS)$ and D*.

Particle	Fiducial cross section	Kinematic region
$BR(\Upsilon \to \mu^+\mu^-) \times \sigma_{\Upsilon(1S)}$	87.7 ± 1.4(stat) $\pm$ 5.3(syst) pb	$20 < p_T < 130$ GeV, $\|y\| < 1.2$
$BR(\Upsilon \to \mu^+\mu^-) \times \sigma_{\Upsilon(2S)}$	39.4 ± 1.0(stat) $\pm$ 2.4(syst) pb	
$BR(\Upsilon \to \mu^+\mu^-) \times \sigma_{\Upsilon(3S)}$	28.2 ± 0.9(stat) $\pm$ 1.9(syst) pb	
σ_{D^*}	380 ± 17(stat) $\pm$ 46(syst) μb	$4 < p_T < 100$ GeV, $\|\eta\| < 2.1$

Legend: Fiducial cross section of $\Upsilon(nS)$ and D* derived from the differencial cross section from the sources.

Source: CMS COLLABORATION, 2018c, p. 224; CMS COLLABORATION, 2021d, p. 12. Adapted by the author.

Since the kinematic region in Tab. 12 are different from the ones chosen in the cross section determination in Sec. 4.6.1 these numbers cannot be used directly in the σ_{eff} calculation. The best approach is to extrapolate the inclusive production cross section measurements for Υ and D* to the same phase space covered by the associated production cross section in Sec. 4.6.1. However, this procedure is more time demanding and can not be reliably performed in time for the conclusion of the thesis. The way adopted to have a preliminary result on the effective cross section is to determine the fiducial cross section in the restricted phase space, which reduces the available statistics.

Table 13 summarizes the values for the σ_{eff} lower bound, as well the relevant quantities needed to obtain it and Fig. 67 displays the projections of the fit performed to determine the yields.

---

[16] This assumption is not far from the expected value. By inspecting the comparison in Fig. 54, in special, the Δy distribution, one can see that the data distribution shapes are better described by the production via DPS. Anyhow, a deeper analysis is needed to determine the fraction of DPS in the data.

Table 13 - Lower bound for $\Upsilon(1S)$ + D* effective cross section per data sample.

Process	eff (%)	N	σ (pb)	σ_{eff} (mb)
$\Upsilon(1S) + D^*$	6.8 ± 1.6	950 ± 84	171 ± 43	$> 7.9 \pm 2.0$
$\Upsilon(2S) + D^*$		456 ± 43	105 ± 27	$> 7.4 \pm 1.9$
$\Upsilon(3S) + D^*$		338 ± 33	69 ± 18	$> 7.1 \pm 1.9$

Legend: Lower bound for $\Upsilon(1S)$ + D* effective cross section per data sample. For the lower bound determination, the fraction of DPS is assumed to be one. Only statistical uncertainties are displayed.

Source: The author, 2023.

Figure 67 - Projections of the two dimensional fit to the selected associated Υ+ D$^{*\pm}$ with restricted phase space.

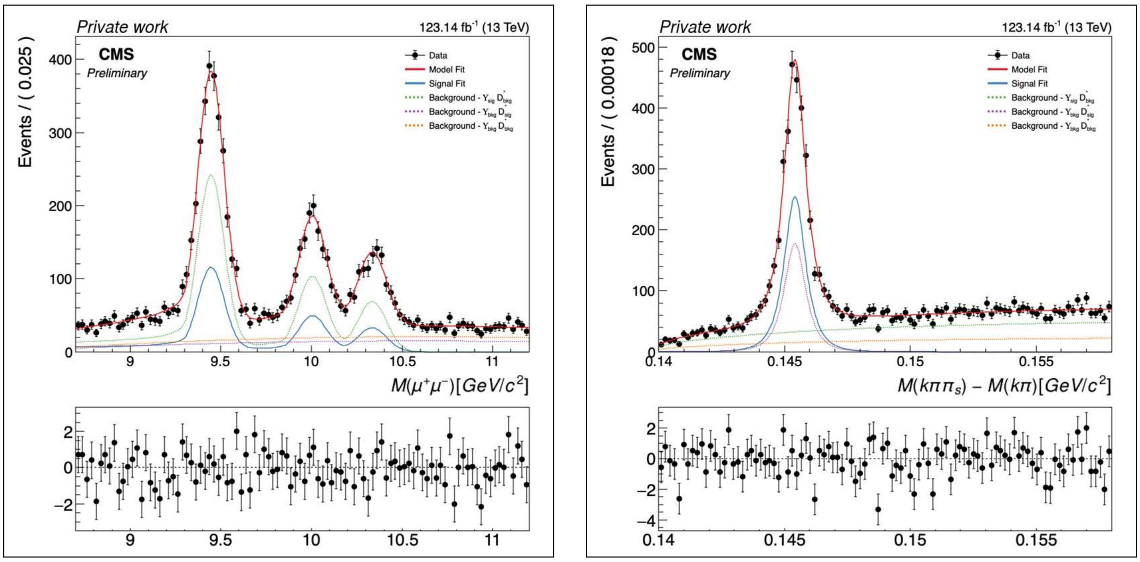

(a) (b)

Legend: Projections to the dimuon invariant mass (a) and D$^{*\pm}$ Δm (b) taken from the fit to the selected associated Υ+ D$^{*\pm}$ combining all data samples. The phase space of the Υ and D* candidates were restricted to match the inclusive cross section measurements. The curves represent the full fit (in red) and each of the components - signal (in blue and continuous line) and background components (dashed lines in green, purple and orange).

Source: The author, 2023.

Finally, combining all the values from Tab. 13, it is possible to determine the limit for the sigma effective:

$$\sigma_{eff} > 7.5 \pm 1.1 \text{ mb}. \tag{42}$$

4.7 **Systematic Uncertainties**

The systematic uncertainties include all the uncertainties that do not arise from the fluctuations in a finite set of measurements. This includes bias coming from the experiment, the assumptions made and models used to make the conclusions. The evaluation of this kind of uncertainty is analysis dependant, as one needs to consider all assumptions made in the measurement process.

That being said, the complete systematic uncertainty definition is not finished in this analysis due to time constraints, but some of them are discussed in the following lines.

- **Integrated Luminosity**: The integrated luminosity uncertainties are given in Refs. (126–128) and are summarized in Tab. 5, The combined uncertainty for the full Run 2 data set is 1.6 %.

- **Branching Fraction**: The uncertainties on the branching fractions of each considered decay channel are given in Ref. (33). The values are pointed out in Sec. 1.5

- **Determination of the yields**: This systematic uncertainty depends on the models used to determine the signal and background yields, in general, the models used to describe the shapes of the distributions should not interfere in the number of events determined, but in reality, there are changes in outcome of the fits depending on the fit model. For D* signal, the model was changed to a double Gaussian and for the background another threshold function was used (133), with the form

  $$f = \left[1 - \exp\left(-\frac{\Delta m - m_\pi}{p_0}\right)\right]\left(\frac{\Delta m}{m_\pi}\right)^{p_1} + p_2\left(\frac{\Delta m}{m_\pi} - 1\right), \tag{43}$$

  where m_π is taken as the pion mass and p_0, p_1 and p_2 are free parameters. The deviations from the yields were taken as systematic uncertainties.

  For Υ signal, a change from CBs to Gaussians resulted to bad fits, as the later one cannot describe well the tails of the invariant mass distribution. Another method is to evaluate the CB shape changes with the change of its parameters. The tail parameters n and α are specially sensitive as they are strongly correlated. n was left as free parameter and α was moved by $\pm 2\sigma$. Half of the maximum observed variation was taken as systematic, because these variations are correlated. Another parameter analyzed was the mean of the CBs, which is defined from a common factor and the mass of the Υ state taken from Ref. (33). The means were left as a free parameter and the deviation in the yield is taken as a systematic.

Finally, the Υ background model was modified to a 3rd order Chebychev polynomials and the deviation was taken as systematic.

- **Selection Cuts**: A study on the impact of the selection cuts choice on the cross section determination was made by slightly changing the cuts and recalculating the cross section. The maximum observed variation on the cross section by varying a single cut was taken as systematic.
- **Tracking Efficiencies**: The tracking efficiency for charged hadrons is given by Ref. (134). The uncertainty depends on the sample and it is combined for the two D^0 tracks. For the slow pion, a different procedure should be done, since it has a soft p_T distribution. The value of 5.2 %, given in Ref. (133) is used.

A summary of the discussed systematic uncertainties after combination are given in Tabs. 14, 15 and 16, for each of the calculated cross sections.

Table 14 - Systematic Uncertainties for $\Upsilon(1S)$+D^* cross section measurement.

Source of uncertainty	**Uncertainty**
Integrated Luminosity	1.6 %
$\Upsilon(1S)$ Branching fraction	2.0 %
D^* Branching fraction	1.1 %
Determination of the yields	4.9 %
Selection Cuts	6.5 %
Tracking Efficiency	4.1 %
Total	**9.5 %**

Legend: Summary of the sources of systematic uncertainties for the $\Upsilon(1S)$+D^* cross section measurement.

Source: The author, 2023.

Table 15 - Systematic Uncertainties for $\Upsilon(2S)$+D* cross section measurement.

Source of uncertainty	**Uncertainty**
Integrated Luminosity	1.6 %
$\Upsilon(2S)$ Branching fraction	8.8 %
D* Branching fraction	1.1 %
Determination of the yields	4.8 %
Selection Cuts	7.3 %
Tracking Efficiency	3.8 %
Total	**13.1 %**

Legend: Summary of the sources of systematic uncertainties for the $\Upsilon(2S)$+D* cross section measurement.

Source: The author, 2023.

Table 16 - Systematic Uncertainties for $\Upsilon(3S)$+D* cross section measurement.

Source of uncertainty	**Uncertainty**
Integrated Luminosity	1.6 %
$\Upsilon(3S)$ Branching fraction	9.6 %
D* Branching fraction	1.1 %
Determination of the yields	6.0 %
Selection Cuts	16.1 %
Tracking Efficiency	3.8 %
Total	**20.1 %**

Legend: Summary of the sources of systematic uncertainties for the $\Upsilon(3S)$+D* cross section measurement.

Source: The author, 2023.

CONCLUSION AND PERSPECTIVES

The associated production of $\Upsilon(nS)$ + D$^{*\pm}$ analysis was presented. The aim was to provide a cross section measurement of the associated production and to determine the σ_{eff} using pp collision data from LHC at $\sqrt{s} = 13$ TeV, recorded by the CMS experiment during the Run 2 between 2016 and 2018. The total integrated luminosity of the data samples is 123 fb^{-1}.

The measured fiducial cross sections for each of the Υ states are

$$\begin{aligned}
&\sigma_{Y(1S)D^{*\pm}} = 498 \pm 151(\text{stat}) \pm 47(\text{syst})\ \text{pb},\\
&\sigma_{Y(2S)D^{*\pm}} = 247 \pm 75(\text{stat}) \pm 32(\text{syst})\ \text{pb},\\
&\sigma_{Y(3S)D^{*\pm}} = 156 \pm 47(\text{stat}) \pm 31(\text{syst})\ \text{pb}.
\end{aligned} \tag{44}$$

It is worth noting that there are further developments needed. In particular, the evaluation of other systematic uncertainty sources is under way, e.g. the uncertainties on the Υ polarization on the efficiencies, which still needs to be investigated.

A determination of the contamination due to non-prompt[17] D* is also lacking, but it is expected to be negligible because of the cuts on the cosine of the pointing angle, which selects events that are aligned to the PV. Also, the vertex fit of the two muons and the slow pion selects only D* candidates coming from the same vertex of the dimuon.

For the effective cross section, the fiducial region had to be restricted to the one used in previous measurements of $\Upsilon(nS)$ and D$^{*\pm}$ production cross sections performed by the CMS experiment. As previously discussed, the estimation of relative contributions of DPS and SPS mechanisms to the measured associated cross section remains to be determined. However, based on Refs. (22,62,63) and supported by the shapes comparison in Fig. 54, a small contribution from SPS is expected and a lower limit for the effective cross section can be obtained by assuming the associated production to be free of SPS contribution:

$$\sigma_{eff} > 7.5 \pm 1.1(\text{stat})\ \text{mb}. \tag{45}$$

This result is compared with previous measurements of σ_{eff} in Fig. 68. The measurement discussed in this thesis is in agreement with other measurements made by CMS, ATLAS and D0, when they involve quarkonia. LHCb hints higher values, more in agreement with measurements involving jets and vector bosons. This differences in the σ_{eff} still needs to be further understood and a better theoretical description of the MPS is needed.

---

[17] D* resulting from decays of B-hadrons

Figure 68 - Comparison of the σ_{eff} measurements.

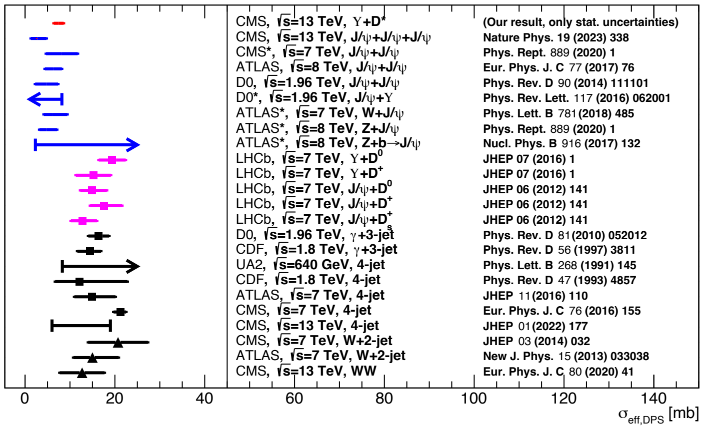

Legend: Comparison of the σ_{eff} measurements. The markers in black are measurements with jets, the ones in magenta are measurements involving quarkonia made in LHCb, the ones in blue are measurements involving quarkonia made by D0, CMS and ATLAS. The one in red is the measurement discussed in this thesis.

Source: The author, 2023.

Also, another method of extracting the σ_{eff} is being studied. By manipulating the Eq. 40 one can write

$$\begin{aligned}\sigma_{eff} &= \frac{\sigma_{\Upsilon(nS)} \cdot \sigma_{D^*}}{\sigma^{DPS}_{\Upsilon(nS)D^*}} \\ &= \frac{N_{\Upsilon(nS)}}{L \cdot eff_{\Upsilon(nS)} \cdot BR_{\Upsilon(nS)}} \cdot \frac{N_{D^*}}{L \cdot eff_{D^*} \cdot BR_{D^*}} \cdot \frac{L \cdot eff_{\Upsilon(nS)D^*} \cdot BR_{\Upsilon(nS)} \cdot BR_{D^*}}{N_{\Upsilon(nS)D^*}} \\ \sigma_{eff} &= \frac{N_{\Upsilon(nS)} \cdot N_{D^*}}{L \cdot N_{\Upsilon(nS)D^*}} \cdot \frac{eff_{\Upsilon(nS)D^*}}{eff_{\Upsilon(nS)} \cdot eff_{D^*}}.\end{aligned} \tag{46}$$

This approach has many advantages – the statistics are higher, since we can extend the measurements to the full CMS phase space, also many terms that are source of systematic uncertainties cancel out (e.g. the branching ratios and the trigger efficiency), resulting in a much preciser measurement.

That being said, this measurement can help to improve the knowledge about the DPS mechanisms as the current results show deviations depending on the final state. This is not expected in the MPS model, but, as pointed out by Ref. (62), as far as quarkonium measurements are concerned, those in the forward region hint at larger σ_{eff} values, thus smaller DPS contributions, than those in the central rapidity region.

Regarding the CMS RPC project, the contributions from the author to its maintenance, operation and R&D have been presented. There are many challenges in the operation and upgrade of these detectors during Phase 2, as they have to maintain the excellent timing, stability and robustness, even in the high radiation environment of the HL-LHC. Finally, because of the regulations imposed to the F-gases, the search for low GWP gases to substitute freon and SF_6 is of utmost importance for the future of this gaseous detector technology.

REFERENCES

1 GLASHOW, S. L. Partial Symmetries of Weak Interactions. *Nucl. Phys.*, [S.l.], v. 22, p. 579–588, 1961.

2 WEINBERG, S. A Model of Leptons. *Phys. Rev. Lett.*, [S.l.], v. 19, p. 1264–1266, 1967.

3 SALAM, A. Elementary particle theory: relativistic groups and analyticity. In: NOBEL SYMPOSIUM, 8., 1968, County of Älvsborg. Proceedings... . [S.l.]: Almqvist & Wiksell, 1968. (Nobel Symposium).

4 ATLAS COLLABORATION. Observation of a new particle in the search for the Standard Model Higgs boson with the ATLAS detector at the LHC. *Phys. Lett. B*, [S.l.], v. 716, p. 1–29, 2012.

5 CMS COLLABORATION. Observation of a New Boson at a Mass of 125 GeV with the CMS Experiment at the LHC. *Phys. Lett. B*, [S.l.], v. 716, p. 30–61, 2012.

6 CAZAROTO, E. R.; GONCALVES, V. P.; NAVARRA, F. S. Heavy quark production in pA collisions: the double parton scattering contribution. *Mod. Phys. Lett. A*, [S.l.], v. 33, n. 25, p. 1850141, 2018.

7 AFS COLLABORATION. Double parton scattering in pp collisions at $\sqrt{s} = 63$ GeV. *Z. Phys. C*, [S.l.], v. 34, p. 163, 1987.

8 CDF COLLABORATION. Study of four-jet events and evidence for double parton interactions in $p\bar{p}$ collisions at $\sqrt{s} = 1.8$ TeV. *Physical Review D*, [S.l.], APS, v. 47, n. 11, p. 4857, 1993.

9 CDF COLLABORATION. Double parton scattering in $p\bar{p}$ collisions at $\sqrt{s} = 1.8$ TeV. *Phys. Rev. D*, [S.l.], v. 56, p. 3811, 1997.

10 D0 COLLABORATION. Double parton interactions in $\gamma + 3$ jet events in $p\bar{p}$ collisions at $\sqrt{s} = 1.96$ TeV. *Physical Review D*, [S.l.], APS, v. 81, n. 5, p. 052012, 2010.

11 D0 COLLABORATION. Double parton interactions in $\gamma + 3$ jet and γ + b/c jet + 2 jet events in $p\bar{p}$ collisions at $\sqrt{s} = 1.96$ TeV. *Physical Review D*, [S.l.], APS, v. 89, n. 7, p. 072006, 2014a.

12 D0 COLLABORATION. Observation and studies of double J/ψ production at the Tevatron. *Physical Review D*, [S.l.], APS, v. 90, n. 11, p. 111101, 2014b.

13 D0 COLLABORATION. Study of double parton interactions in diphoton + dijet events in $p\bar{p}$ collisions at $\sqrt{s} = 1.96$ TeV. *Physical Review D*, [S.l.], APS, v. 93, n. 5, p. 052008, 2016a.

14 D0 COLLABORATION. Evidence for simultaneous production of J/ψ and Υ mesons. *Physical review letters*, [S.l.], APS, v. 116, n. 8, p. 082002, 2016b.

15 LHCb COLLABORATION. Observation of double charm production involving open charm in pp collisions at $\sqrt{s} = 7$ TeV. *Journal of High Energy Physics*, [S.l.], Springer, v. 2012, n. 6, p. 1–36, 2012.

16 ATLAS COLLABORATION. Measurement of hard double-parton interactions in $W(\rightarrow l\nu)$ plus 2-jet events at $\sqrt{s} = 7$ TeV with the ATLAS detector. *New Journal of Physics*, [S.l.], IOP Publishing, v. 15, p. 033038, 2013.

17 CMS COLLABORATION. Study of double parton scattering using W + 2-jet events in proton-proton collisions at $\sqrt{s} = 7$ TeV. *Journal of High Energy Physics*, [S.l.], Springer, v. 2014, n. 3, p. 1–45, 2014a.

18 ATLAS COLLABORATION. Observation and measurements of the production of prompt and non-prompt J/ψ mesons in association with a Z boson in pp collisions at $\sqrt{s} = 8$ TeV with the ATLAS detector. *The European Physical Journal C*, [S.l.], v. 75, 2015a.

19 ATLAS COLLABORATION. Study of hard double-parton scattering in four-jet events in pp collisions at $\sqrt{s} = 7$ TeV with the ATLAS experiment. *Journal of High Energy Physics*, [S.l.], Springer, v. 2016, n. 11, p. 1–52, 2016.

20 ATLAS COLLABORATION. Measurement of the prompt J/ψ pair production cross-section in pp collisions at $\sqrt{s} = 8$ TeV with the ATLAS detector. *The European Physical Journal C*, [S.l.], Springer, v. 77, n. 2, p. 76, 2017.

21 CMS COLLABORATION. Observation of triple J/ψ meson production in proton-proton collisions at $\sqrt{s} = 13$ TeV. [S.l.], 11 2021a. Available in: https://arxiv.org/abs/2111.05370. Access in: 17 feb 2023.

22 LHCb COLLABORATION. Production of associated Υ and open charm hadrons in pp collisions at $\sqrt{s} = 7$ and 8 TeV via double parton scattering. *Journal of High Energy Physics*, [S.l.], Springer, v. 2016, n. 7, p. 1–36, 2016.

23 BURGESS, C. P.; MOORE, G. D. *The standard model: A primer.* [S.l.]: Cambridge University Press, 2006. ISBN 978-0-511-25485-7, 978-1-107-40426-7, 978-0-521-86036-9.

24 PERKINS, D. H. *Introduction to High Energy Physics.* 4. ed. [S.l.]: Cambridge University Press, 2000.

25 PONTECORVO, B. Mesonium and anti-mesonium. *Sov. Phys. JETP*, [S.l.], v. 6, p. 429, 1957.

26 PONTECORVO, B. Neutrino Experiments and the Problem of Conservation of Leptonic Charge. *Zh. Eksp. Teor. Fiz.*, [S.l.], v. 53, p. 1717–1725, 1967.

27 SUPER-KAMIOKANDE COLLABORATION. Evidence for oscillation of atmospheric neutrinos. *Phys. Rev. Lett.*, [S.l.], American Physical Society, v. 81, p. 1562–1567, Aug 1998. Available in: https://link.aps.org/doi/10.1103/PhysRevLett.81.1562. Access in: 9 feb. 2023.

28 GURALNIK, G. S.; HAGEN, C. R.; KIBBLE, T. W. B. Global conservation laws and massless particles. *Phys. Rev. Lett.*, [S.l.], American Physical Society, v. 13, p. 585–587, Nov 1964. Available in: https://link.aps.org/doi/10.1103/PhysRevLett.13.585. Access in: 10 feb. 2023.

29 HIGGS, P. W. Broken symmetries and the masses of gauge bosons. *Phys. Rev. Lett.*, [S.l.], American Physical Society, v. 13, p. 508–509, Oct 1964. Available in: https://link.aps.org/doi/10.1103/PhysRevLett.13.508. Access in: 8 feb. 2023.

30 ENGLERT, F.; BROUT, R. Broken symmetry and the mass of gauge vector mesons. *Phys. Rev. Lett.*, [S.l.], American Physical Society, v. 13, p. 321–323, Aug 1964. Available in: https://link.aps.org/doi/10.1103/PhysRevLett.13.321. Access in: 11 feb. 2023.

31 STANDARD Model of Elementary Particles. 2023. Available in: https://bit.ly/2xk15fQ. Access in: 9 feb. 2023.

32 GELL-MANN, M. *The eightfold way: A theory of strong interaction symmetry.* [S.l.], 1961. Available in: https://www.osti.gov/biblio/4008239. Access in: 9 feb. 2023.

33 WORKMAN, R. L. e. Review of Particle Physics. *PTEP*, [S.l.], v. 2022, p. 083C01, 2022.

34 FRITZSCH, H.; GELL-MANN, M.; LEUTWYLER, H. Advantages of the Color Octet Gluon Picture. *Phys. Lett. B*, [S.l.], v. 47, p. 365–368, 1973.

35 GELL-MANN, M. A Schematic Model of Baryons and Mesons. *Phys. Lett.*, [S.l.], v. 8, p. 214–215, 1964.

36 ZWEIG, G. An SU(3) model for strong interaction symmetry and its breaking. Version 2. In:_________ . *Developments in the quark theory of Hadrons.* [S.l.: s.n.], 1964. v. 1, p. 22–101.

37 KOPPENBURG, P. *List of hadrons observed at the LHC.* [S.l.], 2021. See 2022 update online. Available in: https://cds.cern.ch/record/2693187. Access in: 11 feb. 2023.

38 MATHIEU, V.; KOCHELEV, N.; VENTO, V. The Physics of Glueballs. *Int. J. Mod. Phys. E*, [S.l.], v. 18, p. 1–49, 2009.

39 GROSS, D. J.; WILCZEK, F. Ultraviolet behavior of non-abelian gauge theories. *Phys. Rev. Lett.*, [S.l.], American Physical Society, v. 30, p. 1343–1346, Jun 1973. Available in: https://link.aps.org/doi/10.1103/PhysRevLett.30.1343. Access in: 12 feb. 2023.

40 POLITZER, H. D. Reliable perturbative results for strong interactions? *Phys. Rev. Lett.*, [S.l.], American Physical Society, v. 30, p. 1346–1349, Jun 1973. Available in: https://link.aps.org/doi/10.1103/PhysRevLett.30.1346. Access in: 15 feb. 2023.

41 FUKS, B. et al. Signatures of toponium formation in LHC run 2 data. *Phys. Rev. D*, [S.l.], v. 104, n. 3, p. 034023, 2021.

42 BENNETT, J. V. *Exotic quarkonium physics prospects at Belle II.* 2019. Available in: https://arxiv.org/abs/1906.08627. Access in: 14 feb 2023.

43 OLSEN, S. L.; SKWARNICKI, T.; ZIEMINSKA, D. Nonstandard heavy mesons and baryons: Experimental evidence. *Rev. Mod. Phys.*, [S.l.], American Physical Society, v. 90, p. 015003, Feb 2018. Available in: https://link.aps.org/doi/10.1103/RevMod-Phys.90.015003. Access in: 20 feb. 2023.

44 AUBERT, J. J. et al. Experimental Observation of a Heavy Particle J. *Phys. Rev. Lett.*, [S.l.], v. 33, p. 1404–1406, 1974.

45 AUGUSTIN, J. E. et al. Discovery of a Narrow Resonance in e^+e^- Annihilation. *Phys. Rev. Lett.*, [S.l.], v. 33, p. 1406–1408, 1974.

46 HERB, S. W. et al. Observation of a Dimuon Resonance at 9.5-GeV in 400-GeV Proton-Nucleus Collisions. *Phys. Rev. Lett.*, [S.l.], v. 39, p. 252–255, 1977.

47 CMS COLLABORATION. Observation of a Peaking Structure in the $\mathrm{J}/\psi\phi$ Mass Spectrum from $\mathrm{B}^{\pm} \to \mathrm{J}/\psi\phi K^{\pm}$ Decays. *Phys. Lett. B*, [S.l.], v. 734, p. 261–281, 2014b.

48 LHCb COLLABORATION. Observation of New Resonances Decaying to $\mathrm{J}/\psi K^+$ and $\mathrm{J}/\psi\phi$. *Phys. Rev. Lett.*, [S.l.], v. 127, n. 8, p. 082001, 2021.

49 LHCb COLLABORATION. Observation of an exotic narrow doubly charmed tetraquark. *Nature Phys.*, [S.l.], v. 18, n. 7, p. 751–754, 2022.

50 ATLAS COLLABORATION. Search for Higgs and Z Boson Decays to $\mathrm{J}/\psi\gamma$ and $\Upsilon(\mathrm{nS})\gamma$ with the ATLAS Detector. *Phys. Rev. Lett.*, [S.l.], v. 114, n. 12, p. 121801, 2015b.

51 MATSUI, T.; SATZ, H. J/ψ Suppression by Quark-Gluon Plasma Formation. *Phys. Lett. B*, [S.l.], v. 178, p. 416–422, 1986.

52 WOLSCHIN, G. Upsilon suppression in the QGP at the LHC. *Nucl. Phys. A*, [S.l.], v. 956, p. 729–732, 2016.

53 COLLINS, J. C.; SOPER, D. E.; STERMAN, G. F. Factorization of Hard Processes in QCD. *Adv. Ser. Direct. High Energy Phys.*, [S.l.], v. 5, p. 1–91, 1989.

54 NNPDF COLLABORATION. Parton distributions from high-precision collider data. *Eur. Phys. J. C*, [S.l.], v. 77, n. 10, p. 663, 2017.

55 GAUNT, J. R.; STIRLING, W. J. Double parton distributions incorporating perturbative QCD evolution and momentum and quark number sum rules. *Journal of High Energy Physics*, [S.l.], Springer, v. 2010, n. 3, p. 1–40, 2010.

56 ALITTI, J. et al. A study of multi-jet events at the CERN pp collider and a search for double parton scattering. *Physics Letters B*, [S.l.], Elsevier, v. 268, n. 1, p. 145–154, 1991.

57 LHCb COLLABORATION. Measurement of the J/ψ pair production cross-section in pp collisions at $\sqrt{s} = 13$ TeV. *Journal of High Energy Physics*, [S.l.], Springer, v. 2017, n. 6, p. 1–38, 2017.

58 CMS COLLABORATION. Observation of $\Upsilon(1S)$ pair production in proton-proton collisions at $\sqrt{s} = 8$ TeV. *Journal of high energy physics*, [S.l.], Springer, v. 2017, n. 5, p. 1–34, 2017a.

59 CMS COLLABORATION. Constraints on the double-parton scattering cross section from same-sign W boson pair production in proton-proton collisions at $\sqrt{s}$ = 8 TeV. *Journal of High Energy Physics*, [S.l.], Springer, v. 2018, n. 2, p. 1–38, 2018a.

60 ATLAS COLLABORATION. Study of the hard double-parton scattering contribution to inclusive four-lepton production in pp collisions at $\sqrt{s} = 8$ TeV with the ATLAS detector. *Phys. Lett. B*, [S.l.], v. 790, p. 595–614, 2019.

61 LUSZCZAK, M.; MACIULA, R.; SZCZUREK, A. Production of two $c\bar{c}$ pairs in double-parton scattering. *Phys. Rev. D*, [S.l.], v. 85, p. 094034, 2012.

62 LANSBERG, J.-P. New Observables in Inclusive Production of Quarkonia. *Phys. Rept.*, [S.l.], v. 889, p. 1–106, 2020.

63 BEREZHNOY, A. V.; LIKHODED, A. K. Associated production of Υ and open charm at LHC. *Int. J. Mod. Phys. A*, [S.l.], v. 30, n. 20, p. 1550125, 2015.

64 EVANS, L.; BRYANT, P. LHC machine. *Journal of Instrumentation*, [S.l.], IOP Publishing, v. 3, n. 08, p. S08001–S08001, aug 2008. Available in: https://doi.org/10.1088/1748-0221/3/08/s08001. Access in: 20 feb. 2023.

65 MOBS, E. *The CERN accelerator complex - 2019. Complexe des accélérateurs du CERN - 2019.* 2019. General Photo. Available in: https://cds.cern.ch/record/2684277. Access in: 23 feb. 2023.

66 ALICE COLLABORATION. The ALICE experiment at the CERN LHC. *JINST*, [S.l.], v. 3, p. S08002, 2008.

67 ATLAS COLLABORATION. The ATLAS Experiment at the CERN Large Hadron Collider. *JINST*, [S.l.], v. 3, p. S08003, 2008.

68 CMS COLLABORATION. The CMS Experiment at the CERN LHC. *JINST*, [S.l.], v. 3, p. S08004, 2008.

69 LHCb COLLABORATION. The LHCb Detector at the LHC. *JINST*, [S.l.], v. 3, p. S08005, 2008.

70 CMS Luminosity. 2023. Available in: https://twiki.cern.ch/twiki/bin/view/CMSPublic/LumiPublicResults. Access in: 9 feb. 2023.

71 ABERLE, O. et al. *High-Luminosity Large Hadron Collider (HL-LHC): Technical design report*. Geneva: CERN, 2020. (CERN Yellow Reports: Monographs). Available in: https://cds.cern.ch/record/2749422. Access in: 8 feb. 2023.

72 THE HL-LHC project. 2023. Available in: https://twiki.cern.ch/twiki/bin/view/CMSPublic/LumiPublicResults. Access in: 9 feb. 2023.

73 SAKUMA, T. *Cutaway diagrams of CMS detector*. 2019. Available in: https://cds.cern.ch/record/2665537. Access in: 7 feb. 2023.

74 HOW to draw diagrams in LaTeX with TikZ. 2023. Available in: https://wiki.physik.uzh.ch/cms/latex:tikz. Access in: 9 feb. 2023.

75 DOMINGUEZ, A. et al. *CMS Technical Design Report for the Pixel Detector Upgrade*. [S.l.], 2012. Available in: https://cds.cern.ch/record/1481838. Access in: 6 feb. 2023.

76 CMS COLLABORATION. *The Phase-2 Upgrade of the CMS Muon Detectors*. Geneva, 2017b. This is the final version, approved by the LHCC. Available in: http://cds.cern.ch/record/2283189. Access in: 15 feb. 2023.

77 CMS COLLABORATION. Performance of the CMS Level-1 trigger in proton-proton collisions at $\sqrt{s} = 13$ TeV. *JINST*, [S.l.], v. 15, n. 10, p. P10017, 2020a.

78 CMS COLLABORATION. Particle-flow reconstruction and global event description with the CMS detector. *JINST*, [S.l.], v. 12, n. 10, p. P10003, 2017c.

79 ALEPH COLLABORATION. Performance of the ALEPH detector at LEP. *Nucl. Instrum. Meth. A*, [S.l.], v. 360, p. 481–506, 1995.

80 RUTHERFORD, E.; GEIGER, H. An electrical method of counting the number of particles from radio-active substances. *Proceedings of the Royal Society of London. Series A, Containing Papers of a Mathematical and Physical Character*, [S.l.], The Royal Society London, v. 81, n. 546, p. 141–161, 1908.

81 PESKOV, V.; ABBRESCIA, M.; FONTE, P. *Resistive gaseous detectors: designs, performance, and perspectives*. [S.l.]: John Wiley & Sons, 2018.

82 SHOPOVA, M. F. Performance of the CMS RPC system – from LS1 upgrade to RUN2 at LHC. 2018. Thesis - (PhD. in Physics), Institute of Nuclear Research and Nuclear Energy, Bulgarian Academy of Sciences, Sofiya, 2018. Available in: https://cds.cern.ch/record/2626243. Access in: 1 feb 2023.

83 O'KELLEY, G. D. Detection and measurement of nuclear radiation. [S.l.], 12 1961. Available in: https://www.osti.gov/biblio/4761432. Access in: 2 feb 2023.

84 SAULI, F. *Gaseous radiation detectors: fundamentals and applications*. [S.l.]: Cambridge University Press, 2015.

85 FUKUI, S.; MIYAMOTO, S. A new type of particle detector: the «discharge chamber». *Il Nuovo Cimento (1955-1965)*, [S.l.], Springer, v. 11, n. 1, p. 113–115, 1959.

86 CHARPAK, G. et al. The Use of Multiwire Proportional Counters to Select and Localize Charged Particles. *Nucl. Instrum. Meth.*, [S.l.], v. 62, p. 262–268, 1968.

87 WIRE chamber schematic. 2005. Available in: https://commons.wikimedia.org/wiki/File:Wire_chamber_schematic.svg. Access in: 2 feb. 2023.

88 PARKHOMCHUCK, V.; PESTOV, Y.; PETROVYKH, N. A spark counterwith large area. *Nuclear Instruments and Methods*, [S.l.], v. 93, n. 2, p. 269–270, 1971. ISSN 0029-554X. Available in: https://www.sciencedirect.com/science/article/pii/0029554X71904757. Access in: 5 feb. 2023.

89 SANTONICO, R.; CARDARELLI, R. Development of resistive plate counters. *Nuclear Instruments and Methods in physics research*, [S.l.], Elsevier, v. 187, n. 2-3, p. 377–380, 1981.

90 DEPPNER, I. et al. Performance studies of MRPC prototypes for CBM. *JINST*, [S.l.], v. 11, n. 10, p. C10006, 2016.

91 MONDAL, S. et al. Leak Test of Resistive Plate Chamber Gap by Monitoring Absolute Pressure. *JINST*, [S.l.], v. 14, n. 04, p. P04009, 2019.

92 GUIDA, R.; MANDELLI, B.; RIGOLETTI, G. Studies on alternative eco-friendly gas mixtures and development of gas recuperation plant for RPC detectors. *Nucl. Instrum. Meth. A*, [S.l.], v. 1039, p. 167045, 2022.

93 CORBETTA, M. et al. Gas R&D on gas recirculation and recuperation for the Resistive Plate Chamber detectors. *JINST*, [S.l.], v. 15, n. 10, p. C10028, 2020.

94 SANTONICO, R. et al. Progress in Resistive Plate Counters. *Nucl. Instrum. Meth. A*, [S.l.], v. 263, p. 20–25, 1988.

95 FRANCKE, T. et al. Potential of RPCs for tracking. *Nucl. Instrum. Meth. A*, [S.l.], v. 508, p. 83–87, 2003.

96 ABBRESCIA, M. et al. *Effect of the Linseed Oil Treatment on the Performance of the Resistive Plate Counters*. Geneva, 1997. Available in: http://cds.cern.ch/record/687074. Access in: 10 mar. 2023.

97 LU, C. RPC electrode material study. *Nucl. Instrum. Meth. A*, [S.l.], v. 602, p. 761–765, 2009.

98 COSTANTINI, S. et al. Uniformity and Stability of the CMS RPC Detector at the LHC. Calibration of the RPC working voltage in the CMS experiment at the LHC. *JINST*, [S.l.], v. 8, p. P03017, 2013. Preliminary entry. Available in: https://cds.cern.ch/record/1477020. Access in: 10 mar. 2023.

99 CMS COLLABORATION. *RPC Endcap Chambers*. 2016. Available in: https://twiki.cern.ch/twiki/bin/view/CMSPublic/RPCDPGResultsforVenice. Access in: 10 mar. 2023.

100 GUIDA, R. GIF++: The new CERN irradiation facility to test large-area detectors for HL-LHC. In: IEEE NUCLEAR SCIENCE SYMPOSIUM AND MEDICAL IMAGING CONFERENCE (NSS/MIC), 2015. [Proceedings...]. [S.l.], 2015. p. 1–4.

101 ALY, R.; on behalf of the CMS collaboration. Longevity study on the CMS resistive plate chambers for HL-LHC. *Journal of Instrumentation*, [S.l.], IOP Publishing, v. 17, n. 08, p. C08008, aug 2022a. Available in: https://dx.doi.org/10.1088/17480221/17/08/C08008. Access in: 11 mar. 2023.

102 AMARILO, K. M.; on behalf of CMS Collaboration. CMS RPC data taking during the LHC Run-2 and activities during Long Shutdown 2. *Journal of Physics: Conference Series*, [S.l.], IOP Publishing, v. 2374, n. 1, p. 012150, nov 2022b. Available in: https://dx.doi.org/10.1088/1742-6596/2374/1/012150. Access in: 12 mar. 2023.

103 CMS COLLABORATION. *RPC DPG Results 2021*. 2021b. Available in: https://twiki.cern.ch/twiki/bin/view/CMSPublic/RPCDPGResultsRPC2021. Access in: 12 mar. 2023.

104 CMS COLLABORATION. *RPC DPG Results 2022*. 2022c. Available in: https://twiki.cern.ch/twiki/bin/view/CMSPublic/RPCDPGResultsRPC2022. Access in: 12 mar. 2023.

105 ARCIDIACONO, R. et al. CMS DCS design concepts. *Conf. Proc. C*, [S.l.], v. 051010, p. PO1.062–6, 2005.

106 POLESE, G. et al. The detector control systems for the CMS resistive plate chamber. *J. Phys. Conf. Ser.*, [S.l.], v. 219, p. 022019, 2010.

107 CAEN. *CAEN solution for powering in hostile areas*. 2022. Available in: https://www.caen.it/about-us/caen-solution-for-powering-in-hostile-areas/. Access in: 13 mar. 2023.

108 OPC FOUNDATION. *OPC Foundation Home Page*. 2022. Available in: https://opcfoundation.org/. Access in: 13 mar. 2023.

109 BARILLERE, R. et al. LHC GCS: A homogeneous approach for the control of the LHC experiments gas systems. In: INTERNATIONAL CONFERENCE ON ACCELERATOR AND LARGE EXPERIMENTAL PHYSICS CONTROL SYSTEMS (ICALEPCS 2003), 9., 2003. [Proceedings...]. [S.l.]: Pohang Accelerator Laboratory, 2003. p. 57–59.

110 GUTLEBER, J.; ORSINI, L. Software architecture for processing clusters based on I2O. *Cluster Computing*, [S.l.], Springer, v. 5, n. 1, p. 55–64, 2002.

111 POLESE, G. et al. The commissioning and the first operational experiences of the CMS RPC detector control system at LHC. *Nucl. Instrum. Meth. A*, [S.l.], v. 661, p. S23–S26, 2012.

112 CMS COLLABORATION. *The CMS muon project: Technical Design Report.* Geneva: CERN, 1997. (Technical design report. CMS). Available in: https://cds.cern.ch/record/343814. Access in: 15 feb. 2023.

113 ZHOU, W. et al. Monte Carlo simulation study of RPC-based 0.511 MeV photon detector with GEANT4. *JINST*, [S.l.], v. 9, p. P09003, 2014.

114 AMARILO, K. M. et al. RPC based tracking system at CERN GIF++ facility. *Nuclear Instruments and Methods in Physics Research Section A: Accelerators, Spectrometers, Detectors and Associated Equipment*, [S.l.], p. 168271, 2023. ISSN 0168-9002. Available in: https://www.sciencedirect.com/science/article/pii/S0168900223002619. Access in: 15 apr. 2023.

115 LIPPMANN, C.; RIEGLER, W. Space charge efects in resistive plate chambers. *Nucl. Instrum. Meth. A*, [S.l.], v. 517, p. 54–76, 2004.

116 SHCHABLO, K. et al. Front-end electronics for CMS iRPC detectors. *JINST*, [S.l.], v. 16, n. 05, p. C05002, 2021.

117 AGOSTINELLI, S. et al. GEANT4 – a simulation toolkit. *Nucl. Instrum. Meth. A*, [S.l.], v. 506, p. 250–303, 2003.

118 SJÖSTRAND, T. et al. An introduction to PYTHIA 8.2. *Comput. Phys. Commun.*, [S.l.], v. 191, p. 159–177, 2015.

119 CMS COLLABORATION. Extraction and validation of a new set of CMS Pythia8 tunes from underlying-event measurements. *The European Physical Journal C*, [S.l.], v. 80, n. 1, p. 4, 2020b. Available in: https://doi.org/10.1140/epjc/s10052-019-7499-4. Access in: 15 feb 2023.

120 FENG, Y. et al. Complete study on polarization of hadroproduction at QCD next-to-leading order. *Chinese Physics C*, [S.l.], IOP Publishing, v. 45, n. 1, p. 013117, 2021.

121 LANGE, D. J. The EvtGen particle decay simulation package. *Nucl. Instrum. Meth. A*, [S.l.], v. 462, p. 152–155, 2001.

122 SHAO, H.-S. HELAC-Onia: An automatic matrix element generator for heavy quarkonium physics. *Comput. Phys. Commun.*, [S.l.], v. 184, p. 2562–2570, 2013.

123 SHAO, H.-S. HELAC-Onia 2.0: an upgraded matrix-element and event generator for heavy quarkonium physics. *Comput. Phys. Commun.*, [S.l.], v. 198, p. 238–259, 2016.

124 FRUHWIRTH, R. et al. Vertex reconstruction and track bundling at the LEP collider using robust algorithms. *Comput. Phys. Commun.*, [S.l.], v. 96, p. 189–208, 1996.

125 SPEER, T. et al. *Vertex Fitting in the CMS Tracker.* Geneva, 2006. Available in: https://cds.cern.ch/record/927395. Access in: 10 feb 2023.

126 CMS COLLABORATION. Precision luminosity measurement in proton-proton collisions at $\sqrt{s} = 13$ TeV in 2015 and 2016 at CMS. *Eur. Phys. J. C*, [S.l.], v. 81, n. 9, p. 800, 2021c.

127 CMS COLLABORATION. *CMS luminosity measurement for the 2017 data-taking period at* $\sqrt{s} = 13$ TeV. Geneva, 2018b. Available in: https://cds.cern.ch/record/2621960. Access in: 15 feb 2023.

128 CMS COLLABORATION. *CMS luminosity measurement for the 2018 data-taking period at* $\sqrt{s} = 13$ TeV. Geneva, 2019. Available in: https://cds.cern.ch/record/2676164. Access in: 15 feb 2023.

129 KOM, C. H.; KULESZA, A.; STIRLING, W. J. Pair Production of J/ψ as a Probe of Double Parton Scattering at LHCb. *Phys. Rev. Lett.*, [S.l.], v. 107, p. 082002, 2011.

130 PIVK, M.; DIBERDER, F. R. L. SPlot: A Statistical tool to unfold data distributions. *Nucl. Instrum. Meth. A*, [S.l.], v. 555, p. 356–369, 2005.

131 ZEUS COLLABORATION. Measurement of charm fragmentation fractions in photoproduction at HERA. *JHEP*, [S.l.], v. 09, p. 058, 2013.

132 CMS COLLABORATION. Measurement of quarkonium production cross sections in pp collisions at $\sqrt{s} = 13$ TeV. *Phys. Lett. B*, [S.l.], v. 780, p. 251–272, 2018c.

133 CMS COLLABORATION. Measurement of prompt open-charm production cross sections in proton-proton collisions at $\sqrt{s} = 13$ TeV. *JHEP*, [S.l.], v. 11, p. 225, 2021d.

134 CMS COLLABORATION. Tracking performances for charged pions with Run2 Legacy data. [S.l.], 2022d. Available in: https://cds.cern.ch/record/2810814. Access in: 17 feb 2023.

APPENDIX A – Efficiency maps

All the Efficiency maps used for the efficiency calculation, as explained in Sec. 4.5, are displayed here.

A.1 **Efficiencies for sample 2016APV**

Figure 69 - Υ acceptance of the selected associated Υ+ D* extracted from 2016APV MC sample.

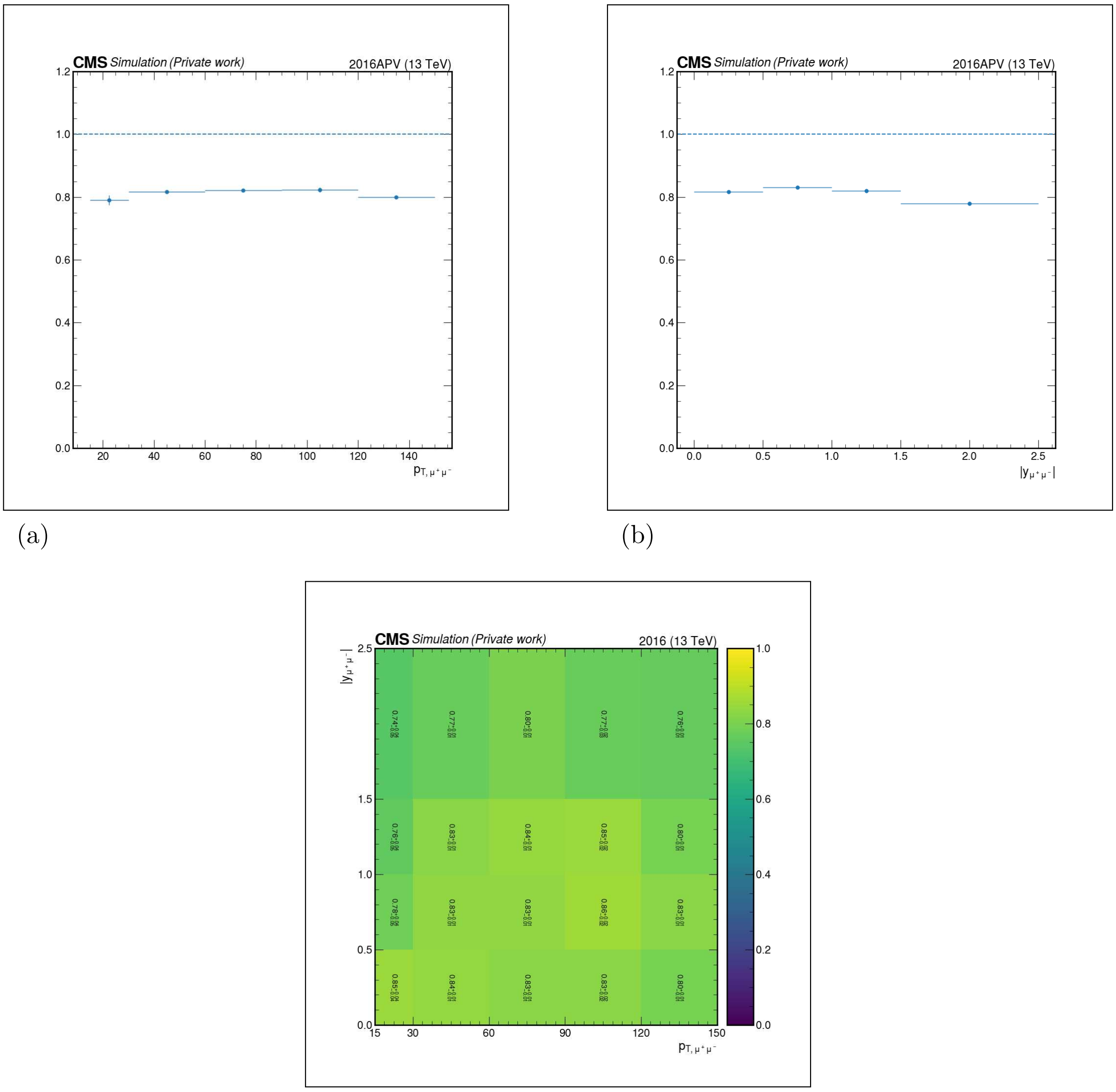

(a) (b)

(c)

Legend: Υ acceptance extracted from the 2016APV MC data sample. The acceptance is given with respect to the dimuon p_T in (a), y in (b), and in both p_T and y in (c). In (a) and (b), the horizontal dashed line is set to the upper limit of the acceptance, one.

Source: The author, 2023.

Figure 70 - D* acceptance of the selected associated Υ+ D* extracted from 2016APV MC sample.

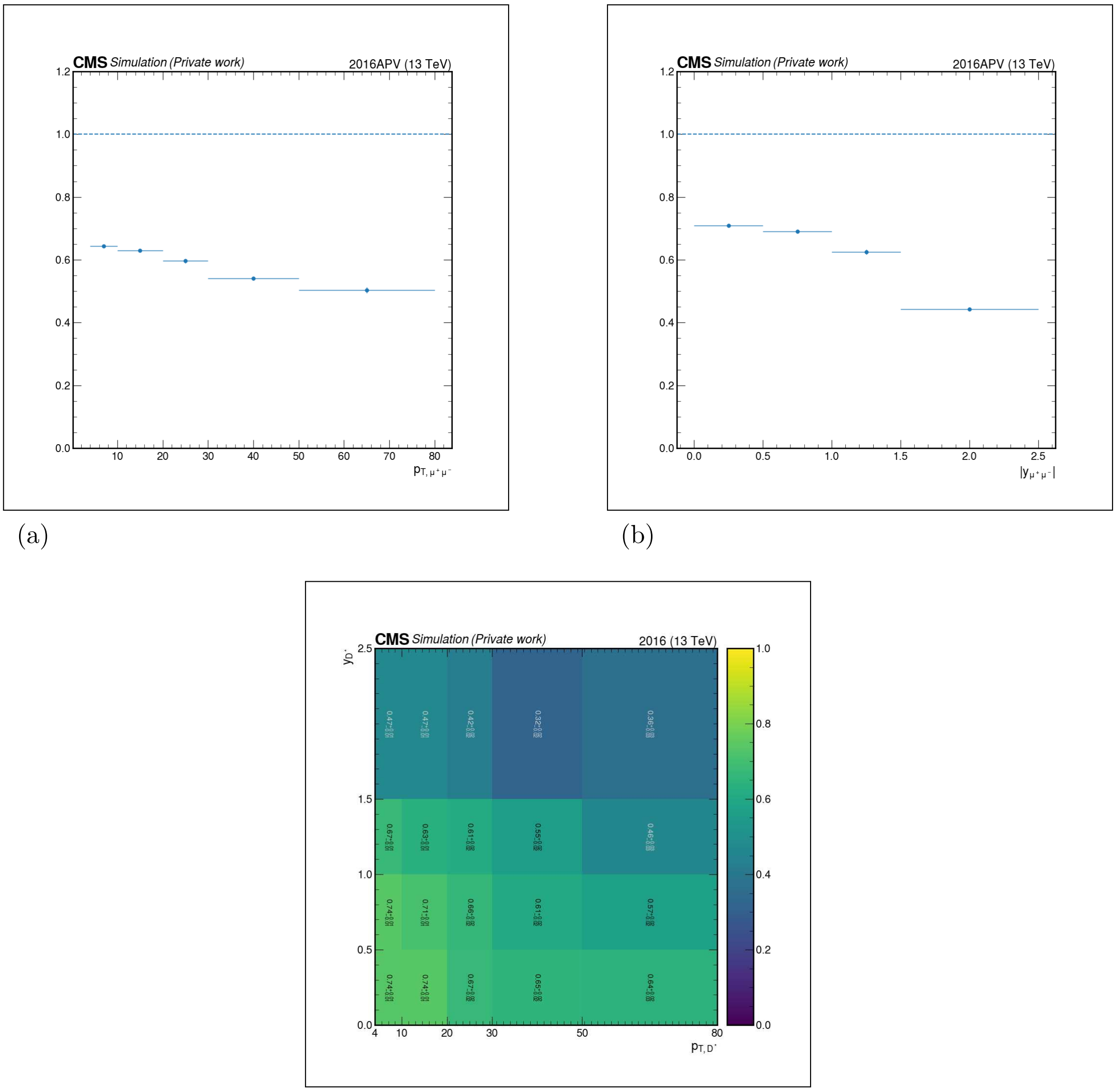

(a)

(b)

(c)

Legend: D* acceptance extracted from the 2016APV MC data sample. The acceptance is given with respect to the reconstructed D* p_T in (a), y in (b), and in both p_T and y in (c). In (a) and (b), the horizontal dashed line is set to the upper limit of the acceptance, one.

Source: The author, 2023.

Figure 71 - Υ selection cut efficiency of the selected associated Υ+ D* extracted from 2016APV MC sample.

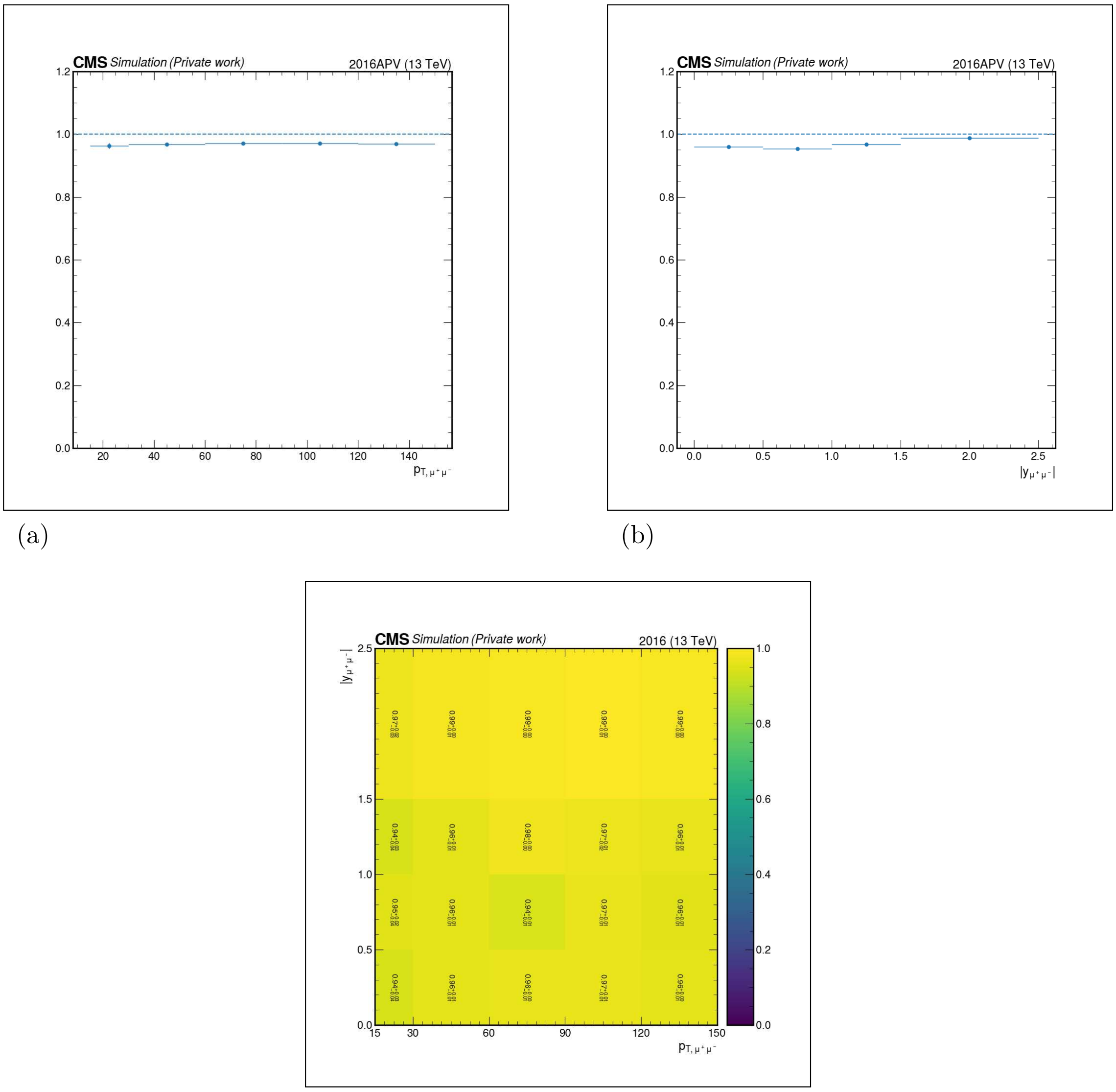

(a) (b)

(c)

Legend: Υ selection cut efficiency extracted from the 2016APV MC data sample. This efficiency is given with respect to the dimuon p_T in (a), y in (b), and in both p_T and y in (c). In (a) and (b), the horizontal dashed line is set to the upper limit of the efficiency.

Source: The author, 2023.

Figure 72 - D* selection cut efficiency of the selected associated Υ+ D* extracted from 2016APV MC sample.

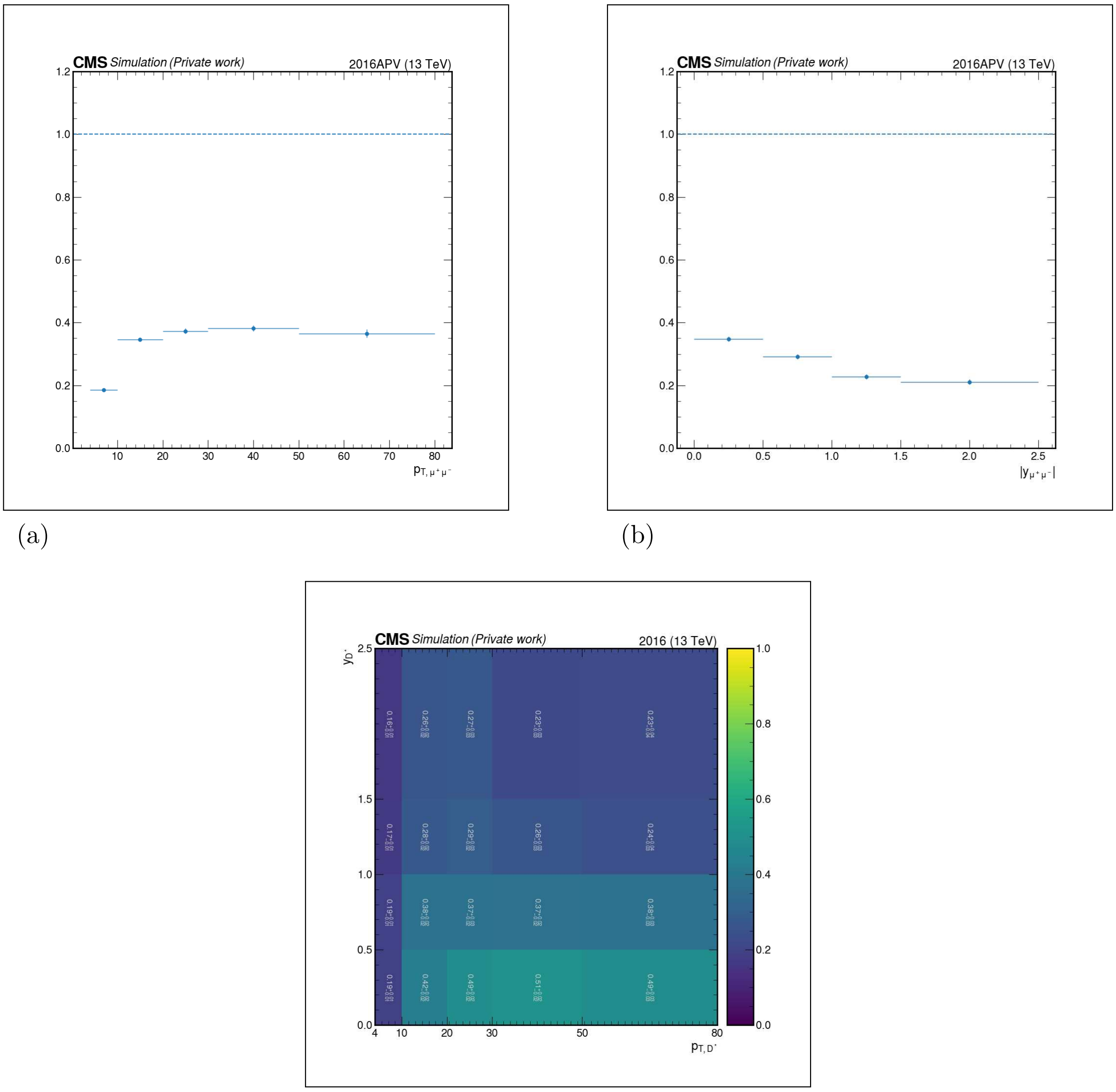

(a)

(b)

(c)

Legend: D* selection cut efficiency extracted from the 2016APV MC data sample. This efficiency is given with respect to the D* p_T in (a), y in (b), and in both p_T and y in (c). In (a) and (b), the horizontal dashed line is set to the upper limit of the efficiency.

Source: The author, 2023.

Figure 73 - Trigger efficiency of the selected Υ extracted from 2016APV MC sample.

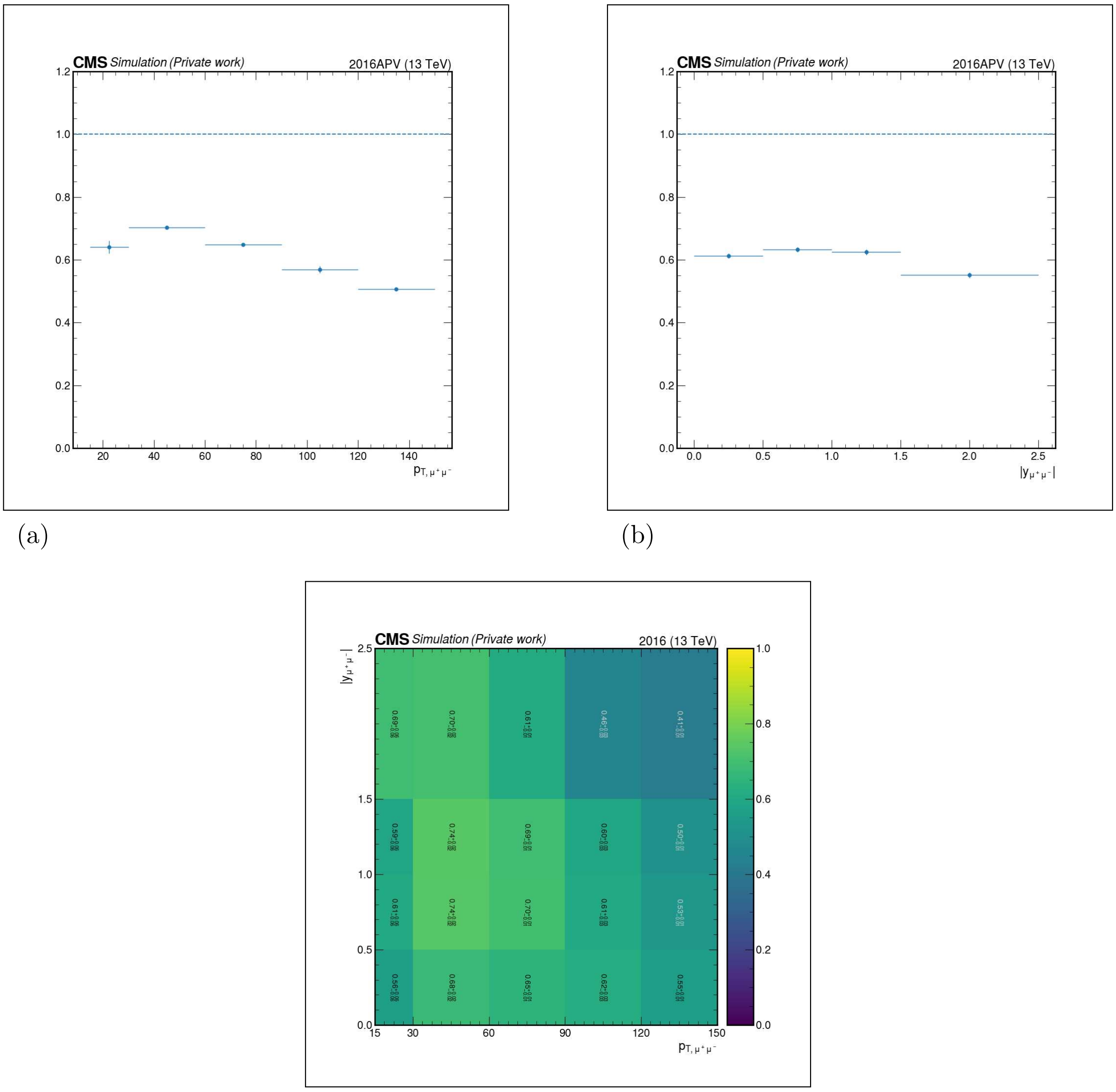

(a) (b)

(c)

Legend: Trigger efficiency extracted from the 2016APV MC data sample. This efficiency is given with respect to the dimuon p_T in (a), y in (b), and in both p_T and y in (c). In (a) and (b), the horizontal dashed line is set to the upper limit of the efficiency.

Source: The author, 2023.

Figure 74 - Association efficiency of the selected associated Υ+ D* extracted from 2016APV MC sample.

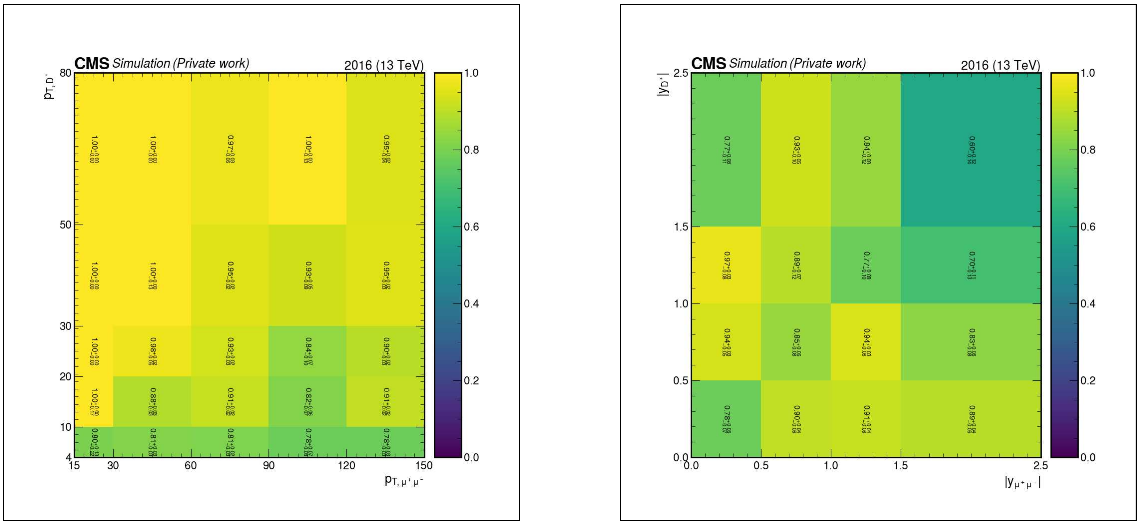

(a) (b)

Legend: Association efficiency extracted from the 2016APV MC data sample. The efficiency maps are given with respect to the dimuon and D* p_T in (a) and y in (b).

Source: The author, 2023.

A.2 Efficiencies for sample 2016

Figure 75 - Υ acceptance of the selected associated Υ+ D* extracted from 2016 MC sample.

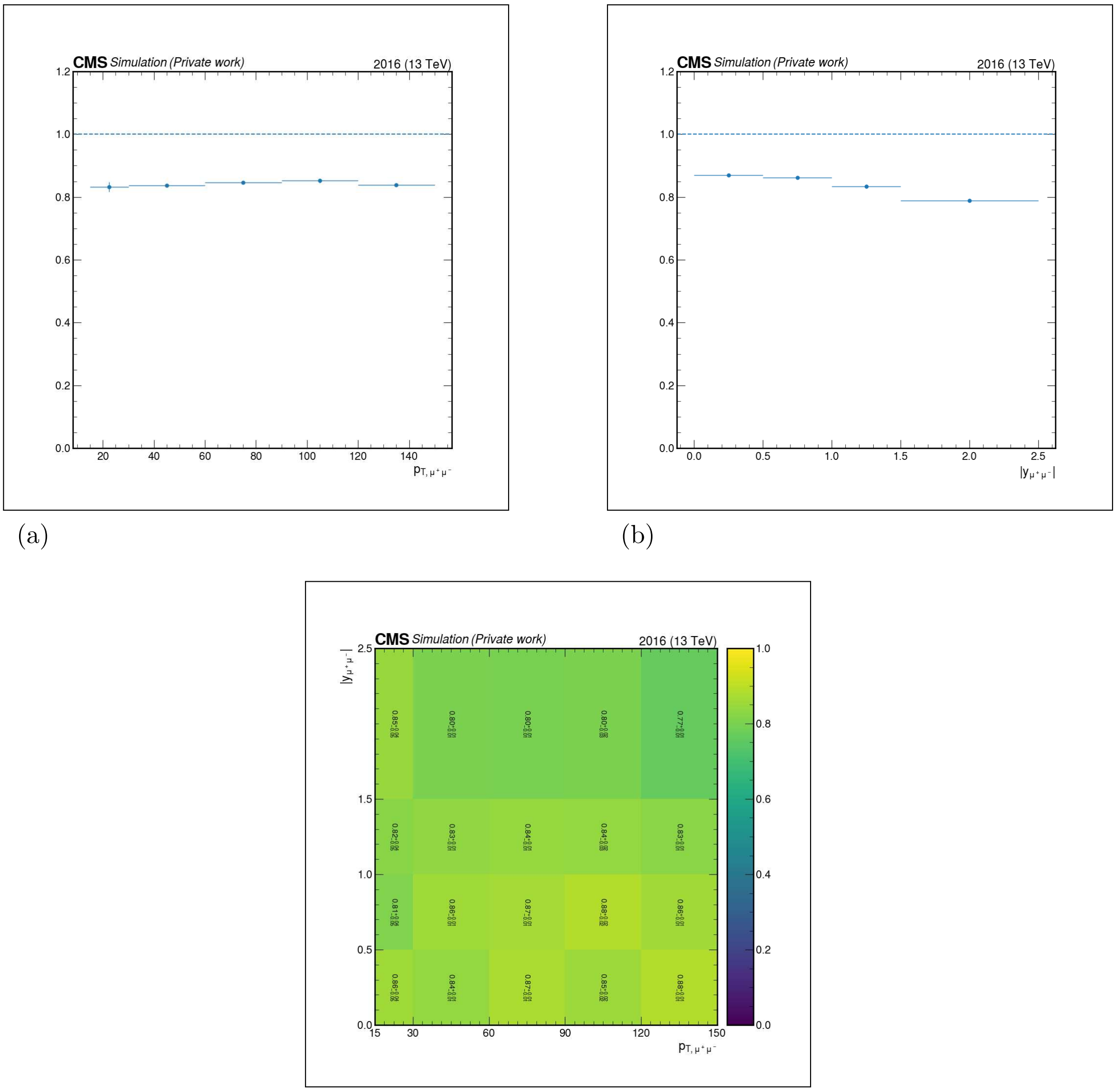

(a)

(b)

(c)

Legend: Υ acceptance extracted from the 2016 MC data sample. The acceptance is given with respect to the dimuon p_T in (a), y in (b), and in both p_T and y in (c). In (a) and (b), the horizontal dashed line is set to the upper limit of the acceptance, one.

Source: The author, 2023.

Figure 76 - D* acceptance of the selected associated Υ+ D* extracted from 2016 MC sample.

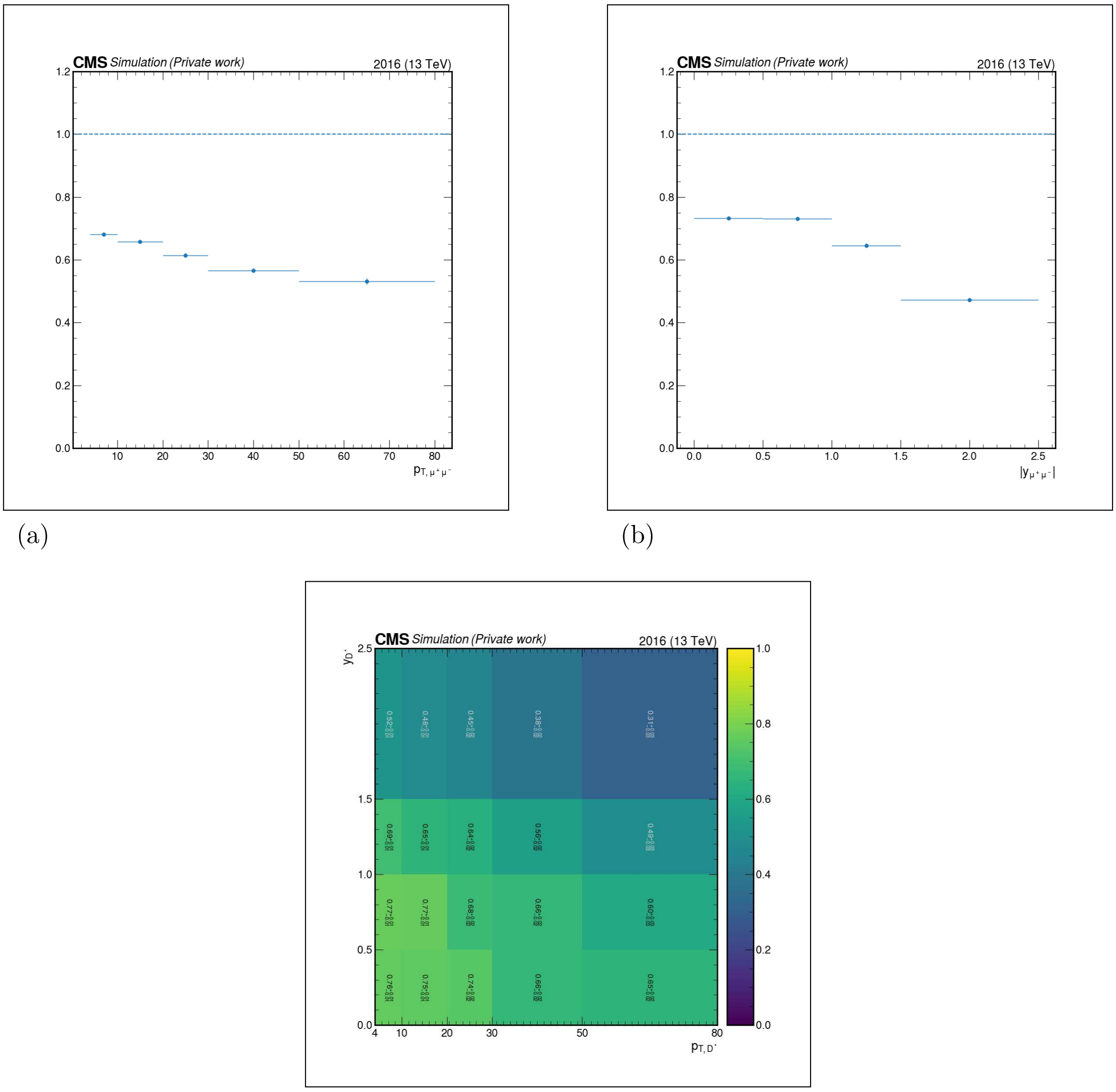

(a)

(b)

(c)

Legend: D* acceptance extracted from the 2016 MC data sample. The acceptance is given with respect to the reconstructed D* p_T in (a), y in (b), and in both p_T and y in (c). In (a) and (b), the horizontal dashed line is set to the upper limit of the acceptance, one.

Source: The author, 2023.

Figure 77 - Υ selection cut efficiency of the selected associated Υ+ D* extracted from 2016 MC sample.

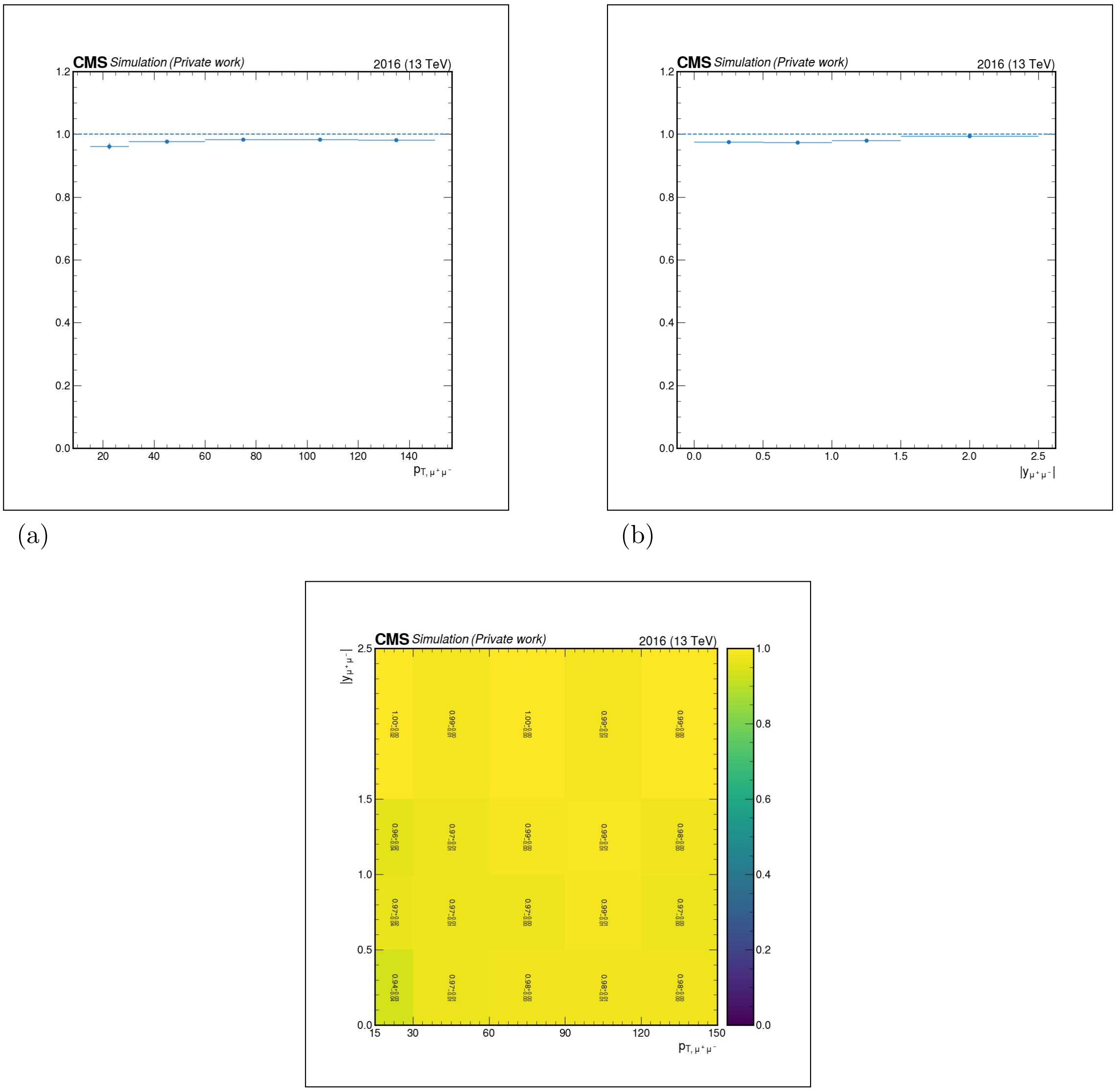

(a)

(b)

(c)

Legend: Υ selection cut efficiency extracted from the 2016 MC data sample. This efficiency is given with respect to the dimuon p_T in (a), y in (b), and in both p_T and y in (c). In (a) and (b), the horizontal dashed line is set to the upper limit of the efficiency.

Source: The author, 2023.

Figure 78 - D* selection cut efficiency of the selected associated Υ+ D* extracted from 2016 MC sample.

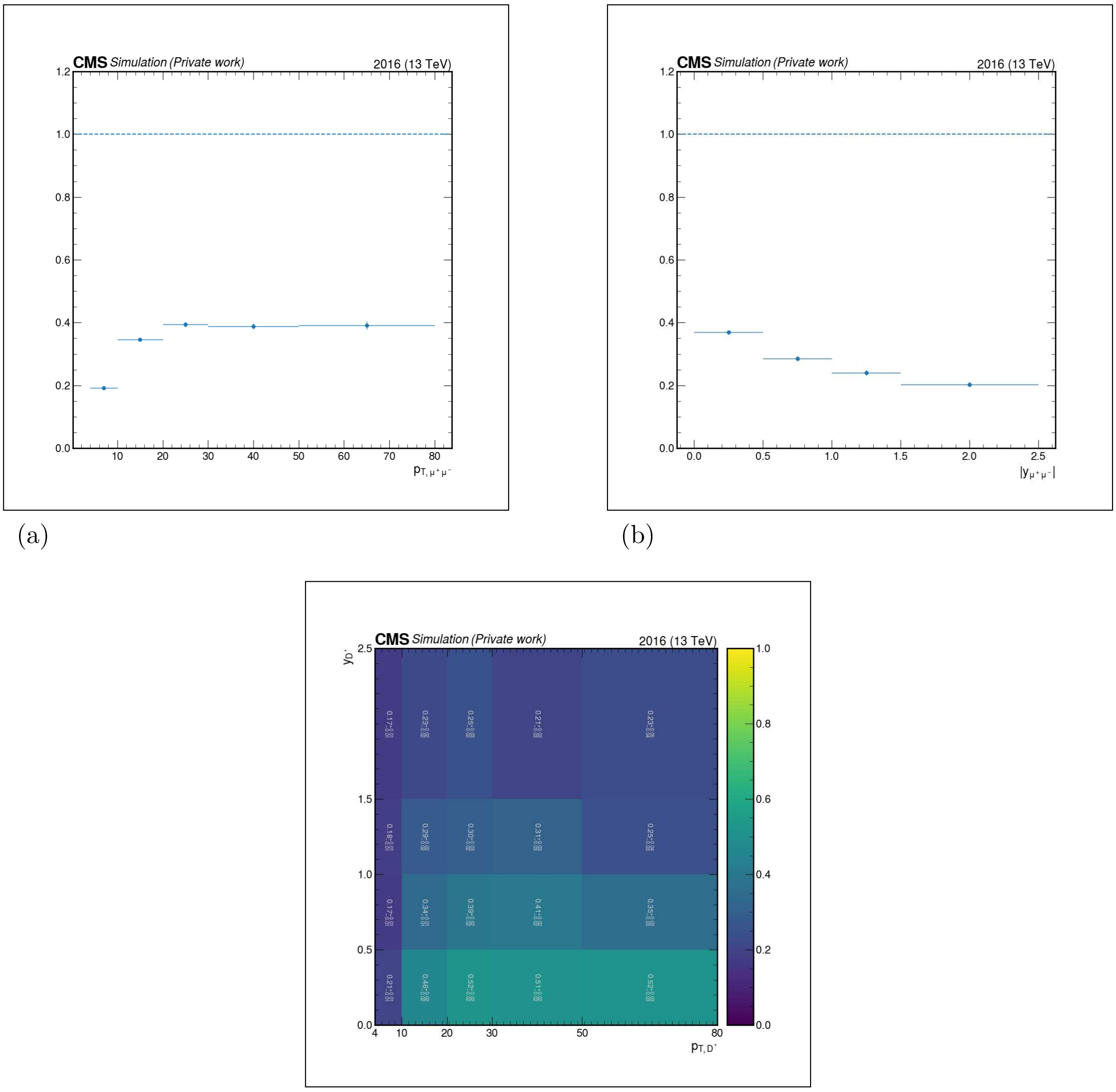

(a) (b)

(c)

Legend: D* selection cut efficiency extracted from the 2016 MC data sample. This efficiency is given with respect to the D* p_T in (a), y in (b), and in both p_T and y in (c). In (a) and (b), the horizontal dashed line is set to the upper limit of the efficiency.

Source: The author, 2023.

Figure 79 - Trigger efficiency of the selected Υ extracted from 2016 MC sample.

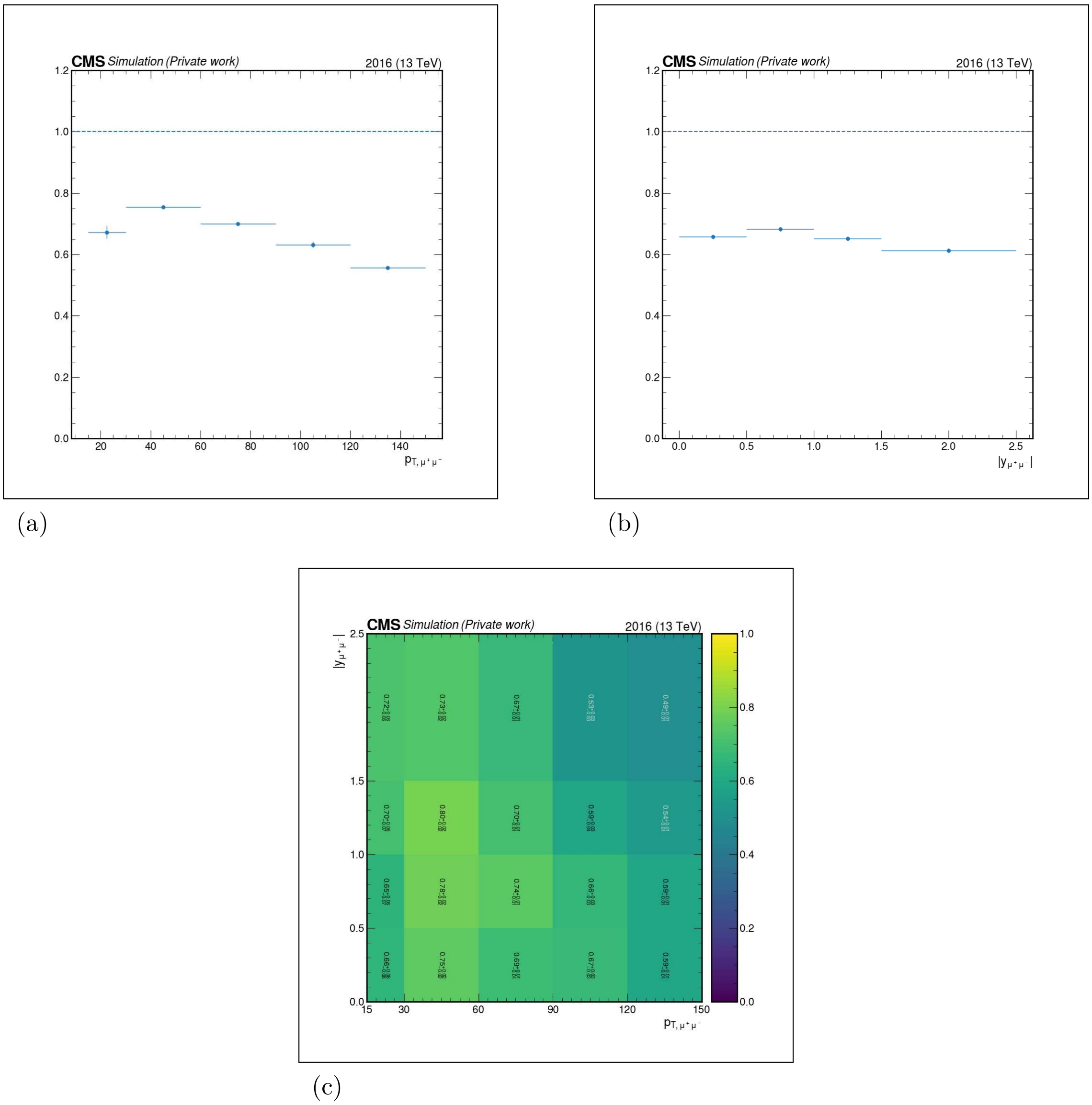

(a)

(b)

(c)

Legend: Trigger efficiency extracted from the 2016 MC data sample. This efficiency is given with respect to the dimuon p_T in (a), y in (b), and in both p_T and y in (c). In (a) and (b), the horizontal dashed line is set to the upper limit of the efficiency.

Source: The author, 2023.

Figure 80 - Association efficiency of the selected associated Υ+ D* extracted from 2016 MC sample.

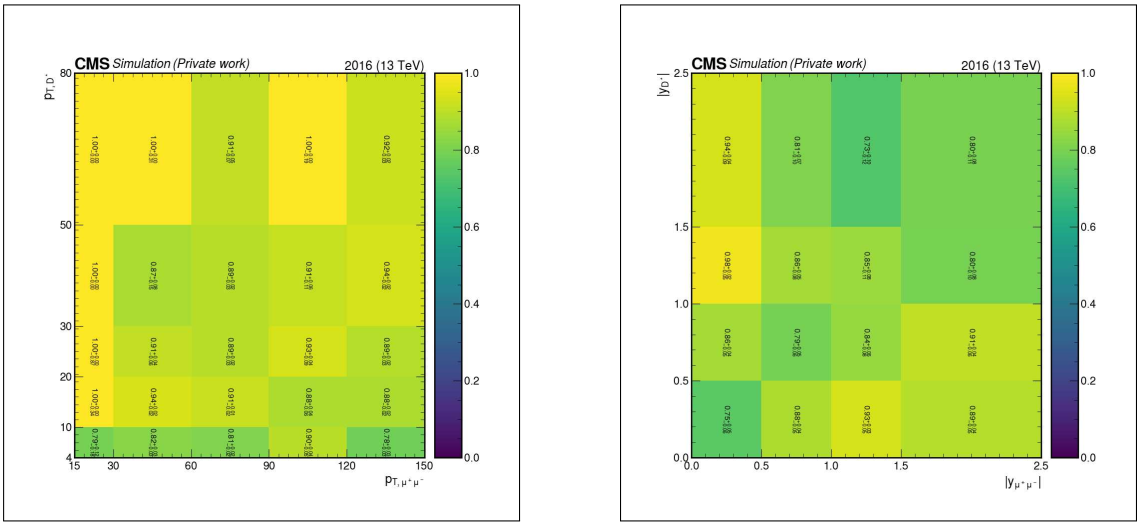

(a) (b)

Legend: Association efficiency extracted from the 2016 MC data sample. The efficiency maps are given with respect to the dimuon and D* p_T in (a) and y in (b).

Source: The author, 2023.

A.3 Efficiencies for sample 2017

Figure 81 - Υ acceptance of the selected associated Υ+ D* extracted from 2017 MC sample.

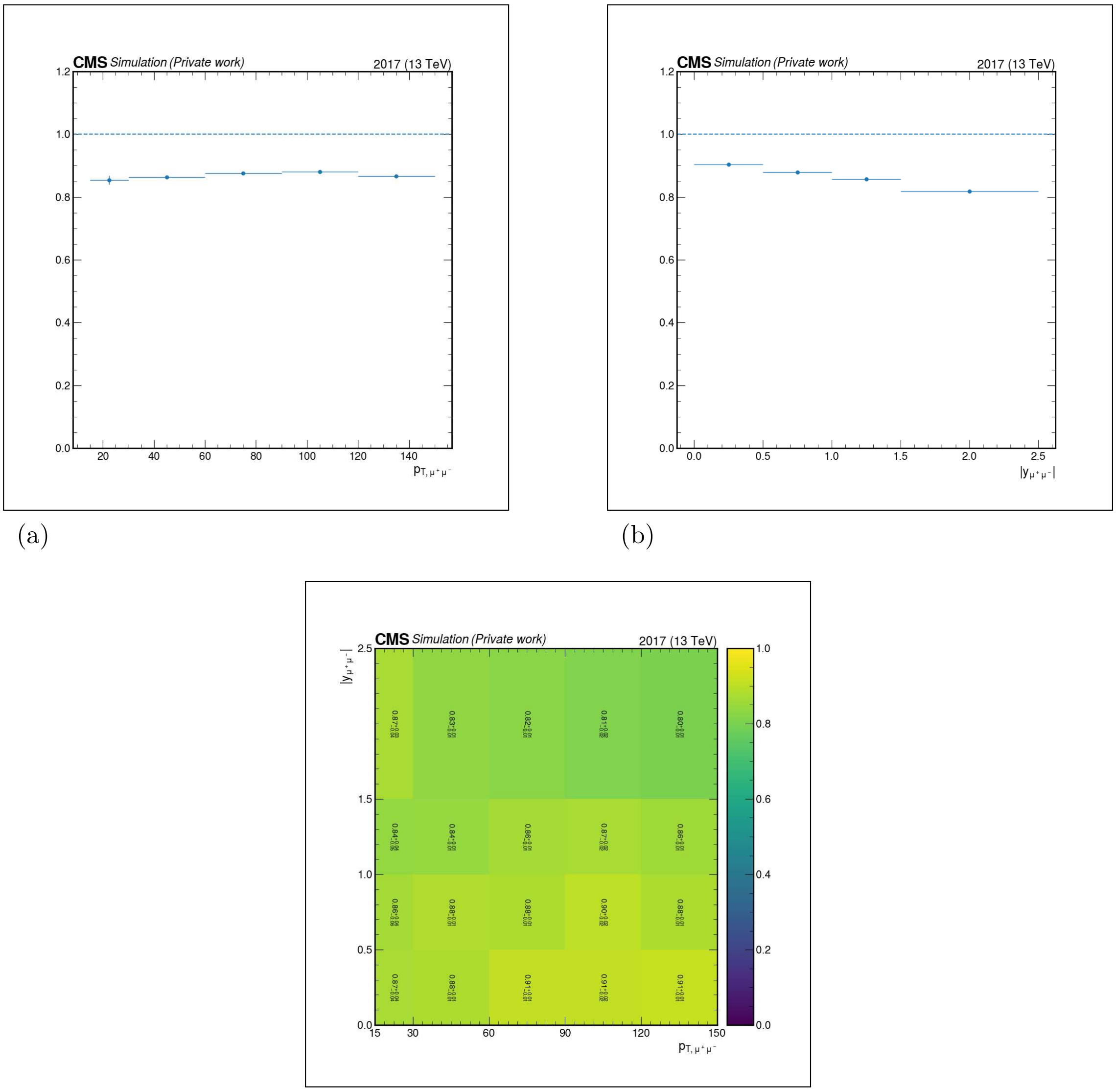

(a) (b)

(c)

Legend: Υ acceptance extracted from the 2017 MC data sample. The acceptance is given with respect to the dimuon p_T in (a), y in (b), and in both p_T and y in (c). In (a) and (b), the horizontal dashed line is set to the upper limit of the acceptance, one.

Source: The author, 2023.

Figure 82 - D* acceptance of the selected associated Υ+ D* extracted from 2017 MC sample.

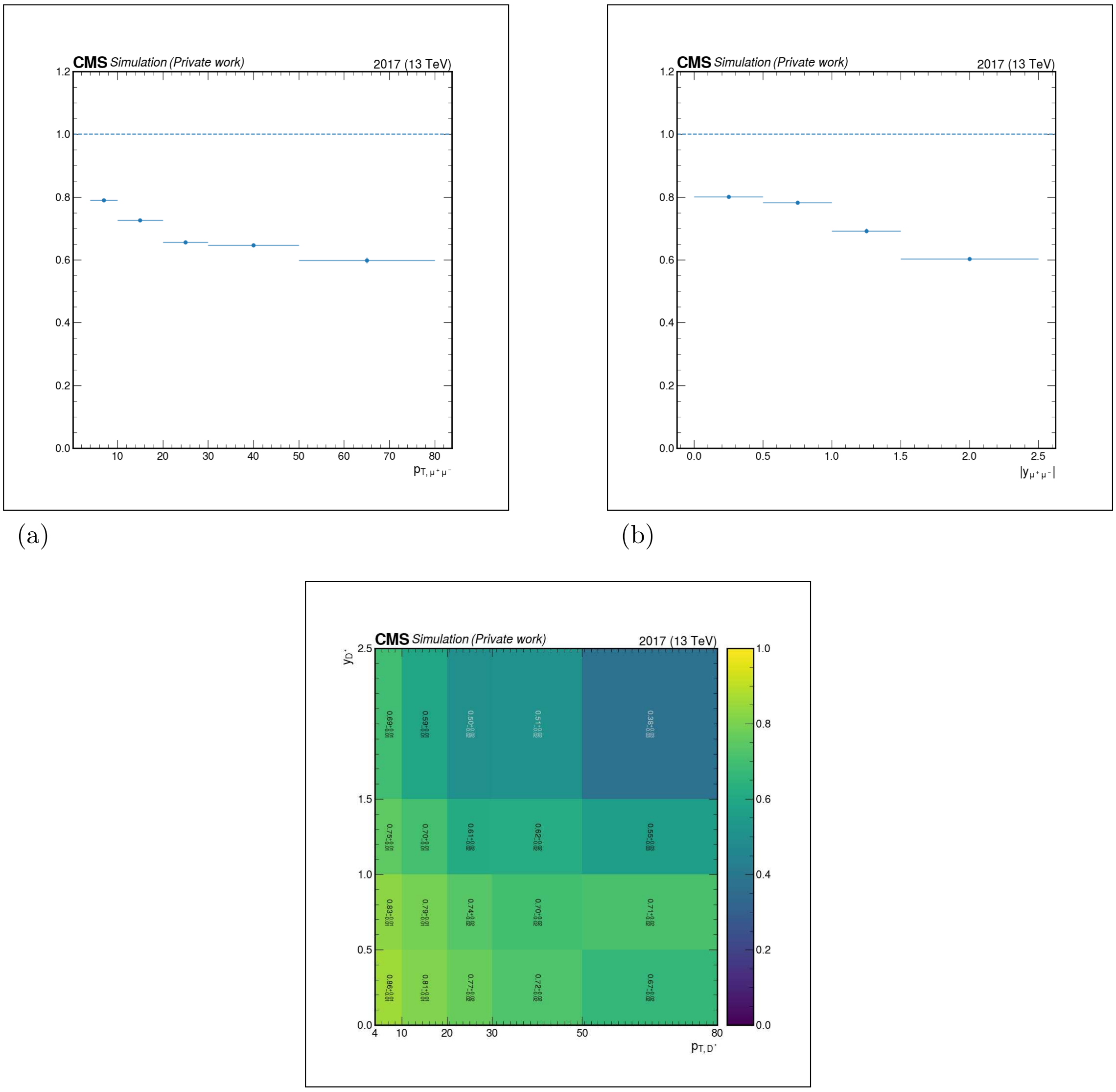

(a)

(b)

(c)

Legend: D* acceptance extracted from the 2017 MC data sample. The acceptance is given with respect to the reconstructed D* p_T in (a), y in (b), and in both p_T and y in (c). In (a) and (b), the horizontal dashed line is set to the upper limit of the acceptance, one.

Source: The author, 2023.

Figure 83 - Υ selection cut efficiency of the selected associated Υ+ D* extracted from 2017 MC sample.

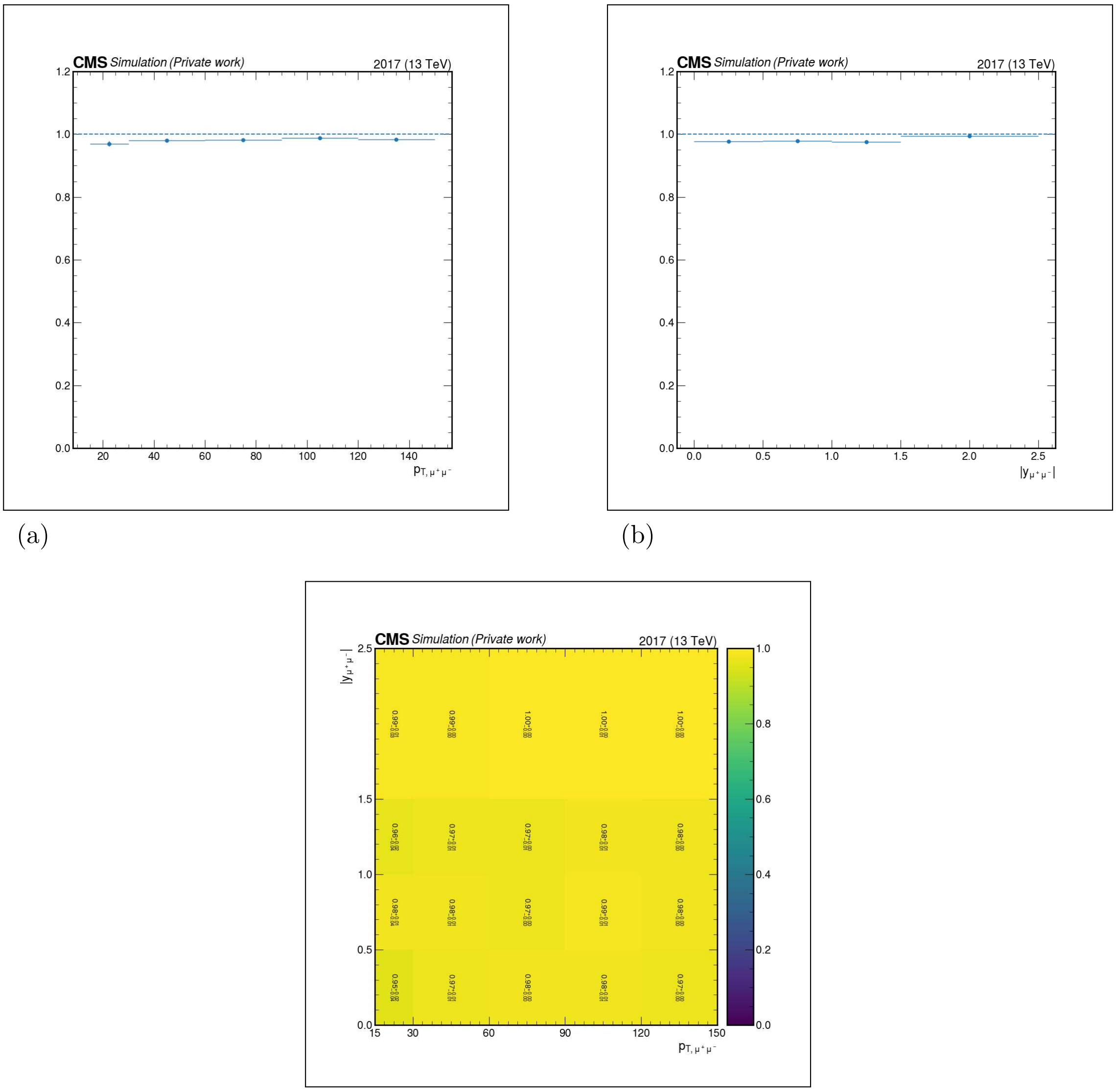

(a)

(b)

(c)

Legend: Υ selection cut efficiency extracted from the 2017 MC data sample. This efficiency is given with respect to the dimuon p_T in (a), y in (b), and in both p_T and y in (c). In (a) and (b), the horizontal dashed line is set to the upper limit of the efficiency.

Source: The author, 2023.

Figure 84 - D* selection cut efficiency of the selected associated Υ+ D* extracted from 2017 MC sample.

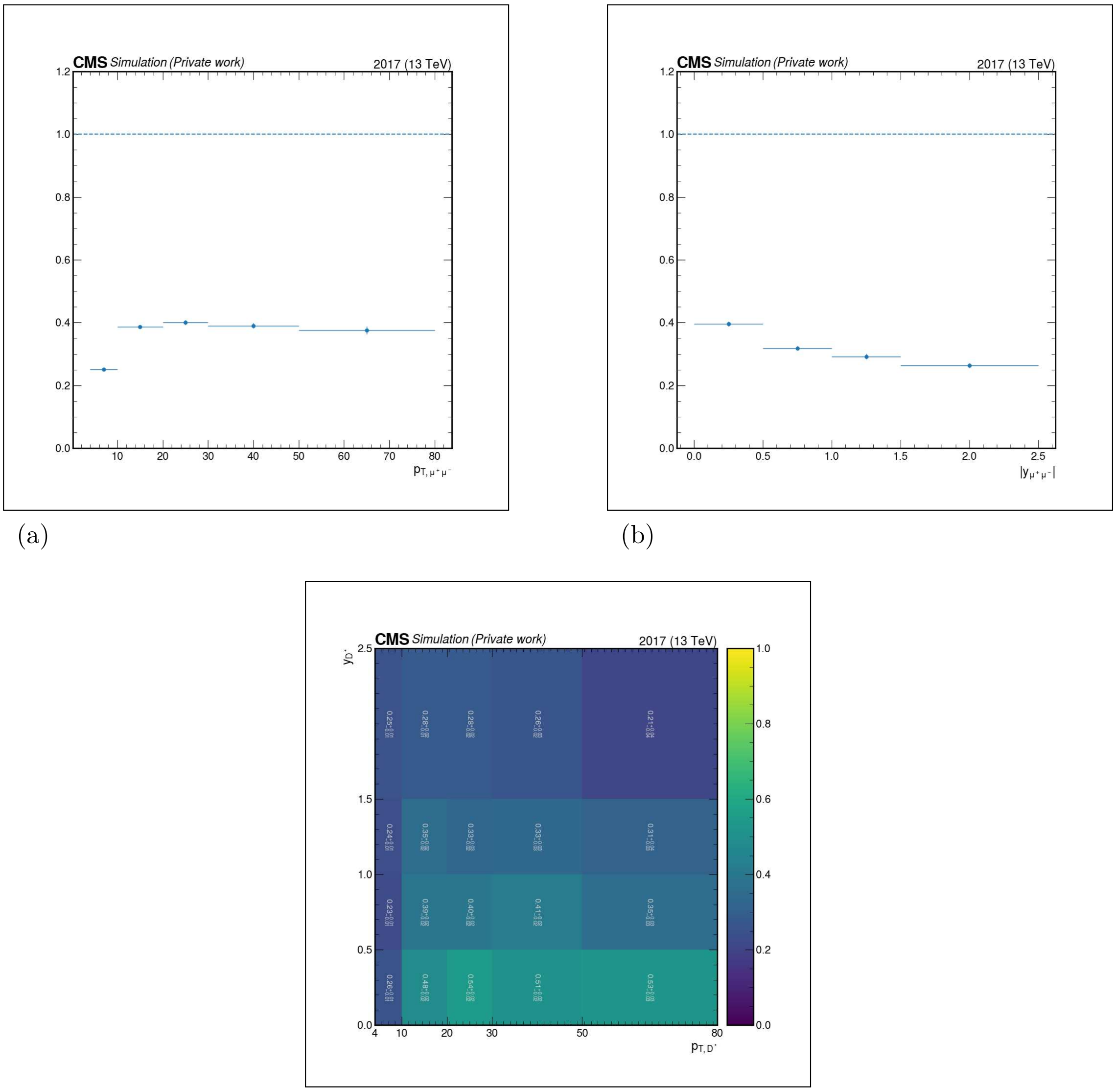

(a)

(b)

(c)

Legend: D* selection cut efficiency extracted from the 2017 MC data sample. This efficiency is given with respect to the D* p_T in (a), y in (b), and in both p_T and y in (c). In (a) and (b), the horizontal dashed line is set to the upper limit of the efficiency.

Source: The author, 2023.

Figure 85 - Trigger efficiency of the selected Υ extracted from 2017 MC sample.

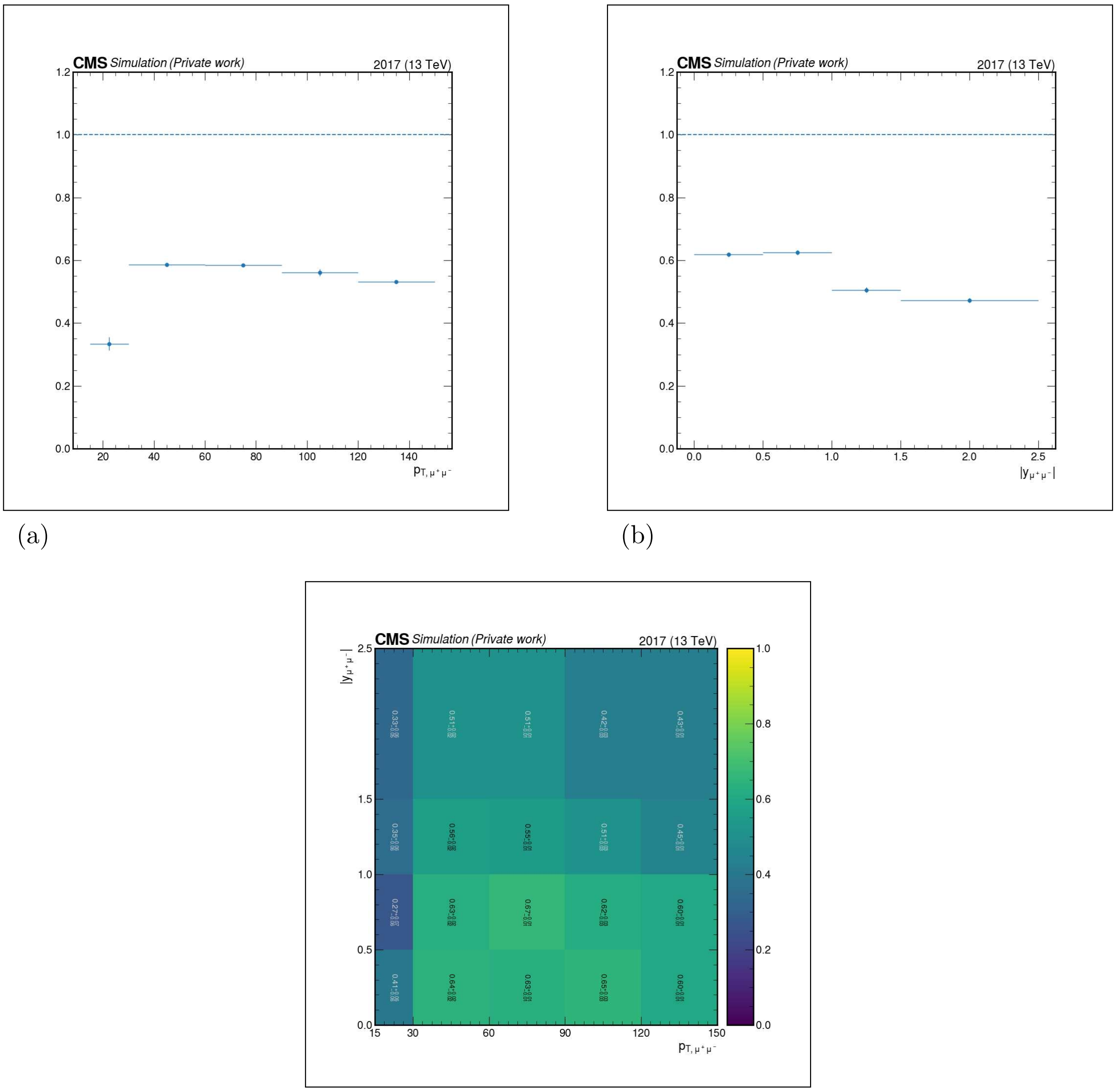

(a)

(b)

(c)

Legend: Trigger efficiency extracted from the 2017 MC data sample. This efficiency is given with respect to the dimuon p_T in (a), y in (b), and in both p_T and y in (c). In (a) and (b), the horizontal dashed line is set to the upper limit of the efficiency.

Source: The author, 2023.

Figure 86 - Association efficiency of the selected associated Υ+ D* extracted from 2017 MC sample.

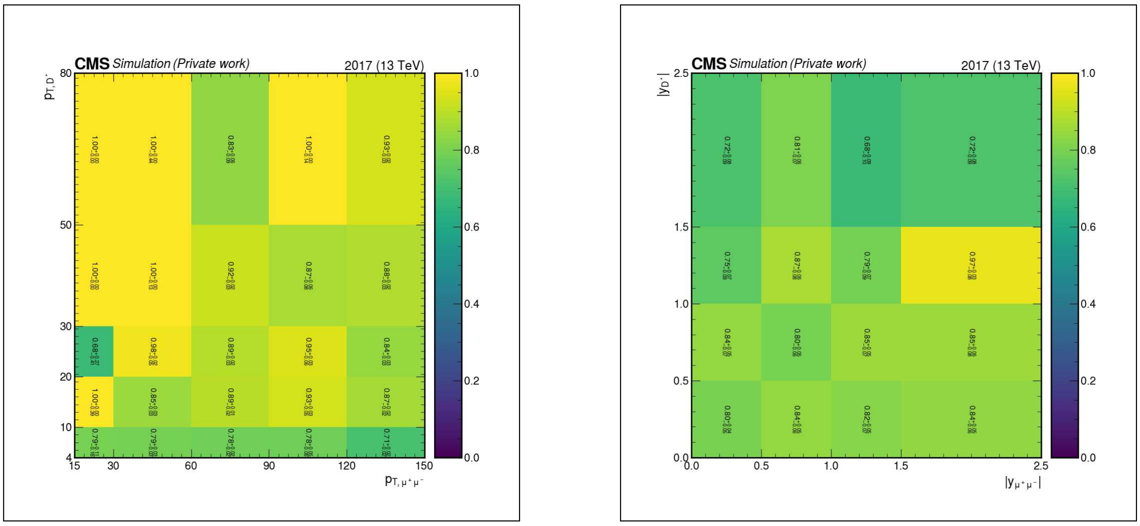

(a) (b)

Legend: Association efficiency extracted from the 2017 MC data sample. The efficiency maps are given with respect to the dimuon and D* p_T in (a) and y in (b).

Source: The author, 2023.

A.4 Efficiencies for sample 2018

The efficiency maps for the 2018 sample were presented in the Sec. 4.5.

APPENDIX B – Data and MC distributions

The plots presented in this section of the appendix were produced with a DPS MC data set with low statistics. A high statistics data set has recently become available and will be used to remake all the plots, which however was not possible in time for the conclusion of the document version to be handed out to the thesis defense panel.

B.1 **Distributions for sample 2016APV**

Figure 87 - Dimuon distributions for 2016APV sample

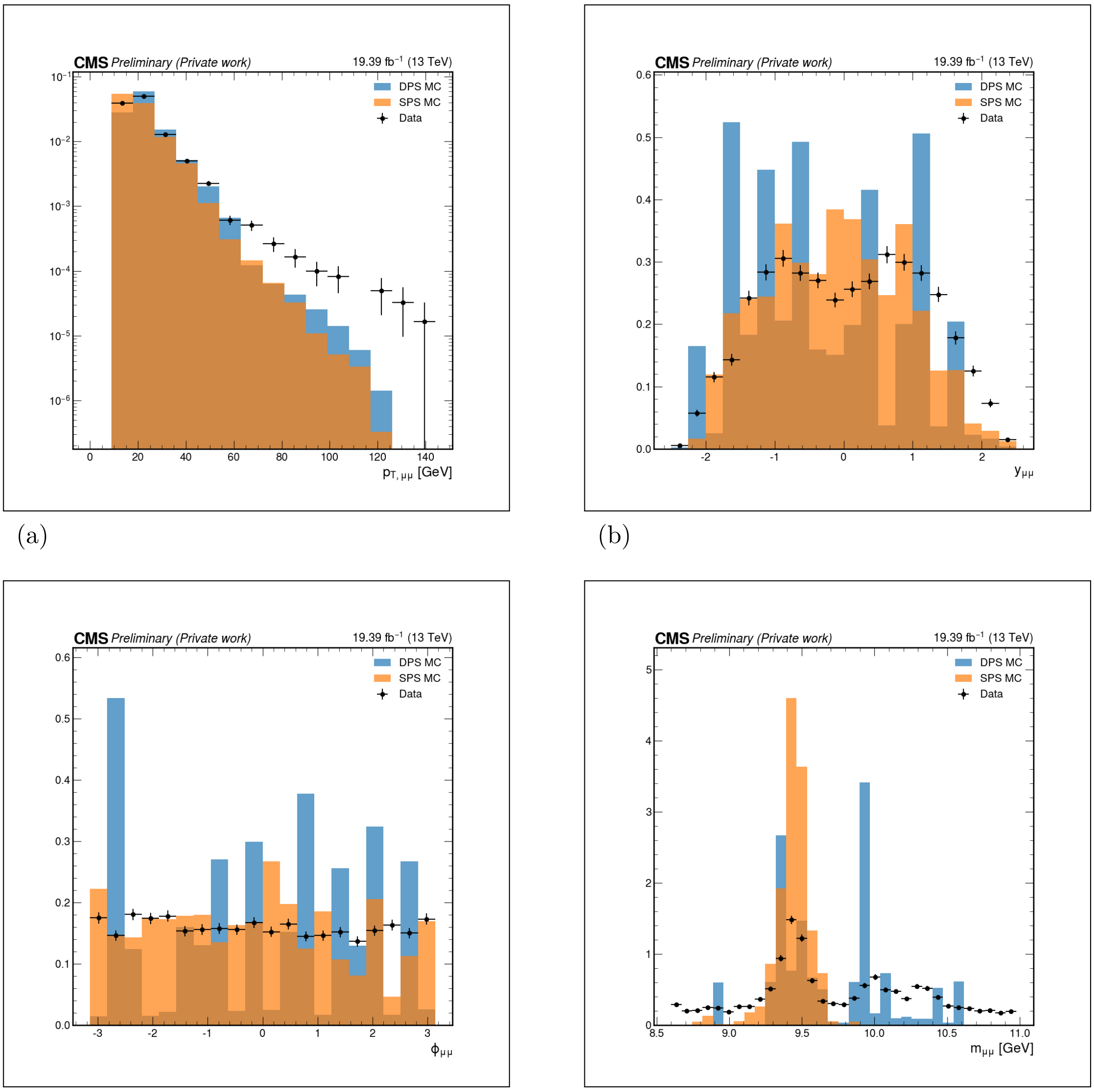

(a) (b) (c) (d)

Legend: p_T (a), y (b) and ϕ (c), invariant mass (d) distributions for the Υ candidate using the 2016APV data sample. The black dots represent the CMS Run 2 data, while the blue distribution represent the signal DPS MC simulation and the orange one the signal SPS MC simulation.

Source: The author, 2023.

Figure 88 - D* distributions for 2016APV sample

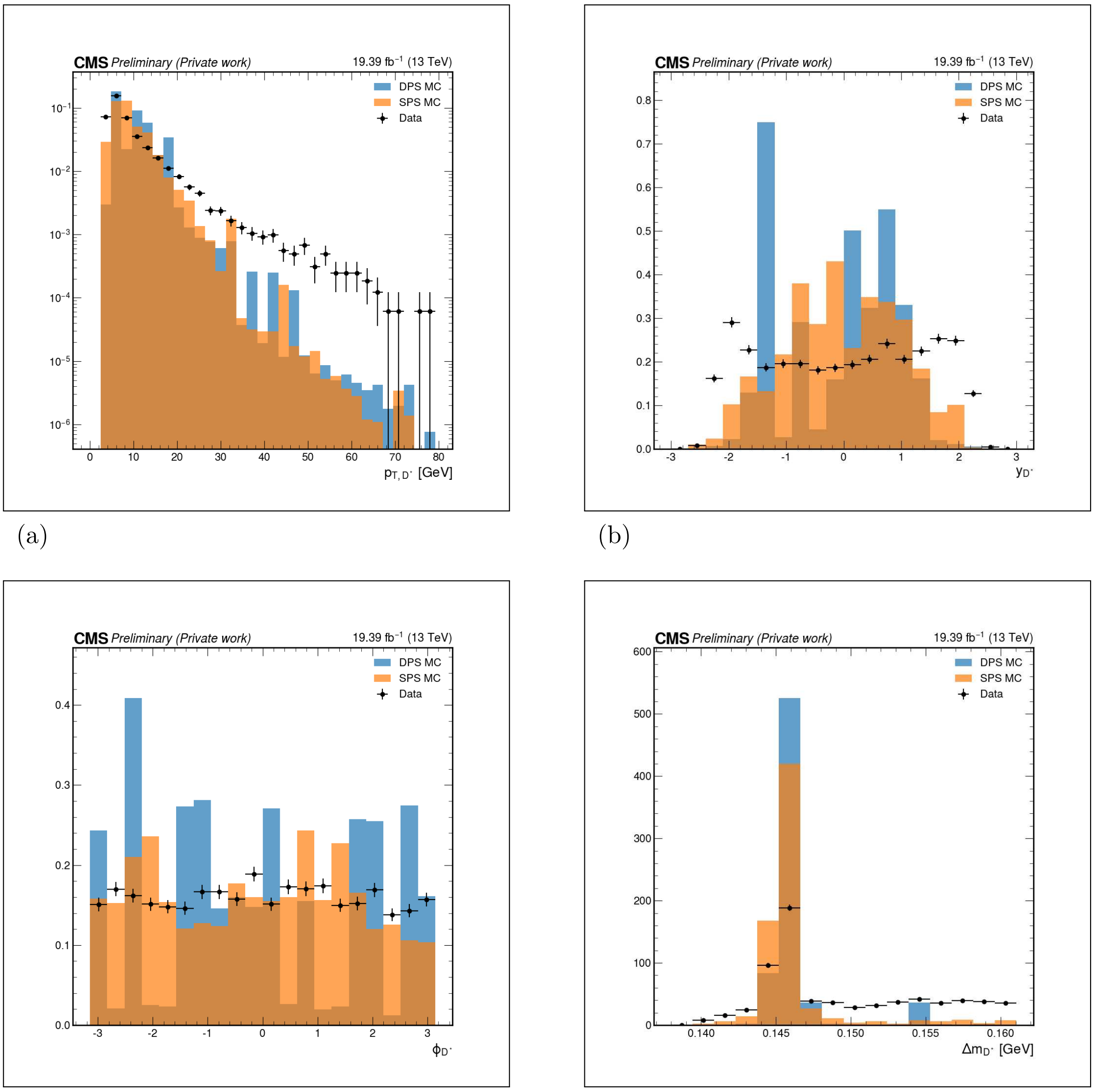

(a) (b) (c) (d)

Legend: p_T (a), y (b), ϕ (c) and Δm (d) distributions for the D* candidate using the 2016APV data sample. The black dots represent the CMS Run 2 data, while the blue distribution represent the signal DPS MC simulation and the orange one the signal SPS MC simulation.

Source: The author, 2023.

Figure 89 - D^0 distributions for 2016APV sample

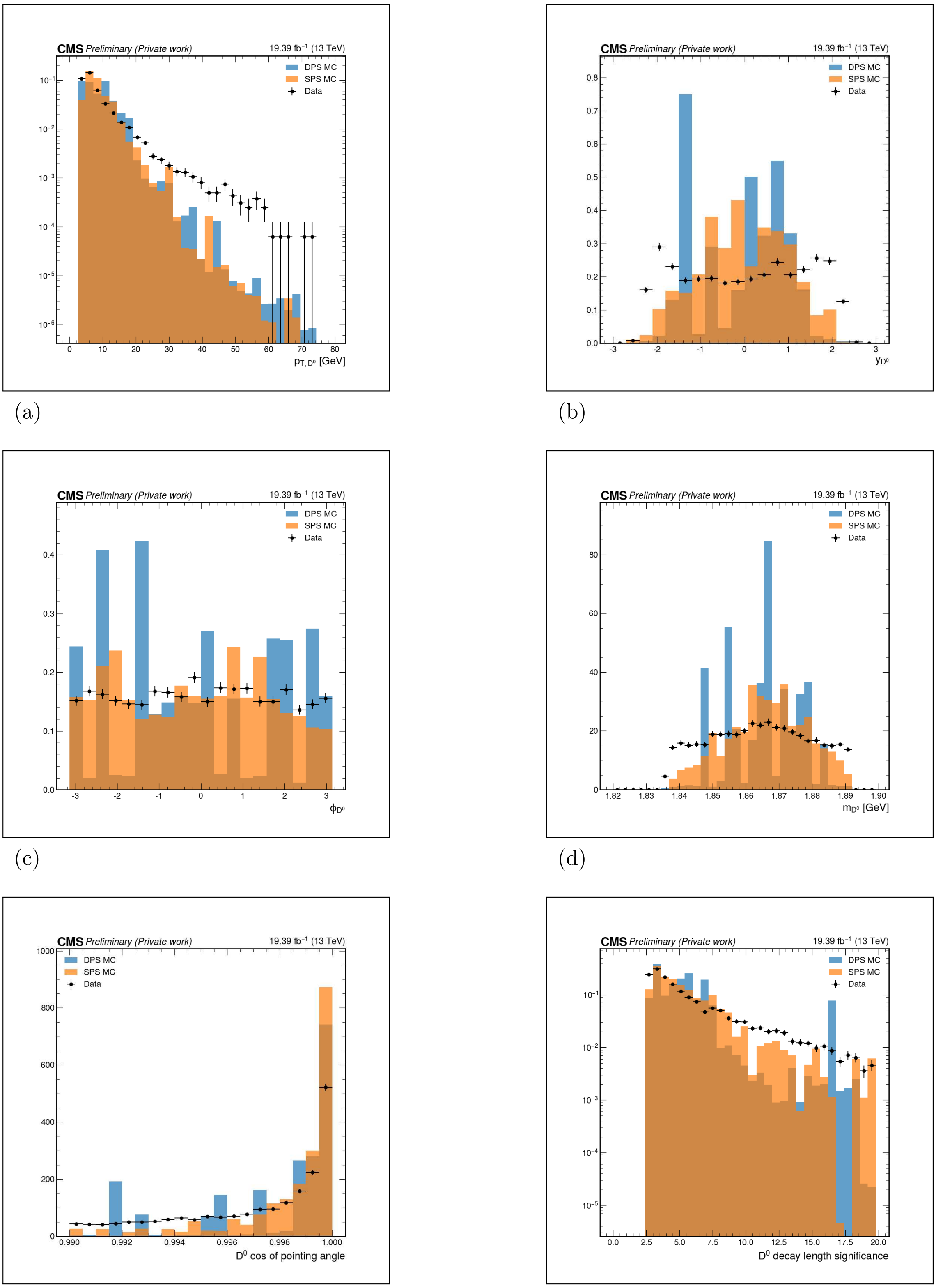

(a) (b)

(c) (d)

(e) (f)

Legend: p_T (a), η (b), ϕ (c), invariant mass (d), $\cos\alpha$ (e) and dl_{sig} (f) distributions for the D^0 using the 2016APV data sample. The black dots represent the CMS Run 2 data, while the blue distribution represent the signal DPS MC simulation and the orange one the signal SPS MC simulation.

Source: The author, 2023.

Figure 90 - Associated Υ and D* distributions for 2016APV sample

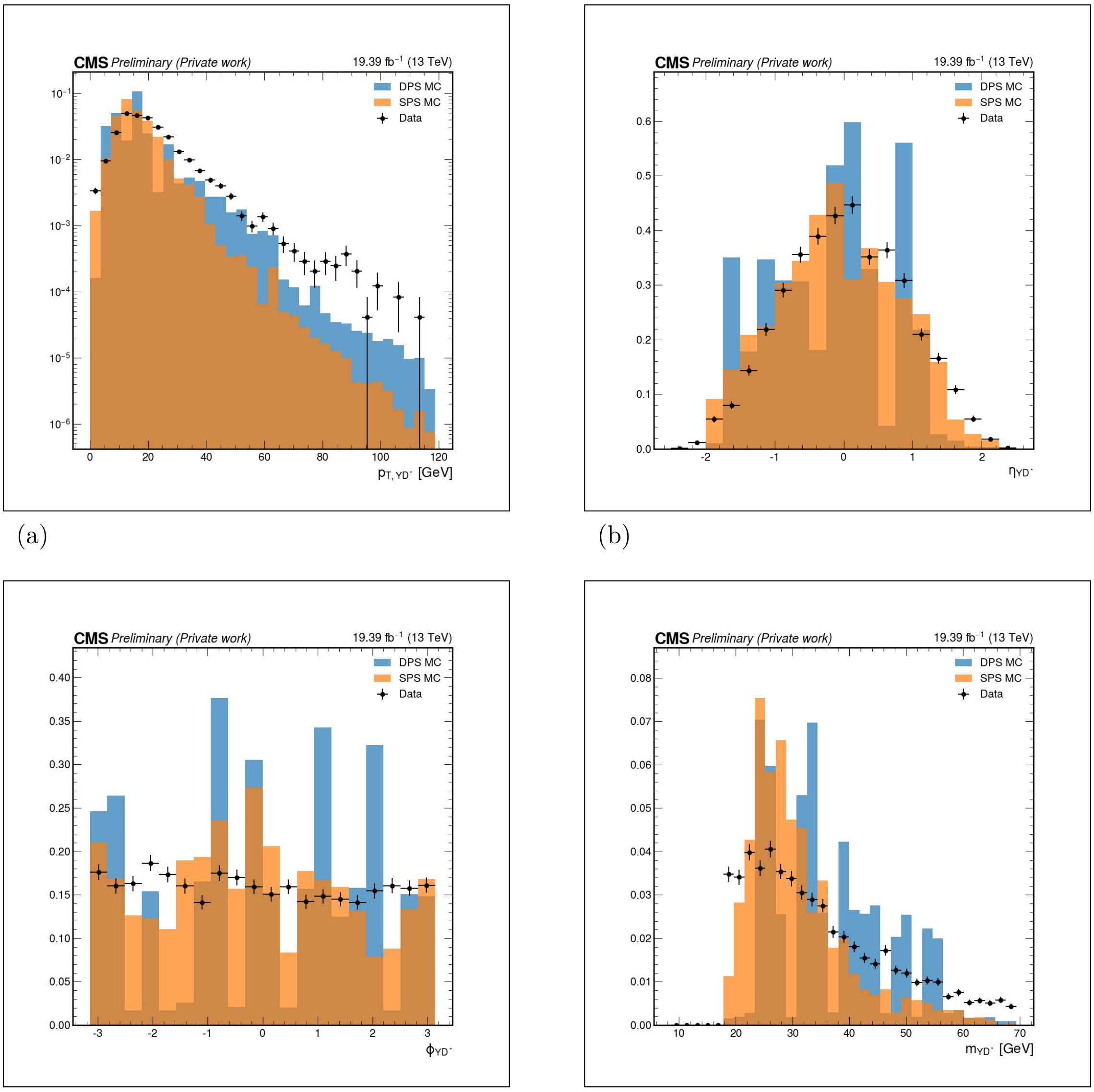

(a) (b)

(c) (d)

Legend: p$_T$ (a), y (b), ϕ (c) and invariant mass (d) distributions for the associated Υ and D* candidate using the 2016APV data sample. The black dots represent the CMS Run 2 data, while the blue distribution represent the signal DPS MC simulation and the orange one the signal SPS MC simulation.

Source: The author, 2023.

Figure 91 - Associated Υ and D* Δp_T, Δy and $\Delta\phi$ distributions for 2016APV sample

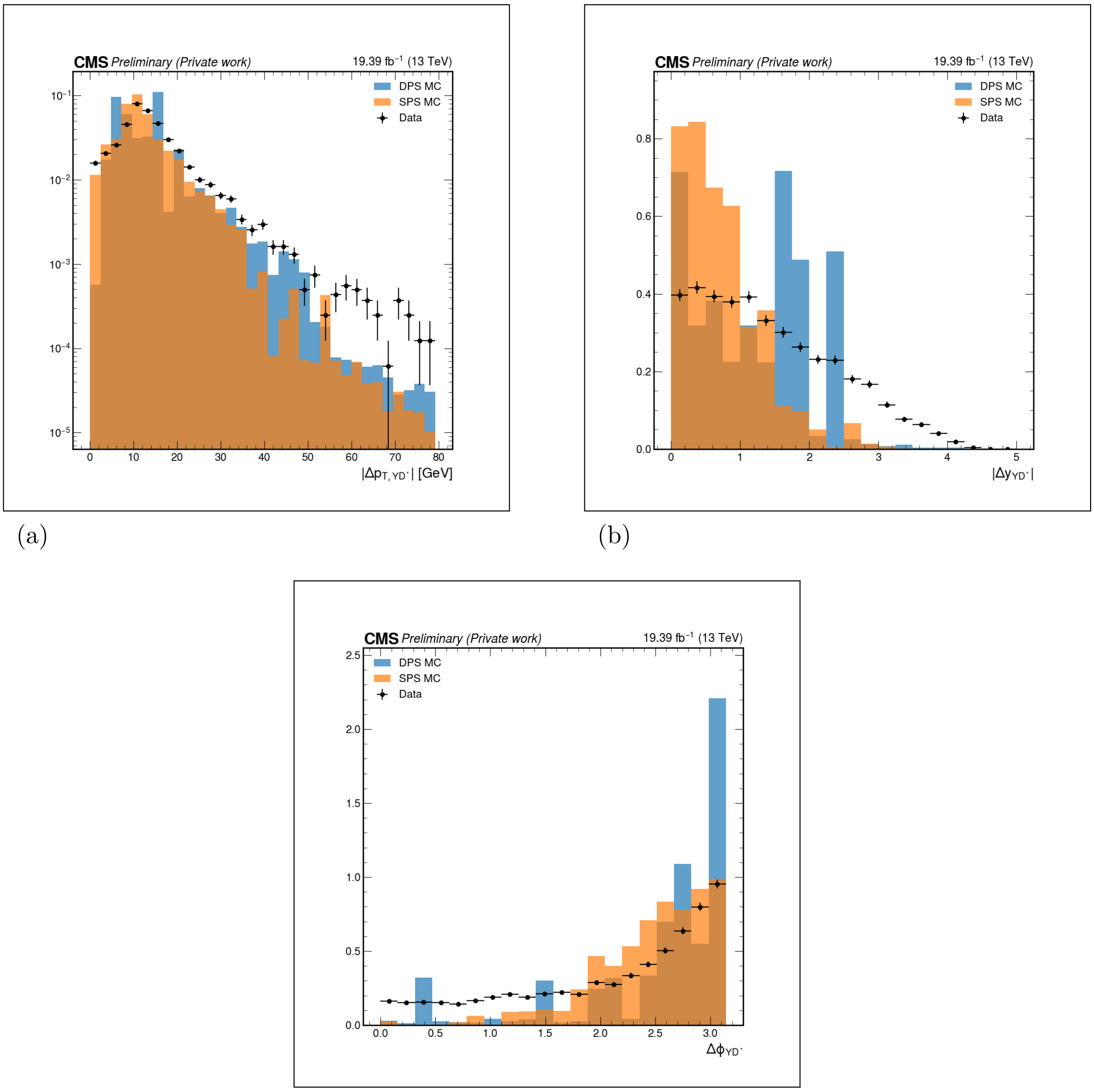

(a)

(b)

(c)

Legend: Δp_T (a), Δy (b) and $\Delta\phi$ (c) distributions for the assocuated Υ and D* candidate using the 2016APV data sample. The black dots represent the CMS Run 2 data, while the blue distribution represent the signal DPS MC simulation and the orange one the signal SPS MC simulation.

Source: The author, 2023.

B.2 Distributions for sample 2016

Figure 92 - Dimuon distributions for 2016 sample

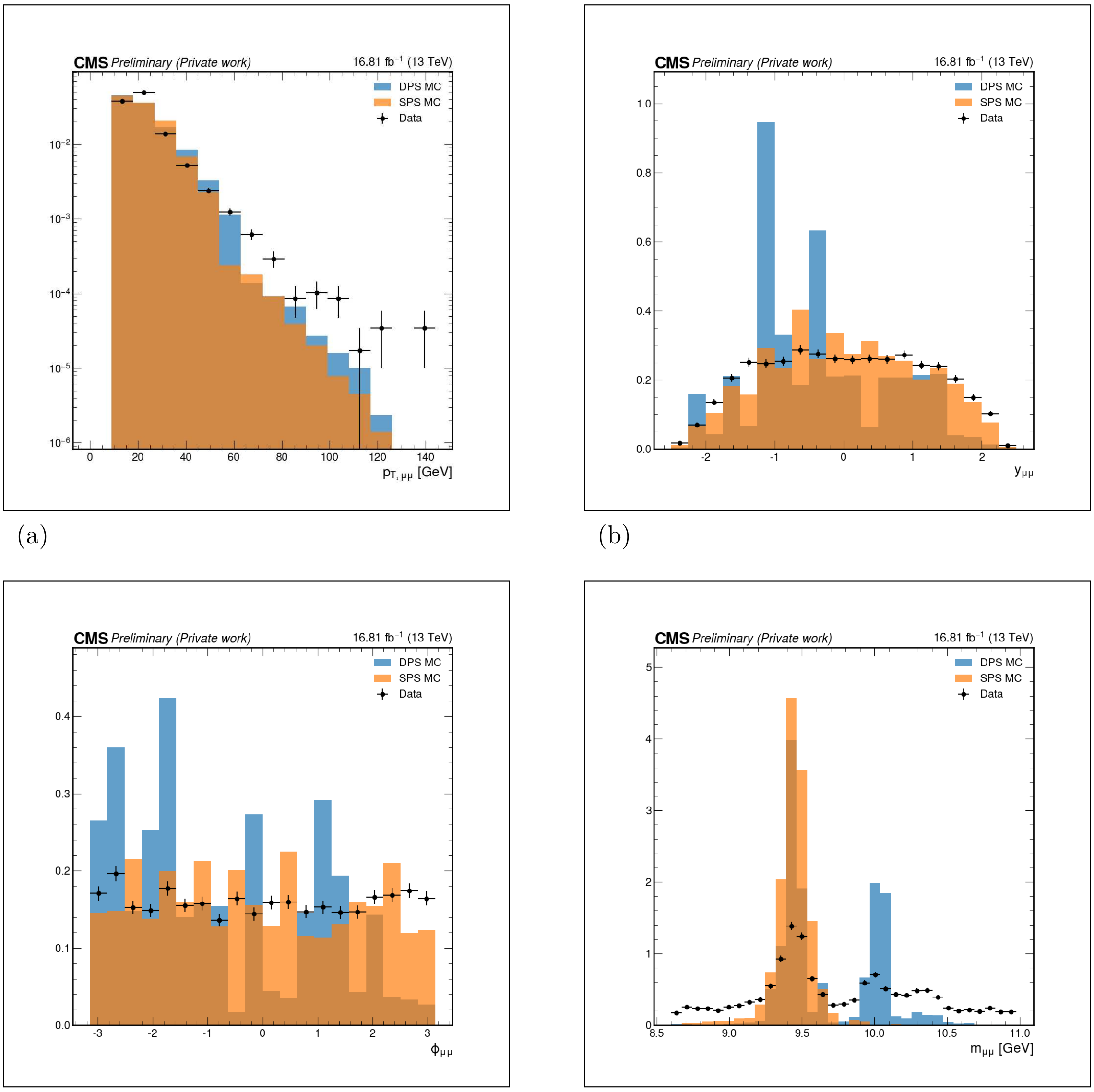

(a)

(b)

(c)

(d)

Legend: p_T (a), y (b) and ϕ (c), invariant mass (d) distributions for the Υ candidate using the 2016 data sample. The black dots represent the CMS Run 2 data, while the blue distribution represent the signal DPS MC simulation and the orange one the signal SPS MC simulation.

Source: The author, 2023.

Figure 93 - D* distributions for 2016 sample

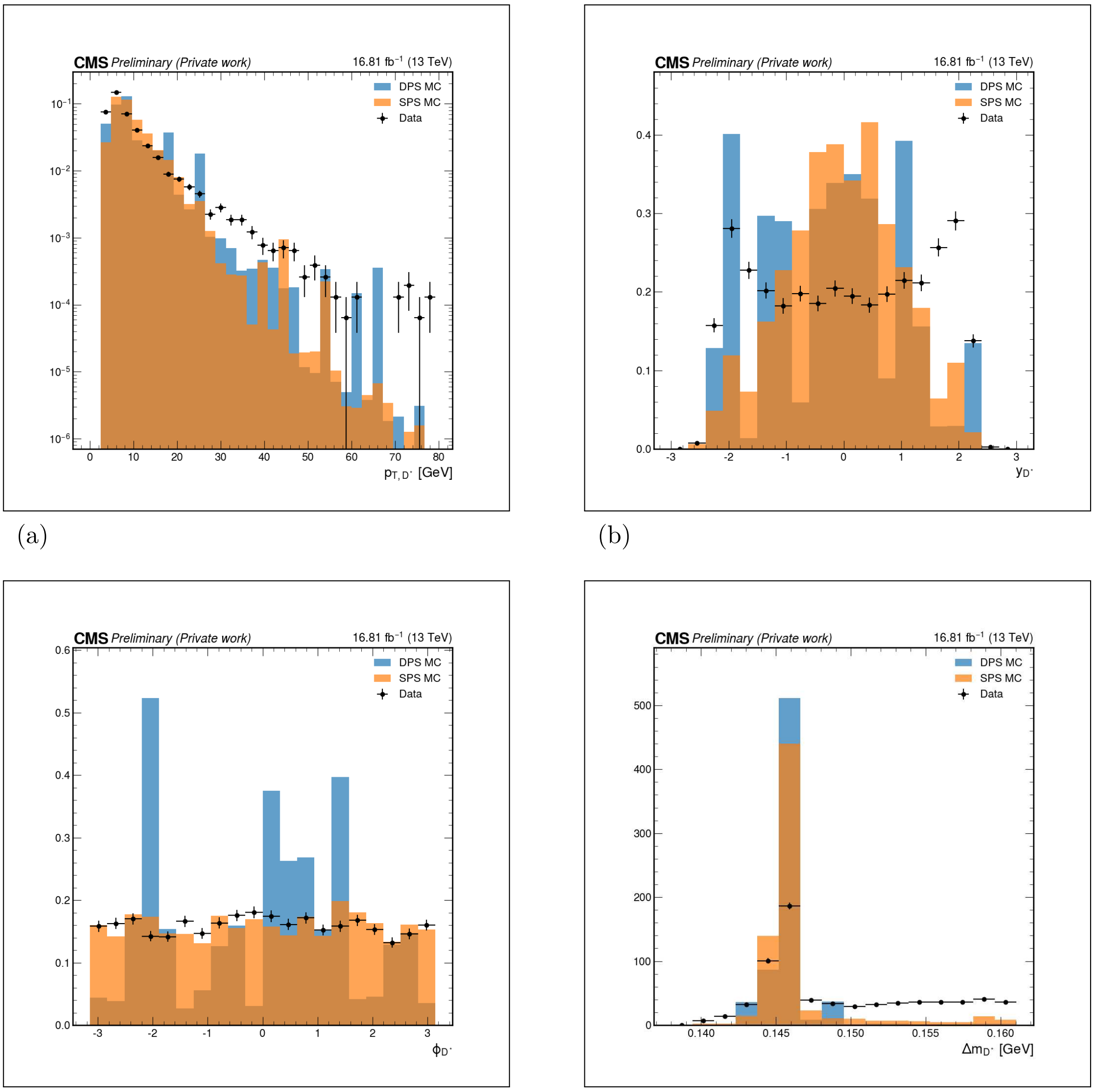

(a) (b) (c) (d)

Legend: p$_T$ (a), y (b), ϕ (c) and Δm (d) distributions for the D* candidate using the 2016 data sample. The black dots represent the CMS Run 2 data, while the blue distribution represent the signal DPS MC simulation and the orange one the signal SPS MC simulation.

Source: The author, 2023.

Figure 94 - D^0 distributions for 2016 sample

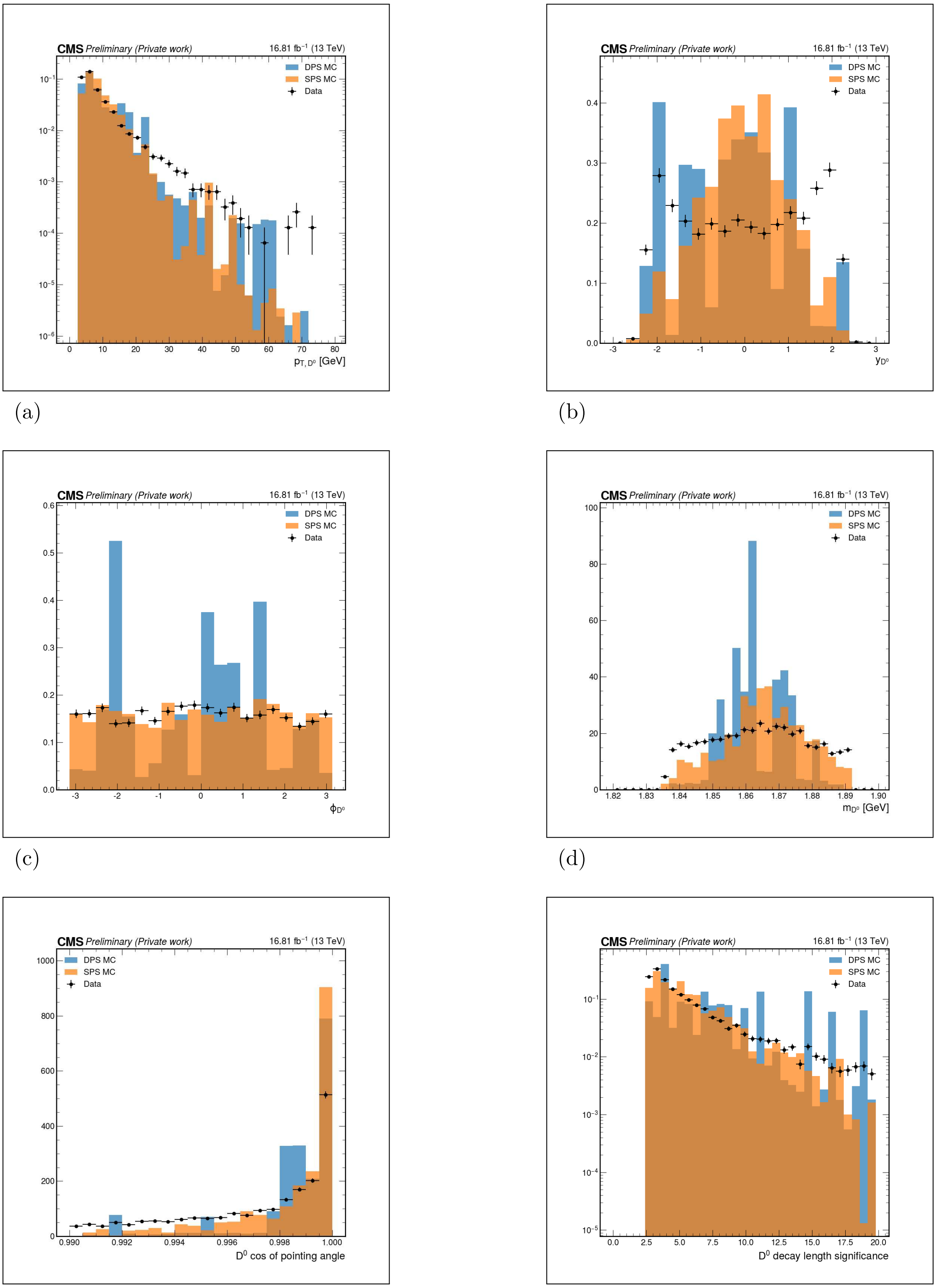

(a) (b) (c) (d) (e) (f)

Legend: p$_T$ (a), η (b), ϕ (c), invariant mass (d), $\cos\alpha$ (e) and dl$_{sig}$ (f) distributions for the D^0 using the 2016 data sample. The black dots represent the CMS Run 2 data, while the blue distribution represent the signal DPS MC simulation and the orange one the signal SPS MC simulation.

Source: The author, 2023.

Figure 95 - Associated Υ and D* distributions for 2016 sample

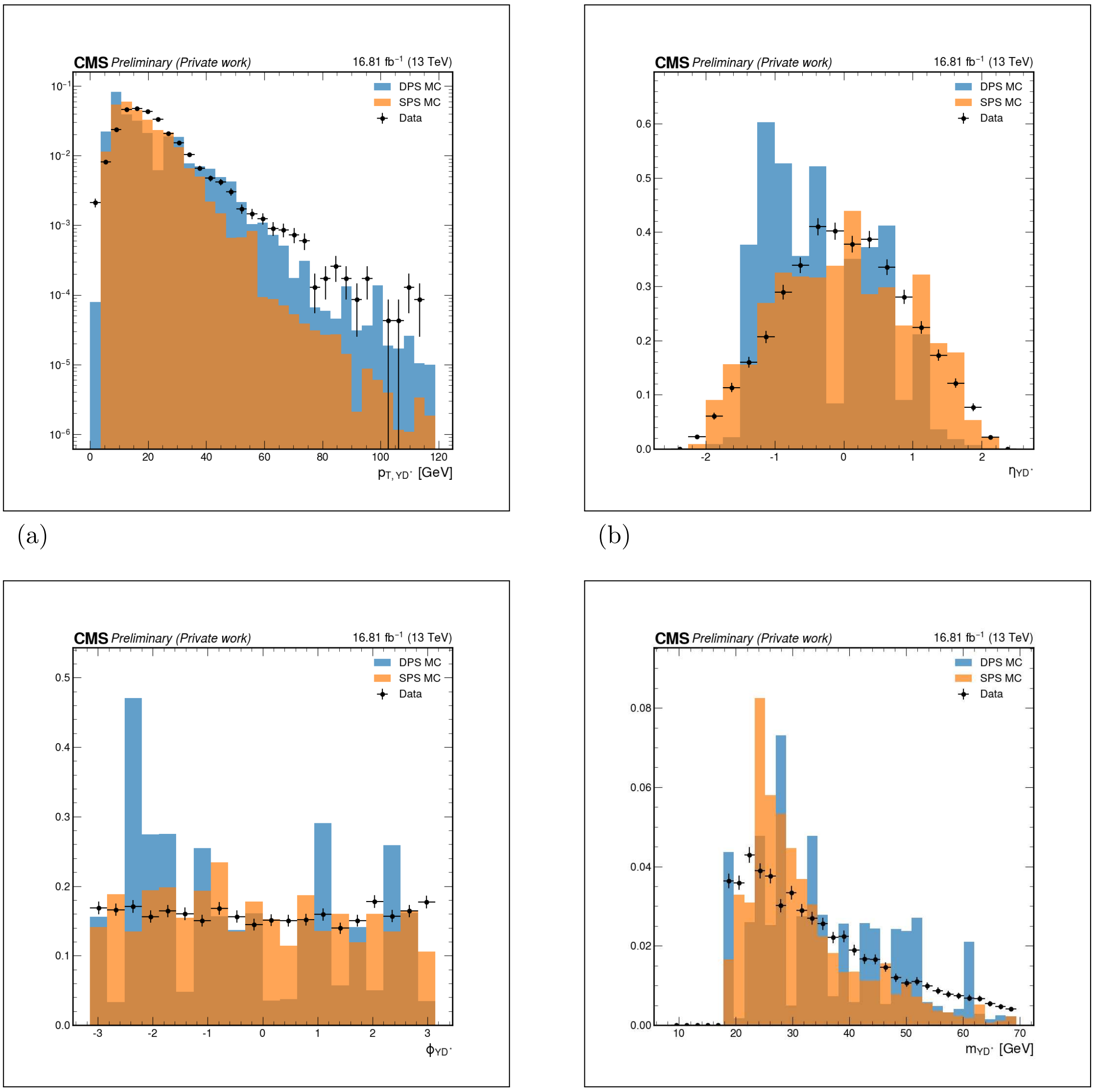

(a) (b)

(c) (d)

Legend: p$_T$ (a), y (b), ϕ (c) and invariant mass (d) distributions for the associated Υ and D* candidate using the 2016 data sample. The black dots represent the CMS Run 2 data, while the blue distribution represent the signal DPS MC simulation and the orange one the signal SPS MC simulation.

Source: The author, 2023.

Figure 96 - Associated Υ and D* Δp_T, Δy and $\Delta\phi$ distributions for 2016 sample

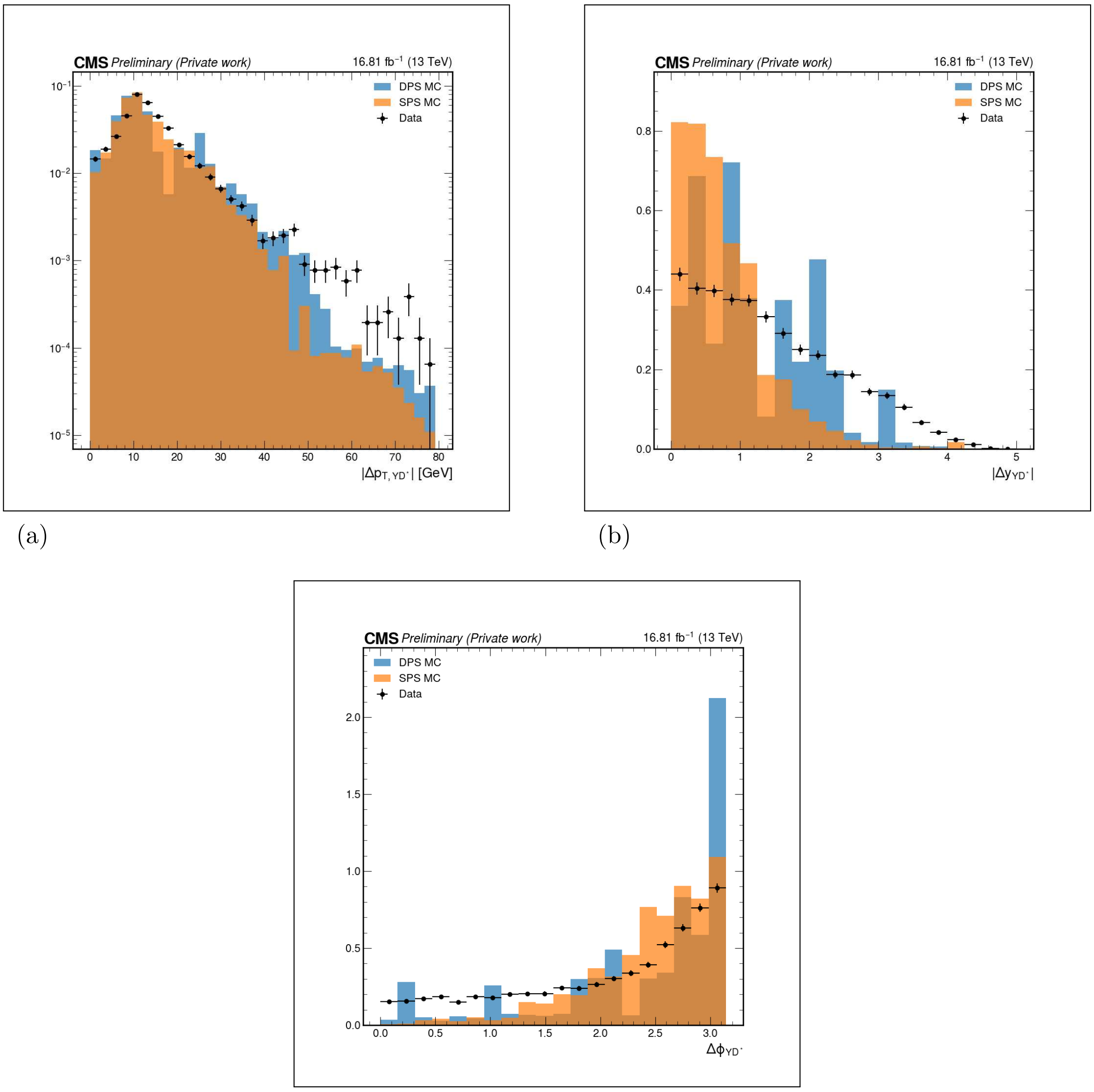

(a)

(b)

(c)

Legend: Δp_T (a), Δy (b) and $\Delta\phi$ (c) distributions for the assocuated Υ and D* candidate using the 2016 data sample. The black dots represent the CMS Run 2 data, while the blue distribution represent the signal DPS MC simulation and the orange one the signal SPS MC simulation.

Source: The author, 2023.

B.3 Distributions for sample 2017

The distributions for the 2017 sample were presented in the Sec. 4.3.4.

B.4 Distributions for sample 2018

Figure 97 - Dimuon distributions for 2018 sample

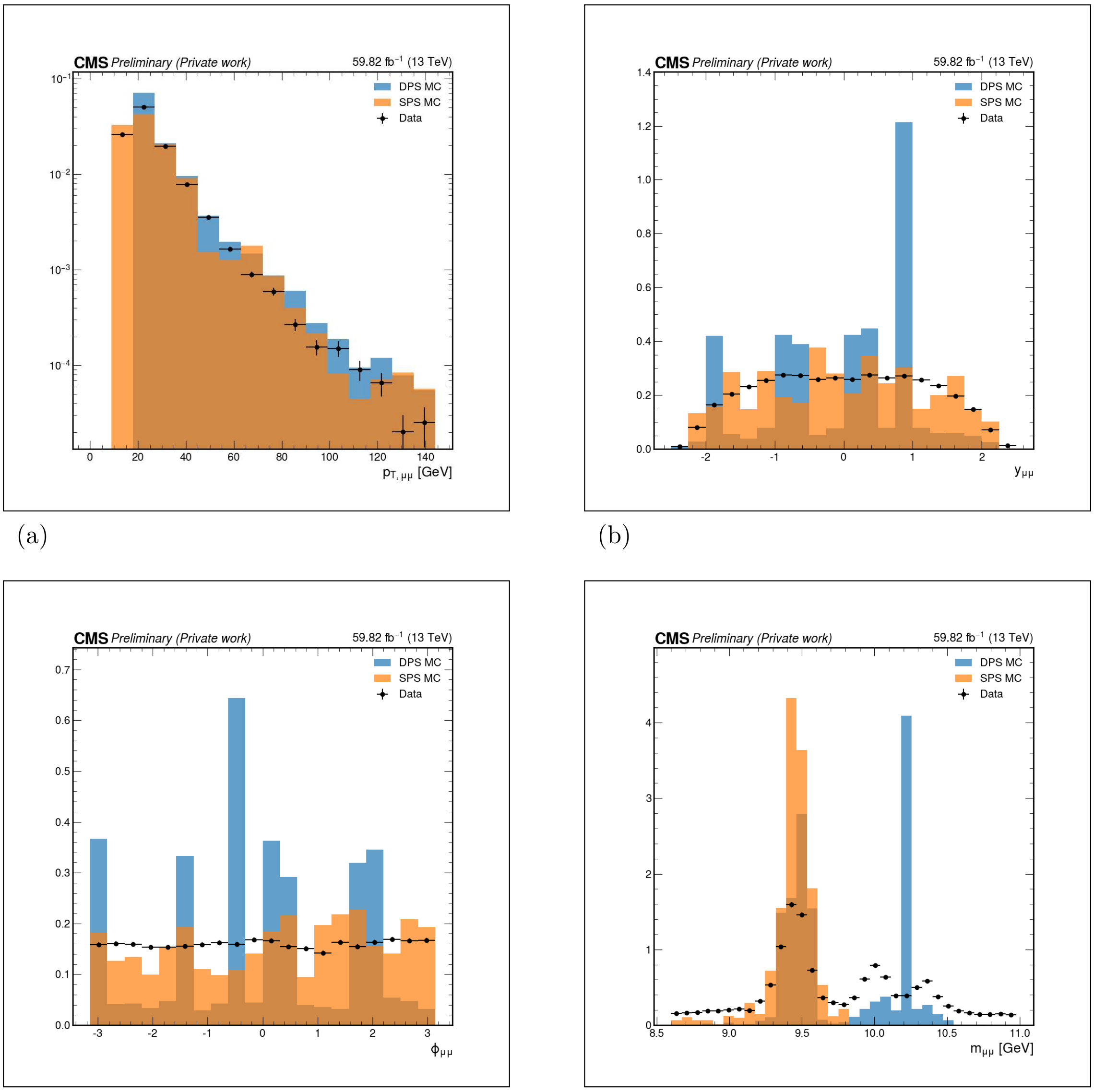

(a) (b) (c) (d)

Legend: p_T (a), y (b) and ϕ (c), invariant mass (d) distributions for the Υ candidate using the 2018 data sample. The black dots represent the CMS Run 2 data, while the blue distribution represent the signal DPS MC simulation and the orange one the signal SPS MC simulation.

Source: The author, 2023.

Figure 98 - D* distributions for 2018 sample

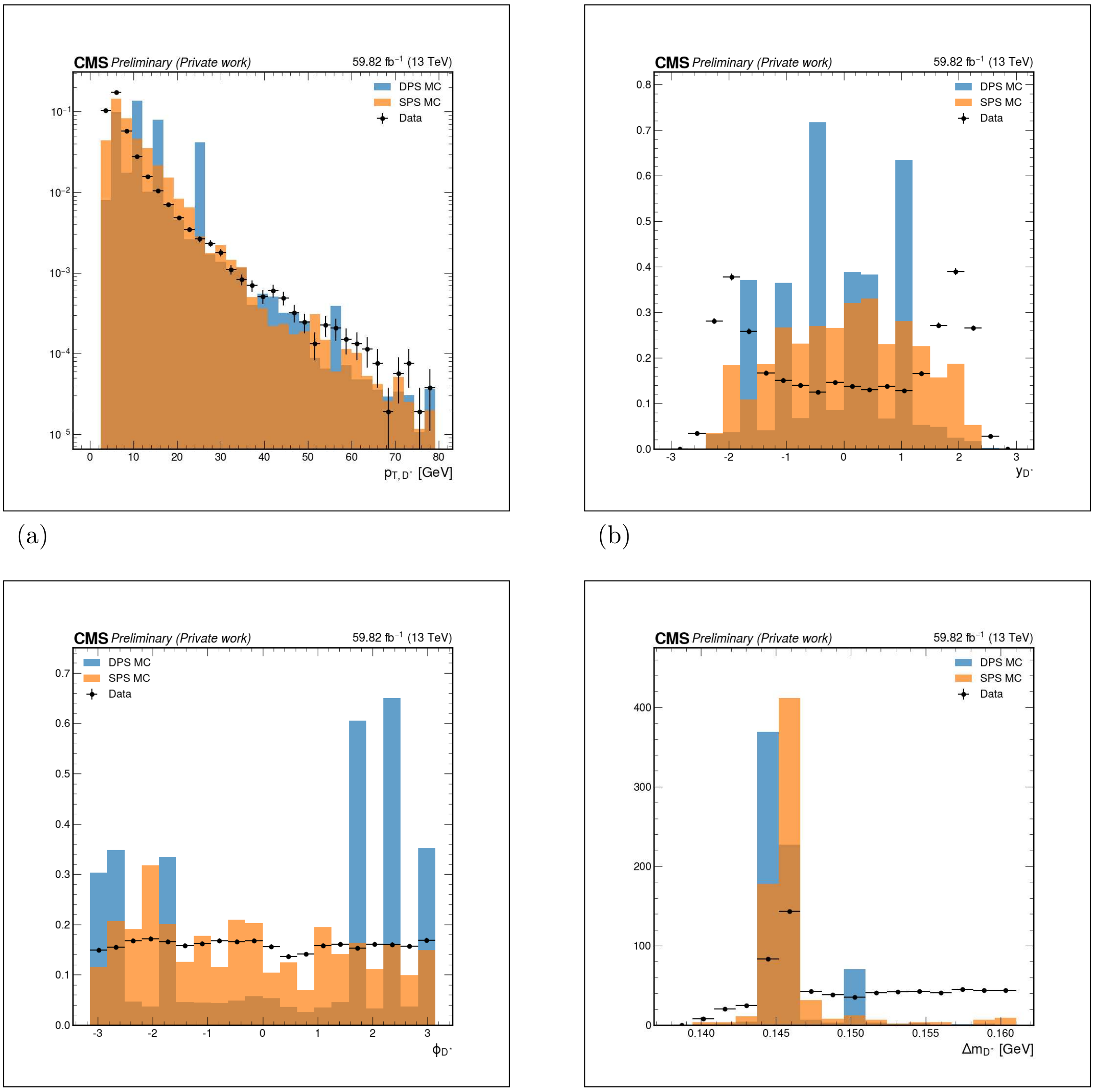

(a) (b)

(c) (d)

Legend: p_T (a), y (b), ϕ (c) and Δm (d) distributions for the D* candidate using the 2018 data sample. The black dots represent the CMS Run 2 data, while the blue distribution represent the signal DPS MC simulation and the orange one the signal SPS MC simulation.

Source: The author, 2023.

Figure 99 - D^0 distributions for 2018 sample

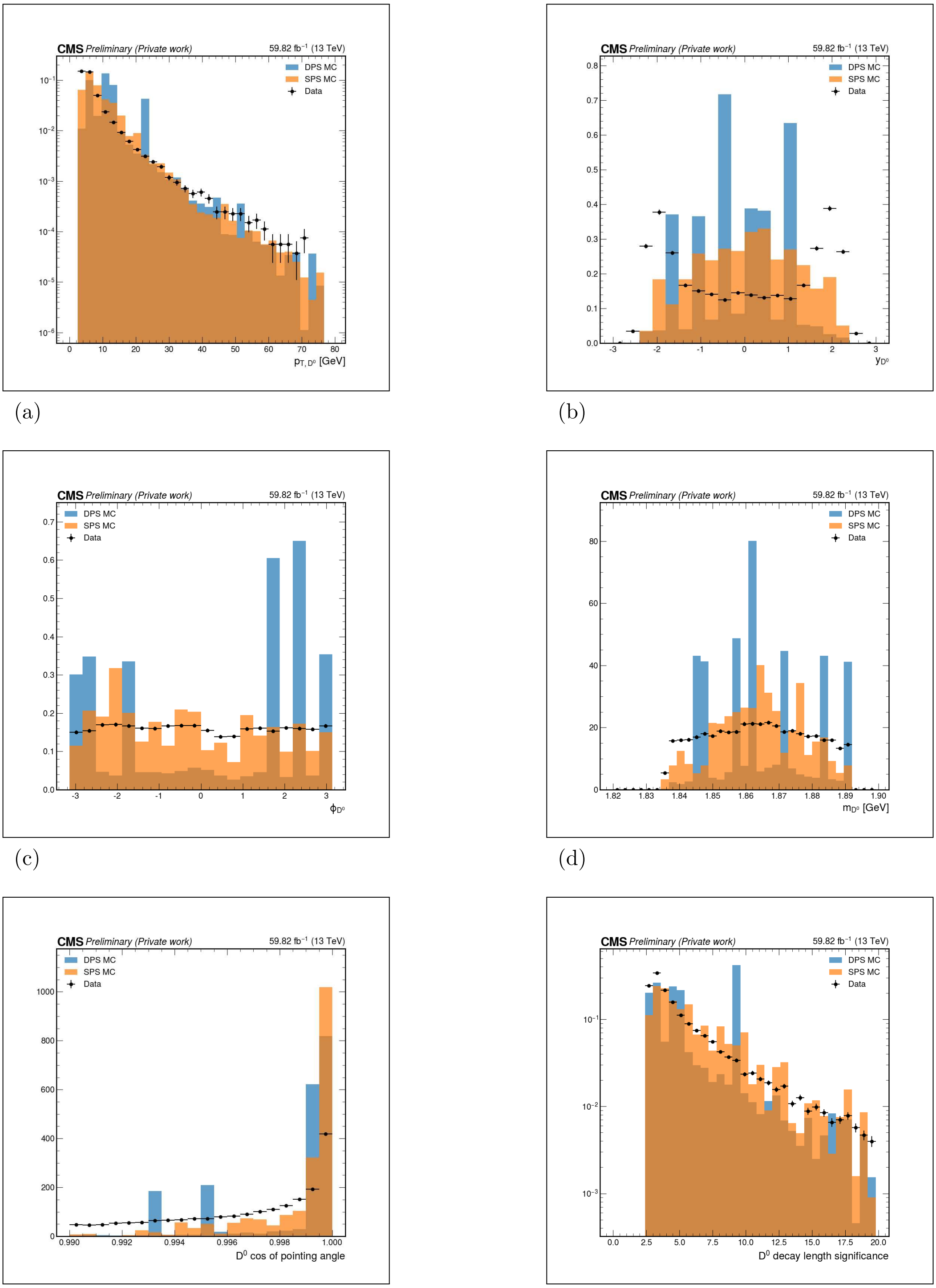

(a) (b) (c) (d) (e) (f)

Legend: p_T (a), η (b), ϕ (c), invariant mass (d), $\cos\alpha$ (e) and dl_{sig} (f) distributions for the D^0 using the 2018 data sample. The black dots represent the CMS Run 2 data, while the blue distribution represent the signal DPS MC simulation and the orange one the signal SPS MC simulation.

Source: The author, 2023.

Figure 100 - Associated Υ and D* distributions for 2018 sample

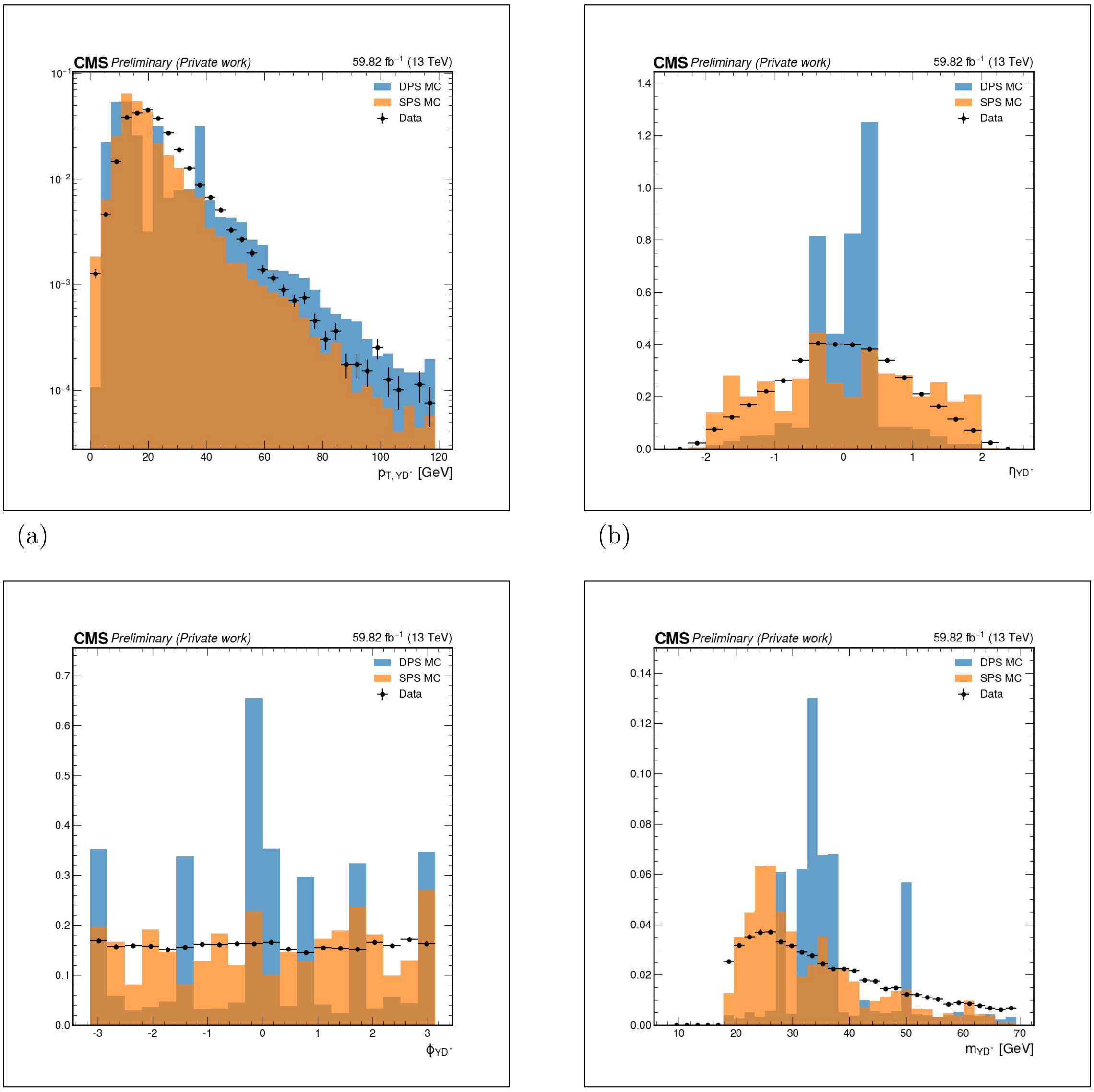

(a) (b)

(c) (d)

Legend: p$_T$ (a), y (b), ϕ (c) and invariant mass (d) distributions for the associated Υ and D* candidate using the 2018 data sample. The black dots represent the CMS Run 2 data, while the blue distribution represent the signal DPS MC simulation and the orange one the signal SPS MC simulation.

Source: The author, 2023.

Figure 101 - Associated Υ and D* Δp_T, Δy and $\Delta\phi$ distributions for 2018 sample

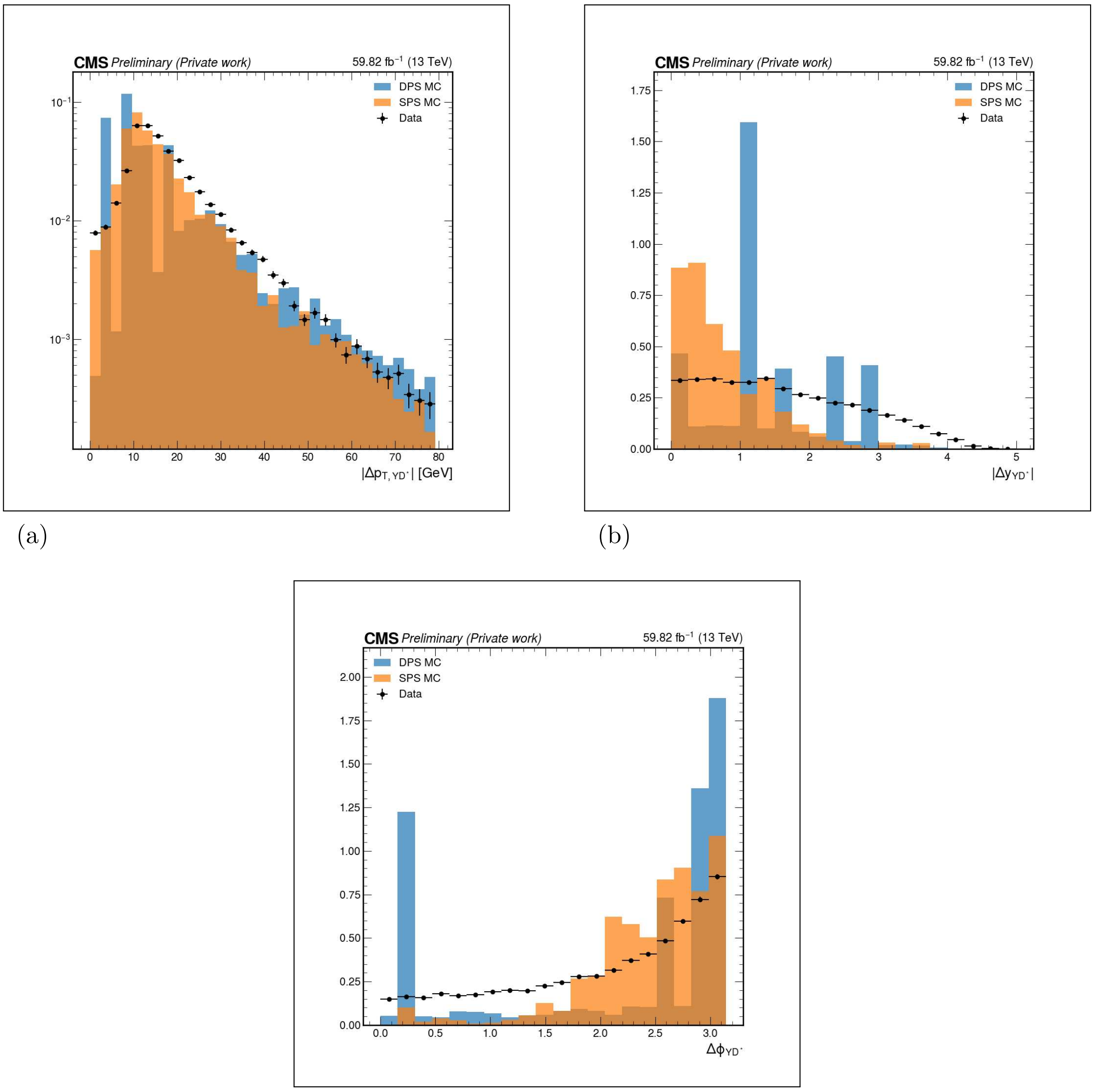

(a) (b)

(c)

Legend: Δp_T (a), Δy (b) and $\Delta\phi$ (c) distributions for the assocuated Υ and D* candidate using the 2018 data sample. The black dots represent the CMS Run 2 data, while the blue distribution represent the signal DPS MC simulation and the orange one the signal SPS MC simulation.

Source: The author, 2023.